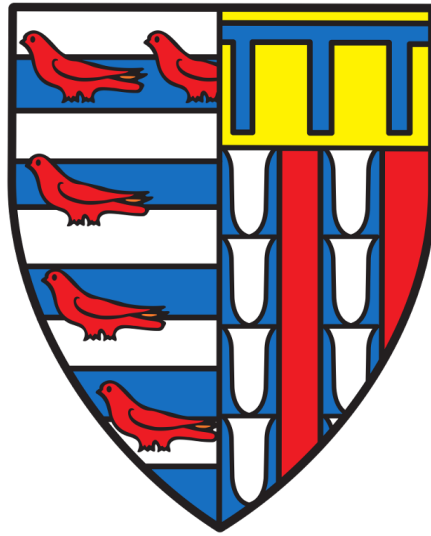


**THERMAL AND RADIATIVE PROPERTIES
OF EXOPLANET ATMOSPHERES
ACROSS THE MASS RANGE**



ANJALI AURÉLIE ALISON PIETTE

UNDER THE SUPERVISION OF
PROF. NIKKU MADHUSUDHAN

*This thesis is submitted
for the degree of Doctor of Philosophy*

PEMBROKE COLLEGE · UNIVERSITY OF CAMBRIDGE · JUNE 2021

Declaration

I hereby declare that except where specific reference is made to the work of others, the contents of this dissertation are original and have not been submitted in whole or in part for consideration for any other degree or qualification in this, or any other university. The following chapters have been published or submitted for publication as follows:

- Chapter 2 has been published in: **Piette, A. A. A.**, & Madhusudhan, N., *Considerations for atmospheric retrieval of high-precision brown dwarf spectra*, MNRAS, 497 (2020), 5136.
- Chapter 3 has been published in: **Piette, A. A. A.**, Madhusudhan, N., McKemmish, L. K., Gandhi, S., Masseron, T., & Welbanks, L., *Assessing spectra and thermal inversions due to TiO in hot Jupiter atmospheres*, MNRAS, 496 (2020), 3870.
- Chapter 4 contains work included in von Essen, C., Mallonn, M., **Piette, A.**, Cowan, N. B., Madhusudhan, N., Agol, E., Antoci, V., Poppenhaeger, K., Stassun, K. G., Khalafnejad, S., & Tautvaišienė, G., *TESS unveils the optical phase curve of KELT-1b. Thermal emission and ellipsoidal variation from the brown dwarf companion along with the stellar activity*, A&A, 648 (2021), A71.
- Chapter 5 has been published in: **Piette, A. A. A.**, & Madhusudhan, N., *On the Temperature Profiles and Emission Spectra of Mini-Neptune Atmospheres*, ApJ, 904 (2020), 154.
- Chapter 6 has been submitted for publication in: **Piette, A. A. A.**, Madhusudhan, N. & Mandell, A. M., *Atmospheric Retrieval of Rocky Exoplanets in Thermal Emission*, submitted to MNRAS.

The work presented in Chapter 3 was conducted in collaboration with the coauthors of Piette et al. (2020) as listed above. In particular, Laura McKemmish provided Figure 3.2 and contributed to the text in the first two paragraphs of Section 3.2 and in parts of

section 3.2.1, both of which I have since modified. Siddharth Gandhi provided support in calculating the TOTO cross sections, and Thomas Masseron provided the line list for the Plez (2012) TiO cross sections. Luis Welbanks provided the model transmission spectra for Figure 3.3.

In Chapter 4, the KELT-1 b TESS data was reduced in von Essen et al. (2021). Parts of the text in this chapter are adapted from text which I contributed to that publication.

This dissertation is my own work and contains nothing which is the outcome of work done in collaboration with others, except as specified explicitly. The molecular and atomic cross sections used in Chapters 1–6 were provided by, or calculated with the support of, Siddharth Gandhi. The Na and K cross sections shown in Chapter 1 and used in Chapter 2 were provided by Luis Welbanks. The GENESIS and HYDRA codes used and adapted in Chapters 2–6 were made available to me in my research group, led by Dr Nikku Madhusudhan. Published and submitted works incorporate the comments of coauthors. The use of ‘we’ instead of ‘I’ represents a stylistic choice.

This thesis is not substantially the same as any that I have submitted, or, is being concurrently submitted for a degree or diploma or other qualification at the University of Cambridge or any other University or similar institution. I further state that no substantial part of my dissertation has already been submitted, or, is being concurrently submitted for any such degree, diploma or other qualification at the University of Cambridge or any other University or similar institution.

This dissertation contains fewer than 60,000 words including the summary, tables, footnotes and appendices and has fewer than 150 figures.

Anjali Aurélie Alison Piette

June 2021

Thermal and Radiative Properties of Exoplanet Atmospheres Across the Mass Range

Anjali Aurélie Alison Piette

Summary

Observations of exoplanet atmospheres have flourished in recent years, revealing a remarkable diversity of thermal, chemical and dynamical conditions. In particular, thermal emission observations of such atmospheres provide unique insights into their temperature profiles, chemistry and energy transport mechanisms. In this thesis, I explore the radiative and thermal conditions in exoplanets across a wide range of masses and irradiation conditions, from isolated brown dwarfs to rocky exoplanets.

I begin by investigating important considerations for the atmospheric retrieval of isolated brown dwarfs. These objects provide remarkable laboratories for understanding atmospheric physics in the low-irradiation regime, and can be observed more precisely than exoplanets. As such, they provide a glimpse into the future of high-SNR observations of exoplanets. I introduce novel retrieval methods for isolated brown dwarfs, including a new temperature profile parameterisation and a method for including model uncertainty. I demonstrate this retrieval framework on both simulated and real data, showing that excellent precisions can be achieved on the inferred chemical abundances.

I further investigate the temperature profiles and thermal emission spectra of hot Jupiters, including thermal inversions in their dayside atmospheres. In particular, TiO has long been proposed to cause thermal inversions in hot Jupiters and its spectral features in the optical and near-infrared have been detected. I investigate how TiO detections can depend on the molecular line list used to interpret the data, and how this sensitivity varies across different types of atmospheric observations. I also explore the occurrence of

thermal inversions due to TiO and assess the performance of photometric metrics used to quantify them over a range in chemical composition, irradiation, gravity and stellar type.

Recent optical observations of hot Jupiters in secondary eclipse are providing new constraints on their albedos and cloud/haze scattering. I investigate this for three hot Jupiters spanning a range of temperatures and gravities: KELT-1 b, WASP-18 b and WASP-43 b. Using self-consistent atmospheric models, I interpret the optical to infrared spectra of these three targets and find that they can be explained by pure thermal emission, without the need for optical scattering by clouds or hazes. Furthermore, I find that inefficient day-night energy redistribution is needed to explain the high infrared fluxes from the daysides of these planets, consistent with previous works.

I then explore the atmospheric conditions in mini-Neptunes, whose observations are beginning to provide constraints on their chemical and thermal properties, while also providing clues about their interiors and potential surfaces. With their relatively large scale heights and large planet-star contrasts, mini-Neptunes are currently ideal targets towards the goal of characterising temperate low-mass exoplanets. I explore the effects of irradiation, internal flux, metallicity, clouds and hazes on the atmospheric temperature profiles and thermal emission spectra of temperate mini-Neptunes. Building on recent suggestions of habitability of the mini-Neptune K2-18 b, I find a range of physically-motivated atmospheric conditions that allow for liquid water under the H₂-rich atmospheres of such planets. I find that observations of thermal emission with the James Webb Space Telescope (JWST) can place useful constraints on the habitability of temperate mini-Neptunes such as K2-18 b. These results underpin the potential of temperate mini-Neptunes such as K2-18 b as promising candidates in the search for habitable exoplanets.

Finally, I explore the characterisation of rocky exoplanet atmospheres across a wide temperature range. JWST will allow unprecedented characterisation of the atmospheres of small, rocky exoplanets. In particular, emission spectroscopy is an ideal technique to observe the secondary atmospheres of rocky exoplanets as such observations are not limited by the small scale height of high-mean-molecular-weight atmospheres. I develop a new retrieval framework tailored for rocky exoplanet atmospheres with unknown atmospheric constituents, and use this to assess the observability of promising, known rocky exoplanet targets. I find that the atmospheres of several known rocky exoplanets across a range of temperatures can be characterised using JWST.

Acknowledgements

First and foremost, I would like to thank my supervisor, Nikku Madhusudhan, for his continued guidance and support throughout my PhD. It has been an amazing experience and I am forever grateful for everything you have taught me. I would also like to acknowledge my collaborators, who have taught me a lot and enriched the work in this thesis. In particular, I am very grateful for insightful discussions with Avi Mandell, Laura McKemmish and Thomas Masseron. A big thank you also to the other students (past and present) in our group for the many dynamic and interesting discussions, both scientific and otherwise! In particular, I'd like to thank Siddharth Gandhi for teaching me to use HYDRA , GENESIS and how to compute cross sections, and for sharing his wisdom in general. Thanks also to Luis Welbanks for many interesting discussions over the past 4 years, and to John Harrison for teaching me to use HSC CHEMISTRY.

I am also very grateful to my PhD examiners, Cathie Clarke and Nathan Mayne. I greatly appreciate their thoughtful comments, interesting questions and the very interesting and enjoyable discussion during the viva.

I would like to thank the people whose support, encouragement and advice has shaped my academic path even before my PhD. In particular, thank you to my summer project and master's supervisors Grant Kennedy, Antonia Rowlinson, Jess Broderick, Mark Wyatt and Rik van Lieshout. Thanks also to Floor, Xiaoxi, Anoj, Yuping and Aarthi for an amazing summer at ASTRON/JIVE and for being such inspiring friends.

The Institute of Astronomy has provided a wonderful environment for the many years I have been here, and I am very grateful to everyone at the IoA who has made the PhD experience so smooth and enjoyable. In particular, a big thank you to Debbie Peterson and Paul Hewett for looking after us all, and to the IoA helpdesk for their incredible support! I would also like to thank the Science and Technology Facilities Council, UK, for funding my PhD and providing additional support following the coronavirus pandemic.

The last four years would not have been the same without the great friends I have made at Pembroke and the IoA. To Antonia, Sophie, Bec, Diney and Maria, I will always be grateful for your friendship and the great times we've had and will have together. Thanks

also to my PhD cohort at the IoA for all the great times we've had together, especially Luis, Amy, Matthew, Laura and Sophie. And to Nimisha, Seba, Matt, Björn, Dominika and Clare - thank you for making my first year so memorable, and for sharing your wisdom on fourth year and beyond...!

Je remercie aussi ma famille: Papa qui m'a appris la science, Maman qui m'a appris le reste, Mimi qui me supporte quand je suis insupportable et Sita qui nous fait tous rire. Merci à Mamie Sasou, Papy Sousou, Mamie Blanche et Papy Raymond, qui resteront toujours les meilleurs grands-parents que j'aurais pu avoir.

And finally, thank you to Matt, who has supported me, made me laugh and kept me sane for the past four years. I'm excited for our journey together in the years to come.

Pour Papa.



Table of contents

List of figures	xv
List of tables	xix
1 Introduction	1
1.1 Detecting Exoplanets and their Atmospheres	3
1.1.1 Exoplanet Detection Methods	3
1.1.2 Atmospheric Characterisation Methods	6
1.1.3 Key Results in Atmospheric Characterisation	11
1.2 Physics of Exoplanet Atmospheres	14
1.2.1 Energy Transport and Atmospheric Temperature Profiles	14
1.2.2 Atmospheric Chemistry and Opacity	18
1.2.3 Radiative Transfer and Thermal Emission Spectra	22
1.3 Modelling Exoplanet Atmospheres	24
1.3.1 Self-Consistent 1D Atmospheric Models	24
1.3.2 Atmospheric Retrievals	26
1.4 Diversity of Exoplanets	30
1.4.1 Poorly-Irradiated Gas Giants and Sub-Stellar Objects	30
1.4.2 Hot Jupiters	31
1.4.3 Mini-Neptunes	33
1.4.4 Rocky Exoplanets	34
1.4.5 Habitable Exoplanets	36
1.5 Overview of this Thesis	37
2 Considerations for Atmospheric Retrieval of High-Precision Brown Dwarf Spectra	39
2.1 Introduction	40
2.2 Atmospheric Model	42

2.3	Treatment of Model Uncertainties	46
2.3.1	Uncertainties in the model spectra	46
2.3.2	Generating Simulated Data	52
2.3.3	Treatment of Uncertainties	53
2.4	A P-T Parameterisation for Brown Dwarfs	54
2.4.1	Thermal and Opacity Structure of Brown Dwarfs	55
2.4.2	P-T Parametrisation	59
2.5	Retrieval of Simulated Data	61
2.6	Application to Data	65
2.6.1	Chemical abundances	66
2.6.2	P-T profile	69
2.6.3	R/d, gravity and tolerance	69
2.7	Summary and Discussion	70
3	Assessing Spectra and Thermal Inversions due to TiO in Hot Jupiter Atmospheres	75
3.1	Introduction	76
3.2	Impact of TiO line lists on exoplanet opacity	79
3.2.1	Quantifying line list suitability for high-resolution spectroscopy . . .	81
3.2.2	Effect of line list choice on Transmission Spectra	83
3.2.3	Effect of line list choice on Emission Spectra	85
3.3	Influence of Chemistry on Thermal Inversions	87
3.4	Metrics for Assessing Thermal Inversions	91
3.5	Metrics as a function of planetary and host star properties	95
3.5.1	Inversion strength	97
3.5.2	Performance of metrics	100
3.5.3	Comparison of data to models	102
3.6	Summary and Discussion	106
4	Cloud Scattering and Thermal Emission across the Hot Jupiter Regime	109
4.1	Introduction	109
4.2	Atmospheric Model	111
4.3	Modelling the Dayside and Nightside Emission of KELT-1 b	113
4.4	Modelling the Dayside Atmospheres of WASP-43 b and WASP-18 b	116
4.5	Summary and Conclusions	119
5	Temperature Profiles and Emission Spectra of Mini-Neptune Atmospheres	121
5.1	Introduction	122

5.2	Atmospheric Model	125
5.2.1	Energy budget and radiative-convective equilibrium	125
5.2.2	Radiative transfer	126
5.2.3	Chemistry, opacities and clouds/hazes	127
5.2.4	System parameters	129
5.2.5	Model comparison	130
5.3	Effects of Atmospheric Parameters	133
5.3.1	Temperature profiles and energy transport	133
5.3.2	Thermal Emission Spectra	138
5.4	Considerations for habitability	141
5.4.1	Conditions for an ocean	143
5.4.2	Effects of cloud/hazes, metallicity and T_{int}	144
5.4.3	Effects of H ₂ O saturation	147
5.5	Observability	149
5.5.1	Constraints on habitability	150
5.5.2	JWST for mini-Neptune habitability	152
5.5.3	JWST for warmer mini-Neptunes	153
5.6	Discussion & Conclusions	155
6	Atmospheric Retrieval of Rocky Exoplanets in Thermal Emission	159
6.1	Introduction	160
6.2	Retrieval Framework & Atmospheric Model	161
6.2.1	Retrieval Framework	162
6.2.2	Self-Consistent Atmospheric Model & Simulated Data	167
6.2.3	Validation of Retrieval Framework	168
6.3	Target Selection	171
6.4	Results	173
6.4.1	Case Study: LHS 3844 b	175
6.4.2	Case Study: GJ 1132 b	181
6.4.3	Case Study: Trappist-1 b	182
6.5	Discussion	184
6.5.1	Degeneracies & Detection Significances	185
6.5.2	Impact of Clouds and Hazes	186
6.5.3	3D effects	187
6.6	Conclusions	188

7	Conclusions and Future Directions	191
7.1	Poorly-Irradiated Giant Exoplanets and Sub-Stellar Objects	191
7.2	Hot Jupiters	193
7.3	Mini-Neptunes	194
7.4	Rocky Exoplanets	195
7.5	Future Directions	196
	References	199
	Appendix A Retrieval of 2MASS J2339+1352 without Na and K	237
	Appendix B Equilibrium TiO Chemistry & High-Resolution Spectroscopy	241
B.1	Equilibrium Chemistry Calculations	241
B.2	Effect of Temperature Gradient on High-Resolution Spectra	241
B.3	Effect of metallicity on equilibrium chemistry	244
	Appendix C Optimal targets for rocky exoplanet thermal emission	245

List of figures

1.1	Exoplanet demographics across radius and temperature	2
1.2	Phase curve of a transiting exoplanet	4
1.3	Atmospheric temperature profiles for non-irradiated and strongly-irradiated giant exoplanets	16
1.4	Equilibrium chemical abundances for important chemical species in exo- planet atmospheres	19
1.5	Absorption cross sections of key chemical species in exoplanet atmospheres	21
1.6	Schematic of the GENESIS self-consistent 1D atmospheric model	25
1.7	Schematic of an atmospheric retrieval framework	27
1.8	The ‘radius valley’ in the radius distribution of low-mass exoplanets	33
2.1	Comparison of model emission spectra for Gl 570D	45
2.2	Model uncertainty for different cross section sampling methods and spectral resolutions	47
2.3	Model uncertainty for different vertical resolutions	48
2.4	Posterior probability distributions obtained with two different tolerance parameters	48
2.5	Model temperature profile and emission spectrum for Gl 570D	55
2.6	Contributions of different chemical species to atmospheric absorption . . .	56
2.7	Effect of changing the slope of the P - T profile at high pressures on the spectrum	57
2.8	‘SPT’ parametric P - T model used in our retrieval framework	57
2.9	Retrieved spectrum and temperature profile for simulated data based on Gl 570D	61
2.10	Marginalised posterior probability distributions from the retrieval of simu- lated data based on Gl 570D	62
2.11	Spectrum and temperature profile retrieved for 2MASS J2339+1352	66

2.12 Marginalised posterior probability distribution from the retrieval of 2MASS J2339+1352	67
2.13 Posterior probability distributions of the NH ₃ abundance from the retrieval of simulated data with input NH ₃ mixing fractions of 10 ^{-4.64} , 10 ⁻⁶ and 10 ⁻⁷ , respectively	68
3.1 Comparison of the TOTO, Schwenke (1998) and Plez (1998) TiO cross sections	80
3.2 Comparison of the full TOTO and MARVEL-only TiO cross sections	82
3.3 Comparison of transmission spectra calculated using the TOTO and Schwenke (1998) TiO cross sections	84
3.4 Comparison of emission spectra calculated using the TOTO and Schwenke (1998) TiO cross sections	86
3.5 Equilibrium abundances of TiO, H ₂ O and CO and the ratio of optical to infrared opacity as a function of temperature and C/O ratio	89
3.6 Temperatures and pressures probed by the J-band, H-band, IRAC 1 and IRAC 2 photometric bands	92
3.7 Optical depth as a function of wavelength and pressure for atmospheres with and without a thermal inversion	94
3.8 Inversion maps showing the strength of the inversion/non-inversion of equilibrium <i>P-T</i> profiles as a function of equilibrium temperature, C/O ratio and metallicity.	98
3.9 Inversion strength as a function of equilibrium temperature, C/O ratio and stellar type of the host star	99
3.10 Inversion strength as a function of equilibrium temperature and C/O ratio for a planet with log(<i>g</i> /cm ⁻²)=4.26	101
3.11 Brightness temperatures probed by HST/WFC3 and Spitzer IRAC 1 and IRAC 2 data for seven hot Jupiters	103
4.1 Model dayside spectra and temperature profiles for KELT-1 b	113
4.2 Model nightside spectra and temperature profiles for KELT-1 b	115
4.3 Self-consistent temperature profiles and thermal emission spectra for the dayside atmospheres of WASP-43 b and WASP-18 b	117
5.1 Comparison with model pressure-temperature profiles of mini-Neptunes in the literature	131
5.2 <i>P-T</i> profiles for model atmospheres with varying haze and cloud opacities .	135
5.3 Self-consistent atmospheric <i>P-T</i> profiles across a range of internal temperatures, irradiation temperatures and infrared opacities	137

5.4	Model thermal emission spectra corresponding to the P - T profiles in Figure 5.2 for varying haze and cloud opacities	139
5.5	Model thermal emission spectra corresponding to the P - T profiles in Figure 5.3, for varying T_{int} , T_{irr} and infrared opacity	140
5.6	Schematic of an atmospheric P - T profile and the corresponding phases of the atmospheric H_2O and of the 100% H_2O layer beneath the atmosphere .	142
5.7	Model dayside P - T profiles for K2-18 b, for a range of metallicities and internal temperatures, that could allow habitable conditions below the atmosphere	145
5.8	Model dayside P - T profiles for a planet resembling K2-18 b with an irradiation temperature of 420 K that could allow habitable conditions below the atmosphere	146
5.9	Model dayside P - T profiles for K2-18 b with 100% relative humidity which allow for a liquid ocean at the surface	148
5.10	Observability of temperate and potentially habitable mini-Neptunes with JWST/MIRI	151
5.11	Observability of thermal emission from warm mini-Neptunes with JWST/MIRI	154
6.1	Prior probability densities for log chemical abundances using the centred-log-ratio parameterisation or log-normal priors	163
6.2	Cross sections of important sources of opacity in the mid-infrared for secondary atmospheres	165
6.3	Retrieved emission spectrum, temperature profile and chemical abundances for simulated data of Trappist-1 b, assuming a Venus-like composition . . .	170
6.4	Observability of known rocky planets in thermal emission as a function of planet radius, equilibrium temperature and K magnitude of the host star . .	174
6.5	Thermal emission spectra and simulated MIRI data for LHS 3844 b, GJ 1132 b and Trappist-1 b assuming Venus-like, 50% CO_2 /50% H_2O or 100% H_2O compositions	176
6.6	Retrieved thermal emission spectra for simulated data of LHS 3844 b, GJ 1132 b and Trappist-1 b	177
6.7	Retrieved temperature profiles for simulated data of LHS 3844 b, GJ 1132 b and Trappist-1 b	178
6.8	Retrieved chemical abundance posterior probability distributions for simulated data of LHS 3844 b, GJ 1132 b and Trappist-1 b	179
A.1	Spectrum and P - T profile retrieved for 2MASS J2339+1352 without including Na and K in the retrieval model	237

A.2	Marginalised posterior probability distributions from the retrieval of 2MASS J2339+1352 without Na and K	239
B.1	Line strengths of high-resolution ($R \sim 10^5$) spectra compared to a blackbody spectrum for different temperature gradients	242
B.2	High-resolution ($R \sim 10^5$) model spectra corresponding to a steep and a shallow P - T profile	243
B.3	Abundances of TiO, H ₂ O and CO as a function of temperature for metallicities of 0.1, 1 and $10 \times$ solar	244

List of tables

2.1	The priors used for each model parameter	44
2.2	Input and retrieved parameter values for the simulated spectrum of Gl 570D	45
2.3	Properties of 2MASS J23391025+1352284 from the literature.	65
2.4	A summary of the retrieved atmospheric properties of 2MASS J2339+1352. .	70
4.1	Planetary properties for KELT-1 b, WASP-18 b and WASP-43 b.	111
6.1	Prior probability distributions for the P - T profile parameters	162
6.2	Planetary and stellar parameters for the rocky exoplanets modelled	169
6.3	Detection significances for chemical detections given different atmospheric compositions and observing strategies for LHS 3844 b, GJ 1132 b and Trappist-1 b	184
A.1	A summary of the retrieved atmospheric properties of 2MASS J2339+1352 without including Na and K in the retrieval. These values are consistent with the results of the retrieval which includes Na and K (Section 2.6).	238
B.1	Species added to the HSC CHEMISTRY equilibrium chemistry calculations, on top of those used in Bond et al. (2010) and Harrison et al. (2018)	242
C.1	Properties of known rocky exoplanets whose thermal emission in secondary eclipse can be measured to $S/N=3$ (at $R \sim 10$) in ≤ 10 eclipses with MIRI LRS	246

1

Introduction

The search for planets and life beyond the solar system is arguably at the heart of the quest to understand our place in the universe. For millennia, the diverse planetary conditions within our own solar system have captured the imagination of humans, from philosophy to spaceflight. Now, in the past few decades, the discovery and characterisation of thousands of exoplanets has expanded this diversity to new proportions. From observations of hot, Jupiter-sized worlds to exoplanets between the sizes of Earth and Neptune and rocky planets orbiting stars not much larger than Jupiter itself, the field of exoplanets has shattered all expectations set by our nearest planetary neighbours. As observational facilities and theoretical advancements steadily improve, increasingly detailed characterisation of these exoplanets continues to reveal exotic and exciting physical phenomena.

The diversity of exoplanet sizes and temperatures discovered to date is summarised in Figure 1.1. Notably, the most common type of exoplanet discovered to date - ‘sub-Neptunes’ - lies between the sizes of Earth and Neptune and is not represented in the solar system. Indeed, Figure 1.1 highlights the incredible variety of conditions present among the known population of exoplanets, from roasting giant planets (‘hot Jupiters’) to exotic mini-Neptunes and rocky exoplanets.

Given the vast distances to these exoplanets, their discovery and characterisation depends on innovative techniques. For example, many exoplanets are discovered, and their atmospheres characterised, by analysing modulations in the light coming from the unresolved star/planet system (e.g. Wright and Gaudi, 2013; Fischer et al., 2014; Kreidberg, 2018). The ability to extract such signals is a testament to the technological advances and creative methods which have been developed. In particular, observations of exo-

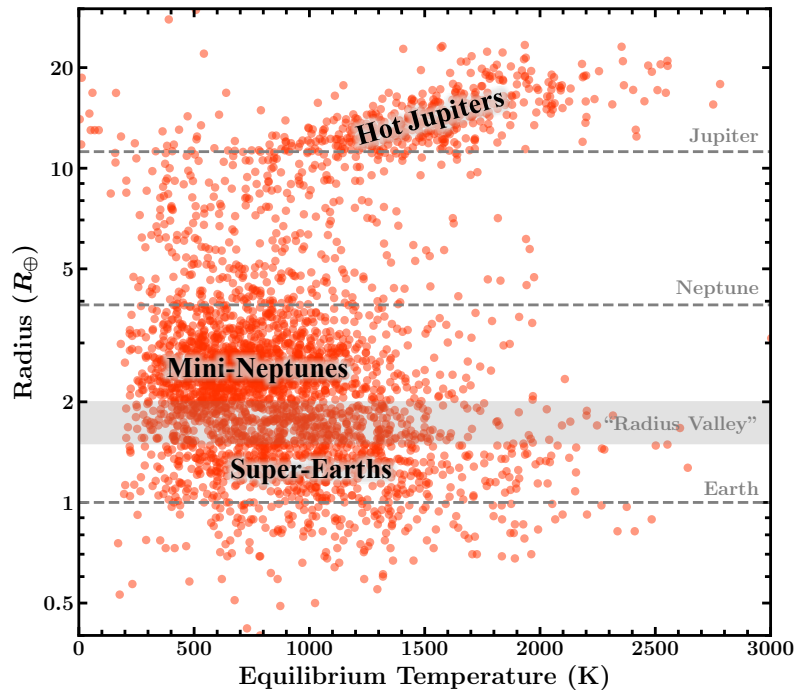


Fig. 1.1 The radii and equilibrium temperatures of known exoplanets with radius measurements. Equilibrium temperature is calculated assuming planet-wide redistribution of incident energy and zero albedo. Hot, Jupiter-sized exoplanets ('hot Jupiters') are the easiest to detect using the transit and radial velocity methods, and form a cluster at the top of this figure. A dearth of exoplanets has been identified between radii of $\sim 1.5\text{-}2 R_{\oplus}$ (the 'radius valley', Fulton et al. 2017), which divides 'mini-Neptunes' from 'super-Earths' and smaller, rocky exoplanets. Collectively, exoplanets between the sizes of Earth and Neptune may be referred to as 'sub-Neptunes'. The radii of Earth, Neptune and Jupiter are shown with dashed grey lines for reference. Exoplanet data is from the NASA Exoplanet Archive: <https://exoplanetarchive.ipac.caltech.edu>

planet atmospheres provide a window into their formation mechanisms, evolution and surface/interior physics.

The field of atmospheric characterisation was initiated two decades ago with the first atmospheric detection of a transiting exoplanet (Charbonneau et al., 2002), and has led to significant strides in the understanding of exoplanetary physics. In this thesis, I explore the properties of exoplanet atmospheres across a wide range of masses and irradiation regimes, from isolated sub-stellar objects to hot Jupiters, temperate mini-Neptunes and rocky exoplanets. I begin by introducing the techniques used to detect and characterise such atmospheres, as well as the theoretical methods used to interpret and understand these observations.

1.1 Detecting Exoplanets and their Atmospheres

The first exoplanet orbiting a main-sequence star was discovered in 1995 (Mayor and Queloz, 1995), and its exotic properties radically changed ideas on planetary physics and formation. This exoplanet, 51 Pegasi b, has a size similar to Jupiter but its orbital period is only ~ 4 days. Such ‘hot Jupiters’ are the easiest type of exoplanet to detect with current methods, and dominated the early findings of exoplanets (e.g. Marcy and Butler, 2000). Since then, progressively smaller and cooler planets have been both detected and characterised, including rocky exoplanets in the habitable zones of their host stars (e.g. Dressing and Charbonneau, 2015; de Wit et al., 2016; Gillon et al., 2016; Winn, 2018; Benneke et al., 2019b; Tsiaras et al., 2019). In what follows, I describe some of the methods used to detect exoplanets and to characterise their atmospheres.

1.1.1 Exoplanet Detection Methods

A range of methods exist to detect the presence of exoplanets around other stars. Each method allows constraints on a particular set of planetary parameters, e.g. mass or radius, and is sensitive to a different range of planetary sizes and orbits. Three of the main detection methods, which are also relevant for atmospheric characterisation, are the transit method, the radial velocity method, and direct detection (see also review by Fischer et al. 2014).

The majority of exoplanets discovered to date ($\sim 76\%$ of the 4364 exoplanets discovered at the time of writing) have been found using the transit method (e.g. Deeg and Alonso, 2018), the first of which was HD 209458 b (Charbonneau et al., 2000; Henry et al., 2000). This method detects planets as they pass in front of their host stars and block a portion of the observed stellar flux. The Kepler telescope in particular (Borucki, 2018) has found $\sim 65\%$ of all confirmed exoplanets using this method, while the Transiting Exoplanet Survey Satellite (TESS, Ricker et al. 2015) has 125 confirmed exoplanet detections and 2684 candidates to date.

Figure 1.2 shows how the passage of a planet in front of its host star relative to an observer (the primary eclipse) results in a lower observed flux. Note that the orbit of the planet must pass between the star and the observer for this effect to be seen; many planets do not satisfy this condition and so cannot be detected using the transit method. Furthermore, planets that are closer to their host stars are more likely to transit, making this method most sensitive to planets on small orbits. Such planets also transit more frequently, allowing for repeated observations and more confident detections. Due to tidal effects, these small-orbit planets are often ‘tidally locked’, meaning that they have

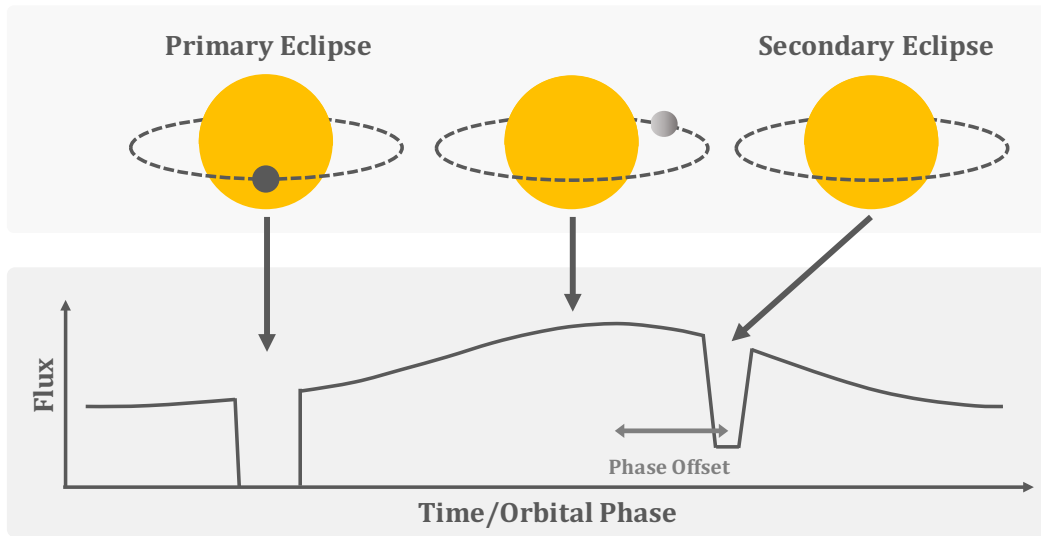


Fig. 1.2 The phase curve of a transiting exoplanet. The primary eclipse occurs when the exoplanet transits the host star, while the secondary eclipse occurs when the planet passes behind the star. For infrared phase curves, if the hottest point on the dayside is shifted away from the sub-stellar point, this results in a phase offset between the peak in the light curve and the secondary eclipse. The shape of the phase curve is sensitive to the wavelength of the observation, e.g. optical phase curves typically probe reflected stellar light while infrared phase curves probe the thermal emission of the planet.

permanent day- and nightsides. Planets with larger radii are also easier to detect as they block more light from the star.

The transit method can be used to determine the radius and semi-major axis of an exoplanet. In particular, the fractional reduction in flux during the transit is defined as $\Delta = (f_{\text{out}} - f_{\text{in}}) / f_{\text{out}}$, where f_{in} and f_{out} are the fluxes of the star in and out of the transit, respectively. It is related to the relative sizes of the planet and star as follows:

$$\Delta = \frac{R_p^2}{R_\star^2} \quad (1.1)$$

where R_p and R_\star are the radii of the planet and the star, respectively. Thus, if the radius of the star is known, the planet radius can be derived. Since the period between consecutive primary transits is equal to the orbital period of the planet, P_t , it can be used to derive the semi-major axis of the planet, a , using Kepler's third law:

$$a^3 = GM_\star \left(\frac{P_t}{2\pi} \right)^2, \quad (1.2)$$

where G is the gravitational constant and M_\star is the mass of the star.

A second method for detecting exoplanets is the radial-velocity (RV) method (Fischer et al., 2016; Wright, 2018). This involves detecting the planet-induced motion of a host star through periodic Doppler shifts in the stellar spectrum, which can be observed using high-resolution spectroscopy. In particular, the radial velocity of the star, $v_{\star,r}$, can be measured. Given the possible inclination, i , of the star-planet system, $v_{\star,r}$ is a lower limit on the true stellar orbital velocity, $v_{\star} = v_{\star,r} / \sin(i)$. Through conservation of momentum, the orbital velocities and masses of the star and planet are related: $M_{\star} v_{\star} = M_p v_p$, where v_p and M_p are the orbital velocity and mass of the planet, respectively. Combined with Kepler's third law (Equation 1.2), and the fact that $M_p \ll M_{\star}$, a lower limit on the planetary mass can be derived given M_{\star} and the observed stellar radial velocity:

$$M_p^3 \sin^3(i) \approx \frac{P_t}{2\pi G} v_{\star,r}^3 M_{\star}^2.$$

The RV method can therefore be used to constrain planetary masses. Furthermore, for transiting exoplanets, the inclination can be determined from transit observations, resulting in an estimate of the true planetary mass. In turn, the planetary mass is useful for the characterisation of the bulk composition and interior of the planet; in combination with the radius measured using the transit method (Equation 1.1), it provides a constraint on the density and surface gravity of the planet. Since larger planetary masses and orbital velocities result in larger Doppler shifts of the stellar spectrum, the RV method is more sensitive to more massive planets with smaller orbits. As with the transit method, smaller orbits also allow repeated observations to be made, resulting in more confident detections.

A third exoplanet detection method is direct detection, also known as direct imaging (e.g. Marois et al., 2008; Lagrange et al., 2010; Lagrange, 2014; Macintosh et al., 2015; Bowler and Nielsen, 2018; Pueyo, 2018). Unlike the transit and RV methods, this involves the direct measurement of planetary flux without contributions from the stellar flux (apart from stellar light reflected from the planet, if present). To achieve this, the planet must be far away from its host star ($\gtrsim 10$ au) and have a large intrinsic flux. This is the case for very young, far-out planets which have not yet lost the internal heat remnant from their formation. Such detections are typically made by blocking the stellar flux, e.g. with a coronagraph. Direct imaging can also be used to detect isolated planetary objects or brown dwarfs with no host star. In this case, there is no stellar flux to be blocked, and the measured flux comes purely from the thermal emission of the planet or brown dwarf.

1.1.2 Atmospheric Characterisation Methods

Beyond the detection of exoplanets, methods exist to observe and characterise their atmospheres (e.g. see reviews by Kreidberg, 2018; Madhusudhan, 2019). These methods are principally used for transiting exoplanets (e.g. detected with the transit method) and directly-imaged planets. For transiting exoplanets, the atmosphere results in very small, wavelength-dependent variations in the flux observed from the star+planet system. For directly-imaged exoplanets, the wavelength-dependent flux emanating from the planet is directly observed, but this is also typically very small as planets are much cooler and less luminous than stars. In both cases, the atmospheric signal is very small meaning that atmospheric characterisation is typically only possible for relatively nearby planetary systems and isolated planetary objects. Here, I describe five key methods used to observe and characterise exoplanet atmospheres: transmission spectroscopy, secondary eclipse spectroscopy, phase curve observations, high-resolution Doppler spectroscopy and thermal emission spectroscopy of directly-imaged objects.

Transmission spectroscopy involves observing the atmosphere of an exoplanet as it passes in front of its host star, i.e. during the primary eclipse (see Figure 1.2). In this geometry, light from the star is blocked by the bulk of the planet, but some stellar light is able to pass through the atmosphere. However, this transmission is frequency-dependent as chemical species in the atmosphere preferentially absorb light at certain wavelengths. At these wavelengths, the atmosphere is therefore more opaque and the apparent radius of the planet is larger. As a result, the primary transit depth, Δ (Equation 1.1), varies with wavelength; this is referred to as the ‘transmission spectrum’. For example, H_2O is known to have a prominent absorption feature at $\sim 1.4 \mu\text{m}$. If Δ is observed to be larger at $\sim 1.4 \mu\text{m}$ compared to neighbouring wavelengths, this is an indication that H_2O vapour is present in the exoplanet’s atmosphere.

Variations in Δ due to the atmosphere can be estimated by considering the atmospheric height, H_A . At wavelengths where the atmosphere is transparent, the apparent radius of the planet is simply R_p , i.e. corresponding to the surface for rocky exoplanets or the deeper, optically thick region of the atmosphere for giant planets. Where the atmosphere is opaque, however, the apparent planetary radius is $R'_p = R_p + H_A$, where $H_A \ll R_p$. The variation in Δ between these two scenarios, δ , is therefore:

$$\delta = \left(\frac{R'_p}{R_\star} \right)^2 - \left(\frac{R_p}{R_\star} \right)^2 \approx \frac{2R_p H_A}{R_\star^2}. \quad (1.3)$$

In turn, H_A is proportional to the scale height, H_{sc} , of the atmosphere. H_{sc} is the lapse rate of pressure, P , or density, ρ , as a function of height, z , in an isothermal atmosphere at temperature T in hydrostatic equilibrium. It can be calculated by considering the equation of hydrostatic equilibrium,

$$\frac{dP}{dz} = -\rho g, \quad (1.4)$$

and the ideal gas law,

$$P = \frac{k_B}{\mu} \rho T, \quad (1.5)$$

where μ is the mean molecular weight of the atmosphere and g is the surface gravity of the planet. Note that for the purposes of estimating the atmospheric scale height, g does not vary significantly within the observable atmosphere since this typically contributes only a very small fraction of the planetary mass and radius. For example, in the case of a hot Jupiter, g would vary by a factor of ~ 0.1 across the observable atmosphere assuming an atmospheric scale height of ~ 400 km and an observable atmospheric height of ~ 10 scale heights. This change is, however, important to consider in models of exoplanet atmospheres (e.g. Section 1.3).

Together, these equations result in an atmospheric scale height of $H_{sc} = \frac{k_B T}{\mu g}$. Combined with equation 1.3, it is clear that features in the transmission spectrum are larger for hotter, larger planets with low μ and surface gravities. ‘Hot Jupiters’, i.e. very hot Jupiter-mass planets orbiting close to their host stars, are therefore ideal for transmission spectroscopy. Conversely, cool, small exoplanets with high- μ atmospheres, e.g. resembling the terrestrial planets in the solar system, have much smaller features and are more difficult to characterise. Furthermore, for any type of planet, the presence of clouds and/or strong hazes can make the atmosphere opaque across a wide range of wavelengths, resulting in a flat transmission spectrum. Cloudy atmospheres can therefore be challenging to characterise using transmission spectroscopy (e.g. Kreidberg et al., 2014a; Barstow, 2021).

Since transmission spectroscopy relies on observing modulated stellar light, it is typically carried out at (or close to) wavelengths where the stellar spectrum is significant, i.e. in the UV, optical and near-infrared. Each of these wavelength ranges is sensitive to different types of absorption features. For example, the UV is sensitive to escaping, extended atmospheres (Bourrier and Lecavelier des Etangs, 2018) while the optical is sensitive to cloud and haze scattering as well as atomic and ionic species and some molecules, e.g. metal oxides and hydrides such as AlO, TiO, VO, MgH and TiH (e.g. Charbonneau et al., 2002; Wakeford and Sing, 2015; Sedaghati et al., 2017). Conversely, the infrared is sensitive to a wide range of molecular species including H₂O, CH₄, CO, CO₂, NH₃ and

HCN (Madhusudhan, 2019). Both space-based and ground-based facilities are used to observe transmission spectra. This includes the Hubble Space Telescope’s (HST’s) Cosmic Origins Spectrograph (COS, 0.0815-0.32 μm , e.g. Linsky et al. 2010; Haswell et al. 2012; Ben-Jaffel and Ballester 2013), Space Telescope Imaging Spectrograph (STIS, 0.115-1 μm , e.g. Charbonneau et al. 2002; Vidal-Madjar et al. 2003) and Wide Field Camera 3 (WFC3, 0.8-1.7 μm in the infrared channel, e.g. Berta et al. 2012; McCullough and MacKenty 2012; Deming et al. 2013), as well as ground-based spectrographs such as CARMENES at the Calar Alto Observatory (0.52-1.71 μm , e.g. Allart et al. 2018; Salz et al. 2018; Yan and Henning 2018), HARPS at the ESO La Silla 3.6 m telescope (0.378-0.691 μm , e.g. Heng et al. 2015; Louden and Wheatley 2015; Wyttenbach et al. 2015), FORS/FORS2 at the VLT (0.33-1.10 μm , e.g. Bean et al. 2010; Sedaghati et al. 2015) and OSIRIS at the Gran Telescopio Canarias (0.365-1.050 μm , e.g. Sing et al. 2011, 2012; Colón et al. 2012).

Secondary eclipse spectroscopy involves observing the thermal flux of a transiting exoplanet (plus any reflected stellar light) by separating it from the total stellar+planetary flux (e.g. see review by Kreidberg, 2018). When the exoplanet is behind the host star relative to the observer (i.e. in secondary eclipse, see Figure 1.2), only the stellar flux is observed, f_\star . However, just before or after the secondary eclipse, the dayside of the exoplanet is visible in addition to the star, resulting in a total observed flux of $f_\star + f_p$, where f_p is the flux due to the planet. The ratio of the out- and in-transit fluxes can therefore be used to determine the emission spectrum of the planet, i.e. f_p/f_\star as a function of wavelength. It can be instructive to approximate this quantity by assuming that the star and planet emit as blackbodies:

$$\frac{f_p}{f_\star} = \frac{R_p^2 B_\lambda(T_p)}{R_\star^2 B_\lambda(T_\star)}, \quad (1.6)$$

where T_p and T_\star are the temperatures of the planet and star, respectively. B_λ is the Planck function:

$$B_\lambda(T, \lambda) = \frac{2hc^2}{\lambda^5} \frac{1}{e^{\frac{hc}{\lambda k_B T}} - 1},$$

where T is temperature, λ is wavelength, h is Planck’s constant, k_B is Boltzmann’s constant and c is the speed of light.

Equation 1.6 shows that the secondary eclipse signal is greater for hotter, larger planets. Furthermore, since the planet is cooler than its host star, $B_\lambda(T_p)$ peaks at longer wavelengths compared to $B_\lambda(T_\star)$ and f_p/f_\star is therefore larger at longer wavelengths. At very long wavelengths (i.e. $\lambda \gg hc/k_B T_p$), $B_\lambda(T) \rightarrow 2ck_B T/\lambda^4$ (the Rayleigh Jeans limit), and $f_p/f_\star \rightarrow \frac{R_p^2 T_p}{R_\star^2 T_\star}$, i.e. a constant. For example, for a 1000 K hot Jupiter ($R_p \approx 1R_J$) orbiting a

sun-like star ($T_{\star} \approx 6000 \text{ K}$, $R_{\star} \approx 1R_{\odot}$), $B_{\lambda}(T_p)$ peaks at $\sim 2.9 \mu\text{m}$ and the maximum value of f_p/f_{\star} is $\sim 0.17 \times 10^{-3}$. In reality, however, the stellar and planetary spectra are not perfect blackbodies. While stellar spectra can often be closely approximated by a blackbody in the infrared (especially for hotter stars), planetary emission spectra typically host a range of spectral features due to absorption or emission from chemical species in the atmosphere (this is described in more detail in section 1.2). By identifying such features, the chemical composition of the atmosphere can be inferred. Furthermore, secondary eclipse spectroscopy is very sensitive to the temperature gradient in the atmosphere and can therefore be used to constrain the thermal profiles of exoplanet atmospheres.

Since secondary eclipse spectra have stronger signals in the infrared, such observations typically focus on this wavelength range. For example, HST/WFC3 and the Spitzer Space Telescope's Infrared Array Camera (IRAC, 3.6-8 μm) have been used extensively for this purpose (e.g. Kreidberg et al., 2014b; Line et al., 2016; Deming and Knutson, 2020). While planetary thermal emission is typically minimal in the optical, this wavelength range can be used to detect reflected light from the host star, and therefore infer the presence of reflective clouds and/or hazes in exoplanet atmospheres (e.g. Cowan and Agol, 2011; Angerhausen et al., 2015; Mallonn et al., 2019). Recent photometric observations from TESS (0.6-1 μm) have been used to search for such reflected light from the atmospheres of hot Jupiters (e.g. Beatty et al., 2020; von Essen et al., 2021), as discussed further in Chapter 4.

For both transmission and secondary eclipse spectroscopy, the properties of the host star also affect the observability of exoplanet atmospheres. The primary and secondary eclipse depths (Equations 1.1 and 1.6) are inversely proportional to R_{\star}^2 , meaning that smaller stellar hosts result in a larger observed signal. Conversely, smaller stars are typically less luminous than large ones and therefore have larger observational uncertainties, given a fixed distance from the observer. Therefore, for smaller exoplanets whose primary and secondary eclipse depths are more challenging to observe compared to hot Jupiters, small nearby host stars are advantageous as these benefit from both small radii and bright magnitudes (e.g. Scalo et al., 2007). This is commonly referred to as the 'M-dwarf opportunity' as many nearby M-dwarfs have been discovered to host planetary systems (Hardegree-Ullman et al., 2019). These M-dwarf planets also typically have short orbital periods, allowing for repeated observations. Many of these represent ideal targets for atmospheric characterisation (e.g. Benneke et al., 2019b; Lustig-Yaeger et al., 2019; Tsiaras et al., 2019).

Similar to secondary eclipse observations, **phase curve observations** involve observing the thermal emission and reflected light from a transiting exoplanet. However, the

exoplanet is observed throughout its entire orbit rather than just around the secondary eclipse (e.g. Harrington et al., 2006; Knutson et al., 2007, 2009b; Snellen et al., 2009; Crossfield et al., 2010; Cowan et al., 2012; Stevenson et al., 2014b). The observed flux as a function of time/phase is referred to as the phase curve (Figure 1.2, Kreidberg 2018; Parmentier and Crossfield 2018). This allows the atmosphere to be characterised as a function of longitude. For example, if the hottest point on the dayside of an exoplanet (the hotspot) is shifted away from the sub-stellar point (e.g. due to winds in the atmosphere), this can be seen in the shape of the phase curve (Parmentier and Crossfield, 2018). In particular, the phase curve peaks either before or after the secondary eclipse, depending on the direction of the hotspot shift and/or the presence of reflective clouds (Parmentier et al., 2016). Phase curves can also be used to determine the day-night temperature contrasts in tidally-locked planets, which in turn are indicative of day-night energy redistribution in the atmosphere (e.g. Showman and Guillot, 2002; Cowan and Agol, 2011; Komacek and Showman, 2016). Similar to secondary eclipse observations, phase curve observations are very sensitive to wavelength, with different wavelengths probing different regions and processes in the atmosphere (e.g. Parmentier and Crossfield, 2018). For example, optical phase curves typically probe reflected light and the albedo properties of the atmosphere, while infrared phase curves typically probe thermal emission from the atmosphere itself, providing information about its temperature and chemical composition. Furthermore, thermal phase curves within/outside a molecular absorption band probe shallower/deeper pressures in the atmosphere, respectively (e.g. Showman et al., 2009).

Another technique used to characterise exoplanet atmospheres is **high-resolution Doppler spectroscopy**, which can be used for both transiting and non-transiting exoplanets (e.g. Snellen et al., 2010; Brogi et al., 2012; Birkby, 2018). By observing high-resolution spectra ($R \sim 25,000$ - $100,000$) of the star+planet system over a range of orbital phases, planetary spectral features can be separated from those of the host star thanks to their relative Doppler shift. These high-resolution spectroscopic observations are typically analysed using the cross-correlation technique, i.e. by cross-correlating the observed spectrum with model spectra containing features due to different chemical species (e.g. Birkby, 2018). Models containing the same chemical species as the observed atmosphere result in large cross-correlation peaks in velocity space. Molecular absorption cross-sections typically include thousands of very narrow lines, and it is this large volume of lines which allows a strong cross-correlation signal. The planetary spectral features can also be Doppler shifted due to winds in the atmosphere, and so the shifts observed in the spectrum can place constraints on the dynamics of the atmosphere (e.g. Snellen et al., 2010; Brogi et al., 2016).

Finally, for directly-imaged exoplanets or sub-stellar bodies (Section 1.1.1), **direct thermal emission spectroscopy** can be performed by measuring the planetary flux as a function of wavelength (e.g. Macintosh et al., 2015; Bonnefoy et al., 2016; Chauvin et al., 2017; Biller and Bonnefoy, 2018). The quantity measured with this method is f_p (compared to f_p/f_* for secondary eclipse spectroscopy), and similar to secondary eclipse spectroscopy, the thermal emission signal is typically strongest at infrared wavelengths and for hotter, larger planets. Both ground-based and space-based facilities have been used to characterise directly-imaged planets and sub-stellar objects, including the GRAVITY and SPHERE instruments on the Very Large Telescope (VLT) and HST/WFC3 (e.g. Gravity Collaboration et al., 2020; Mollière et al., 2020; Zhou et al., 2020). Similar to secondary eclipse spectra, thermal emission spectra of directly-imaged exoplanets are very sensitive to the chemical composition and thermal profile of the atmosphere, which both impact the spectral features present in the observed spectrum (e.g. Lee et al., 2013; Lavie et al., 2017; Gravity Collaboration et al., 2020; Mollière et al., 2020). Indeed, similar methods can be used to interpret both secondary eclipse and direct thermal emission spectra of exoplanet atmospheres. In this thesis, I will explore the thermal and radiative properties of exoplanets across the mass range, primarily focusing on thermal emission spectroscopy both in secondary eclipse and through direct imaging.

1.1.3 Key Results in Atmospheric Characterisation

The atmospheric characterisation methods described above have led to numerous discoveries in the past two decades, from chemical detections to thermal and dynamical constraints. The first detection of an exoplanet atmosphere was made using transmission spectroscopy of the hot Jupiter HD 209458 b (Charbonneau et al., 2002), through the detection of atmospheric absorption due to Na. Since then, a wide range of atomic and molecular chemical species have been detected using transmission spectroscopy, including H₂O (e.g. Deming et al., 2013; Mandell et al., 2013; Fraine et al., 2014; Kreidberg et al., 2014b; Madhusudhan et al., 2014b; McCullough et al., 2014; Evans et al., 2016; Wakeford et al., 2018), Na (e.g. Charbonneau et al., 2002; Redfield et al., 2008; Huitson et al., 2012; Sing et al., 2012; Nikolov et al., 2014; Wyttenbach et al., 2015; Nikolov et al., 2016; Sing et al., 2016; Casasayas-Barris et al., 2017, 2018; Chen et al., 2017b, 2018; Khalafinejad et al., 2017; Nikolov et al., 2018), K (e.g. Sing et al., 2011; Colón et al., 2012; Sing et al., 2015, 2016; Chen et al., 2018), Li (Chen et al., 2018), Ca (Astudillo-Defru and Rojo, 2013), Mg (Fossati et al., 2010; Vidal-Madjar et al., 2013), H (Vidal-Madjar et al., 2003; Jensen et al., 2012; Bourrier et al., 2013; Ehrenreich, 2015), He (Spake et al., 2018), C (Vidal-Madjar et al., 2004), O (Vidal-Madjar et al., 2004), AlO (von Essen et al., 2019) and TiO (Sedaghati et al., 2017).

More recently, high-resolution Doppler spectroscopy has proven to be a powerful method for chemical detections given its sensitivity to each species' unique high-resolution spectral fingerprints. This method has uncovered a plethora of molecular, atomic and ionic species, including H₂O (Birkby et al., 2013; Brogi et al., 2014; Birkby et al., 2017; Hawker et al., 2018), CO (Snellen et al., 2010; Brogi et al., 2012, 2013, 2014, 2016; Rodler et al., 2013), TiO (Nugroho et al., 2017), HCN (Hawker et al., 2018; Cabot et al., 2019), Ti, Ti⁺ and Fe (Hoeijmakers et al., 2015), Cr and V (Ben-Yami et al., 2020).

Several molecular species have also been detected using thermal emission spectroscopy, including H₂O (e.g. Konopacky et al., 2013; Lee et al., 2013; Crouzet et al., 2014; Kreidberg et al., 2014b; Line et al., 2016; Evans et al., 2017; Lavie et al., 2017; Samland et al., 2017) and CO (Konopacky et al., 2013; Lee et al., 2013; Sheppard et al., 2017). Since secondary eclipse spectroscopy can be used to probe the high-temperature atmospheres of hot Jupiters, it has also been used to detect high-temperature species such as TiO (Haynes et al., 2015), VO (Evans et al., 2017) and HCN (Hawker et al., 2018). On the other hand, direct imaging has been used to probe cooler, less irradiated atmospheres, resulting in detections of the low-temperature species CH₄ (e.g. Janson et al., 2013; Barman et al., 2015; Line et al., 2015; Samland et al., 2017) and NH₃ (Line et al., 2015, 2017) in both exoplanets and brown dwarfs.

On top of these chemical detections, the atmospheric abundances of several chemical species have been measured from transmission and thermal emission spectra using atmospheric retrieval methods, which are described in more detail in section 1.3. In particular, H₂O abundances of hot Jupiters measured using transmission spectroscopy have been found to be consistently lower than those expected for solar elemental abundances (Madhusudhan et al., 2014b; Barstow et al., 2017; Pinhas et al., 2019; Welbanks et al., 2019). While most chemical constraints to date have been for hot Jupiters, recent observations have also begun to constrain chemical abundances in lower-mass exoplanets, including Neptune-like exoplanets and 'mini-Neptunes' (planets with radii between $\sim 1.6\text{--}4 R_{\oplus}$, see section 1.4.3). These include HAT-P-11 b (Chachan et al., 2019), HAT-P-26 b (Wakeford et al., 2017) and GJ 3470 b (Benneke et al., 2019a). Of note is the first detection of H₂O and atmospheric abundance constraints for a habitable-zone exoplanet, for the mini-Neptune K2-18 b (Benneke et al., 2019b; Tsiaras et al., 2019; Madhusudhan et al., 2020).

Atmospheric observations have also indicated the presence of clouds and hazes for several exoplanets. For example, the optical to near-infrared transmission spectra of several hot Jupiters suggest a range of cloud and haze properties, which are inferred from steep optical slopes (e.g. due to Rayleigh scattering) and/or the attenuation of spectral

features due to clouds (e.g. Pont et al., 2013; Sing et al., 2016; Barstow et al., 2017; Pinhas et al., 2019; Welbanks et al., 2019). Featureless transmission spectra of Neptune-mass and sub-Neptune exoplanets have also indicated the presence of clouds in the low-mass regime (e.g. Knutson et al., 2014a,b; Kreidberg et al., 2014a). Furthermore, phase curve observations have been used to infer the presence of clouds in giant exoplanets through the inference of large optical albedos and phase curve offsets (e.g. Demory et al., 2013; Angerhausen et al., 2015; Esteves et al., 2015; Garcia Munoz and Isaak, 2015; Shporer and Hu, 2015; Parmentier et al., 2016).

Besides chemical and cloud constraints, thermal emission spectra and phase curve observations have also been used to place constraints on the temperature profiles and energy transport in exoplanet atmospheres. Notably, secondary eclipse spectra have revealed thermal inversions (temperature increasing with altitude) in several hot Jupiters (Haynes et al., 2015; Evans et al., 2017; Sheppard et al., 2017). Phase curve observations of hot Jupiters have further shown that more strongly-irradiated atmospheres typically have larger day-night temperature contrasts, suggesting less efficient energy redistribution between the permanent day- and nightsides, while less-irradiated atmospheres show a wider range of redistribution efficiencies (e.g. Cowan and Agol, 2011; Schwartz and Cowan, 2015; Garhart et al., 2020). For example, HD 189733 b (Bouchy et al., 2005) has a dayside brightness temperature of ~ 1200 - 1300 K in the near-infrared, and phase curve observations have shown that it has efficient day-night energy redistribution (Knutson et al., 2007, 2009c, 2012). Conversely, WASP-12 b (Hebb et al., 2009) has a dayside temperature of ~ 3000 K and has been found to have a very poor day-night energy redistribution efficiency (Cowan et al., 2012).

A simplified explanation for these day-night energy redistribution trends is that radiative timescales are shorter than advective timescales at high temperatures, and 3D atmospheric models including both this and other effects have reproduced this trend (e.g. Showman and Guillot, 2002; Perez-Becker and Showman, 2013; Komacek and Showman, 2016). As expected, these hotter planets have also been found to typically have smaller hotspot offsets (Perez-Becker and Showman, 2013; Komacek and Showman, 2016; Zhang et al., 2018); this corroborates the theory of poor redistribution efficiency as atmospheric winds act to move the hotspot away from the sub-stellar point (e.g. Showman and Guillot, 2002; Showman et al., 2009; Parmentier et al., 2018). It has been suggested, however, that in the regime of extreme irradiation (e.g. for WASP-33 b and WASP-12 b), hotspot offsets increase with irradiation, potentially due to magnetic effects (Zhang et al., 2018).

1.2 Physics of Exoplanet Atmospheres

In order to interpret atmospheric observations of exoplanets, it is important to understand the underlying physical and chemical processes which shape them. Equally, such observations have added to the understanding of atmospheric processes, refining existing theoretical models. Ultimately, the energy sources and chemical building blocks of the atmosphere determine its thermal profile, energy transport mechanisms and chemistry, which in turn determine the emergent thermal emission spectrum.

A key physical property which links together these thermal, chemical and radiative properties is the optical depth, τ_ν . At an altitude z_0 in the atmosphere, τ_ν is defined as

$$\tau_\nu(z_0) = - \int_{z_0}^{\infty} (\kappa_\nu + \sigma_\nu) \rho dz,$$

where κ_ν and σ_ν are the absorption and scattering opacities (i.e. cross section per unit mass), respectively. The optical depth describes the extent to which radiation is impeded by the constituents of the atmosphere, which are determined by its chemical composition. τ_ν is small in the low-density, upper regions of the atmosphere, and increases in the deeper, denser regions. In particular, at the altitude where $\tau_\nu = 1$, the distance to the edge of the atmosphere is equal to the mean free path of the radiation. The thermal emission spectrum of an atmosphere therefore primarily originates in this region, known as the photosphere.

The optical depth encapsulates the interaction between matter and radiation in the atmosphere and therefore impacts energy transport, the atmospheric temperature profile and the emergent thermal emission spectrum. In what follows, I describe these atmospheric properties, and the processes which shape them, in more detail.

1.2.1 Energy Transport and Atmospheric Temperature Profiles

The two principal sources of energy in irradiated exoplanet atmospheres are incident irradiation from the host star and internal heat emanating from the centre of the planet (e.g. Fortney et al., 2007). Internal heat encapsulates a range of energy sources, and can for example be a remnant from the planet formation process (Marley et al., 2007; Baraffe et al., 2008) or a result of tidal heating (i.e. the dissipation of energy resulting from tidal distortions, e.g. see Moses et al. 2013a; Agúndez et al. 2014b; Morley et al. 2017a). In the case of poorly-irradiated or isolated planets and sub-stellar objects, this internal heat becomes the primary energy source in the atmosphere. Conversely, irradiation is the dominant energy source for highly-irradiated exoplanets. The bolometric flux emanating

from an exoplanet atmosphere can therefore be written as a sum of the fluxes from these two energy sources: $F_{\text{tot}} = F_{\text{int}} + F_{\text{irr}}$. The fluxes due to internal heat and irradiation are typically described by the internal and irradiation temperatures, T_{int} and T_{irr} , respectively, where

$$T_{\text{irr}} = \frac{1}{2^{1/4}} \sqrt{\frac{R_{\star}}{a}} T_{\star}. \quad (1.7)$$

T_{irr} is a measure of the stellar irradiation incident on the dayside, and represents the day-side atmospheric temperature of a tidally-locked planet if this energy is evenly distributed across the dayside only (i.e. it is not transported to the nightside or reflected by clouds).

A variety of energy transport mechanisms distribute energy from these sources through the atmosphere. Two key energy transport mechanisms are radiative and convective energy transport. Radiative energy transport occurs where the atmosphere is sufficiently optically thin for radiation to efficiently transport energy. This is typically the case in the lower-density, upper regions of the atmosphere. Conversely, in optically-thick regions of the atmosphere where radiative transport is inefficient, convection takes over as the primary mechanism for energy transport. This typically occurs deeper in the atmosphere, where density (and therefore opacity) increases. In particular, the onset of convection occurs when the temperature gradient in the atmosphere exceeds the following limit, known as the Schwarzschild criterion:

$$\left| \frac{d \ln T}{d \ln P} \right| \geq \frac{\gamma - 1}{\gamma},$$

where $\gamma = C_p/C_v$ and C_p , C_v are the specific heat capacities of the atmospheric gas at constant pressure and volume, respectively. This transition between the radiative and convective regimes is known as the radiative-convective boundary. On top of radiative and convective energy transport, other mechanisms such as large-scale circulation also transport energy. For example, in the case of tidally-locked exoplanets, such mechanisms can transport incident energy from the permanent dayside to the permanent nightside (e.g. Showman et al., 2009; Kataria et al., 2016; Komacek and Showman, 2016).

Given the local and global conservation of energy in the atmosphere, these energy sources, energy transport mechanisms and the atmospheric opacity collectively determine the temperature profile of the atmosphere. In particular, in any given layer of the atmosphere, the energy entering that layer must be balanced by the energy leaving it. The equilibrium temperature of the atmospheric layer is therefore the temperature which

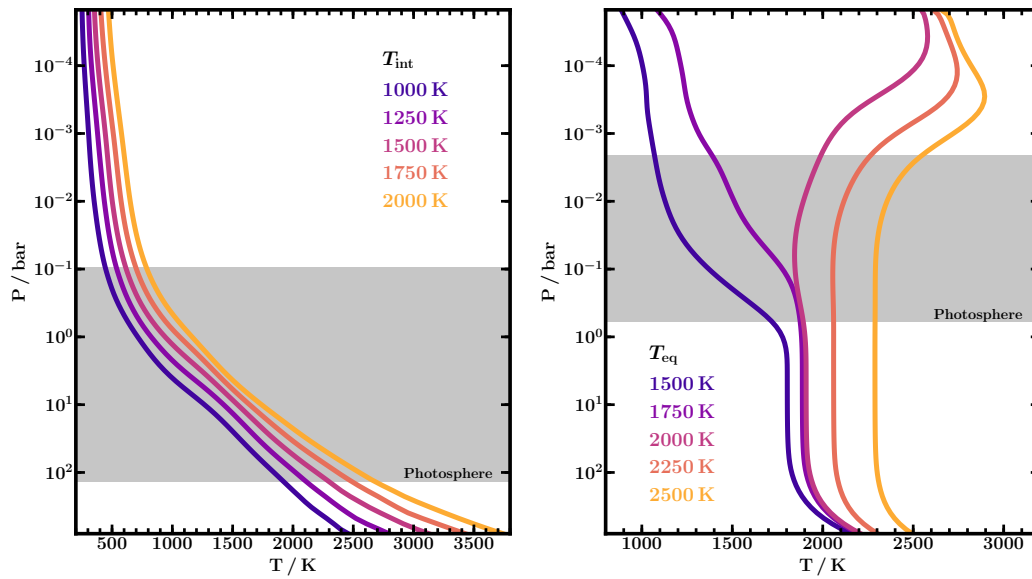


Fig. 1.3 Examples of atmospheric temperature profiles for non-irradiated (left) and strongly-irradiated (right) giant exoplanets. The non-irradiated (irradiated) temperature profiles are dominated by internal energy, T_{int} (incident irradiation, characterised by T_{eq}). The models assume equilibrium chemistry and solar elemental abundances. In the most strongly-irradiated cases, optical opacity due to TiO, Na and K results in a thermal inversion. Grey shaded regions indicate the 0.4-50 μm photosphere at a resolution of $R \sim 50$ for the $T_{\text{int}} = 1500$ K (left) and $T_{\text{eq}} = 2000$ K (right) cases, respectively.

maintains this energy balance. This can be described mathematically as follows:

$$\int_0^{\infty} \kappa_{\nu}(J_{\nu} - B_{\nu})d\nu = 0, \quad (1.8)$$

where J_{ν} is the mean intensity of the local radiation field and B_{ν} is the Planck function corresponding to the local temperature. The $\kappa_{\nu}J_{\nu}$ term represents the incoming energy in a given layer while the $\kappa_{\nu}B_{\nu}$ term represents the outgoing energy, following Kirchhoff's Law and assuming local thermodynamic equilibrium. Where convective transport also occurs, the incoming energy also includes a contribution from the convective flux, F_{conv} , and equation 1.8 becomes

$$\int_0^{\infty} \kappa_{\nu}(J_{\nu} - B_{\nu})d\nu + \frac{g}{4\pi} \frac{dF_{\text{conv}}}{dP} = 0. \quad (1.9)$$

The equilibrium atmospheric temperature profiles which result from this energy balance vary depending on the irradiation, internal heat and chemistry of the atmosphere. In particular, strongly- and poorly-irradiated atmospheres exhibit distinct thermal profiles (e.g. Hubeny et al., 2003; Fortney et al., 2007; Burrows et al., 2008a). As shown in Figure 1.3, poorly-irradiated atmospheres have a temperature gradient which gradually increases with pressure until a deep convective region is reached. Conversely, in a highly-irradiated atmosphere, a deep isotherm is present between the upper and deeper atmospheric regions (see Figure 1.3). Furthermore, the temperature gradient in the upper atmosphere can vary from decreasing with altitude to increasing with altitude, i.e. a thermal inversion (e.g. Hubeny et al., 2003; Burrows et al., 2008a), depending on the irradiation and atmospheric opacity.

Thermal inversions are caused when the opacity in the upper atmosphere is greater at the peak wavelengths of the stellar irradiation compared to that at the peak wavelengths of the thermal emission of the planet (Hubeny et al., 2003). For example, in the case of a hot Jupiter orbiting a Sun-like star, the stellar irradiation peaks in the optical while the planetary thermal emission peaks in the infrared. Therefore, if the chemical composition in the upper atmosphere results in a greater optical opacity relative to the infrared opacity, incident irradiation is deposited high up in the atmosphere. An equilibrium state is therefore reached when the temperature in the upper atmosphere is high enough that the outgoing thermal emission balances the deposited energy. In hot Jupiters, a number of chemical species can contribute to the optical opacity and cause thermal inversions, including TiO, VO, Na, K, AlO, CaO, NaH, MgH, sulfur compounds and H^- (e.g. Hubeny et al., 2003; Zahnle et al., 2009; Madhusudhan, 2012; Mollière et al., 2015; Arcangeli et al., 2018; Parmentier et al., 2018; Gandhi and Madhusudhan, 2019). For exoplanets orbiting

cooler host stars, the incident irradiation peaks at longer wavelengths and infrared opacity due to species such as CO₂ can also result in thermal inversions (Malik et al., 2019).

Other effects can act to cool the atmospheres of irradiated exoplanets, ranging from highly-irradiated to more temperate atmospheres. Notably, optical scattering from clouds and hazes can reflect incident irradiation from the host star and thereby cool the atmosphere (e.g. Selsis et al., 2007; Morley et al., 2013; Yang et al., 2013). The reflectivity of the atmosphere is typically described using the Bond or geometric albedo (A_B and A_g , respectively). While the Bond albedo describes the bolometric fraction of incident energy reflected from the atmosphere (regardless of phase), the geometric albedo is wavelength-dependent and describes the ratio of the planet's flux at zero phase angle to the flux from a Lambert disc at the same distance and subtending the same solid angle as the planet. For tidally-locked planets, energy redistribution between the permanent day- and nightsides can also act to cool the dayside (e.g. Burrows et al., 2008a). This energy transport can occur as a result of atmospheric dynamics such as day-night winds (e.g. Showman et al., 2008, 2009; Kataria et al., 2016; Komacek and Showman, 2016) as well as latent heat from chemical species which recombine or condense on the nightside (Bell and Cowan, 2018; Komacek and Tan, 2018; Mansfield et al., 2020).

Both albedo and day-night energy redistribution efficiency affect the average day-side temperature for tidally-locked exoplanets, in addition to the incident stellar flux. A measure for the resulting dayside temperature is the equilibrium temperature,

$$T_{\text{eq}} = \frac{(1 - A_B)^{1/4}(1 - f)^{1/4}}{2^{1/4}} \sqrt{\frac{R_\star}{a}} T_\star = (1 - A_B)^{1/4}(1 - f)^{1/4} T_{\text{irr}}. \quad (1.10)$$

which represents the temperature required for equilibrium between the incident irradiation and outgoing planetary flux (not including the internal flux). In particular, T_{eq} is representative of the temperature in the photosphere, as this is where the planetary thermal emission primarily originates from.

1.2.2 Atmospheric Chemistry and Opacity

The chemical species present in the atmosphere contribute to both the temperature profile (through κ_ν in equations 1.8 and 1.9) and the emergent thermal emission spectrum. The abundances of these species are determined by the elemental composition of the atmosphere, the temperature structure and chemical equilibrium and disequilibrium processes. For an atmosphere in thermochemical equilibrium, the chemical abundances are those for which the Gibbs free energy of the system is minimised (e.g. White et al.,

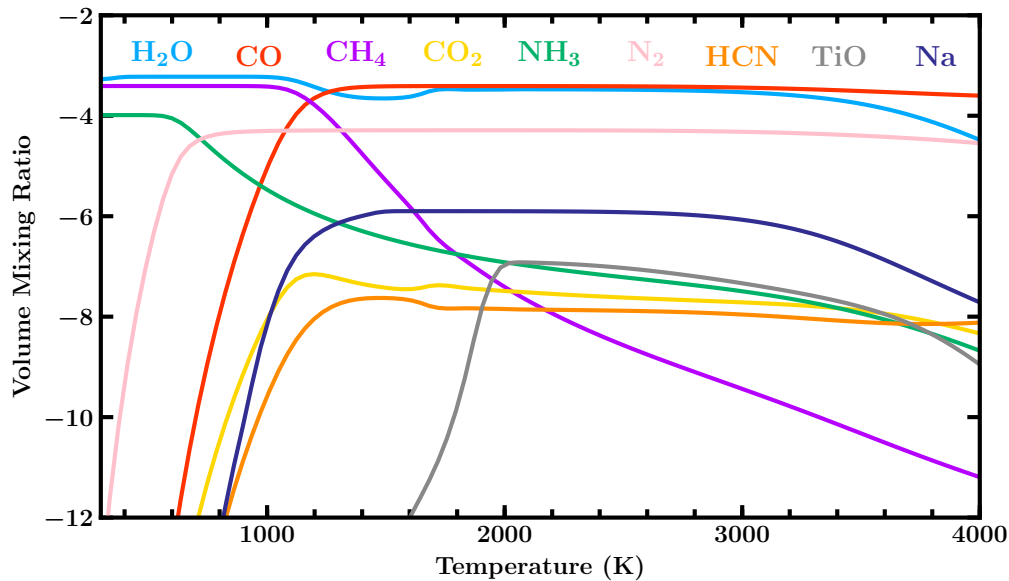


Fig. 1.4 Equilibrium chemical abundances as a function of temperature, assuming a pressure of 1 bar and C/O ratio of 0.5. Key transitions include those between CH_4 and CO at ~ 1200 K and between NH_3 and N_2 at ~ 750 K.

1958; Lodders and Fegley, 2002; Seager, 2010; Woitke et al., 2018). These abundances are therefore dependent on both pressure and temperature as well as the ratios of elemental abundances and the atmospheric metallicity. In particular, the C/O ratio has been found to be an important metric for describing the chemistry of hot, hydrogen-rich atmospheres as this affects the abundances of key, spectroscopically active molecules such as H_2O , CH_4 and TiO (Madhusudhan, 2012; Moses et al., 2013b). Furthermore, evidence from both the solar system and atmospheric observations of exoplanets suggests that atmospheric metallicity increases with decreasing mass (e.g. Atreya et al., 2018; Pinhas et al., 2019; Welbanks et al., 2019).

Figure 1.4 shows the equilibrium abundances of several key species in hydrogen-rich atmospheres as a function of temperature and at a pressure of 1 bar, i.e. roughly photospheric pressures for the thermal emission spectrum. Notable transitions in this thermochemical space include the transition from CH_4 to CO at ~ 1200 K and that of NH_3 to N_2 at ~ 750 K. Furthermore, at higher temperatures, thermal dissociation results in lower abundances for several species (e.g. H_2O at $\gtrsim 3000$ K). However, CO is more resistant to high temperatures thanks to its strong triple bond. At lower temperatures, certain species can also condense and be removed from the gas phase, resulting in lower observed abundances. The condensed phase can either gravitationally settle to lower altitudes (i.e. ‘rain out’) or form a cloud deck.

Atmospheric chemical abundances can, however, deviate from equilibrium expectations due to disequilibrium processes (e.g. Venot et al., 2012; Moses et al., 2011, 2013b; Drummond et al., 2018a,b). One such process is vertical mixing, which may dredge up high-temperature species (such as CO) from the deeper, hotter regions of the atmosphere up to the cooler photosphere (e.g. Cooper and Showman, 2006; Moses et al., 2011, 2013b; Visscher and Moses, 2011; Drummond et al., 2018a,b). Conversely, gravitational settling can deplete certain heavier molecules (e.g. TiO) from the photosphere as they sink deeper down, unless vertical mixing is able to loft them back to higher altitudes (Spiegel et al., 2009; Beatty et al., 2017a). Horizontal transport due to winds can also result in chemical disequilibrium (e.g. Cooper and Showman, 2006; Agúndez et al., 2014a; Drummond et al., 2018a,b, 2020), for example affecting the expected abundances of CH₄ and NH₃ in the observable dayside atmospheres of hot Jupiters (e.g. Drummond et al., 2020). Such horizontal transport can further lead to day-night ‘cold traps’ due to which species can be depleted on the dayside as a result of condensation and rainout on the cooler nightside (e.g. Beatty et al., 2017a,b; Parmentier et al., 2013). Photochemical reactions are further thought to destroy certain molecules, e.g. CH₄ and NH₃, and deplete their atmospheric abundances (e.g. Zahnle et al., 2009; Line et al., 2010; Moses et al., 2011; Venot et al., 2012; Miguel and Kaltenegger, 2014).

In addition to gaseous species, clouds and hazes can also contribute to the atmospheric opacity. The formation processes of clouds and hazes are complex, and depend on a range of factors including the chemical environment, UV flux, nucleation processes, and atmospheric dynamics (e.g. Ackerman and Marley, 2001; Helling, 2019; Morley et al., 2014; Gao et al., 2018; He et al., 2018; Hörst et al., 2018; Moran et al., 2020). A range of models have been developed to include the effects of clouds into atmospheric studies, ranging from more complex microphysical models (e.g. Helling et al., 2008; Gao et al., 2018; Lines et al., 2018) to somewhat simpler parametric models (e.g. Ackerman and Marley, 2001; Morley et al., 2014, 2015). Similarly, for hazes, some works have used the scattering properties of expected haze particles (e.g. Howe and Burrows, 2012; Miller-Ricci Kempton et al., 2012; Morley et al., 2013) while others use a more simplified power-law relation (e.g. Sing et al., 2016; MacDonald and Madhusudhan, 2017; Pinhas et al., 2018). Given the complexities and current uncertainties in cloud and haze formation in exoplanet atmospheres, the simpler of these approaches are useful when exploring the broader effects of clouds and hazes on the thermal and radiative properties of an atmosphere. Meanwhile, the more complex models (as well as laboratory experiments, e.g. He et al. 2018; Hörst et al. 2018; Moran et al. 2020) continue to advance the field’s knowledge of exoplanet clouds and hazes.

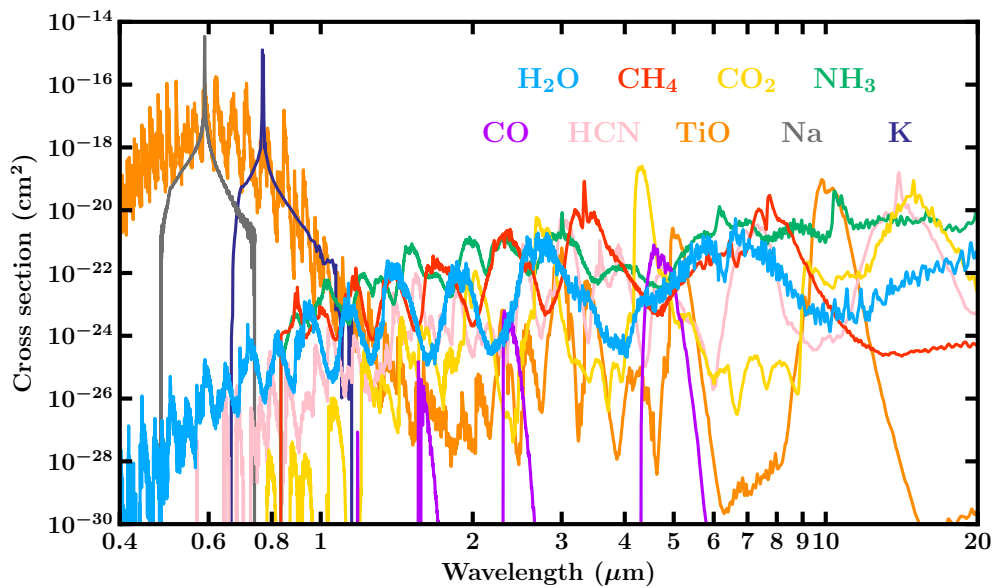


Fig. 1.5 Absorption cross sections of key molecular and atomic species for exoplanet atmospheres, assuming a pressure of 0.1 bar and temperature of 800 K. The optical regime is dominated by atomic and heavy-metal molecular species such as TiO, while the infrared is dominated by molecular species such as H₂O, CH₄ and CO. Molecular cross sections are calculated using the methods of Gandhi and Madhusudhan (2017) using line list data from Rothman et al. (2010) (H₂O, CO and CO₂), Yurchenko et al. (2013); Yurchenko and Tennyson (2014) (CH₄), Yurchenko et al. (2011) (NH₃), Harris et al. (2006); Barber et al. (2014) (HCN) and McKemmish et al. (2019) (TiO). Na and K cross sections are from Allard et al. (2019) and Allard et al. (2016), respectively.

The chemical species and cloud/haze particles in the atmosphere interact with the local radiation field via their absorption and scattering cross sections. In particular, molecular, atomic and ionic opacity due to electronic transitions can be calculated using the relevant line lists (e.g. from the HITEMP, HITRAN and EXOMOL databases, Rothman et al., 2010, 2013; Tennyson et al., 2016) and by applying thermal, pressure and natural broadening (e.g. Gray, 1976; Hill et al., 2013; Allard et al., 2019; Gandhi et al., 2020a). Another important source of opacity is collision-induced absorption (CIA), for example between H₂ molecules (e.g. Richard et al., 2012). The absorption cross sections for several key species in exoplanet atmospheres are shown in Figure 1.5. Several heavy metal species (e.g. TiO) and atomic species are primarily active in the optical, while the infrared is dominated by molecular opacity. Scattering due to clouds and hazes is also typically larger in the optical (e.g. Wakeford and Sing, 2015; Pinhas and Madhusudhan, 2017). In particular, Rayleigh scattering due to molecules and small haze particles follows a well-defined power-law in wavelength: $\sigma \propto \lambda^{-4}$. Cloud and haze scattering in exoplanet atmospheres can therefore reflect incident irradiation and thereby cool the atmosphere below.

1.2.3 Radiative Transfer and Thermal Emission Spectra

Given the energy sources, temperature profile and opacity sources in an exoplanet atmosphere, radiative transfer determines the emergent thermal emission spectrum (e.g. Seager, 2010; Hubeny and Mihalas, 2014; Hubeny, 2017). In particular, as a beam of radiation passes through the gas, energy is both lost (due to absorption and scattering) as well as added (due to thermal emission and scattering into the beam). It is useful to formulate such changes in energy, ΔE , in terms of the specific intensity, I_ν , where

$$I_\nu = \frac{\Delta E}{dA \cos\theta d\Omega d\nu dt}.$$

$dA \cos\theta$ is the area perpendicular to the beam which has solid angle $d\Omega$, and ν and t are frequency and time, respectively. The energy removed from the beam due to absorption and scattering is therefore:

$$\Delta E_{\text{abs}} + \Delta E_{\text{sc}} = (\kappa_\nu + \sigma_\nu) I_\nu d\Omega d\nu dt dm$$

where $dm = \rho dAdz$. Assuming local thermodynamic equilibrium (LTE), the energy added to the beam due to thermal emission and scattering is:

$$\Delta E_{\text{th}} + \Delta E_{\text{sc,in}} = (\kappa_{\nu} B_{\nu} + \sigma_{\nu} J_{\nu}) d\Omega dv dt dm.$$

Note that J_{ν} can be defined in terms of I_{ν} as $J_{\nu} = \frac{1}{2} \int_{-1}^1 I_{\nu} d\mu_{\theta}$, where $\mu_{\theta} = \cos\theta$. The equation of radiative transfer, which describes the overall change in I_{ν} , can therefore be written as

$$\mu_{\theta} \frac{dI_{\nu}}{d\tau_{\nu}} = I_{\nu} - S_{\nu}, \quad (1.11)$$

where $S_{\nu} = (\kappa_{\nu} B_{\nu} + \sigma_{\nu} J_{\nu}) / (\kappa_{\nu} + \sigma_{\nu})$ and $d\tau_{\nu} = -(\kappa_{\nu} + \sigma_{\nu}) \rho dz$.

Equation 1.11 can be used to understand how features arise in the emergent thermal emission spectrum of an atmosphere (e.g. Seager, 2010). For example, in the simplified case of a non-scattering ($\sigma_{\nu} = 0$) semi-infinite atmosphere with $\tau_{\nu} = \infty$ at low altitudes and $\tau_{\nu} = 0$ at high altitudes, the solution for the emergent specific intensity is

$$I_{\nu}(\tau_{\nu} = 0) = \frac{1}{\mu} \int_0^{\infty} B_{\nu} e^{-\tau_{\nu}/\mu} d\tau_{\nu}. \quad (1.12)$$

In the core of a spectral line, the opacity κ_{ν} is, by definition, larger than in the continuum. As a result, the $\tau_{\nu} \approx 1$ surface from which the emission spectrum originates occurs at a higher altitude in the line core compared to the continuum. If the temperature profile decreases with altitude, this means that B_{ν} , and therefore I_{ν} , are smaller in the line core, resulting in an absorption feature. Similarly, if temperature increases with altitude, the result is an emission line feature. In the case of an isothermal temperature profile, B_{ν} is independent of τ_{ν} and therefore acts as a constant in the integral in equation 1.12. The emergent thermal emission spectrum is therefore a blackbody corresponding to the isothermal temperature of the atmosphere. Given I_{ν} at the outer edge of the atmosphere, the observed flux can be calculated by integrating over the solid angle subtended by the planet at the observer, i.e.

$$F_{\nu,\text{obs}} = \frac{R_p^2}{d^2} \pi I_{\nu}, \quad (1.13)$$

where d is the distance to the system from the observer and I_{ν} is assumed to be uniform across the visible face of the planet.

1.3 Modelling Exoplanet Atmospheres

Both atmospheric models and observations are required in tandem to learn about the interplay of physical processes, and the resulting conditions, in exoplanets. In this thesis, I use two main modelling/analysis methods: 1D self-consistent atmospheric models and atmospheric retrievals. While self-consistent models allow an exploration of physical processes and their interplay, atmospheric retrievals involve a data-driven approach to gain maximal information from observations. These approaches are highly complementary and can, for example, be used to identify disequilibrium conditions in exoplanet atmospheres (e.g. Gandhi and Madhusudhan, 2018). In what follows, I describe the key elements of each of these methods.

1.3.1 Self-Consistent 1D Atmospheric Models

Given the macroscopic properties of an exoplanet (e.g. irradiation, elemental atmospheric abundances, internal heat), self-consistent atmospheric models solve the physical atmospheric equations, e.g. those in Section 1.2, in order to determine the emission spectrum of the atmosphere and its thermal and chemical profiles (e.g. see review by Madhusudhan, 2019). Models exploring different aspects of atmospheric physics and with a range of complexities exist in the literature, including both 1D models (e.g. see reviews by Marley and Robinson, 2015; Hubeny, 2017; Madhusudhan, 2019) and 3D general circulation models (GCMs, e.g. Showman and Guillot 2002; Menou and Rauscher 2009; Showman et al. 2009, 2020; Lewis et al. 2010; Rauscher and Menou 2010; Dobbs-Dixon and Agol 2013; Parmentier et al. 2013; Amundsen et al. 2014, 2016; Mayne et al. 2014, 2017; Helling et al. 2016; Kataria et al. 2016; Lee et al. 2016; Boutle et al. 2017).

Self-consistent models with different levels of complexity and dimensionality are extremely complementary as they can be used to explore different aspects of exoplanetary atmospheres. For example, GCMs are commonly used to investigate atmospheric dynamics and to interpret phase curve observations (e.g. Showman et al., 2009; Dobbs-Dixon and Agol, 2013; Amundsen et al., 2016; Kataria et al., 2016; Mayne et al., 2017; Lines et al., 2018; Crossfield et al., 2020). Such models can include important 3D effects such as detailed atmospheric dynamics, horizontal transport of both energy and chemical species, and cloud processes including the advection of cloud particles (e.g. Cooper and Showman, 2006; Showman et al., 2009; Lee et al., 2016; Lines et al., 2018; Drummond et al., 2020). Meanwhile, 1D models can be used to resolve detailed aspects of radiative transfer, thermal profiles and chemical processes and to interpret secondary eclipse observations (e.g. Mollière et al., 2015; Drummond et al., 2016; Gandhi and Madhusudhan, 2017; Malik et al.,

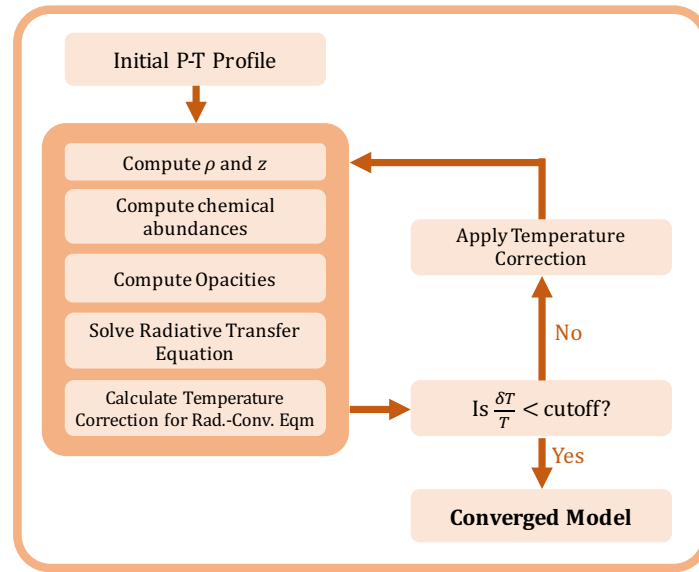


Fig. 1.6 A schematic of the GENESIS self-consistent 1D atmospheric model (adapted from Gandhi and Madhusudhan 2017). Radiative-convective equilibrium is achieved by iteratively correcting the temperature profile using the Rybicki linearisation method.

2017; Goyal et al., 2020). Furthermore, given their relatively lower computational expense, 1D models can be used to explore a wide range in parameter space, making them very complementary to more complex 3D models.

In this thesis, I use adaptations of the GENESIS self-consistent 1D plane-parallel atmospheric model (Gandhi and Madhusudhan, 2017) to explore the conditions in a range of exoplanetary atmospheres. GENESIS solves hydrostatic equilibrium (equation 1.4), radiative-convective equilibrium (equation 1.9), thermochemical equilibrium and radiative transfer (equation 1.11) in order to find the equilibrium temperature profile, chemical profile and thermal emission spectrum of an atmosphere. The structure of this model is shown schematically in Figure 1.6. The inputs to such 1D models typically include the incident irradiation, internal temperature and the elemental abundances in the atmosphere (which can be parameterised by metallicity and C/O ratio), as well as the mass and radius of the exoplanet. Beyond the equilibrium conditions described above, self-consistent models can also include disequilibrium processes including photochemistry, vertical mixing or gravitational settling of heavy molecules (e.g. Spiegel et al., 2009; Line et al., 2010; Moses et al., 2011; Venot et al., 2012; Miguel and Kaltenecker, 2014). Clouds and hazes can also affect the temperature profile and thermal emission spectrum, and are often included in a parametric form given the complexity of cloud and haze formation processes (e.g. Ackerman and Marley 2001; Morley et al. 2015, see also section 1.2.2).

The self-consistent atmospheric models present in the literature differ not only in the physics included in each model, but also in the methods used to solve the relevant atmospheric equations (e.g. see review by Hubeny, 2017). In particular, a range of algorithms are used to solve the equations of radiative-convective equilibrium and of radiative transfer. For example, models stemming from planetary science applications typically use the two-stream approximation (Toon et al., 1989) for the solution of radiative transfer (e.g. Fortney et al., 2006b, 2008; Malik et al., 2017), while models originating from stellar applications typically use direct solutions to the radiative transfer equation, such as the Feautrier or Discrete Finite Element methods (e.g. Barman et al., 2005; Seager et al., 2005; Burrows et al., 2008a; Mollière et al., 2015; Gandhi and Madhusudhan, 2017). Furthermore, a range of methods can be used for the inclusion of opacity in the atmosphere, including correlated-k (e.g. Fortney et al., 2006b; Drummond et al., 2016; Mollière et al., 2015; Malik et al., 2017) and line-by-line opacities (e.g. Seager et al., 2005; Barman et al., 2005; Burrows et al., 2008a; Gandhi and Madhusudhan, 2017). The GENESIS self-consistent atmospheric model used in this thesis uses line-by-line opacities as well as direct solutions to solve both the radiative transfer and radiative-convective equilibrium equations (i.e. the Feautrier, Discrete Finite Element and Rybicki linearisation methods, e.g. see Hubeny and Mihalas 2014; Hubeny 2017). The adaptations I have made to this model for the cases of hot Jupiters, mini-Neptunes and rocky exoplanets are described in Chapters 3 & 4, 5 and 6, respectively.

1.3.2 Atmospheric Retrievals

Atmospheric retrievals are an inverse-modelling method used to derive atmospheric properties from spectroscopic observations of exoplanets. Pioneered for exoplanets by Madhusudhan and Seager (2009), such methods allow data-driven inferences to be made by using a parametric model of the atmosphere. This parametric model is then coupled to a statistical sampling algorithm such as Markov Chain Monte Carlo (MCMC, e.g. Trotta 2017) or Nested Sampling (Skilling, 2006), which compares numerous spectral models to the data and determines posterior probability distributions for the model parameters. A schematic representation of this retrieval structure is shown in Figure 1.7.

The input parameters of an atmospheric retrieval for thermal emission spectra typically include the volume mixing ratios of relevant chemical species (assuming constant-with depth abundances) and parameters related to the temperature profile (e.g. see review by Madhusudhan, 2018). Based on these input parameters, the emergent emission spectrum can be calculated using a range of radiative transfer methods. In order to reduce computation time, approximative methods are typically used rather than exact solutions

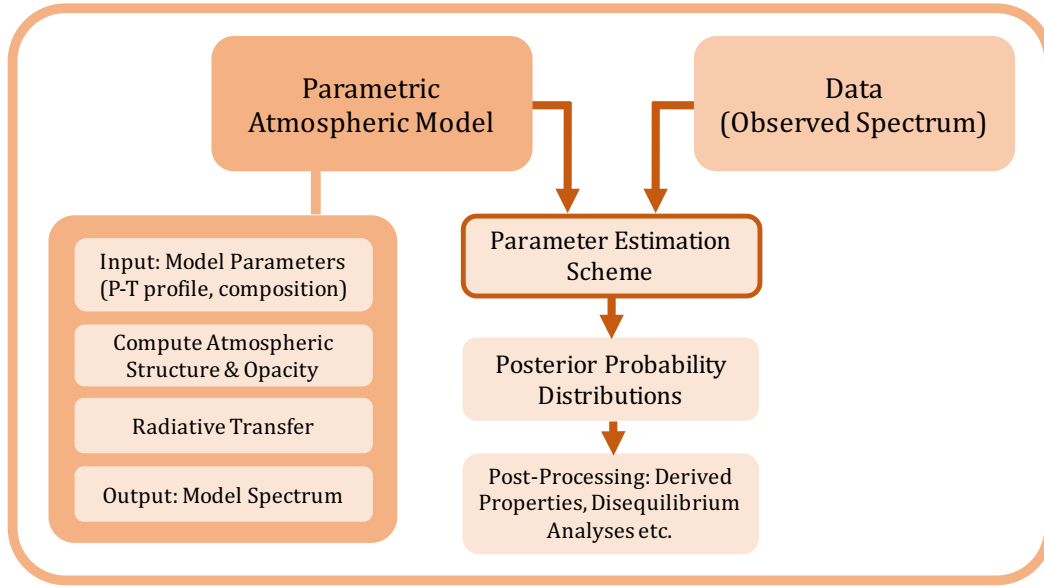


Fig. 1.7 A schematic of an atmospheric retrieval framework (adapted from Madhusudhan 2018). The model parameters typically include those for the pressure-temperature (P - T) profile and chemical abundances. The parameter estimation scheme (e.g. MCMC or Nested Sampling) then derived posterior probability distributions for each model parameter.

such as the Feautrier method (e.g. Gandhi and Madhusudhan, 2018). In this thesis, following Gandhi and Madhusudhan (2018), I use the two-angle Gaussian quadrature method assuming a non-scattering atmosphere. In the limit of no scattering, the specific intensity emerging from a thin atmospheric layer with temperature T and optical depth τ_ν is

$$I_{\nu,1} = I_{\nu,0} e^{-\tau_\nu/\mu_\theta} + B_\nu(T)(1 - e^{-\tau_\nu/\mu_\theta}),$$

where $I_{\nu,0}$ is the specific intensity entering the layer (i.e. similar to equation 1.12 but for a single atmospheric layer). The observed flux is then

$$F_{\nu,\text{em}} = 2\pi \frac{R_p^2}{d^2} \int_0^1 I_{\nu,\text{em}}(\mu_\theta) \mu_\theta d\mu_\theta, \quad (1.14)$$

where $I_{\nu,\text{em}}$ is the specific intensity emerging from the uppermost atmospheric layer. In the two-angle Gaussian quadrature method, the integral over μ_θ is performed using the two-angle Gaussian quadrature approximation (e.g. see Gandhi and Madhusudhan, 2018).

Unlike the self-consistent atmospheric models described in section 1.3.1, the atmospheric models used in retrievals do not typically have self-consistent temperature profiles, and instead use a parametric temperature profile (e.g. Madhusudhan and Seager, 2009;

Guillot, 2010; Heng et al., 2012; Robinson and Catling, 2012; Parmentier and Guillot, 2014). The advantages of a parametric temperature profile are that (i) it is much faster to compute compared to a self-consistent temperature profile, allowing millions of models to be evaluated and compared to the data, and (ii) it allows the retrieved temperature profile to be data-driven. As such, the space of solutions which are able to fit the data can be comprehensively determined, as long as the parametric temperature profile is sufficiently well suited to the atmosphere being studied.

A number of temperature profile parameterisations have been used for atmospheric retrievals in the literature (e.g. Madhusudhan and Seager, 2009; Guillot, 2010; Heng et al., 2012; Robinson and Catling, 2012; Parmentier and Guillot, 2014; Waldmann et al., 2015). For example, the 6-parameter parameterisation of Madhusudhan and Seager (2009) has been used extensively for both thermal emission and transmission observations, across a range of exoplanet types including hot Jupiters to low-mass exoplanets (e.g. Haynes et al., 2015; Sheppard et al., 2017; von Essen et al., 2019; Welbanks et al., 2019). It has also been validated against self-consistent temperature profiles determined by 3D atmospheric models (Blecic et al., 2017). Thermal emission spectra in particular are very sensitive to the atmospheric temperature profile and using a suitable temperature profile is therefore especially important. In Chapter 6, I use the Madhusudhan and Seager (2009) parameterisation for retrievals of rocky exoplanet emission spectra and find that it is able to fit self-consistently derived temperature profiles. Conversely, in Chapter 2, I investigate the requirements for temperature profile parameterisations of isolated exoplanets and brown dwarfs, and develop a new parameterisation tailored specifically for high-precision thermal emission observations of these objects.

Given a parametric atmospheric model, an atmospheric retrieval framework explores a large number of solutions in order to fit an observed spectrum. While one approach is to pre-compute a grid of models across the parameter space (e.g. Madhusudhan and Seager, 2009), a more efficient approach is to use Bayesian parameter estimation methods such as optimal estimation (e.g. Lee et al., 2012; Line et al., 2014b; Barstow et al., 2017), MCMC (e.g. Madhusudhan and Seager, 2010; Madhusudhan et al., 2011a, 2014b; Line et al., 2014b; Waldmann et al., 2015; Todorov et al., 2016; Evans et al., 2017; Wakeford et al., 2017; Harrington et al., 2021) or Nested Sampling (e.g. Benneke and Seager, 2013; Waldmann et al., 2015; Lavie et al., 2017; MacDonald and Madhusudhan, 2017; Oreshenko et al., 2017; Gandhi and Madhusudhan, 2018).

Bayesian parameter estimation methods calculate the posterior probability distribution for each model parameter using Bayes' theorem:

$$p(\theta|\text{data}) = \frac{p(\text{data}|\theta)p(\theta)}{p(\text{data})} \quad (1.15)$$

where θ represents the vector of model parameters. $p(\theta|d)$ is the posterior probability distribution, $p(\theta)$ is the prior probability distribution of the parameters, $p(d|\theta)$ is the likelihood function of the data given the model parameters, and $p(d)$ is the Bayesian evidence, i.e. the probability of the data given the parametric model used. The posterior probability distributions produced by these algorithms indicate both the best-fit values of each model parameter as well as the uncertainty in this value. Notably, atmospheric retrievals are commonly used to place constraints on the chemical abundances and temperature structure in the atmosphere.

A key advantage of the Nested Sampling algorithm is that the Bayesian evidence of the retrieval model is calculated. In turn, the Bayesian evidence of a retrieved model fit can be used to statistically and robustly compare different retrieval models (e.g. Trotta, 2008). Bayesian model comparison is commonly used to assess the statistical significance of molecular detections by comparing retrieval models which include/exclude a certain molecule (e.g. Benneke and Seager, 2013; Gandhi and Madhusudhan, 2018). For two different retrieval models, a and b , the ratio of their Bayesian evidences (i.e. the Bayes factor),

$$\mathcal{B}_{a,b} = \frac{p(\text{data}|\text{model } a)}{p(\text{data}|\text{model } b)}, \quad (1.16)$$

provides a measure of how likely model a is relative to model b . For example, $\ln(\mathcal{B}_{a,b}) = 1.0, 2.5$ or 5.0 suggests weak, modest and strong evidence for model a over model b , respectively (Trotta, 2008). The Bayes factor can further be converted to a 'sigma' value to represent the confidence of the detection (Benneke and Seager, 2013).

While atmospheric retrievals of emission spectra are commonly performed in 1D, recent works have also developed multi-dimensional retrievals to account for the non-uniformity of exoplanet atmospheres and to interpret phase curve observations. For example, multi-dimensional retrievals can include multiple temperature profiles (compared to only one in 1D), accounting for the variable temperature profile across the planetary disc, to interpret both secondary eclipse observations and phase curves (e.g. Feng et al., 2016, 2020; Irwin et al., 2020; Taylor et al., 2020). An alternative method to interpret phase curve observations is to decompose the phase curve into spectra for individual longitudinal 'slices', and to apply a 1D retrieval to each slice (Cubillos et al., 2021). As observational capabilities improve, the quality of thermal emission observations will increasingly permit

the detection of inhomogeneities in the planetary disc (e.g. Taylor et al., 2020). Therefore, multi-dimensional methods such as these will become increasingly important in the future.

In this thesis, I develop adaptations of the `HyDRA` retrieval framework (Gandhi and Madhusudhan, 2018) for use with thermal emission spectra of isolated exoplanets and brown dwarfs (Chapter 2) and rocky exoplanets (Chapter 6). `HyDRA` uses `PyMultiNest` (Feroz et al., 2009; Buchner et al., 2014), a nested sampling Bayesian parameter estimation algorithm, for the parameter estimation and can therefore be used to evaluate the confidence of chemical detections.

1.4 Diversity of Exoplanets

The exoplanets discovered to date encompass a considerable diversity, going far beyond the planetary types known in the solar system. Spectroscopic observations of such exoplanets have the goal of not only characterising their atmospheres, but in doing so to understand their origins and evolution. Furthermore, atmospheric observations can in some cases be used to understand the physical processes occurring deeper in the interior of the planet. In what follows, I describe the four classes of exoplanets studied in this thesis: poorly-irradiated gas giants/sub-stellar objects, hot Jupiters, mini-Neptunes and rocky exoplanets. I also describe the concept of habitable exoplanets, and considerations for identifying these.

1.4.1 Poorly-Irradiated Gas Giants and Sub-Stellar Objects

Poorly-irradiated gas giants and sub-stellar objects include objects orbiting at large distances from their host stars, as well as isolated (i.e. free-floating) exoplanets and brown dwarfs. As described in section 1.2, the dominant source of energy in the atmospheres of such objects is internal energy, typically remnant from the planet formation process. As this internal energy is radiated over time, the object cools and contracts with age and the corresponding chemistry also evolves (e.g. Baraffe et al., 2003; Kirkpatrick, 2005; Burrows et al., 2011). The hotter temperatures and larger radii of younger objects make them more conducive for detection and atmospheric characterisation; the poorly-irradiated exoplanets known to date therefore belong to young systems (e.g. Marois et al., 2008, 2010; Lagrange et al., 2010; Biller and Bonnefoy, 2018).

The atmospheres of a number of poorly-irradiated giant exoplanets have been characterised using both coronagraphic and interferometric facilities to separate the stellar

and planetary fluxes. For example, detections of H₂O, CO and CH₄ have been made in the HR 8799 b-e planets using the VLT's SPHERE instrument and the Keck/OSIRIS spectrograph (Barman et al., 2011; Konopacky et al., 2013; Barman et al., 2015; Bonnefoy et al., 2016; Zurlo et al., 2016). These observations have suggested a range of atmospheric metallicities ranging from sub-solar to super-solar across the four planets (Lee et al., 2013; Lavie et al., 2017). Both SPHERE and the GPI instrument at the Gemini Observatory have been used to detect H₂O, CH₄ and clouds in the atmosphere of 51 Eri b (Samland et al., 2017; Macintosh et al., 2015). Furthermore, H₂O and CO have been detected in the poorly-irradiated exoplanet β Pictoris b using GPI and the GRAVITY instrument of the Very Large Telescope Interferometer (VLTI) (Chilcote et al., 2017; Gravity Collaboration et al., 2020).

Isolated brown dwarfs bear many similarities to directly-imaged giant planets, given their H₂-rich atmospheres and lack of incident irradiation. Consequently, the physical processes in both classes of objects may be expected to be similar for comparable effective temperatures, making brown dwarfs exquisite analogs to investigate the physical characteristics of exoplanets at large orbital separations (e.g. Burgasser, 2011; Line et al., 2017). Furthermore, brown dwarfs can be observed more precisely than wide-orbit exoplanets thanks to their lack of host star and larger surface gravities, which result in deeper spectral features and more precise chemical constraints (e.g. Line et al., 2015, 2017). Indeed, recent works have begun to explore the chemical abundances and temperature profiles of brown dwarfs using atmospheric retrieval methods (e.g. Line et al., 2015, 2017; Burningham et al., 2017; Zalesky et al., 2019). Recent observations using HST/WFC3 have also resulted in very high-precision spectra for a number of field brown dwarfs (e.g. Buenzli et al., 2014). In Chapter 2, I explore important considerations for the interpretation of such spectra, including the modelling of the temperature profile and inclusion of model uncertainties. Such considerations will also be important for the interpretation of high-precision wide-orbit exoplanet spectra in the future.

1.4.2 Hot Jupiters

Hot Jupiters are giant planets which orbit very close to their host stars, with typical orbital periods $\lesssim 10$ days. Given their small orbits, hot Jupiters are typically tidally locked and have very high equilibrium temperatures, ranging from ~ 800 K to over 3000 K (e.g. see Figure 1.1). In particular, hot Jupiters with equilibrium temperatures ≥ 2200 K are commonly referred to as 'ultra-hot Jupiters'. Given their large radii and small orbital distances, hot Jupiters are optimally suited for detection and characterisation with the transit and RV

methods. As such, this type of planet dominated the first discoveries of exoplanets and still dominates the exoplanet atmospheres characterised to date.

As discussed in Section 1.2, the strong irradiation incident upon hot Jupiter atmospheres results in isothermal temperature structures in their lower atmospheres, and can also lead to thermal inversions in the observable atmosphere (e.g. Hubeny et al., 2003). To date, three exoplanets are known to host thermal inversions; WASP-18b (Sheppard et al., 2017), WASP-33b (Haynes et al., 2015) and WASP-121b (Evans et al., 2017). Such inferences of thermal inversions are made by identifying emission features in their thermal spectra. Although thermal inversions are known to exist in the atmospheres of solar system planets (e.g. Moses et al., 2005; Robinson and Catling, 2014), the molecules which cause them (e.g. ozone in Earth's atmosphere and hydrocarbon hazes on Jupiter) cannot exist at the high temperatures present in hot Jupiter atmospheres. However, Hubeny et al. (2003) suggested that alternative, high-temperature, absorbers such as TiO or VO could produce thermal inversions in strongly-irradiated exoplanets, opening up the field of exoplanet atmospheres to a new class of thermal structures (e.g. Fortney et al., 2006a; Burrows et al., 2007). TiO also has spectral features in the optical and near-infrared that have been detected. However, interpretations of TiO signatures rely on the accuracy of TiO opacity used in the models. In Chapter 3, I explore how detections of TiO can depend on the molecular line list assumed. I further explore how the presence and strength of thermal inversions caused by TiO depends on properties such as irradiation and chemical composition.

Recent observations of hot Jupiters have also begun to place constraints on the clouds/hazes which may be present in their atmospheres (e.g. Demory et al., 2013; Evans et al., 2013; Parmentier et al., 2016; Sing et al., 2016). Given the high atmospheric temperatures, these aerosols have been suggested to consist of species such as silicates and hydrocarbon hazes, based on transmission spectroscopy observations (e.g. Gao et al., 2020). The presence of photospheric clouds can also be inferred by a high optical albedo, as incident irradiation from the star is scattered by the cloud (e.g. Demory et al., 2011b, 2013; Evans et al., 2013; Angerhausen et al., 2015; Esteves et al., 2015; Mallonn et al., 2019; Wong et al., 2020b). While several hot Jupiters have been found to have reasonably high optical albedos (e.g. Kepler-7 b, Demory et al. 2011b, 2013; Kepler-13A b, Shporer et al. 2014; KELT-19 b, Wong et al. 2020a; WASP-100 b, Jansen and Kipping 2020), the majority of hot Jupiters with albedo constraints have in fact been found to have low albedos (e.g. Rowe et al., 2006, 2008; Angerhausen et al., 2015; Esteves et al., 2015; Bell et al., 2017; Hooton et al., 2018; Močnik et al., 2018; Shporer et al., 2019; Mallonn et al., 2019; Kane et al., 2020; Wong et al., 2020b). Optical photometric observations from TESS and HST are now beginning to expand the population of hot Jupiters with albedo constraints (e.g.

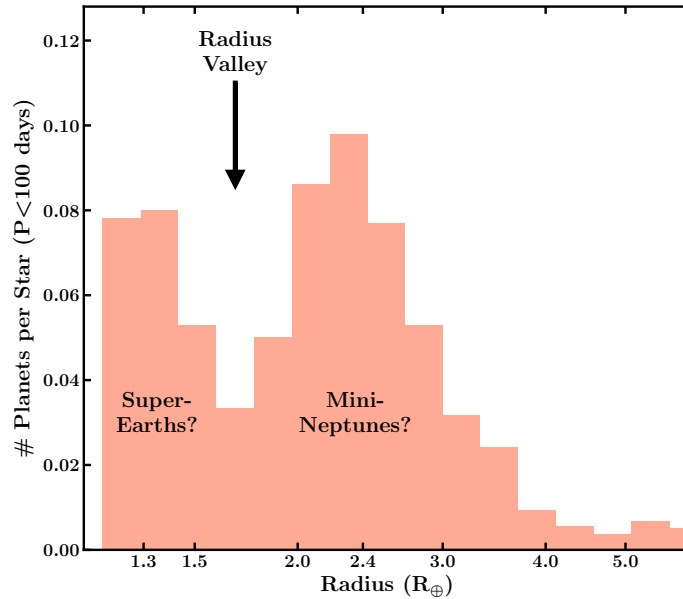


Fig. 1.8 The observed distribution of radii for low-mass exoplanets (adapted from Fulton et al. 2017). A ‘radius valley’ at $\sim 1.5\text{--}2 R_{\oplus}$ separates peaks at ~ 1.3 and $\sim 2.4 R_{\oplus}$, which may correspond to rocky ‘super-Earths’ and more volatile-rich ‘mini-Neptunes’, respectively.

Beatty et al., 2020; Wong et al., 2020a,b; Fraine et al., 2021; von Essen et al., 2021), and will provide a broader perspective on the scattering properties of these exoplanets. In Chapter 4, I investigate secondary eclipse observations of three hot Jupiters from the optical to the infrared: KELT-1 b, WASP-43 b and WASP-18b. I use self-consistent atmospheric atmospheric models (Section 1.3.2) in order to establish whether clouds are needed to explain the TESS, HST and Spitzer data available for these targets.

1.4.3 Mini-Neptunes

Mini-Neptunes are exoplanets with radii in the range $\sim 1.6\text{--}4 R_{\oplus}$, i.e. lying between the rocky planet and Neptune-like regimes (e.g. Rogers, 2015, see also Figure 1.1). Given their radii and masses, a number of interior structures are possible for such planets, ranging from dense rocky cores with thick hydrogen-rich envelopes to low-density water-rich interiors with thinner atmospheres (e.g. Rogers and Seager, 2010a,b; Valencia et al., 2013; Zeng and Sasselov, 2013; Lopez and Fortney, 2014; Madhusudhan et al., 2020). Notably, while no such planets are known to exist in the solar system, mini-Neptunes are the most common type of exoplanet detected to date (e.g. Fressin et al., 2013; Fulton et al., 2017). This peak in the radius distribution of known exoplanets (with a maximum occurrence rate at $\sim 2.4 R_{\oplus}$) is one of two peaks in the low-mass regime, with the second occurring

at $\sim 1.3 R_{\oplus}$ (Figure 1.8, Fulton et al. 2017; Owen and Wu 2017). The dip in exoplanet occurrence between ~ 1.5 - $2 R_{\oplus}$ is known as the ‘radius valley’ and is thought to arise as a result of atmospheric loss mechanisms; exoplanets with smaller primary atmospheres are more susceptible to atmospheric loss by photoevaporation or core-powered mass loss and are therefore stripped, while larger atmospheres remain less susceptible to these loss mechanisms (e.g. Ginzburg et al., 2018; Gupta and Schlichting, 2019; Owen et al., 2020).

Atmospheric observations of mini-Neptunes have begun to place constraints on their compositions, clouds/hazes and thermal properties. For example, HST transmission spectroscopy of the $2.9 R_{\oplus}$ radius exoplanet GJ 1214 b (which has an equilibrium temperature of ~ 600 K) has revealed a high-precision flat spectrum in the near-infrared, suggesting the presence of clouds and/or hazes (Kreidberg et al., 2014a; Morley et al., 2013). More recently, H_2O has been detected in the atmosphere of a habitable-zone mini-Neptune, K2-18 b (Benneke et al., 2019b; Tsiaras et al., 2019). This is the first detection of H_2O in any habitable-zone exoplanet and places K2-18 b as a prime candidate for further characterisation.

Interior structure models have been used to explore the possible interior compositions of K2-18b given its mass of $8.63 M_{\oplus}$ and radius of $2.6 R_{\oplus}$ (Madhusudhan et al., 2020). Madhusudhan et al. (2020) find that the mass, radius and atmospheric properties of K2-18 b are consistent with an interior structure comprising a silicate/Fe core, a H_2O layer and a H_2 -rich atmosphere. While a range of degenerate solutions are possible, the pressure below the atmosphere can be as low as ~ 1 bar with temperatures $\lesssim 400$ K, allowing habitable conditions in the H_2O layer underneath. The temperature conditions at this potential ocean surface depend strongly on the atmospheric conditions above it. In Chapter 5, I explore how a range of atmospheric properties can affect the temperature profiles and thermal emission spectra of mini-Neptune atmospheres. Using K2-18 b as a case study, I then explore the range of atmospheric conditions which could allow a liquid water surface to exist beneath the atmosphere.

1.4.4 Rocky Exoplanets

While rocky planets are represented in the solar system, rocky exoplanets may encompass a wider variety of interior and atmospheric conditions. In particular, rocky exoplanet atmospheres can be a result of the primary atmosphere accreted, atmospheric loss processes, secondary outgassing and surface-atmosphere exchanges, which together allow for a wide variety of outcomes (e.g. Elkins-Tanton and Seager, 2008; Kite et al., 2016; Owen et al., 2020). Given their smaller radii compared to mini-Neptunes and giant exoplanets, rocky exoplanets and their thin atmospheres are more challenging to detect. However, this

challenge is mitigated in the case of M-dwarf host stars, whose smaller radii result in larger signals for both primary and secondary eclipse observations, as described in section 1.1 (e.g. Morley et al., 2017b). Many of the known rocky exoplanets suitable for atmospheric characterisation therefore orbit M-dwarfs (e.g. Gillon et al., 2017b; Southworth et al., 2017; Kreidberg et al., 2019; Ment et al., 2019).

Recent observations have probed the atmospheres of several rocky exoplanets. For example, transmission spectroscopy of GJ 1132 b has previously suggested an atmosphere with a high μ and/or high-altitude clouds (Southworth et al., 2017; Diamond-Lowe et al., 2018), while more recent observations indicate an H₂-rich atmosphere (Swain et al. 2021, though c.f. Mugnai et al. 2021). Furthermore, potential detections of HCN have been reported in H₂-rich atmospheres of rocky exoplanets 55 Cnc e and GJ 1132 b (Tsiaras et al., 2016; Swain et al., 2021). This could provide insights into their geophysical conditions, as argued in these works, as well as being consistent with predictions for atmospheres of carbon-rich planets (Madhusudhan et al., 2011b, 2012). On the other hand, transmission spectra of rocky exoplanets Trappist-1 d, e and f have ruled out clear, H₂-rich atmospheres for these planets (de Wit et al., 2018; Moran et al., 2018).

Thermal phase curves have also been used to place constraints on rocky exoplanet atmospheres. The phase curve of 55 Cnc e displays a strong hot-spot shift, indicating the presence of an atmosphere (Demory et al., 2016a; Hammond and Pierrehumbert, 2017; Angelo and Hu, 2017). In contrast, the strong day-night contrast and lack of hot-spot shift in the phase curve of LHS 3844 b suggests that this planet does not host a clear, H₂-rich atmosphere deeper than ~ 0.1 bar and may instead host a high- μ and/or cloudy atmosphere, or no atmosphere at all (Kreidberg et al., 2019; Diamond-Lowe et al., 2020). Future observations, e.g. with JWST, will provide chemical constraints on rocky exoplanet atmospheres, leading to unprecedented constraints on their formation and evolution.

Theoretical models of rocky planet atmospheres and surface-atmosphere interactions predict a wide range of possible atmospheric compositions beyond those seen in the solar system (Leconte et al., 2015). For example, volcanic/surface outgassing could result in atmospheres composed of H₂O, CO₂, SO₂, O₂ and H₂ depending on the surface conditions and bulk planetary properties (e.g. Gaillard and Scaillet, 2014; Dorn et al., 2018; Herbort et al., 2020). Degassing during accretion can further result in a wide range of atmospheric compositions including hydrogen, water and carbon compounds (Elkins-Tanton and Seager, 2008). Furthermore, Hu et al. (2012b) find that UV irradiation from an M-dwarf such as Trappist-1 could drive chemical reactions producing >1 bar of CO and/or O₂.

Given the possible diversity of atmospheric compositions for rocky exoplanets, the methods used to analyse their atmospheric spectra must be sufficiently flexible. While

a H₂-rich atmosphere can safely be assumed for giant planets, this is not the case for rocky exoplanets. In chapter 6, I present a new atmospheric retrieval framework (based on the HyDRA framework of Gandhi and Madhusudhan 2017) for thermal emission spectra of rocky exoplanet atmospheres, which does not make prior assumptions about the atmospheric composition. I then use this framework to explore the observations needed with JWST to constrain the atmospheric compositions of some of the most promising known rocky exoplanets.

1.4.5 Habitable Exoplanets

One of the primary goals of exoplanet exploration is to find habitable worlds outside the solar system. Given the diversity of known exoplanets and the challenges in observing their atmospheric and surface conditions, it is therefore useful to define the basic criteria assumed to be necessary for life. It is important to note, however, that while our current knowledge is limited by the types of life on earth, life on exoplanets may be as diverse and surprising as the exoplanets themselves. The metrics used to determine potential habitability therefore act as a guide and life may in fact be possible beyond these confines (e.g. Irwin, 2018).

The primary condition assumed to be necessary for life is the presence of liquid water (e.g. Meadows and Barnes, 2018). Furthermore, extremophiles on Earth are known to survive up to pressures of ~ 1000 bar and temperatures of ~ 400 K (e.g. Rothschild and Mancinelli, 2001; Merino et al., 2019). Therefore, liquid water satisfying these conditions may be thought to be ‘potentially habitable’. Beyond the presence of water, the radiation received from the host star is also an important factor for habitability (e.g. Segura, 2018). For example, M-dwarfs are known to be more active compared to Sun-like stars, including stellar flares and increased UV radiation which could be harmful to life on M-dwarf planets. However, this could potentially be mitigated by thicker atmospheres or molecules such as O₃, which could shield the surface from harmful radiation (e.g. Segura et al., 2003). While many other factors may also be important for the presence of life, e.g. plate tectonics, (e.g. Meadows and Barnes, 2018), in this thesis I will focus on the presence of liquid surface water as a necessary condition for life. In particular, in Chapter 5, I investigate the atmospheric conditions which could allow liquid water to exist at the surface of mini-Neptunes such as K2-18 b, if such a surface is present.

1.5 Overview of this Thesis

In this thesis, my overarching goal is to investigate the diversity of thermal and radiative properties in exoplanetary atmospheres across the wide range of exoplanet types discovered, spanning non-irradiated to highly-irradiated giant planets, temperate mini-Neptunes and rocky exoplanets across the temperature range. I pursue this investigation in two complementary directions: (i) conducting detailed self-consistent theoretical modelling to understand the interplay between physical and chemical processes across this vast planetary diversity, and (ii) constraining the thermal and chemical properties of a range of exoplanetary atmospheres with state-of-the-art observations, and exploring the limits of the constraints which will be possible with future facilities. Both of these avenues are synergistic with observational advances in the field which are allowing increasingly detailed insights into exoplanetary atmospheres. Beginning with poorly-irradiated giant planets and sub-stellar objects in Chapter 2, I progress to exoplanets of decreasing mass in Chapters 3 to 6, including hot Jupiters, mini-Neptunes and rocky exoplanets.

In Chapter 2, I investigate important considerations for the atmospheric retrieval of high-precision brown dwarf spectra, which also have implications for retrievals of poorly-irradiated giant exoplanets. In particular, I develop a new temperature profile parameterisation tailored for such objects, and propose a method for including model uncertainty in the retrieval. In Chapter 3, I focus on the temperature profiles and thermal emission spectra of hot Jupiters with thermal inversions due to TiO. I investigate the effects of various TiO opacities on different types of atmospheric observations, and assess the performance of photometric thermal inversion metrics across a range of chemical compositions, irradiation conditions and gravities using self-consistent 1D models. In Chapter 4, I use similar self-consistent models to investigate observations of thermal emission from three hot Jupiters. In particular, recent TESS and HST observations of hot Jupiters can provide constraints on their scattering properties, and I investigate the relative contributions of thermal emission vs scattering required to explain their optical to near-infrared spectra.

In Chapters 5 and 6, I turn towards the atmospheres of smaller and cooler exoplanets. I firstly investigate the thermal and radiative properties of mini-Neptune atmospheres in Chapter 5, and assess the atmospheric conditions which may allow habitable surface conditions in temperate mini-Neptunes such as K2-18 b using self-consistent 1D atmospheric models. In Chapter 6, I then develop a retrieval framework for thermal emission spectra of rocky exoplanets, and investigate the chemical and thermal constraints which will be

possible with JWST for case studies across a range of temperatures. Finally, in Chapter 7, I summarise the conclusions of this thesis and discuss promising future avenues.

2

Considerations for Atmospheric Retrieval of High-Precision Brown Dwarf Spectra

In this chapter, we investigate the atmospheres of isolated sub-stellar objects, i.e. the high-mass, low-irradiation regime.¹ In particular, isolated brown dwarfs provide remarkable laboratories for understanding atmospheric physics in the low-irradiation regime, and can be observed more precisely than exoplanets. As such, they provide a glimpse into the future of high-SNR observations of exoplanets. In this chapter, we investigate several new considerations that are important for atmospheric retrievals of high-quality thermal emission spectra of sub-stellar objects. We pursue this using an adaptation of the HyDRA atmospheric retrieval code. We propose a parametric pressure-temperature (P-T) profile for brown dwarfs consisting of multiple atmospheric layers, parameterised by the temperature change across each layer. This parameterisation allows the steep temperature gradient of brown dwarf atmospheres to be accurately retrieved while avoiding commonly-encountered numerical artefacts. The P-T parameterisation is especially flexible in the photosphere, which can reach a few tens of bar for T-dwarfs. We demonstrate an approach to include model uncertainties in the retrieval, focusing on uncertainties introduced by finite spectral and spatial resolution in the atmospheric model used for retrieval (~8% in the present case). We validate our retrieval framework by applying it to a simulated data set and then apply it to the HST/WFC3 spectrum of the T-dwarf 2MASS J2339+1352. We retrieve sub-solar abundances of H₂O and CH₄ in the object at

¹This work has been published in Piette and Madhusudhan (2020a).

~0.1 dex precision. Additionally, we constrain the temperature structure to within ~100 K in the photosphere. Our results demonstrate the promise of high-SNR spectra to provide high-precision abundance estimates of sub-stellar objects.

2.1 Introduction

As described in Chapter 1, the field of exoplanet and brown dwarf atmospheres is undergoing rapid progress, with increasingly detailed characterisation made possible by state-of-the-art spectroscopic observations and sophisticated retrieval methods. Directly-imaged brown dwarfs can provide a glimpse into the future of exoplanet observations as their lack of stellar companion and prominent spectral features make them ideal for very high-precision observations and characterisation, while their atmospheres bear many similarities with those of giant planets in the low-irradiation regime (e.g. Basri and Brown, 2006; Burgasser, 2011; Marley and Robinson, 2015). Isolated brown dwarfs are also excellent probes of unknown sub-stellar formation mechanisms, as they lie in the transitional domain between planetary and stellar masses where such mechanisms are still in debate (e.g. Whitworth et al., 2007; Luhman, 2012; Chabrier et al., 2014; Maldonado and Villaver, 2017; Lodieu et al., 2021). Determining their compositions may contribute to constraining such formation mechanisms by finding (dis)similarities with planetary and stellar properties.

Similarly to exoplanets, brown dwarf spectra have traditionally been analysed by identifying specific molecular features or fitting them with grids of equilibrium models (e.g. Mohanty et al., 2004a,b). Based on the presence of various combinations of species in different objects, this has led to the classification of brown dwarfs into the spectral types L, T and Y, analogous to those of stars (Kirkpatrick, 2005; Cushing et al., 2011). Although the L-T classification is based only on spectral features, estimates of the effective temperatures of L and T dwarfs (Vrba et al., 2004; Dahn et al., 2002; Golimowski et al., 2004; Kirkpatrick, 2005) have shown that the spectral sequence follows a sequence in temperature, where early L dwarfs are hottest and late T dwarfs are coolest. Furthermore, L dwarfs show signs of clouds and dust which are not typically seen in T-dwarfs (e.g. Marley et al., 2002; Tsuji, 2002). Cloud formation and sedimentation, as well as dynamical processes and disequilibrium chemistry, have been explored through both self-consistent models and observations of brown dwarf spectra (e.g. Saumon et al., 2000; Burrows et al., 2006a; Cushing et al., 2008; Apai et al., 2013; Marley and Robinson, 2015).

More recently - as with exoplanet atmospheres - atmospheric retrievals have begun to be used with brown dwarf spectra (e.g. Line et al., 2014a, 2015, 2017; Burningham et al.,

2017; Zalesky et al., 2019; Kitzmann et al., 2020). Since brown dwarfs closely resemble giant planets, the retrieval methods used are similar, though with some notable differences. For example, unlike exoplanets, the gravities, distances and radii of brown dwarfs are not necessarily known and these quantities are included as free parameters in the retrieval. Furthermore, since isolated sub-stellar objects are not expected to exhibit thermal inversions or deep isotherms, their P - T profiles can be parameterised differently to those of irradiated exoplanets (e.g. Line et al., 2015; Burningham et al., 2017; Gravity Collaboration et al., 2020; Kitzmann et al., 2020). Retrieval methods also differ between L and T dwarfs, as L dwarfs are known to have clouds, which must therefore be included in the retrieval analyses of their spectra (Burningham et al., 2017). In contrast, Line et al. (2015) show that the inclusion of clouds in their retrievals of T-dwarf spectra does not affect their results.

One of the principal differences between brown dwarf retrieval approaches in the literature is the treatment of the pressure-temperature (P - T) profile (e.g. Burningham et al., 2017; Line et al., 2017; Kitzmann et al., 2020). For example, Line et al. (2015, 2017) use 15 temperature parameters, corresponding to fixed pressures, and interpolate between them in order to compute radiative transfer at a higher spatial resolution. Since these temperature parameters are degenerate, they also penalise the second derivative of the temperature profile in order to prevent unphysical oscillations in temperature. Burningham et al. (2017), however, find that this method - originally used with T-dwarfs - presents challenges with cloudy L-dwarfs as the spectral contrast of their data is not able to shift the P - T profile away from the linear fit that is preferred by the second derivative minimisation. Instead, Burningham et al. (2017) use the parametric P - T model from Madhusudhan and Seager (2009). Kitzmann et al. (2020) consider two further approaches to model the P - T profile: a piecewise polynomial and an approximate solution to radiative transfer assuming radiative equilibrium in a gray atmosphere, both chosen to avoid unphysical oscillations.

In this chapter, we present various considerations that can affect the accuracy of brown dwarf retrievals, focusing especially on T-dwarfs. Motivated by the high-quality spectra available for brown dwarfs, we seek ways to maximise the precision and accuracy of the results obtained. We begin by introducing a way of considering uncertainties in the retrieval, in particular taking into account the uncertainties in the model. We find that it can be important to explicitly factor in model uncertainty in order to accurately retrieve the properties of an atmosphere from a high signal-to-noise-ratio (SNR) spectrum. We also introduce a new multi-layer P - T parametrisation in which the average slope of each layer is a parameter and the temperature nodes between the layers are interpolated such that the first derivative of the P - T profile is continuous throughout the atmosphere. The

priors on the slope parameters, as well as the interpolation method, are chosen to prevent numerical artefacts. We implement this P - T parameterisation in the HyDRA retrieval code (Gandhi and Madhusudhan, 2018). We then test our approach on simulated data and apply it to a high-SNR spectrum of the T-dwarf 2MASS J2339+1352.

We begin by giving a general outline of the retrieval framework we use in Section 2.2. Our developments in considering uncertainties and parameterising the P - T profile are then described in Sections 2.3 and 2.4, respectively. We test the method on synthetic data in Section 2.5 and apply it to a real T-dwarf spectrum in Section 2.6. Our conclusions and discussion are presented in Section 2.7.

2.2 Atmospheric Model

In this chapter, we use the retrieval method of Gandhi and Madhusudhan (2018) (HyDRA, as described in Section 1.3.2), with some modifications. HyDRA has thus far been used to retrieve the thermal emission spectra of transiting exoplanets. Here, we adapt the retrieval method to apply it to high-SNR brown dwarf spectra. In particular, HyDRA uses a parametric P - T profile (Madhusudhan and Seager, 2009) which allows for features that can be present in irradiated atmospheres, such as deep isotherms and thermal inversions. In this chapter, we develop a new parametric P - T profile which is more suitable for non-irradiated objects. The spectra we consider have a much higher SNR than typical exoplanet spectra. As a result, the data is better able to constrain the P - T profile and a more flexible P - T parameterisation is desirable to fully capture the information in the spectrum. In addition to a new P - T parameterisation, we also adapt the retrieval method to include sources of model uncertainty, which can become significant when observational uncertainty is very small.

Another important difference between transiting planets and directly imaged brown dwarfs is that the radius and mass of transiting planets can be obtained through primary transit and radial velocity observations, and the distance to the host star (and therefore the planet) is typically known. In contrast, these quantities are unknown for isolated brown dwarfs and, hence, need to be included as free parameters in the model. We include them as the radius-distance ratio (R/d) and log gravity ($\log(g)$) as these quantities are independent in the calculation of the spectrum (note that radius and distance only affect the spectrum through the quantity R/d so are perfectly degenerate, as shown in Equation 1.14).

Since giant planets and brown dwarfs both have H_2 -rich atmospheres, the chemical species we include in the forward model are largely similar to those in exoplanet studies.

To decide which species to include, we turn to previous analyses of T-dwarf spectra, which have shown that H₂O, CH₄ and collision-induced absorption (CIA) from H₂-H₂ and H₂-He interactions dominate their spectra (Kirkpatrick, 2005). Na and K are also known to be present in the near-infrared spectra of T-dwarfs, especially towards shorter wavelengths in the wings of their strong optical lines. Although CO is not expected to occur in equilibrium at the temperatures in T-dwarfs, it has been observed in some cases including the first discovered T dwarf, GJ 229b (Noll et al., 1997; Kirkpatrick, 2005), and is likely indicative of atmospheric vertical mixing (Moses et al., 2011). NH₃ is also expected to appear in T-type spectra, although not as strongly as H₂O and CH₄ (Roellig et al., 2004). For completeness, we also retrieve the abundances of CO₂ and HCN which could potentially be significant in H₂-rich atmospheres. The cross sections we use in our models, apart from those of Na and K, are calculated as in Gandhi and Madhusudhan (2017) from the HITEMP, HITRAN and ExoMol line list databases (H₂O, CO and CO₂: Rothman et al. (2010), CH₄: Yurchenko et al. (2013); Yurchenko and Tennyson (2014), NH₃: Yurchenko et al. (2011), HCN: Harris et al. (2006); Barber et al. (2014), CIA: Richard et al. (2012)). The broadening we use for Na and K is described in detail in Section 2.3.1. Note that, since clouds are not typically detected in T-dwarfs, we do not include them in the model (e.g. Tsuji 2002; Kirkpatrick 2005; Line et al. 2015, but see also Morley et al. 2012; Buenzli et al. 2014).

The forward model spectrum is generated from the P - T parameters, chemical abundances and bulk parameters by solving radiative transfer, hydrostatic equilibrium and the ideal gas law successively across thin layers of the atmosphere (Gandhi and Madhusudhan, 2018), as described in Section 1.3.2 of Chapter 1. In the retrieval, the abundances of the chemical species are characterised by their mixing ratios, $X_i = n_i/n$, where n and n_i are the overall number density and the number density of species i , respectively. We nominally use 100 thin atmospheric layers for the radiative transfer calculation, but investigate the effect of this number on the accuracy of the spectrum in Section 2.3.1. At the top of the atmosphere, the emergent flux is given by Equation 1.14. This model spectrum is convolved with HST's PSF and then binned into simulated data points at the resolution of HST/WFC3 data.

The parameters listed above are estimated for a given observed spectrum using the Nested Sampling algorithm (Skilling, 2006), implemented using PyMultiNest (Buchner et al., 2014). This method returns the posterior probability distributions of each model parameter following Bayes' theorem (Equation 1.15). The priors used for each parameter are shown in Table 2.1. In this chapter, we assume a Gaussian form for the likelihood

Table 2.1 The priors used for each model parameter. All ΔT_i parameters below pressures of 3.2 bar have the same prior range.

Parameter	Prior	Range
X_i	log-uniform	$10^{-10} - 10^{-2}$
R/d (R_J/pc)	uniform	$10^{-3} - 1$
$\log(g/\text{cms}^{-2})$	uniform	2 - 7
x_{tol}	uniform	8% - 100%
$T_{3.2\text{b}}$ (K)	uniform	300 - 4000
$\Delta T_{100-32\text{b}}$ (K)	uniform	0 - 2500
$\Delta T_{32-10\text{b}}$ (K)	uniform	0 - 2000
$\Delta T_{10-3.2\text{b}}$ (K)	uniform	0 - 1500
$\Delta T_{3.2-1\text{b}} - \Delta T_{10-1\text{mb}}$ (K)	uniform	0 - 1000

function:

$$\mathcal{L}(\text{data}|\theta) = \sum_i \frac{1}{\sqrt{2\pi\sigma_i^2}} \exp\left[-\frac{(\text{model}_i - \text{data}_i)^2}{2\sigma_i^2}\right], \quad (2.1)$$

where the summation is over all data points and the uncertainties, σ_i , will be discussed in Section 2.3.

In order to test this retrieval method - and various P - T parameterisations within it - we create a simulated spectrum with known input parameters (black spectrum in right panel of Figure 2.5). A successful method should then be able to accurately retrieve these inputs. Throughout this chapter, we base our simulated spectrum on the well-studied T-dwarf Gl 570D (e.g. Burgasser et al., 2000, 2003, 2006; Geballe et al., 2001, 2009; Leggett et al., 2002; Cushing et al., 2006; Patten et al., 2006; Saumon et al., 2006; Hubeny and Burrows, 2007; Line et al., 2014a, 2015). For the input P - T profile, we use the equilibrium P - T profile shown in figure 3 of Line et al. (2015) (based on Saumon and Marley (2008), shown here in the left panel of Figure 2.5). The abundances for H_2O , CH_4 , NH_3 , CO , CO_2 , Na and K as well as the radius-distance ratio and gravity are those retrieved by Line et al. (2015), and are listed in Table 2.2. In order to test our forward parameterisation, we recreate the median retrieved spectrum from Line et al. (2015) using their median retrieved P - T profile (different from the equilibrium P - T profile that we use for our simulated data) and the parameters listed in Table 2.2. The spectrum we generate with these inputs is consistent with that of Line et al. (2015), validating our forward model (Figure 2.1).

Table 2.2 Atmospheric parameters used to simulate the HST/WFC3 spectrum of Gl 570D, from the retrieval of Line et al. (2015). Also shown are the parameter values we obtain from the retrieval of this simulated data, which are consistent with the true input values (Section 2.5). CO, HCN and CO₂ are not constrained by the retrieval.

Parameter	Input value	Retrieved value
$\log(X_{\text{H}_2\text{O}})$	-3.45	-3.4 ± 0.1
$\log(X_{\text{CH}_4})$	-3.40	-3.3 ± 0.1
$\log(X_{\text{NH}_3})$	-4.64	-4.6 ± 0.1
$\log(X_{\text{CO}})$	-7.53	–
X_{HCN}	0.00	–
$\log(X_{\text{CO}_2})$	-7.76	–
$\log(X_{\text{Na}})$	-5.50	–
$\log(X_{\text{K}})$	-6.69	$6.8^{+0.3}_{-1.1}$
R/d (R_J/pc)	0.1952	0.20 ± 0.01
$\log(g/\text{cms}^{-2})$	4.76	4.8 ± 0.2
x_{tol}	-	$8.05^{+0.07}_{-0.03} \%$

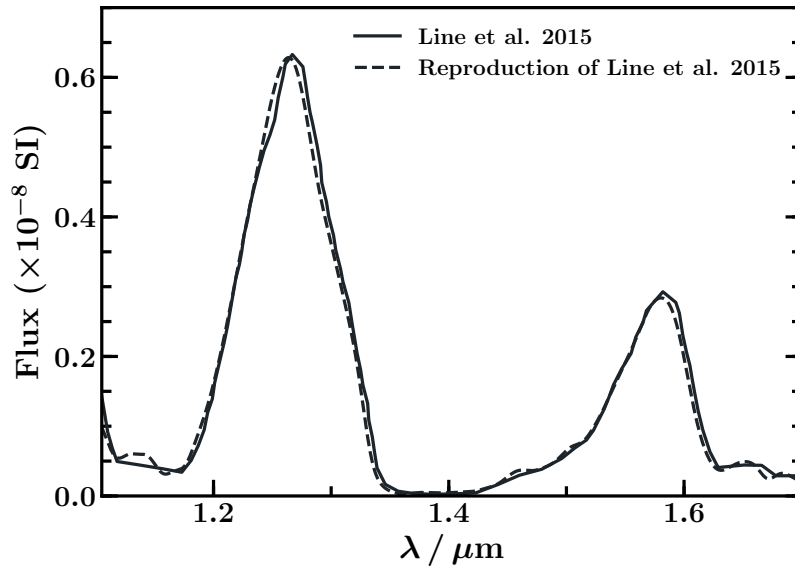


Fig. 2.1 Model spectra for validation. The retrieved spectrum of Gl 570D by Line et al. (2015) is shown by the solid line, and our reproduction of this spectrum using the same P - T profile and atmospheric parameters is shown by the dashed line. The two spectra are consistent with each other. Flux axis is shown in SI units ($\text{Wm}^{-2}\text{m}^{-1}$).

2.3 Treatment of Model Uncertainties

Retrievals performed on exoplanet and brown dwarf spectra to date have had sufficiently low SNR that model uncertainties may not have been significant. However, for high-precision spectra, it can be important to consider model uncertainties in addition to observational uncertainties. The data considered in this chapter, obtained by the Hubble Space Telescope's Wide-Field Camera 3 (HST/WFC3), has an extremely high SNR at only a $\sim 0.1\%$ noise level. The uncertainties in models could therefore add a potentially significant contribution to the σ_i term in the likelihood function (Equation 2.1). We discuss sources of model uncertainty in Section 2.3.1, and quantify the magnitude of uncertainty due to resolution effects. In Section 2.3.2, we describe how simulated data are generated such that the effects of these uncertainties on a retrieval can be tested (Section 2.5). In Section 2.3.3, we discuss how quantified model uncertainties can be incorporated in a retrieval, along with a 'tolerance' parameter which captures unknown sources of model and/or observational uncertainty.

2.3.1 Uncertainties in the model spectra

In this chapter, we focus on quantifying two important sources of model uncertainty: spectral and vertical resolution. In particular, we explore various methods and spectral resolutions for sampling molecular cross sections, as well as the number of atmospheric layers used to calculate the radiative transfer (i.e. vertical resolution). In this section, we assess the magnitude of these uncertainties. As a compromise between precision and computational runtime, we choose to use spectral and vertical resolutions which result in a combined uncertainty of $\sim 8\%$ in the spectrum. We also consider uncertainties due to the broadening of Na and K lines and briefly discuss other potential sources of model error which could be addressed in future work.

Spectral resolution: Since the calculation of each model in the retrieval must be very fast, the resolution to which a model spectrum can be calculated (before binning) is limited. The molecular cross sections are typically computed at very high resolution with a grid spacing of $0.01\text{-}0.1\text{cm}^{-1}$. The cross sections of each species must be sampled at lower resolution, which affects the accuracy of the generated spectrum. This can be done in several ways, e.g. sampling individual points, log-averaging the cross sections over wavelength bins or using the correlated-k method (e.g. Irwin et al., 2008; Amundsen et al., 2017). Here we compare the accuracies of four sampling methods:

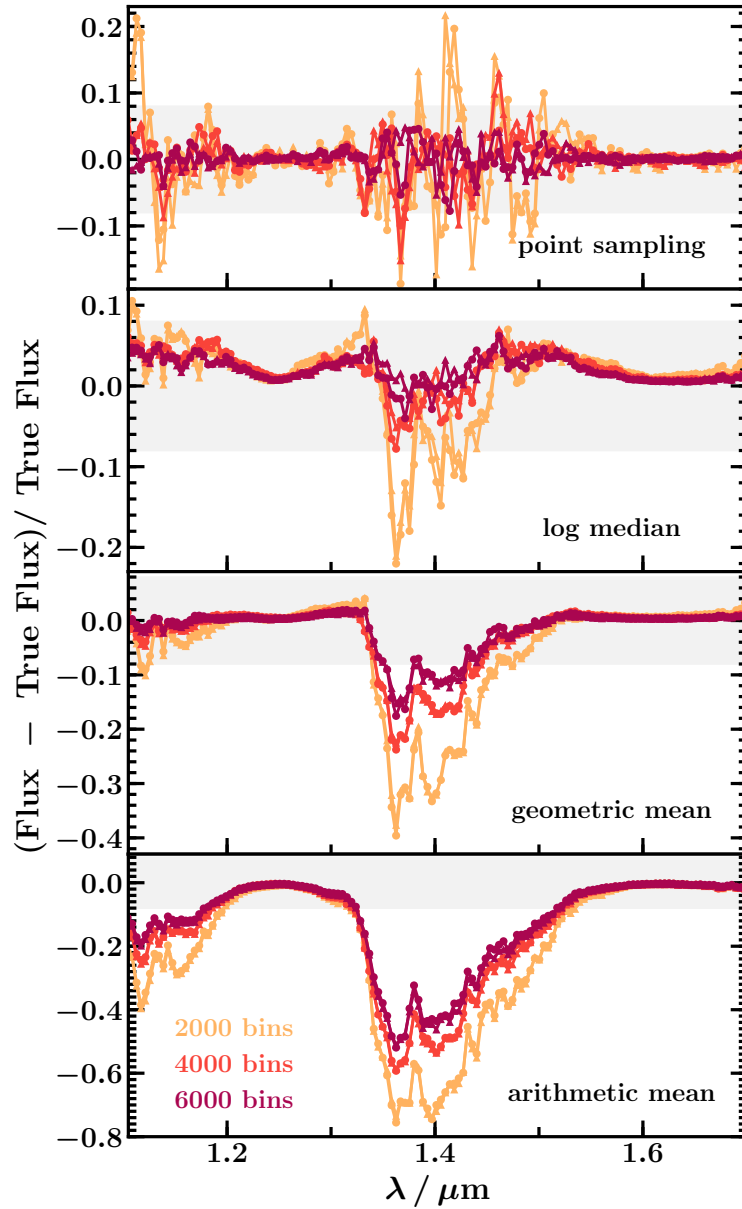


Fig. 2.2 Fractional error in the spectrum for different cross section sampling methods. Orange, red and maroon lines and markers correspond to different spectral resolutions, i.e. 2000, 4000 and 6000 linearly-spaced wavelength bins in the range 1.1-1.7 μm , respectively. Whether the cross sections being sampled have a native resolution of 0.01cm^{-1} (triangles) or 0.1cm^{-1} (circles) does not have a significant effect on the spectral error. The region of $\leq 8\%$ error is shaded in grey.

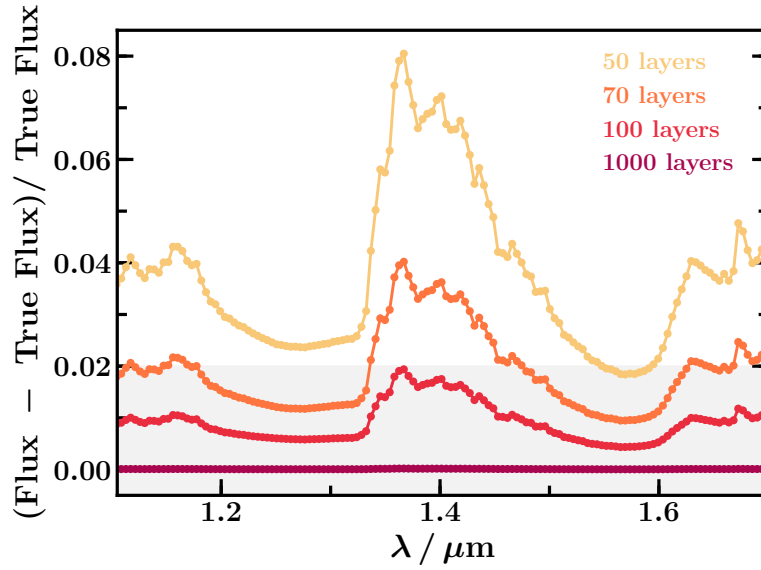


Fig. 2.3 Fractional error in the spectrum for different numbers of atmospheric layers in the model (between 100 and 10^{-3} bar). The region of $\leq 2\%$ error is shaded in grey.

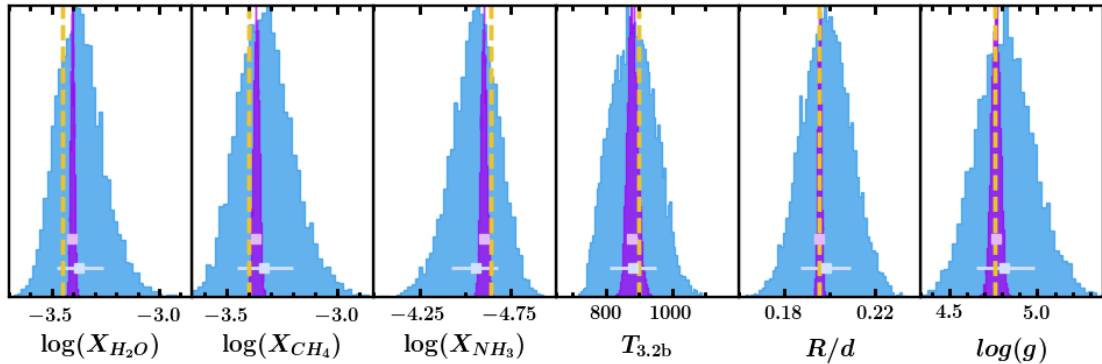


Fig. 2.4 Posterior probability distributions obtained with two different tolerance parameters. Squares and error bars show the median retrieved parameter values and 68% confidence intervals, respectively, and the true input values are shown by yellow dashed lines. Purple histograms and light purple squares (top) show the retrieval output when the tolerance parameter takes the form in Equation 2.2, with a prior which allows a negligibly small value of the tolerance to be retrieved (note that the error bars are smaller than the symbol). In this case, the uncertainty in the retrieved parameters is noticeably underestimated. Blue histograms and light blue squares and error bars (bottom) correspond to the tolerance parameter described in Equation 2.3, with a prior which explicitly accounts for known model uncertainties. This form of the tolerance parameter successfully retrieves the atmospheric parameters to within one standard deviation.

1. point-sampling: values of the cross sections are taken at the chosen spectral resolution
2. geometric mean : the cross sections are divided into bins at the chosen spectral resolution, and the representative cross sections in each bin are log-averaged from the native resolution. The averaged cross section is associated with the central wavelength of the bin.
3. taking the arithmetic mean: similar to (ii) , but the arithmetic mean is taken rather than log-averaging.
4. taking the log median : similar to (ii) again, but the median log cross section of the bin is used rather than the log average.

We also wish to test how the native resolution of the cross sections affects the accuracy of the spectrum, i.e. is sampling from a 0.1cm^{-1} resolution cross section less accurate than sampling from a 0.01cm^{-1} resolution cross section? Since the model spectra are ultimately binned to the resolution of the data ($R\sim 100$), spectral information is lost and using very high-resolution cross sections is likely unnecessary. In our models, we use molecular cross sections for the various species at a native spacing of 0.1cm^{-1} . Here, we also test models with an even higher resolution (spacing of 0.01cm^{-1}) to evaluate its effect on spectral accuracy. Since the cross section profile of CIA from H_2 and He is very smooth, we use a resolution of 1cm^{-1} for CIA opacity throughout this chapter; a higher resolution is not needed as no sharp absorption features are revealed by doing this. In order to test the effect of the native resolution on the spectrum, we use a model atmosphere including only H_2 , He and H_2O and compare the 0.01cm^{-1} and 0.1cm^{-1} native resolutions of the H_2O cross sections. We generate the spectra assuming a H_2O mixing ratio of $10^{-3.45}$ and using the P - T profile shown in the left panel of Figure 2.5.

In Figure 2.2, we show the effect of spectral resolution and sampling method on the accuracy of spectra. We consider three sampling resolutions: 2000, 4000 and 6000 linearly-spaced wavelength points in the range 1.1 - $1.7\mu\text{m}$ (i.e. $R\sim 5000$, 10000 and 15000 in the WFC3 band). We investigate the four sampling methods mentioned previously, which are performed on cross sections of H_2O for which the native resolution is either 0.1cm^{-1} (shown by squares) or 0.01cm^{-1} (shown by triangles). The accuracy of these spectra is evaluated against a spectrum generated at native resolution using the higher-resolution (0.01cm^{-1}) H_2O cross sections.

We confirm that, as expected, the native resolution of the cross sections which are sampled (between 0.01cm^{-1} - 0.1cm^{-1}) makes very little difference to the binned spectrum.

The effects of the four sampling methods are, however, quite different. The geometric and arithmetic mean methods result in very large inaccuracies in the spectrum in some wavelength ranges, so we choose not to use these methods. Point-sampling and taking the log median introduce comparable magnitudes of uncertainty to the spectrum, but taking the log median performs slightly better; using 4000 wavelength points results in up to >10% uncertainty with point-sampling, but $\leq \sim 8\%$ with using the log median. Using the log median sampling method therefore results in a better accuracy pay-off for a given spectral resolution of the model.

We therefore choose to use the median sampling method in our retrieval framework. The number of wavelength bins used to compute the model spectra is then a compromise between computation time and accuracy. We choose to use 4000 bins as the $\leq \sim 8\%$ uncertainty it introduces still allows very good constraints to be placed on the atmospheric model parameters, while preserving a reasonable computation time.

Vertical resolution: As described in Section 2.2, hydrostatic equilibrium, radiative transfer and the ideal gas law are solved iteratively through each discrete layer in the model atmosphere between a maximum and minimum pressure. These pressure limits should be sufficiently generous that the spectrum is not affected by them, but narrow enough that not too many layers are needed to cover the pressure range. The minimum pressure, P_{min} , is dictated by the pressure at which the optical depth of the atmosphere is low enough not to affect the spectrum significantly. From Figure 2.5, we see that using $P_{min} = 10^{-3}$ should generously allow the photosphere to be probed. Since the spectrum is not affected by the deep regions of the atmosphere where the optical depth is very high, P_{max} should lie deeper than the deepest pressure which affects the spectrum. Figure 2.5 shows that contributions to the spectrum become small below ~ 70 bar, making 100 bar a suitable choice which amply captures the photosphere.

Given this pressure range, increasing the number of atmospheric layers increases the accuracy of the model spectrum, akin to the improvement in accuracy of a numerical integrator by decreasing its step size. However, since the computation time of one model spectrum scales linearly with the number of atmospheric layers, the optimal number of layers should be the minimum number needed for the contribution to the model uncertainty to be relatively insignificant. Figure 2.3 shows that using 100 layers between 100 bar and 10^{-3} bar only contributes $\sim 2\%$ uncertainty to the model, and this also allows for a manageable computation time. We therefore choose to calculate model spectra in the retrieval using 100 layers between 100 bar and 10^{-3} bar.

Our chosen spectral and vertical resolutions in the current models therefore result in a combined $\sim 8\%$ uncertainty when added in quadrature. Given that the majority of

the error is from the spectral resolution, this model uncertainty could be reduced if we were to consider higher spectral resolution, albeit at a greater computational cost. In what follows, we consider that the uncertainty in our present model has a lower limit of $\sim 8\%$. In Section 2.3.3, we describe how this lower limit is included in our retrievals.

Na and K cross sections:

Na and K both have strong features in the optical (at $\sim 0.6\mu\text{m}$ and $\sim 0.8\mu\text{m}$, respectively) with broad wings which extend into the near-infrared, as well as smaller lines in the optical and infrared. In particular, the K lines at $\sim 1.25\mu\text{m}$ produce a clear spectral feature present in the spectra of several T-dwarfs, including that of 2MASS J2339+1352 (Buenzli et al., 2014) which we discuss in Section 2.6. In the past, various treatments have been used for the broadening of both the strong optical and weaker infrared lines (Burrows and Volobuyev, 2003; Allard et al., 2007). We use the recent line profiles of Allard et al. (2016) and Allard et al. (2019) for the strong lines. However, for the smaller lines, there is some uncertainty as to which broadening profile is most appropriate.

In this chapter, we attempt to address the uncertainty in this broadening by using a simple parameterisation for the cross sections of the strongest K lines in the spectral range of interest. We apply the broadening profiles of Allard et al. (2016), scaled by line strength (Kramida et al., 2019), to the K lines at 1.169, 1.177, 1.178, 1.244 and $1.253\mu\text{m}$, and modulate their cross sections with a multiplicative factor which is a free parameter in the retrieval. We use two multiplicative factors: one (m_{K1}) for the lines at 1.244 and $1.253\mu\text{m}$ and another (m_{K2}) for the group of lines at 1.169, 1.177 and $1.178\mu\text{m}$. To avoid degeneracies between these parameters and the retrieved abundance of K (X_K), we choose to retrieve $X_{K1} = m_{K1} \times X_K$ and $X_{K2} = m_{K2} \times X_K$. As well as the opacity due to these K lines, we also include the wings of the broadened optical lines at $\sim 0.6\mu\text{m}$ and $\sim 0.8\mu\text{m}$ from Na and K, respectively, which we parameterise according to the abundances of Na and K (X_{Na} and X_K , respectively).

We apply this parameterisation in the retrieval of the HST/WFC3 spectrum of 2MASS J2339+1352 (Section 2.6). In the spectral range we consider in this chapter ($1.1\text{-}1.7\mu\text{m}$), the wing of the Na optical line is fairly weak so we do not expect a strong constraint on the abundance of Na. However, since the K lines at $\sim 1.25\mu\text{m}$ correspond to a noticeable feature in the spectrum of 2MASS J2339+1352, we expect that X_{K1} will be strongly constrained. Note that without a detection of the K wing (i.e. a constraint on X_K), the retrieved value of X_{K1} does not result in an estimate of m_{K1} ; instead, this parameter simply allows the K feature at $\sim 1.25\mu$ to be fitted. More data at shorter wavelengths, where the wings of the Na and K optical lines are stronger, would allow better constraints on the absolute abundances of these species.

Other sources of uncertainty: Although we only quantify two sources of model uncertainty in this chapter, we stress that other sources of error can also play an important role. This is especially true if uncertainty due to prominent effects (e.g. spectral resolution) is substantially reduced (e.g. by significantly increasing the spectral resolution or potentially using correlated-k, e.g. Amundsen et al. 2017), at which point other effects may dominate as the principal sources of model uncertainty. Such effects include potential inaccuracies in molecular and atomic line lists, or indeed in the broadening of these lines as discussed above in the case of Na and K. The assumption of constant-with-depth chemical abundances may also impact model uncertainties, though in the case of T-dwarfs the abundances of H₂O and CH₄ (the dominant absorbers) are typically found to be constant with depth in equilibrium models (e.g. Line et al., 2017). The presence of clouds and any horizontal structure (including patchy clouds) could also be important, especially for objects with known variability (e.g. Apai et al., 2013; Buenzli et al., 2013). In future work, consideration of these effects could lead to an increasingly comprehensive understanding of model uncertainties and the potential to interpret brown dwarf spectra with ever increasing precision and accuracy.

2.3.2 Generating Simulated Data

As described in Section 2.2, we investigate different aspects of our model using a simulated data set based on Gl 570D. A simple way of doing this is to generate a reference model spectrum using the atmospheric model from the retrieval framework. However, such a spectrum would not factor in the model uncertainties described in Section 2.3.1 as, unlike real data, the simulated spectrum would be exactly described by the atmospheric model. In order to emulate real data as closely as possible and thereby test the retrieval framework's robustness to model uncertainties, we instead use the atmospheric model to generate the reference spectrum as accurately as possible, i.e. at the highest feasible resolution in both wavelength and pressure space. While this does not incorporate physical features that are not included in the atmospheric model (e.g. the presence of Na and K), the main numerical sources of uncertainty in the retrieval's atmospheric model are addressed and their effects on the retrieval can be tested.

We calculate the reference spectrum at the native resolution of the cross sections (0.1cm^{-1}), which is then binned in the same way as HST/WFC3 data. Since the real HST/WFC3 data that we analyse has uncertainties of 0.1-0.2%, each binned model point is then shifted by a value randomly drawn from a Gaussian distribution with standard deviation equal to 0.2% of the simulated data point's flux value. The simulated uncertainty is 0.2% of the flux in the respective spectral bin. The radiative transfer calculation is

done over 1000 layers (compared to 100 in the retrieval). Note that the simulated data is generated with the same pressure limits as the model in the retrieval framework and no Na or K is included, so uncertainties due to these factors are not present.

2.3.3 Treatment of Uncertainties

We have considered the magnitude of uncertainty in our model spectra in Section 2.3.1. We now wish to include this information in the retrieval such that the retrieved atmospheric parameters are not biased by the model uncertainties. In addition, we would also like to allow for any unknown sources of error which may affect either the data or the model. This can be achieved by adding a ‘tolerance’ parameter to the model which characterises the ‘extra’ uncertainty in addition to the known observational uncertainties. Previous studies have done this by adding a wavelength-independent parameter in quadrature to the uncertainty of each data point (e.g. Line et al., 2015; Burningham et al., 2017). The σ_i term in Equation 2.1 that Line et al. (2015) use is given by:

$$\sigma_i = \sqrt{\sigma_{i,d}^2 + 10^b}, \quad (2.2)$$

where $\sigma_{i,d}$ is the uncertainty in the i^{th} data point and b is a free parameter with a uniform prior. The prior bounds on b are such that the minimum possible value of 10^b is very small (typically less than the smallest error bar in the data), meaning that the retrieval is not obliged to account for the known model uncertainty. Otherwise put, this form of the tolerance parameter relies on the retrieval being able to ascertain the model uncertainty without it being included in the prior information. We test whether this can work by implementing this form of the tolerance parameter in our retrieval framework, with the uniform prior on b going from $\log_{10}(0.01 \sigma_{d,min}^2)$ to $\log_{10}(10000 \sigma_{d,max}^2)$, where $\sigma_{d,min}^2$ and $\sigma_{d,max}^2$ are the minimum and maximum uncertainties in the data.

Figure 2.4 shows the posterior distributions of a selection of model parameters from a retrieval that uses this tolerance parameter (in purple). The retrieved value of b is equivalent to adding an uncertainty of $10^b = 6.5 \times 10^{-23} \text{ Wm}^{-2}\text{m}^{-1}$, i.e. many orders of magnitude smaller than the estimated $\sim 8\%$ uncertainty in the model ($10^b < 2 \times 10^{-10}\%$ of the minimum flux value in the simulated data). This underestimate in uncertainty is manifested as very narrow posterior distributions which, for parameters such as the H_2O abundance, result in the median retrieved value being consistently offset from the true value by more than one standard deviation. Effectively, the ‘noise’ introduced by the known model uncertainty is easily overfitted by a slight offset in the model parameter

values. This can be remedied by explicitly accounting for known model uncertainties in the tolerance parameter, as discussed below.

Another potential issue with the tolerance parameter in Equation 2.2 is that it is wavelength-independent, whereas the model uncertainty is not. From Figures 2.2 and 2.3, the uncertainties from cross section sampling and the number of atmospheric layers used are, to within a few percent, proportional to flux (for a sufficiently large number of atmospheric layers and cross section sampling resolution). We therefore investigate a new form of the tolerance parameter:

$$\sigma_i = \sqrt{\sigma_{i,d}^2 + x_{\text{tol}}^2 f_{i,m}^2}, \quad (2.3)$$

where $f_{i,m}$ is the value of the i^{th} model binned point and changes in each iteration of the nested sampling algorithm, and x_{tol} is a free parameter with a uniform prior. In order to fully account for the model uncertainty that is known, the lower bound of this prior is chosen to be the estimated level of uncertainty of the model, i.e. $\sim 8\%$. The upper bound of the prior on x_{tol} is arbitrarily set to the large value of 100%. Using this form for the tolerance parameter in the retrieval framework results in the posteriors shown in Figure 2.4 (in blue). As expected, the posteriors are much wider and the atmospheric parameters are successfully retrieved within 1 standard deviation of the true value. We therefore choose to use the x_{tol} tolerance parameter in the work that follows. Note that when retrieving real data, unknown uncertainties (taken into account by the x_{tol} parameter) may be of the order of 8% or more. In this case, imposing a lower limit of 8% on x_{tol} does not make much difference and the retrieved posteriors are similar for both of the aforementioned uncertainty consideration methods. Nevertheless, it is worth accounting for the model uncertainty in case the unknown uncertainties are smaller.

2.4 A P-T Parameterisation for Brown Dwarfs

In this section we present a new parametric P - T parameterisation for brown dwarfs, which comprises of multiple atmospheric layers and is parameterised according to the changes in temperature across those layers, as well as a fiducial temperature. While several parametric P - T parameterisations are available for exoplanet atmospheres, we consider a new parameterisation for the following reasons: firstly, isolated brown dwarfs have much steeper temperature profiles compared to irradiated planets, and changes in the P - T gradient can have significant effects on the emergent spectrum. This, combined with the high precision of brown dwarf spectra, means that the P - T parameterisation must

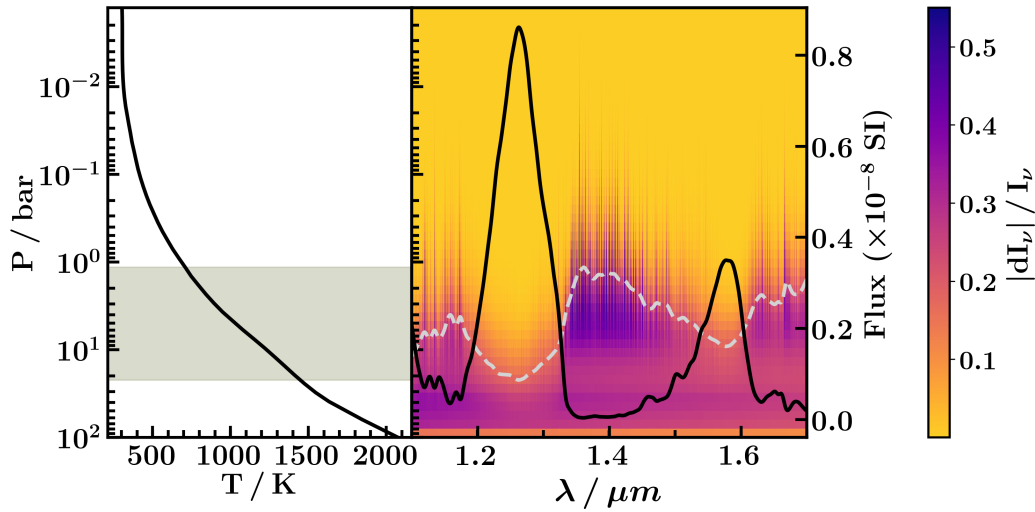


Fig. 2.5 Left panel: approximation of the P - T profile of Gl 570D, based on the equilibrium profile from (Line et al., 2015). The range of pressures probed by the $\tau = 1$ surface is shaded in gray. Right: colour map shows fractional change in spectral intensity, $|dI_v|/I_v$, where darker regions denote more absorption. The solid black line is the smoothed emergent spectrum for this atmosphere. The smoothed $\tau = 1$ surface is shown by the dashed gray line and is indicative of the pressure to which a given part of the spectrum is most sensitive to. Flux axis is shown in SI units ($\text{Wm}^{-2}\text{m}^{-1}$).

be adequately flexible such that the parameter space of P - T gradients can be properly explored in the retrieval. Secondly, since the thermal profiles of brown dwarfs are so different to those of irradiated planets, the photospheres of brown dwarfs can occur at different pressure ranges compared to planets. As such, it is important that the P - T parameterisation is able to capture this and provide flexibility in the photosphere, which is the atmospheric region best constrained by the spectrum. We begin by exploring these properties of brown dwarfs in Section 2.4.1, with the purpose of informing our P - T parameterisation. In Section 2.4.2, we present the P - T parameterisation and discuss the challenges of developing a P - T parameterisation which satisfies the above requirements given known numerical artefacts which have been encountered in existing prescriptions.

2.4.1 Thermal and Opacity Structure of Brown Dwarfs

The majority of retrieval analyses to date have been performed on hot Jupiters. However, the thermal structure of an isolated brown dwarf differs greatly from that of a hot Jupiter as it does not receive stellar irradiation. Thus, these objects are not expected to exhibit thermal inversions or to have isotherms deep in their atmospheres (~ 1 bar), as found in hot Jupiters (Hubeny et al., 2003; Fortney et al., 2008). This has implications on how deeply

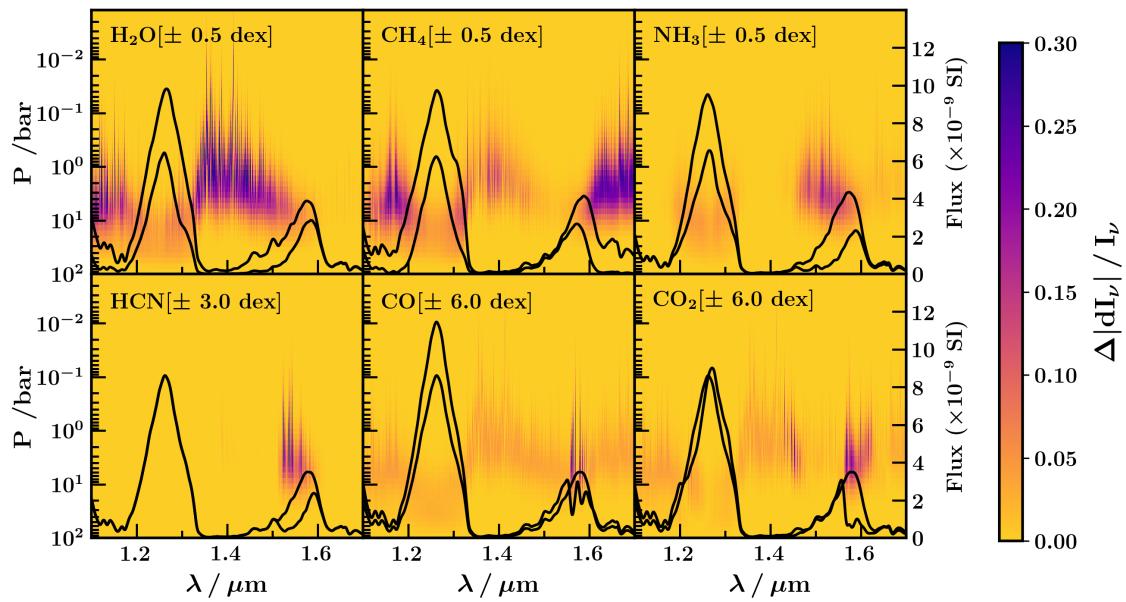


Fig. 2.6 Contributions of each species to atmospheric absorption. We take the synthetic spectrum of an atmosphere described by Table 2.2, and perturb each species' abundance by the amount stated in the top left corner of each panel. The two black lines in each panel show the smoothed spectra with the positive and negative perturbations, respectively. Each colour map is the difference in $|dI_\nu|/I_\nu$ between the positive and negative perturbations. Note that larger perturbations in the abundances of HCN, CO and CO_2 (compared to H_2O , CH_4 and NH_3) are needed to make comparable changes in the spectrum. Note that HCN has been included in the reference model with an arbitrary mixing ratio of 10^{-7} , and all other abundances are the same as in Table 2.2. Flux axes are shown in SI units ($\text{Wm}^{-2}\text{m}^{-1}$).

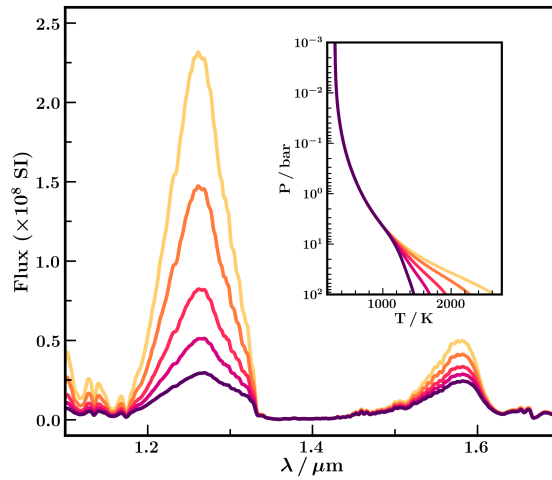


Fig. 2.7 Effect of changing the slope of the P - T profile at high pressures on the spectrum. Each P - T profile in the inset corresponds to the spectrum with the matching colour. The slope of the P - T profile at pressures greater than 10 bar has a significant effect on the flux peaks in the spectrum. Flux axis is shown in SI units ($\text{Wm}^{-2}\text{m}^{-1}$).

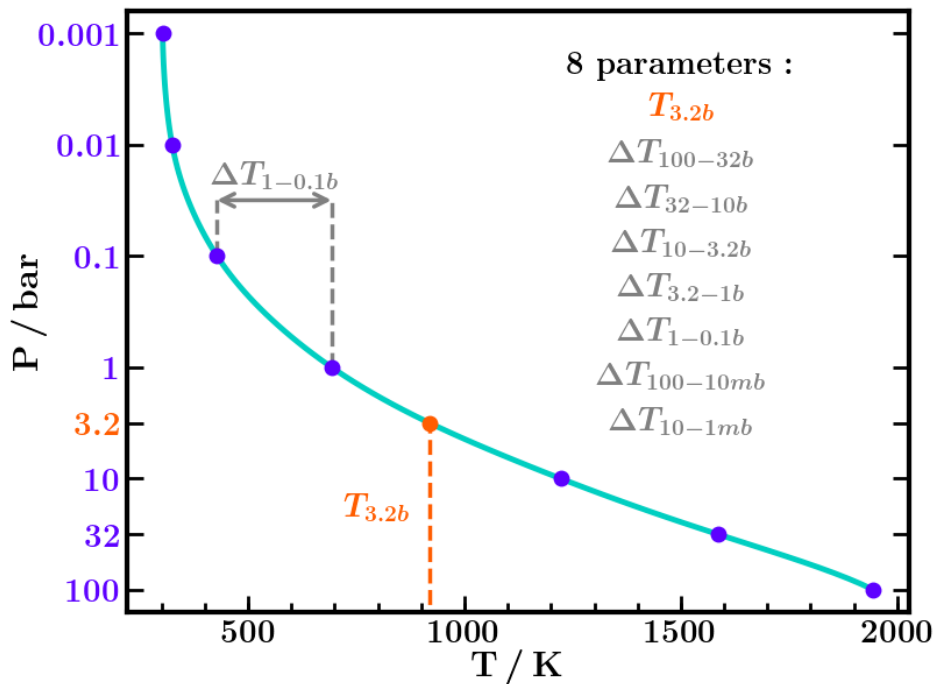


Fig. 2.8 ‘SPT’ parametric P - T model used in our retrieval framework. The P - T points are defined by the changes in temperature between them, as well as the absolute temperature at 3.2 bar. They are then interpolated using a monotonic spline fit and smoothed with a Gaussian kernel of width 0.3 dex in pressure.

we can probe the atmosphere of a brown dwarf; in known hot Jupiters, the isotherm at $\sim 0.1 - 1$ bar (Gandhi and Madhusudhan, 2017) means that the spectrum is not sensitive to the atmosphere below this point. However, this limit does not exist for isolated objects, whose temperatures increase monotonically with pressure. Instead, the maximum depth which we are sensitive to in a brown dwarf is limited by the height at which the atmosphere becomes optically thick.

To investigate how a brown dwarf atmosphere is probed by its spectrum, we consider the origins of the spectrum as a function of pressure and wavelength. To quantify this, we define the fractional change in spectral intensity, $|dI_\nu|/I_\nu$, where I_ν is the incoming spectral intensity at the bottom of an atmospheric layer, and dI_ν is the change in the spectral intensity across that layer. We plot this quantity for our simulated model of Gl 570D in Figure 2.5, showing the depths which each point in the spectrum is sensitive to. The line of unit optical depth, $\tau = 1$, represents the depth which the spectrum at a given wavelength is most sensitive to. In the case of this model atmosphere, we find that the spectrum is highly sensitive to pressures between 1 and 20 bar, and significantly affected by pressures up to several tens of bar.

The implications of such a deep photosphere are that (i) we are able to probe T-dwarf atmospheres much more deeply than hot Jupiters; (ii) the choice of parametrisation for the P - T profile should allow for a lot of flexibility between ~ 1 and ~ 100 bar, as the spectrum is able to strongly constrain this part of the profile. It is also informative to see how each species in the model contributes to the absorption map in Figure 2.5. Figure 2.6 shows these contributions, from which it is clear that H_2O , CH_4 and NH_3 have the strongest features in this spectral range and are most likely to be constrained by the retrieval. It is also clear that there are degeneracies between the contributions of each molecule, although high-quality data is able to distinguish between their individual fingerprints.

Degeneracies also exist between the abundances of certain species and aspects of the P - T profile. This can be understood by considering the effects of the slope of the P - T profile on the spectrum, as shown in Figure 2.7. The slope of the deepest part of the P - T profile has a significant effect on the high-flux regions of the spectrum, which is expected since those parts of the spectrum are formed in the high-pressure regions of the atmosphere. These flux peaks are also strongly shaped by the abundances of the most active species in the atmosphere (in this case, H_2O , CH_4 and NH_3). As a result, the slope of the deepest part of the P - T profile is degenerate with the abundances of H_2O , CH_4 and NH_3 . Flexibility in the high-pressure region of the P - T parameterisation is therefore crucial, as any deviation from the true P - T profile may be propagated to the retrieved chemical abundances.

We further note that the slope of the P - T profile can have important implications for energy transport in the atmosphere. Tremblin et al. (2015) find that atmospheric models of T-dwarfs better match the observed spectra of such objects if the temperature gradient is somewhat reduced compared to typical self-consistent models, e.g. due to the onset of fingering convection caused by the condensation of very thin dust. Similar fingering convection could also be responsible for the L-T transition, e.g. as a result of the CO/CH₄ chemical gradient (Tremblin et al., 2016, 2017). Tremblin et al. (2015, 2016, 2017) model this lower temperature gradient by using a modified adiabatic gradient, analogous to P - T parameterisations in atmospheric retrievals which allow the temperature gradient to vary freely.

2.4.2 P - T Parametrisation

In existing work on the retrieval of exoplanet atmospheres, a common approach has been to describe the P - T profile with an analytic model (e.g. Madhusudhan and Seager, 2009; Guillot, 2010). Studies using brown dwarf spectra (e.g. Burningham et al., 2017) have also considered such profiles (e.g. that of Madhusudhan and Seager, 2009). These analytic models are well suited to atmospheric retrievals as they are able to capture a broad variety of P - T profiles with only a few parameters. Indeed, they have been proven to work well with the current data quality of exoplanet spectra (e.g. Blecic et al., 2017; Gandhi and Madhusudhan, 2018). However, this simplicity can come at a cost as an analytic function may not always be capable of exactly capturing the underlying P - T profile, particularly for very high-quality data. In the case of T-dwarfs, an incorrect P - T slope could potentially introduce biases into other retrieved parameters, as discussed in Section 2.4.1.

A second approach which has been used for retrievals of isolated or poorly-irradiated sub-stellar objects is to use physically-motivated non-irradiated P - T profiles. For example, one of the models considered by Kitzmann et al. (2020) is an approximate solution to radiative transfer assuming a gray atmosphere and radiative equilibrium. They find that such a solution struggles to fit the temperature profile at lower pressures. Gravity Collaboration et al. (2020) use a parametric P - T model which applies the Eddington approximation in the photosphere and a moist adiabat below the radiative-convective boundary.

An alternative way of describing the P - T profile is to allow the temperatures at certain pressures in the atmosphere to be free parameters, which can then be interpolated to the resolution at which radiative transfer is calculated (e.g. Line et al., 2015, 2017; Zalesky et al., 2019; Kitzmann et al., 2020). This form of parametrisation has the advantage of allowing a lot of freedom in the P - T profile, but this freedom is susceptible to over-fitting.

In particular, oscillations in the P - T profile (or ‘ringing’) are a common problem. Line et al. (2015, 2017) overcome this by penalising the second derivative of the P - T profile in the likelihood function, disfavoring features in the profile which are not required by the data. Kitzmann et al. (2020) consider a different approach and fit the P - T profile with a piecewise polynomial.

We present a new approach to describing the P - T profile which allows for a high level of freedom but excludes unphysical features. In particular, we aim to avoid ringing and large oscillations which resemble thermal inversions, as these can easily overfit the data but are evidently not physical. Large oscillations in the P - T profile rely on the freedom to have temperature increasing towards lower pressures, and so one way to avoid this is to exclude P - T models with a negative gradient at any point. This can be done by assigning a very low likelihood to any models with a temperature profile which does not monotonically increase with pressure. However, this typically results in a very low acceptance rate in the nested sampling algorithm and hinders its convergence. To overcome this, we instead characterise the temperature profile by the changes in temperature, ΔT_i , across multiple atmospheric layers, plus a temperature parameter which acts as an anchor point (‘slope’ P - T parameterisation, or ‘SPT’; see Figure 2.8). The temperature parameter is placed in the photosphere as this is where the P - T profile is best constrained by the data. Based on Figure 2.7, the range of pressures covered by the photosphere is expected to include ~ 1 - 10 bar, so we place the temperature parameter at 3.2 bar ($T_{3.2b}$).

In each atmospheric layer, ΔT_i is the increase in temperature from the low-pressure side of the layer to the high-pressure side. We therefore set the lower bound of the prior distributions on the ΔT_i to 0K such that only models where temperature increases with pressure are considered. The upper bounds of the priors are shown in Table 2.1. The prior for each ΔT_i parameter is chosen to be a very generous temperature range given typical P - T profiles of T-dwarfs. We avoid placing unrealistically high limits on the ΔT_i priors as this would result in many models extending to unfeasibly high or low temperatures. Instead, we choose a suitably wide prior for each individual ΔT_i parameter.

For given ΔT_i and $T_{3.2b}$, the temperature nodes defined by these parameters are interpolated with a monotonic spline and smoothed with a Gaussian kernel of width 0.3 dex in pressure. Note that we do not use a ‘traditional’ spline fit as this is prone to introducing oscillations, even if the nodes it is fitting are monotonically decreasing. The number of ΔT_i parameters and the thicknesses of the atmospheric layers between them are free to be chosen - we use the 7 layers defined between pressures of 100, 32, 10, 3.2, 1, 0.1, 0.01 and 0.001 bar as this concentrates the ΔT_i parameters at deeper pressures, where more flexibility is needed, and has fewer parameters at lower pressures, where the

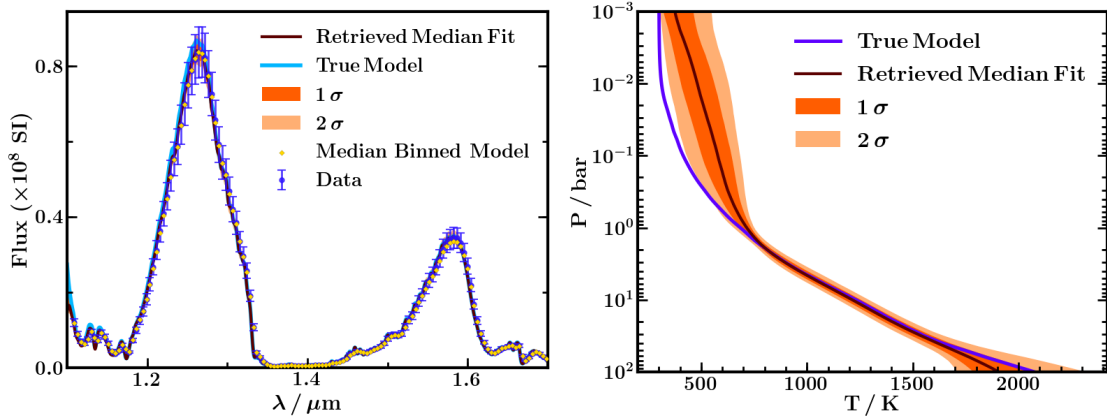


Fig. 2.9 Left: The median retrieved spectrum (maroon line) from the retrieval of our simulated data. 1σ and 2σ confidence intervals are shown by dark and light orange shading, respectively. The simulated data points are shown by blue circles, and error bars show the median retrieved tolerance. Yellow diamonds show the median binned model. Flux axis is shown in SI units ($\text{Wm}^{-2}\text{m}^{-1}$). Right: The input (blue line) and median retrieved (maroon line) P - T profiles. 1σ and 2σ confidence intervals are shown by dark and light orange shading, respectively.

spectrum does not strongly constrain the P - T profile. We note, however, that this P - T parameterisation is not strongly sensitive to the chosen atmospheric layers as long as enough flexibility is given in the photosphere.

2.5 Retrieval of Simulated Data

We now present a test retrieval on our simulated data (described in Section 2.3.2) using the chosen tolerance parameter and the SPT P - T parameterisation from Sections 2.3 and 2.4, respectively. There are a total of 19 parameters: 8 chemical abundances, 8 P - T parameters, gravity, radius-to-distance ratio and the tolerance parameter. The cross sections we use for Na and K include the wings of the strong optical lines (at $0.6\ \mu\text{m}$ and $0.8\ \mu\text{m}$, respectively) as well as the other Na and K lines present in the spectral range 1.1 - $1.7\ \mu\text{m}$ (Kramida et al., 2019). We use the broadening profiles of Allard et al. (2016) and Allard et al. (2019) for all of the lines, scaled appropriately according to line strength. We run this retrieval on the simulated data described in Section 2.3.2, for which the input parameters are known.

The retrieved parameter values match the known parameter values excellently (Figures 2.9 and 2.10, Table 2.2). All of the constrained parameters are retrieved within 1σ of the true values, and the simulated data points are successfully fitted by the median retrieved spectrum. In particular, the abundances of H_2O , CH_4 , NH_3 and K as well as gravity and

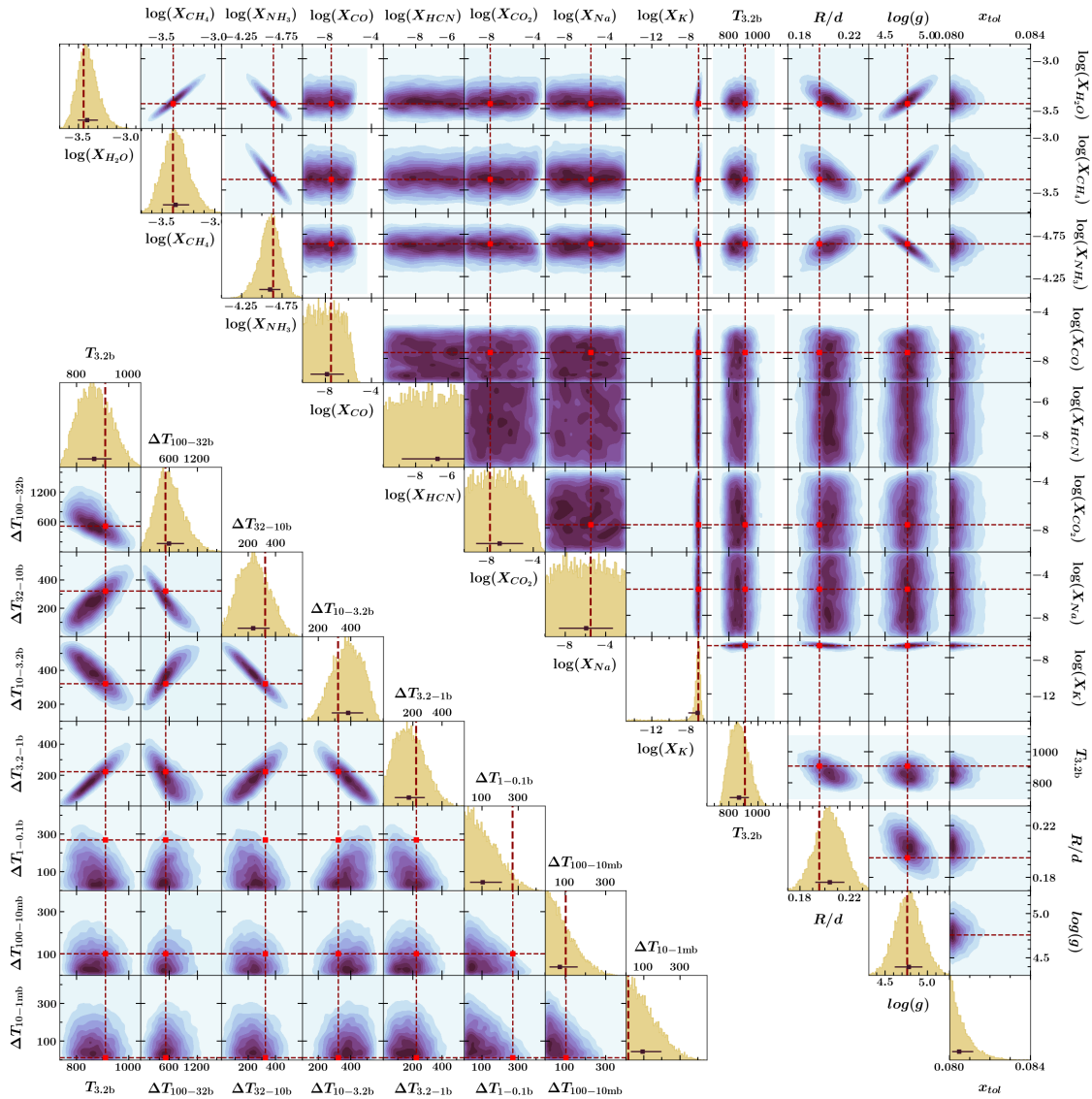


Fig. 2.10 Marginalised posterior probability distributions from the retrieval of simulated data based on Gl 570D. Off-axis plots are 2D marginalised posteriors and show the correlations between pairs of parameters. 1D marginalised posteriors are shown for each parameter along the diagonals, with median values and 68% confidence intervals shown by the dark squares and error bars, respectively. Dashed lines show the input values of each parameter, used to generate the simulated data.

the radius-to-distance ratio are strongly constrained. The abundances of CO, HCN, CO₂ and Na are not constrained but this is expected since they do not have strong features in this spectral range. The retrieved P - T profile in Figure 2.9 is an excellent fit to the input profile in the photosphere, where it is most tightly constrained by the spectrum. We note, however, that below pressures of ~ 1 bar and above ~ 30 bar the P - T profile has little influence on the spectrum and is not tightly constrained. As a result, the retrieved P - T profile outside the photosphere should not be used to infer subsequent physical properties. We therefore conclude that this retrieval framework is consistent, in the sense that it is able to accurately retrieve a high-precision brown dwarf spectrum generated using its parametric model. Furthermore, the retrieval is able to successfully use a lower-resolution atmospheric model to retrieve a model spectrum generated with higher spectral and vertical resolution.

The test retrieval also highlights degeneracies which exist between certain pairs of parameters, although they do not prevent the retrieval from finding the true parameter values. It is informative to understand the origins of these degeneracies, which we describe below. The strongest degeneracies between the parameters, visible in the marginalised posterior probability distributions in Figure 2.10, are between the chemical abundances, gravity and R/d .

1. **Gravity and Chemical Abundances:** Gravity and the chemical abundances are positively correlated because they both affect the optical depth of the atmosphere. Since pressure is an independent variable in our atmospheric model, the equation of hydrostatic equilibrium (Equation 1.4) scales the physical depth of each atmospheric layer across which radiative transfer is calculated. A larger $\log(g)$ results in a smaller scale height and a lower optical depth. Conversely, greater chemical abundances result in a greater optical depth:

$$d\tau_v = \sum_i \sigma_i n_i dz, \quad (2.4)$$

where σ_i is the absorption cross section of species i . This can be expressed by combining Equations 2.4 and 1.4:

$$\frac{dP}{d\tau} = \frac{\rho g}{\sum_i \sigma_i n_i},$$

where the sum is over all species. The optical depth can be kept constant for an increasing g if the following expression also increases:

$$\frac{\sum_i \sigma_i n_i}{\rho} = \sum_i \frac{\sigma_i X_i}{\bar{m}}$$

where \bar{m} is the average particle mass. In a hypothetical spectral range in which only one species is absorbing, this can be achieved by increasing that species' abundance. However, for a spectral band in which multiple species are absorbing, those with stronger cross sections will have increased abundances while those with weaker cross sections will have decreased abundances (since $\sum_i X_i = 1$). In this case, H_2O , CH_4 and K are the strongest absorbers in their respective bands so their abundances are positively correlated with $\log(g)$. However, NH_3 has a much weaker effect on the spectrum and is negatively correlated with $\log(g)$. Since different species dominate in different spectral bands, the effect of varying the chemical abundances has a different wavelength dependence to varying the gravity. As such, this degeneracy does not prevent the true abundances and gravity from being determined in the retrieval.

2. **R/d and Gravity:** Gravity and R/d are negatively correlated as they both scale the flux level of the spectrum. As discussed above, a larger value of $\log(g)$ results in a lower optical depth and a higher flux. Since R^2/d^2 is a direct multiplicative factor in the flux (Equation 1.14), increasing it also results in a larger flux. An increase in $\log(g)$ can therefore be somewhat offset by a decrease in R/d , resulting in a negative correlation. Nevertheless, the wavelength dependences of these effects are different, meaning that this is not a strong degeneracy and is broken in the retrieval.
3. **P – T parameters:** The ΔT parameters deeper than 1 bar are all degenerate with each other and show an interesting pattern of negative correlations between adjacent atmospheric layers and positive correlations between ΔT s separated by an odd number of layers. This pattern is indicative of oscillations in the P - T profile and is significantly accentuated by the smoothing of the profile, as profiles with small oscillations become equivalent to ones without them.
4. **Chemical Abundances:** The abundances of some of the constrained species (H_2O , CH_4 and K) are strongly positively correlated. If the spectral fingerprints of these molecules were not entirely distinguishable, one would expect a negative correlation

Table 2.3 Properties of 2MASS J23391025+1352284 from the literature.

Property	Value	References
RA (deg, J2000)	354.792715	1,2
DEC (deg, J2000)	+13.874577	1,2
IR Spectral Type	T5	3
Estimated distance (pc)	18.8±3.8	4
2MASS J mag	16.239±0.108	1,2
2MASS H mag	15.822±0.151	1,2
W1 mag	15.218±0.044	5
W2 mag	13.818±0.044	5
μ_α (mas yr ⁻¹)	396.0±41.6	6
μ_δ (mas yr ⁻¹)	-1018.7±34.6	6

References: 1. Cutri et al. (2003a), 2. Skrutskie et al. (2006), 3. Burgasser et al. (2006), 4. Buenzli et al. (2014), 5. Wright et al. (2010), 6. Schneider et al. (2016)

between their abundances. However, the data is able to distinguish each species and the degeneracy instead comes from the fact that the chemical abundances are degenerate with bulk properties of the atmosphere such as gravity and R/d . For example, an increase in the abundance of H₂O can be offset by changes in $\log(g)$ or R/d , but these quantities are also degenerate with the abundances of CH₄ and K which must then also increase.

2.6 Application to Data

We now demonstrate our retrieval framework on an emission spectrum of the brown dwarf 2MASS J23391025+1352284 (Buenzli et al., 2014). Properties of 2MASS J2339+1352 from the literature are shown in Table 2.3. This object was discovered by the Two Micron All-Sky Survey (2MASS; Cutri et al. 2003a; Skrutskie et al. 2006) and identified as a T-dwarf by Burgasser et al. (2002). Its infrared spectral sub-type is T5 (Burgasser et al., 2006) and it is therefore expected to have an effective temperature in the range ~ 1000 -1500 K (e.g. Kirkpatrick, 2005). A high proper motion has also been measured for this object (Schneider et al. 2016; see Table 2.3), consistent with its nearby estimated distance of 18.8±3.8 pc (Dupuy and Liu, 2012; Buenzli et al., 2014). Buenzli et al. (2014) observed 2MASS J2339+1352 using the HST's Wide Field Camera 3 (WFC3) in the range 1.1-1.7 μm , which is the spectrum we use for this retrieval. These data are part of a spectroscopic survey searching for brown dwarf variability, which in turn may indicate the presence of patchy photospheric clouds. Buenzli et al. (2014) find that, in contrast to many of the brown dwarfs in their survey, 2MASS J2339+1352 is only tentatively variable. This object is

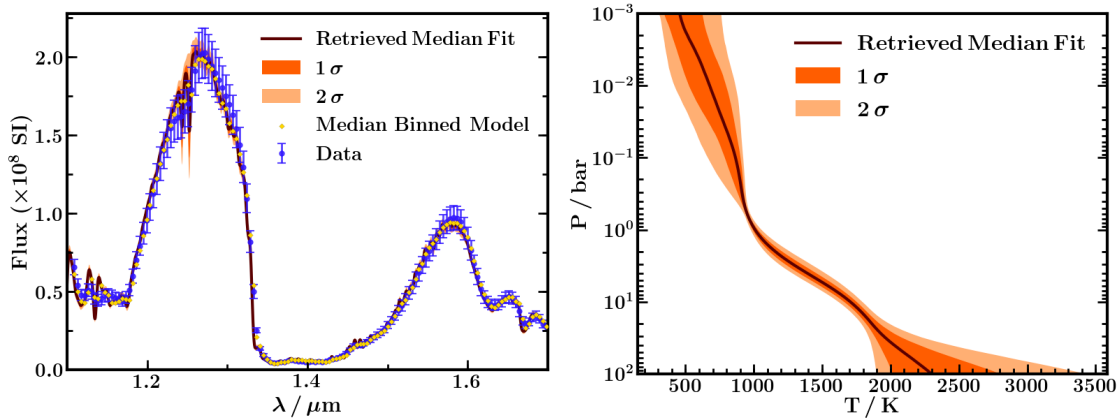


Fig. 2.11 Spectrum and P - T profile retrieved for 2MASS J2339+1352. Left: The median retrieved spectrum (maroon line) and 1σ and 2σ confidence intervals (dark and light orange shading, respectively). Data points are shown by blue circles, and error bars depict the median retrieved tolerance. Yellow diamonds show the median binned model. Flux axis is shown in SI units ($\text{Wm}^{-2}\text{m}^{-1}$). Right: Median retrieved P - T profile (maroon line) and 1σ and 2σ confidence intervals (dark and light orange shading, respectively).

therefore a suitable demonstration for our cloud-free retrieval. The uncertainties on the data are of order 0.1%, with an estimated 2% systematic flux calibration uncertainty. The model uncertainties considered in Section 2.3 are therefore significant and justify the use of the tolerance parameter. As described in Section 2.3, we also parameterise the cross sections of the strongest K lines in this spectral range.

Figures 2.11 and 2.12 show the results of the retrieval. In what follows, we describe the retrieved values of the model parameters.

2.6.1 Chemical abundances

H_2O and CH_4 : We obtain strong detections of H_2O and CH_4 with log abundances of -3.88 ± 0.09 and -4.5 ± 0.1 , respectively. The ~ 0.1 dex precisions of these abundances are smaller than the ~ 0.5 dex achievable with current exoplanet spectra (e.g. Gandhi and Madhusudhan, 2018) thanks to the precision of the data. Furthermore, these retrieved abundances are lower than expectations based on solar elemental abundances in chemical equilibrium (Burrows and Sharp, 1999; Madhusudhan, 2012). Using H_2O and CH_4 as proxies for the abundances of oxygen and carbon, respectively, their abundances suggest that oxygen is 0.13 ± 0.03 times sub-solar and that carbon is $0.07^{+0.03}_{-0.02}$ times sub-solar (Asplund et al., 2009). However, we note that other sources of oxygen and carbon (e.g. silicates or CO) which are not detectable in the near-infrared spectrum would alter these estimates.

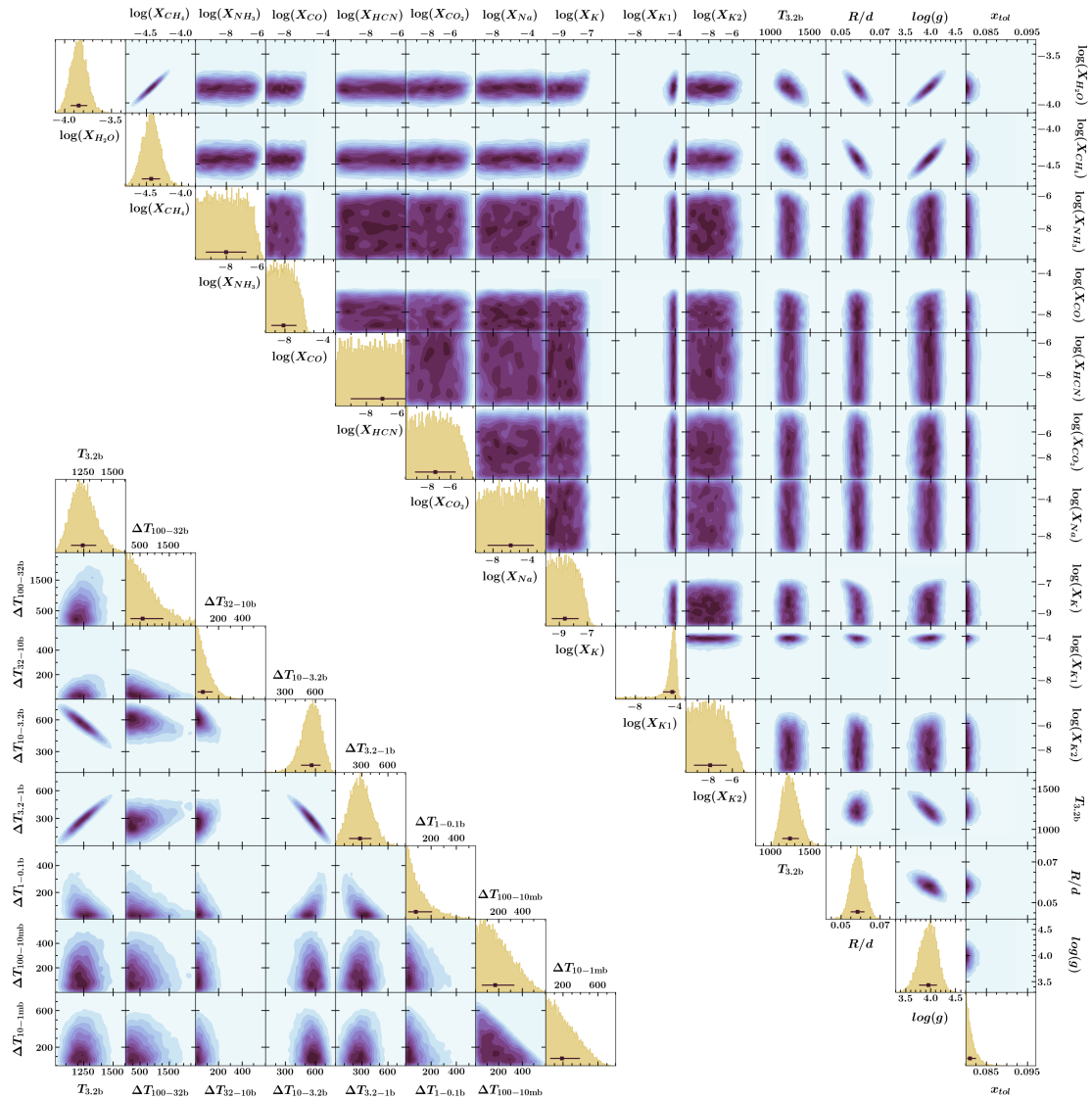


Fig. 2.12 Marginalised posterior probability distribution from the retrieval of 2MASS J2339+1352. Off-axis plots show 2D marginalised posteriors. 1D marginalised posteriors are shown for each parameter along the diagonals, with median values and 68% confidence intervals shown by the dark squares and error bars, respectively.

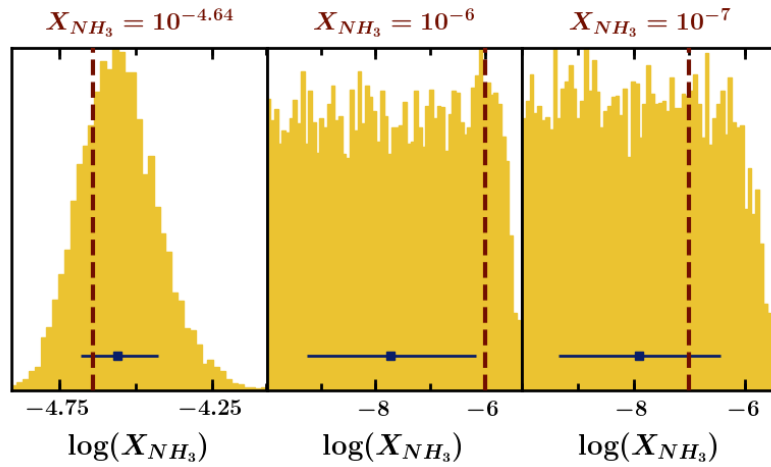


Fig. 2.13 Posterior probability distributions of the NH_3 abundance from the retrieval of simulated data with input NH_3 mixing fractions of $10^{-4.64}$, 10^{-6} and 10^{-7} , respectively. Median retrieved values and 68% confidence intervals shown by the dark blue squares and error bars, respectively. Vertical dashed lines show the true NH_3 abundance for each case. NH_3 is not detected when the mixing fraction is 10^{-6} or 10^{-7} .

NH_3 : Although we found that NH_3 could be retrieved from our simulated data, we only retrieve an upper limit from the spectrum of 2MASS J2339+1352. This could potentially be due to a low abundance of NH_3 , and to test this we create and retrieve two further sets of simulated data identical to that described in Section 2.3.2, but with reduced NH_3 mixing ratios of 10^{-6} and 10^{-7} , respectively. In both cases, we retrieve a flat posterior for the NH_3 abundance, indicating that NH_3 is not detected (Figure 2.13). It is therefore plausible that we are seeing signs of a very low abundance of NH_3 in the spectrum of 2MASS J2339+1352. This is consistent with the retrieved P - T profile since NH_3 is not expected to be abundant at higher temperatures, when it is preferentially locked up in N_2 ; for example, the equilibrium solar mixing ratio of NH_3 at 1bar drops from $\sim 10^{-3.7}$ at 500K to $\sim 10^{-5.2}$ at 1000K (Burrows and Sharp, 1999; Moses et al., 2013b).

CO, CO_2 and HCN: We retrieve an upper limit on the abundance of CO of $10^{-5.9}$ (99% confidence interval). However, the abundances of CO_2 and HCN are unconstrained by the retrieval. This is expected since these species do not have strong cross sections in the spectral range of the data (Figure 2.6).

Na and K: We place an upper limit on the K mixing ratio of $10^{-6.9}$ (at the 99% confidence level). We also find that the spectral feature visible in the data at $\sim 1.25 \mu\text{m}$ is fitted by the K lines in this region, resulting in a strong constraint on $X_{\text{K}1}$. $X_{\text{K}2}$ is not constrained by the retrieval, suggesting that these lines are in fact too weak to be recovered from the

spectrum. Na is completely unconstrained by the retrieval, as expected from the test retrieval in Section 2.5, as it has very little impact on the spectrum.

In order to test the effects of Na and K on the other retrieved parameters, we also performed a retrieval without Na and K (Figures A.1 and A.2, Table A.1). The retrieved values of all the other parameters are consistent between the two retrievals, though the feature at $\sim 1.25 \mu\text{m}$ is not fitted when K is not included. This indicates that, while including the K lines at $\sim 1.25 \mu\text{m}$ improves the fit to the data, it does not impact the other retrieved parameters.

2.6.2 P-T profile

The retrieved P - T profile is well constrained, especially in the photosphere. Between ~ 0.6 and ~ 20 bar, the temperature is constrained to within ~ 100 K. We retrieve the temperature at 3.2 bar (i.e. the fiducial temperature in the photosphere, see Section 2.4.2) to be 1240^{+110}_{-100} K. As expected, the temperature in the deepest and shallowest regions of the atmosphere are not well constrained by the retrieval, as can be seen by the larger 1σ and 2σ margins in the right panel of Figure 2.11. This shows that the retrieval is able to fit parts of the P - T profile which inform the spectrum while remaining agnostic about parts which are not constrained by the data. Note that the retrieved P - T profile outside the photosphere should therefore not be used to infer subsequent physical properties.

2.6.3 R/d, gravity and tolerance

We retrieve a radius-distance ratio of $0.058 \pm 0.004 R_J/\text{pc}$ and a log gravity (in cms^{-2}) of 4.0 ± 0.2 . Using a distance estimate, these quantities can be used to infer a mass and radius for 2MASS J2339+1352. Although a parallax measurement is not available for this object, Buenzli et al. (2014) calculate a distance estimate based on the relation between spectral type and absolute H-band magnitude given by Dupuy and Liu (2012). Using this estimate of 18.8 ± 3.8 pc, we derive a radius of $1.1 \pm 0.2 R_J$ and a mass of $5^{+3}_{-2} M_J$. We note, however, that a direct parallax measurement could provide more accurate mass and radius estimates. These mass and radius values are discussed further in Section 2.7.

The posterior probability distribution retrieved for the tolerance parameter is stacked against the lower prior of 8%, suggesting that no significant uncertainties above this level were found by the retrieval. However, forcing the lower prior of this parameter to be the minimum known uncertainty in the model (i.e. $\sim 8\%$) means that this uncertainty has been propagated to the posterior distributions of the other retrieved parameters, preventing underestimates in their uncertainties.

Table 2.4 A summary of the retrieved atmospheric properties of 2MASS J2339+1352. Upper limits show 99% confidence intervals. The abundances of CO, HCN, CO₂, and Na are not constrained. The abundances of H₂O and CH₄ are both found to be significantly sub-solar, at $\sim 0.2\times$ and $\sim 0.1\times$ solar, respectively (Gandhi and Madhusudhan, 2017).

Parameter	Retrieved value
$\log(X_{\text{H}_2\text{O}})$	-3.85 ± 0.09
$\log(X_{\text{CH}_4})$	-4.44 ± 0.1
$\log(X_{\text{NH}_3})$	< -5.9
$\log(X_{\text{CO}})$	< -5.9
$\log(X_{\text{K}})$	< -6.9
$T_{3.2\text{b}}$ (K)	1240^{+110}_{-100}
R/d (R_{J}/pc)	0.058 ± 0.004
$\log(g/\text{cms}^{-2})$	4.0 ± 0.2
x_{tol}	$8.1^{+0.2}_{-0.07} \%$

2.7 Summary and Discussion

In this chapter we investigate important considerations for accurate atmospheric retrievals of high-precision spectra of brown dwarfs. This is motivated by the availability of very high-SNR HST infrared thermal emission spectra of brown dwarfs. These data present the potential to determine the atmospheric and chemical properties of brown dwarfs with unprecedented precision. To utilise this potential we find that certain approaches in modelling technique contribute significantly to the accuracy of the results obtained. We introduce several key developments as follows.

Firstly, we consider the uncertainty in our atmospheric model and explicitly include it in the retrieval framework as prior information on a variable ‘tolerance’ parameter. This allows the retrieval to constrain unknown sources of uncertainty (e.g. Line et al., 2017; Burningham et al., 2017), while also accounting for known sources of uncertainty in the model. Two main sources of model uncertainty are the sampling of chemical cross sections and the resolution of the pressure grid in the model atmosphere, i.e. the spectral and spatial resolution, respectively. We approximate these effects as being proportional to model flux, and as such choose a tolerance parameter (x_{tol}) proportional to flux, which is then added in quadrature to the data uncertainties. The lower bound of the prior on x_{tol} is then set to the level of known model uncertainties ($\sim 8\%$ in the present case). This

error, which comes largely from our chosen spectral resolution, can be reduced by using a higher spectral resolution at a higher computational cost. Although we find that using a tolerance parameter proportional to flux works well in estimating model uncertainties, other wavelength dependences are not accounted for and could be considered in future work. There are also potential sources of uncertainty in the model, such as depth-varying chemical abundances and atmospheric dynamics, which we do not include here but which could be considered in future work.

The second development we make is a new parametrisation of the P - T profile. We begin by investigating the thermal and opacity structure of brown dwarfs in order to inform our choice of P - T parameterisation and find that pressures of up to several tens of bar can be probed by the spectrum; almost two orders of magnitude deeper than for typical hot Jupiters. This means that the P - T parameterisation should be sufficiently flexible at high pressures as the spectrum will be able to constrain it there. Indeed, we find that the slope of the P - T profile at high pressures has a very strong effect on the high-flux regions of the spectrum.

A potential P - T parametrisation is one with a series of free temperature parameters, which allows for considerable freedom in the retrieval. However, this can result in over-fitting due to unphysical oscillations in temperature, which must be corrected for (e.g. Line et al., 2015; Kitzmann et al., 2020). Our new P - T parameterisation overcomes this issue by excluding certain unphysical, over-fitted P - T profiles. The profile is characterised by the slopes of the P - T profile across given atmospheric layers, and the priors on these slopes are chosen such that atmospheric temperature always increases with pressure. This eliminates large oscillations and makes the model more robust to changes in the number of P - T parameters compared to a model with free temperature parameters. Although it would be preferable to allow for the possibility of finding a thermal inversion even though brown dwarfs are not expected to exhibit these, it would be difficult to distinguish the discovery of an inversion from over-fitting.

We then apply the adapted retrieval framework to the HST/WFC3 spectrum of the T5 brown dwarf 2MASS 2339+1352 (Buenzli et al., 2014). To test the accuracy of the method, we first apply it to a simulated spectrum with known input parameters. The retrieval is able to accurately retrieve these inputs, confirming that the method is self-consistent. When applied to 2MASS 2339+1352, the retrieval strongly constrains the mixing fractions of H_2O and CH_4 at $10^{-3.7}$ and $10^{-4.3}$, respectively, with 1σ uncertainties of ~ 0.1 dex (Table 2.4). These abundances suggest sub-solar elemental abundances for oxygen and carbon: 0.13 ± 0.03 and $0.07^{+0.03}_{-0.02}$ times solar values, respectively (Asplund et al., 2009). We place an upper limit of $10^{-5.9}$ on the mixing ratio of NH_3 (at the 99% confidence level), which

is expected from the retrieved P - T profile as nitrogen is expected to be mostly locked in N_2 at these temperatures (e.g. above 500K at 1bar (Burrows and Sharp, 1999; Moses et al., 2013b)). We also place an upper limit of $10^{-6.9}$ on the mixing ratio of K and confirm that, in this spectral range, uncertainties in the Na and K cross sections do not have a significant effect since a retrieval which does not include these species produces the same results for all other model parameters. The retrieval also strongly constrains the P - T profile in the photosphere between ~ 0.6 -20 bar. We estimate the effective temperature of 2MASS J2339+1352 by extending the median retrieved model to longer wavelengths, obtaining a value of ~ 1100 K. This is consistent with the expected range of effective temperatures for T5 dwarfs, i.e. ~ 1000 -1500 K (e.g. Kirkpatrick, 2005).

Using a distance estimate for 2MASS J2339+1352 (Dupuy and Liu, 2012; Buenzli et al., 2014), we further estimate its mass and radius based on our retrieval results. The values we obtain are $5_{-2}^{+3} M_J$ and $1.1 \pm 0.2 R_J$ for the mass and radius, respectively. This radius estimate is in good agreement with the expected radius for a fairly young brown dwarf or giant planet (e.g. Baraffe et al., 2003). The mass estimate, however, suggests that 2MASS J2339+1352 could be a planetary object rather than a brown dwarf. We discuss two possible scenarios which can explain this. First, that 2MASS J2339+1352 may potentially be a planetary mass object. Second, that the low mass and metallicity that we retrieve for 2MASS J2339+1352 may be a result of the $\log(g)$ -abundance degeneracy discussed in Section 2.5, and could potentially be rectified with a wider spectral coverage.

Microlensing observations have shown that unbound planets are very common (e.g. Sumi et al., 2011). While the low metallicity we derive for this object could be consistent with an old age (and therefore inconsistent with a planetary mass, given the spectral type), this could also be a result of planetary formation processes. For example, Madhusudhan et al. (2014a) find that formation through gravitational instability at large orbital separations can result in both sub-solar O and C abundances in giant exoplanets (also see e.g., Helled and Bodenheimer, 2010; Öberg et al., 2011). We also compare our derived mass and gravity estimates to evolutionary models in the literature. Assuming an effective temperature in the range 1000-1500 K, figure 9 of Burrows et al. (1997) suggests an age of $\sim 10^{6.5} - 10^{7.5}$ yr, assuming a solar composition. Baraffe et al. (2003) predict a similar age ($\sim 10^7$ yr) for a $5M_J$ planet with an effective temperature in the range ~ 1000 -1500 K. For a sub-solar composition, this age estimate would be even lower (e.g. Burrows et al., 2001). Sumi et al. (2011) find that unbound planetary-mass objects have a different mass function to field brown dwarfs, suggesting different formation pathways. In particular, they suggest that the planetary-mass objects may form in protoplanetary discs and subsequently be ejected (e.g. Veras et al., 2009). If 2MASS J2339+1352 is indeed a planetary-mass

object, this would mean that it formed and was ejected from its stellar system very quickly. Since giant planet formation due to disk instability can occur on relatively fast timescales compared to core accretion (e.g. $\lesssim 10^4$ yr; Durisen et al. 2007 and references therein), this may be possible in some scenarios (Veras et al., 2009).

An alternative explanation for the low mass and metallicity derived from the retrieval is that these quantities may be affected by the strong $\log(g)$ -abundance degeneracy. As discussed in Section 2.5, both gravity and the abundances of the dominant species shaping the spectrum have similar effects on the emergent spectrum, such that a low gravity (i.e. low mass), low metallicity solution is similar to a higher gravity, higher metallicity solution. One way to break this degeneracy would be to use a wider spectral coverage, probing a larger number of molecular and/or atomic features. Other studies of brown dwarf and poorly-irradiated planet retrievals have also found unexpected and/or unphysical results for some parameters, in some cases possibly due to degeneracies between various model parameters. For example, Lavie et al. (2017) and Kitzmann et al. (2020) both find smaller radii than expected when an uninformative prior is assumed. Conversely, Todorov et al. (2016) find that gravity is not constrained in their retrieval of κ Andromedae b. This highlights the challenging nature of retrievals for isolated objects, for which the mass and radius are unknown and add further degeneracies compared to atmospheric retrievals of transiting exoplanets for which masses and radii are known a priori. However, future facilities such as JWST will have the capability of providing high-precision spectra over a wide spectral range, mitigating such biases and allowing for high-precision abundance estimates.

Our technique shows great potential for high-precision abundance determinations; the 0.1 dex precision we obtain here for the H_2O and CH_4 mixing ratios is comparable to the precision achieved with brown dwarf retrievals in the literature (e.g. Line et al., 2017; Zalesky et al., 2019), and is significantly more stringent than the ~ 0.5 dex achievable with current exoplanet emission spectra (e.g. Gandhi and Madhusudhan, 2018). Given the availability of numerous high-quality brown dwarf spectra, this method can therefore enable accurate metallicity and compositional estimates for a large number of objects, allowing for detailed population studies and the testing of formation scenarios. Furthermore, given distance estimates, the retrieved radius-distance ratio and gravity can be used to place independent constraints on the masses and radii of brown dwarfs. Combined with self-consistent forward models, these estimates can contribute to the understanding of the physical processes and evolution of brown dwarfs. In the future, exoplanet spectra will also reach this level of quality, with large facilities such as the James Webb Space Tele-

scope and the Extremely Large Telescope. The considerations investigated here therefore provide a step towards the accurate interpretation of these much-awaited observations.

This new retrieval framework for brown dwarfs provides insight for two areas of atmospheric characterisation: precise atmospheric characterisation of brown dwarfs and considerations for the analysis of high-quality exoplanet spectra in the future. As we have shown in this chapter, it is essential to understand the uncertainties of our models and their effects on data interpretation as we approach a new era of high-SNR exoplanet and brown dwarf spectroscopy.

3

Assessing Spectra and Thermal Inversions due to TiO in Hot Jupiter Atmospheres

Following Chapter 2, we continue to explore the high-mass regime, but consider the opposite extreme in irradiation conditions, i.e. focusing on hot Jupiters.¹ Recent detections of thermal inversions in the dayside atmospheres of some hot Jupiters are motivating new avenues to understand the interplay between their temperature structures and other atmospheric conditions. In particular, TiO has long been proposed to cause thermal inversions in hot Jupiters, depending on other factors such as stellar irradiation, C/O , and vertical mixing. TiO also has spectral features in the optical and near-infrared that have been detected. However, interpretations of TiO signatures rely on the accuracy of TiO opacity used in the models. The recently reported TOTO TiO line list provides a new opportunity to investigate these dependencies, which is the goal of the present work. First, we investigate how the TOTO line list affects observable transmission and emission spectra of hot Jupiters at low and high resolution. The improvement in the TOTO line list compared to a previous line list results in observable differences in the model spectra, particularly in the optical at high resolution. Secondly, we explore the interplay between temperature structure, irradiation and composition with TiO as the primary source of optical opacity, using 1D self-consistent atmospheric models. Among other trends, we find that the propensity for thermal inversions due to TiO peaks at $C/O \sim 0.9$, consistent with recent studies. Using these models, we further assess metrics to quantify thermal

¹This work has been published in Piette et al. (2020).

inversions due to TiO, compared to frequently-used Spitzer photometry, over a range in C/O, irradiation, metallicity, gravity and stellar type.

3.1 Introduction

The phenomenon of thermal inversions in exoplanet atmospheres has been the focus of much work for over a decade, with approaches from both theory and observation (e.g. Hubeny et al., 2003; Burrows et al., 2008b; Fortney et al., 2008; Spiegel et al., 2009; Knutson et al., 2010; Madhusudhan, 2012; Menou, 2012; Mollière et al., 2015; Beatty et al., 2017a; Parmentier et al., 2018; Lothringer and Barman, 2019; Gandhi and Madhusudhan, 2019). As described in Chapter 1, species such as TiO and VO have long been proposed to cause thermal inversions in hot Jupiter atmospheres. Further developments in the theory of thermal inversions have been driven by both trends observed in exoplanet emission spectra and theoretical considerations. For example, Fortney et al. (2008) suggested a two-way classification of hot Jupiters based on stellar irradiation, arguing that inversion-causing species such as TiO and VO would only be present in the gas phase for the hotter, more strongly-irradiated class. This was in agreement with inferences of thermal inversions at the time, with HD 209458 b at the boundary between the two classes (Burrows et al., 2008b; Knutson et al., 2008 but cf. Diamond-Lowe et al., 2014).

Not all stellar irradiation aids the formation of thermal inversions, however. Knutson et al. (2010) found a negative correlation between host star activity and the presence of thermal inversions, leading them to suggest that the increased UV flux from active stars could result in the photodissociation of inversion-causing compounds and hinder the presence of thermal inversions. However, inferences of thermal inversions in some planets have since been updated, e.g. HD 209458b, see Diamond-Lowe et al. (2014).

Beyond photodissociation, there are further challenges in creating thermal inversions with TiO/VO. One is the cold trap effect, whereby these compounds condense out either on the nightside or in certain (cooler) regions in the atmosphere, which can deplete the abundance of gaseous TiO/VO (Spiegel et al., 2009; Beatty et al., 2017a). Another is the fact that TiO and VO are heavy compounds relative to a H₂-dominated atmosphere and will gravitationally settle if they are not kept aloft by other means (Spiegel et al., 2009). However, both of these effects could be mitigated by vertical mixing in the most irradiated atmospheres (e.g. Spiegel et al., 2009). Indeed, Parmentier et al. (2013) find that TiO can be kept aloft in the atmosphere by vertical mixing as long as it forms sufficiently small particles when condensed on the night side.

Inferences of thermal inversions are typically made using a combination of thermal emission spectra obtained with the HST WFC3 spectrograph (1.1-1.7 μm) and broadband photometry in the Spitzer IRAC bands at 3.6 and 4.5 μm . Whereas the HST WFC3 band is a good probe of H_2O opacity and the spectral continuum, the IRAC 4.5 μm band has strong opacity due to CO, which is expected to be abundant in hot Jupiter atmospheres. For solar compositions and sufficiently high temperatures, the IRAC 3.6 μm band has relatively low opacity and is therefore used as a measure of the spectral continuum against which the IRAC 4.5 μm band can be compared. Under these conditions, a higher brightness temperature in the IRAC 4.5 μm band relative to the 3.6 μm band indicates the presence of a CO emission feature and an inverted temperature profile. This metric has commonly been used to assess the presence of thermal inversions in hot Jupiter atmospheres (Burrows et al., 2007; Knutson et al., 2010; Madhusudhan and Seager, 2010).

On the other hand, many highly-irradiated ultra-hot Jupiters (with effective temperature $\gtrsim 2000$ K) have emission spectra consistent with blackbody curves in the near-infrared (e.g. Crossfield et al., 2012; Delrez et al., 2018). One explanation for this observation is an isothermal temperature profile (e.g. Crossfield et al., 2012), though an absence of strong near-infrared absorbers such as H_2O would also result in a featureless spectrum in the NIR (e.g. Madhusudhan et al., 2011a). Such a depletion in H_2O could be caused by either a super-solar C/O ratio (Madhusudhan, 2012; Moses et al., 2013b) or due to its thermal dissociation in ultra-hot Jupiters (Parmentier et al., 2018). Several recent studies also suggest that the continuum opacity in the near-infrared due to H^- ions, which can exist in ultra-hot Jupiters, could reduce the amplitude of the H_2O features in the WFC3 band (e.g. Arcangeli et al., 2018; Lothringer et al., 2018; Parmentier et al., 2018).

Among the factors which shape the thermal profile of an atmosphere, chemistry is a critical component. In particular, the C/O ratio has an important role in determining atmospheric chemistry, with high C/O ratios limiting the abundance of O-bearing species including H_2O , TiO and VO in hot Jupiter atmospheres (Madhusudhan et al., 2011b; Madhusudhan, 2012). Here we are focusing on typical hot Jupiters orbiting Sun-like stars. Since a thermal inversion requires a high optical opacity relative to the infrared opacity (e.g. Hubeny et al., 2003; Hansen, 2008; Guillot, 2010), a decrease in H_2O abundance due to a high C/O ratio can to some extent make it easier for a thermal inversion to occur (Mollière et al., 2015; Gandhi and Madhusudhan, 2019). Furthermore, it has been found that the optical opacity causing thermal inversions may come from a variety of compounds besides TiO/VO, including sulfur compounds (Zahnle et al., 2009), Na/K (Mollière et al., 2015), H^- ions (Arcangeli et al., 2018; Parmentier et al., 2018; Lothringer et al., 2018), and various oxides, hydrides and atomic metals (Lothringer et al., 2018; Gandhi and Madhusudhan,

2019). State-of-the-art observations and chemical characterisation are allowing the first detections of such compounds in exoplanet atmospheres. Recent examples include detections of TiO in high resolution (Nugroho et al., 2017) and low resolution (Sedaghati et al. 2017, but cf. Espinoza et al. 2019) as well as an indication of AlO (von Essen et al., 2019), both species thought to be capable of creating thermal inversions (e.g. Hubeny et al., 2003; Fortney et al., 2008; Gandhi and Madhusudhan, 2019).

These detailed chemical detections rely on the accuracy and completeness of the molecular cross sections used to interpret spectroscopic observations (e.g. Schwenke, 1998; Patrascu et al., 2015). While in the past, cross sections were not designed specifically for use with exoplanet spectra, the recent need for such cross sections has led to the development of several state-of-the-art line lists for various molecules at temperatures relevant to exoplanetary atmospheres. (e.g. Rothman et al., 2010, 2013; Tennyson et al., 2016). Accurate and complete molecular cross sections also play a key role in determining the spectral appearance and thermal profile of an atmosphere. In particular, for high-resolution spectra, line position accuracy is important as chemical detections are typically made using cross-correlation methods, which are very sensitive to line position (Brogi et al., 2012; Birkby, 2018; Nugroho et al., 2017). Conversely, completeness of a line list affects the strength of spectral features in low-resolution spectra.

In this chapter, our goal is to explore important factors for assessing thermal inversions in the spectra of hot Jupiters. We begin by investigating the importance of up-to-date molecular cross sections of TiO for inferring the effects of this molecule on the thermal structures and spectra of hot Jupiters. To this end, we compare the latest TiO line list, TOTO (McKemmish et al., 2019), against a previous line list (Schwenke, 1998), assessing the differences they make to both transmission and emission spectra for low-resolution as well as high-resolution spectroscopic observations.

We also embark on a reassessment of the criteria used for quantifying thermal inversions in hot Jupiters. Traditionally, thermal inversions have been assessed based on the relative flux differential between the Spitzer IRAC 1 and IRAC 2 bands at $3.6\ \mu\text{m}$ and $4.5\ \mu\text{m}$, respectively (e.g. Knutson et al., 2008; Sheppard et al., 2017; Haynes et al., 2015; Kreidberg et al., 2018), which relies on the assumption that there is strong CO opacity in the $4.5\ \mu\text{m}$ band relative to the $3.6\ \mu\text{m}$ band (i.e. the $3.6\ \mu\text{m}$ band is a continuum) for hot Jupiters. However, factors such as C/O ratio could affect this assumption. As a result, the IRAC 1/IRAC 2 flux differential may not necessarily be a robust or optimal metric across all atmospheric chemistries. Furthermore, chemical properties such as the C/O ratio have also been shown to influence thermal inversions (e.g. Madhusudhan et al., 2011b; Mollière et al., 2015; Gandhi and Madhusudhan, 2019), so the way in which they affect the

performance of the IRAC 1/IRAC 2 metric may be non-trivial. In this study, we explore the performance of the IRAC 1/IRAC 2 metric as well as an alternative metric as a function of C/O ratio, irradiation, metallicity and gravity.

In what follows, we begin with comparisons of different TiO line lists and their effects on model spectra under different conditions in Section 3.2. Here we show how the choice of line list could impact the interpretation of emission and transmission spectra at low and high resolution. Using semi-analytic considerations of radiative equilibrium, we then explore in Section 3.3 how the optical versus infrared opacity varies as a function of C/O ratio and temperature, thereby assessing the dayside equilibrium temperatures at which thermal inversions could occur when TiO is a primary optical absorber. In Section 3.4, we assess metrics for quantifying the presence and strength of thermal inversions in the context of solar-composition atmospheres. In Section 3.5, we then use self-consistent atmospheric models to explore the dependence of thermal inversion strength on irradiation, C/O ratio, metallicity and gravity. We also use these models to investigate the performance of the metrics discussed in Section 3.4 as a function of these atmospheric parameters. We summarize our findings and discuss our conclusions in Section 3.6.

3.2 Impact of TiO line lists on exoplanet opacity

Accurate chemical cross sections are essential when inferring the presence and abundances of chemical species from atmospheric observations. Prior to 2019, the two main line lists available for TiO were intended for modelling M dwarfs: the Schwenke (1998) line list developed in 1998, and the Plez line list originally constructed in 1998 (Plez, 1998), with the latest update in 2012 (Ryabchikova et al., 2015). However, high-resolution Doppler spectroscopy of exoplanet atmospheres (e.g. Hoeijmakers et al., 2015) has motivated the need for high-accuracy line lists with line position accuracies better than $\sim 0.1 \text{ cm}^{-1}$ ($R \gtrsim 10^5$) for strong lines.

The recent TOTO line list for TiO (McKemmish et al., 2019) makes use of new experimental data in order to improve the accuracy of the predicted line positions. The MARVEL algorithm (Furtenbacher et al., 2007; Császár et al., 2007; Furtenbacher and Császár, 2012) is used to produce accurate, empirically-derived energies for more than 8000 rovibronic states based on both old and new data. Model energy levels calculated by the DUO software package (Yurchenko et al., 2016) are then replaced with empirical values from MARVEL, where appropriate, which significantly improves the accuracy of the line positions. This process is referred to as ‘MARVELisation’, and the resulting TOTO line list spans the spectral range up to $30,000 \text{ cm}^{-1}$ (i.e. $0.33 \mu\text{m}$).

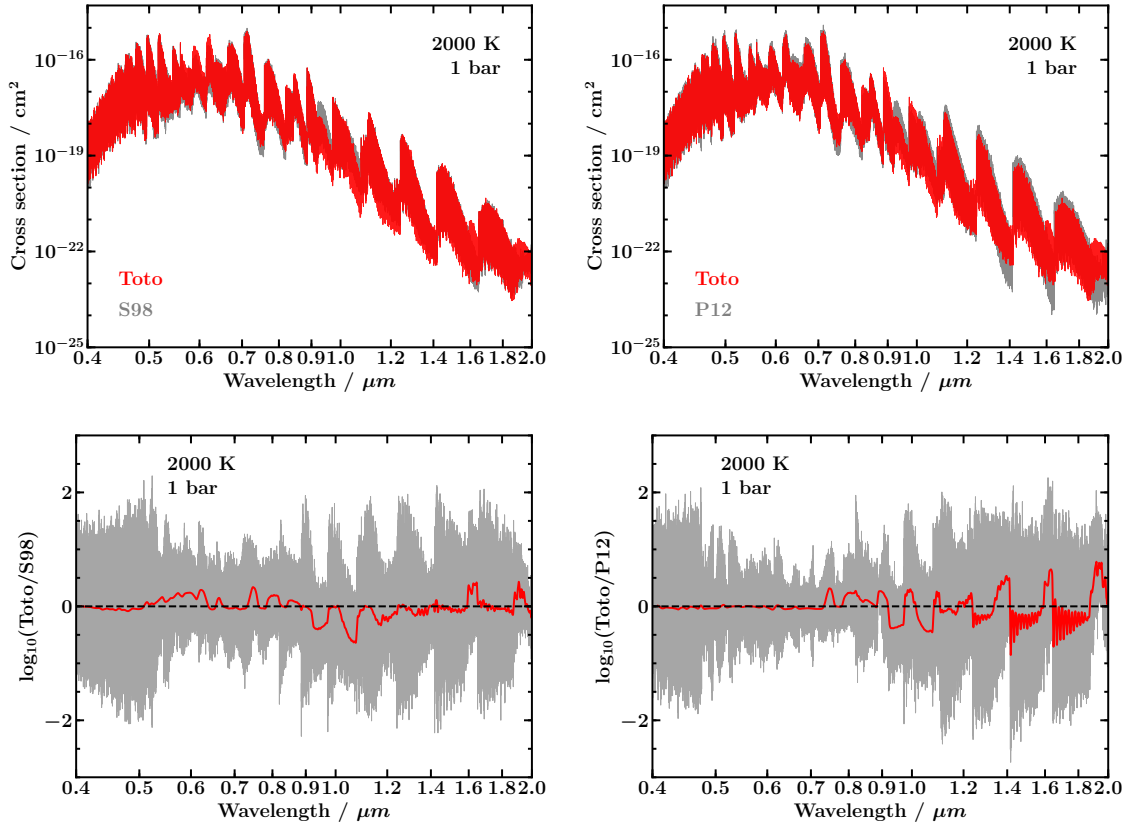


Fig. 3.1 Top panels: the S98 (grey, left panel)/ P12 (grey, right panel) and TOTO (red) cross sections over-plotted in the range $0.4\text{-}2.0\mu\text{m}$. Bottom panels: the log difference between the S98 (left)/ P12 (right) and TOTO cross sections in the same wavelength range, at native resolution (grey) and smoothed with a Gaussian of width 2.3 nm (red, similar to the PSF of HST/WFC3). At certain wavelengths, the cross sections differ by almost a factor of ~ 10 when smoothed. The amplitudes of the residuals decrease for lower resolutions, indicating that differences in line position contribute significantly to the differences between the line lists. In all panels, the cross sections are taken at 2000 K and 1 bar.

In what follows, we first quantify the extent of ‘MARVELisation’ in the TOTO line list. We then assess the impact of different TiO cross sections on the transmission and emission spectra of hot Jupiter spectra (Sections 3.2.2 and 3.2.3, respectively).

3.2.1 Quantifying line list suitability for high-resolution spectroscopy

The importance of line list choice depends on the resolution of the observations. Figure 3.1 shows the Schwenke (1998) and Plez (2012) (sourced from Ryabchikova et al., 2015) cross sections (hereafter S98 and P12) alongside the TOTO cross sections in the optical and near-infrared at 2000 K, as well as the differences between them. In this spectral range, the two cross sections differ by up to almost 3 orders of magnitude at native resolution and one order of magnitude when smoothed by a Gaussian PSF similar to that of HST/WFC3 (see grey and red lines in lower panel of Figure 3.1, respectively). This can have a significant impact on the interpretation of both optical and near-infrared spectra at low and high resolutions, but is clearly much more important for high-resolution observations. In Sections 3.2.2 and 3.2.3, we focus on the differences between the TOTO and S98 cross sections as these differ more in the optical (where TiO is most spectrally active) than the TOTO-P12 comparison, therefore providing an upper limit on the effects of these differences on hot Jupiter spectra.

Use of high-resolution Doppler spectroscopy to identify molecules in exoplanets relies on the availability of very accurate line positions. For complex molecules like TiO, the necessary accuracy can only usually be obtained if model energy levels are explicitly replaced by experimentally-derived energy levels and/or transition frequencies. This replacement has not been done for the early 1998 Plez and Schwenke line lists, but is done for the Plez (2012) line list (sourced from Ryabchikova et al., 2015) and the new TOTO line list; the former two line lists are thus not preferable for use in high-resolution cross-correlation techniques. Clear identification of the line list used in exoplanet high-resolution cross-correlation studies is thus essential for accurate chemical detections (Brogi et al., 2012; Hoeijmakers et al., 2015; Birkby, 2018; Nugroho et al., 2017).

Previous studies (McKemmish et al., 2019) have compared the results of the TOTO line list to the Plez (2012) line list (sourced from Ryabchikova et al., 2015) in the context of high-resolution Doppler spectroscopy, including cross-correlation of both line lists against high-resolution M star spectra in different spectral regions. TOTO had superior performance, which can be attributed to the fact that the line list is "MARVELised".

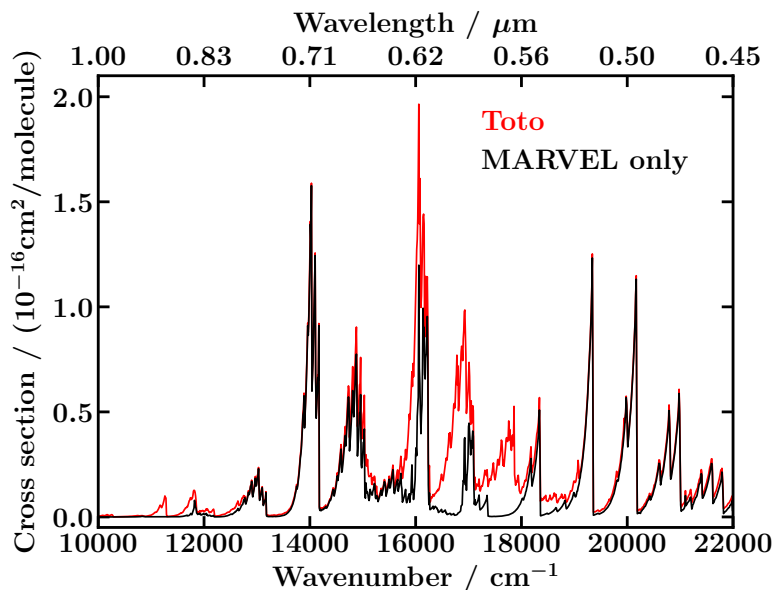


Fig. 3.2 The full TOTO (red) and MARVEL-only (black) cross sections, calculated at 2000 K using Gaussian broadening with a half-width half-maximum (hwhm) of 2 cm^{-1} calculated using EXOCROSS (Yurchenko et al., 2018). Here, we focus on comparisons between the strongest lines as these are the regions where experimentally derived transitions are most accessible. Furthermore, it is the strongest lines which have the greatest impact on the interpretation of high-resolution Doppler spectroscopy with cross-correlation.

The extent to which a given line list explicitly includes experimental or experimentally-derived (e.g. MARVEL) energy levels and/or transitions has not previously been quantified, yet this is an essential factor in determining the suitability of a given line list for use in high-resolution cross-correlation studies. Note that strong lines have the greatest contribution in the cross-correlation so their accuracy is especially important.

The most straightforward metric is that, in TOTO, 17,365 model energy levels out of 301,245 (or 5.76%) are replaced by experimentally-derived MARVEL energy levels for the main isotopologue. The energy levels that are MARVELised, however, are the most populated energy levels; MARVELised energy levels contribute 95% and 86% to the total partition function at 2000 K and 3000 K, respectively.

In terms of the transitions themselves, 1,373,936 out of the total 58,983,952 transitions for the main isotopologue in TOTO are between two MARVELised energy levels and thus have very accurately determined line positions. We can examine the importance of these transitions to the overall line list by considering Figure 3.2, which shows the cross section from only MARVELised transitions compared to the total TOTO line list. The completeness of the MARVEL-only data varies considerably between spectral bands with some almost entirely complete, e.g. around 0.71, 0.52 and 0.49 μm , and some almost

entirely missing, e.g. around $0.57 \mu\text{m}$. The most important bands missing in the MARVEL-only data involve $\nu = 2$ and higher vibrational excitations of the $B^3\Pi$ state, which have not yet been experimentally analysed; in light of their importance to high-resolution Doppler spectroscopy, these levels are thus of most importance for future experimental study.

More quantitatively, we can quantify the number of MARVELised transitions compared to the total number of transitions in the TOTO line list at a given temperature above a certain intensity threshold by computing stick spectra using EXOCROSS (Yurchenko et al., 2018). Approximately 83% of the 4491 strongest transitions (line intensities above 10^{-17} cm/molecule at 2000 K) are MARVELised, with this number dropping to 64% of 50,408 transitions if the threshold is chosen as 10^{-18} cm/molecule.

3.2.2 Effect of line list choice on Transmission Spectra

The first detections of TiO in an exoplanet atmosphere have recently been made using transit spectra (Haynes et al., 2015; Sedaghati et al., 2017). In particular, Sedaghati et al. (2017) have detected TiO in the transmission spectrum of WASP-19b (though Espinoza et al. (2019) do not detect TiO at a later epoch). Here, we investigate the effect of the TOTO TiO line list, relative to the S98 line list, on transmission spectra by comparing two spectra for a canonical hot Jupiter. Throughout this chapter, model spectra are calculated for this canonical hot Jupiter using planetary/stellar properties similar to WASP-12b/WASP-12; the planetary radius and log gravity are taken as $1.79 R_J$ and 2.989 (cgs), respectively, and the stellar radius, log gravity, [Fe/H] metallicity and effective temperature are taken as $1.63 R_\odot$, 4.38 (cgs), 0.3 and 6300 K, respectively (Hebb et al., 2009; Stassun et al., 2017). We generate cross sections from the TOTO and S98 line lists using the methods described in Gandhi and Madhusudhan (2017). Using these, we generate two model transmission spectra which are identical other than the TiO cross sections used in each. The model spectra are generated using the transmission model described in Welbanks and Madhusudhan (2019) (see also Pinhas et al., 2018). We assume an isothermal pressure-temperature (P - T) profile at 2000 K and a constant-with-depth TiO mixing ratio of 10^{-7} . For simplicity, no other chemical species are included in these models.

The two spectra and their residuals are shown in Figure 3.3. The grey line in the lower panel shows the residual for smoothed spectra; spectra in the top panel are smoothed with a Gaussian of width 0.16 nm before calculating the residual, to represent smoothing by the PSF of a ground-based instrument. At this resolution, differences of up to 400 ppm can be seen, which are comparable to observational uncertainties with current instruments. When making inferences from optical transmission spectra, choice of TiO line list can therefore have a significant impact on the conclusions drawn.

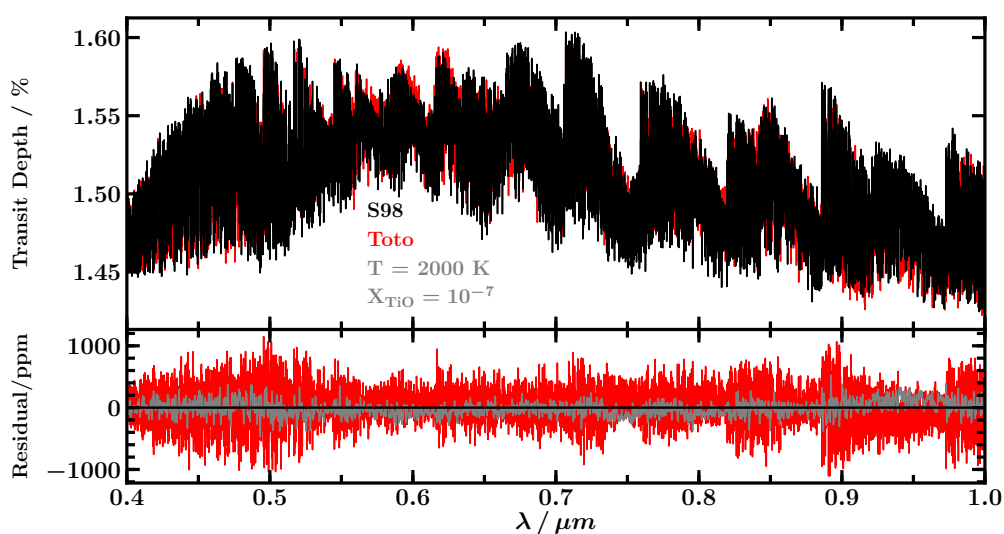


Fig. 3.3 Upper panel: Transmission spectra calculated using the TOTO (red) and S98 (black) cross sections at a resolution of $R \sim 10000$. The P - T profile is assumed to be an isotherm at 2000 K, and the planetary properties are those listed in Section 3.2. Lower panel: red line shows the residual between the red and black spectra in the top panel (TOTO spectrum - S98 spectrum). Grey line is calculated by smoothing the red and black spectra with a Gaussian of width 0.16 nm (to represent the PSF of a ground-based instrument) and finding the residual between them.

3.2.3 Effect of line list choice on Emission Spectra

Here, we consider the effects of the Toto and S98 TiO cross sections on the emission spectrum of a hot Jupiter. We do this by comparing emission spectra from two models which are identical apart from the TiO cross sections used to generate them.

To generate these spectra, we use the GENESIS model (Gandhi and Madhusudhan, 2017), which calculates full, line-by-line radiative transfer under radiative-convective equilibrium. In order to calculate equilibrium chemical abundances as a function of pressure, temperature and elemental abundances we use the software package HSC CHEMISTRY (version 8). This software has been used in several studies in the field of exoplanets, planet formation and the solar nebula (e.g. Pasek et al., 2005; Bond et al., 2010; Elser et al., 2012; Madhusudhan, 2012; Moriarty et al., 2014; Harrison et al., 2018), and calculates abundances by minimising the total Gibbs free energy of the system using the GIBBS solver (White et al., 1958). We include all the chemical species used in Bond et al. (2010) and Harrison et al. (2018), plus extra ionic and molecular forms of H, O, C, N, Ti and OH (listed in Table B.1), including H^- . In this section, all elemental abundances are taken to be solar.

Throughout this chapter, the cross sections we use for all molecules are calculated as in Gandhi and Madhusudhan (2017) from the HITEMP, HITRAN and ExoMol line list databases (H_2O , CO and CO_2 : Rothman et al. 2010, CH_4 : Yurchenko et al. 2013; Yurchenko and Tennyson 2014, C_2H_2 : Rothman et al. 2013; Gordon et al. 2017, NH_3 : Yurchenko et al. 2011, HCN: Harris et al. 2006; Barber et al. 2014, VO: McKemmish et al. 2016, Collision-Induced Absorption (CIA): Richard et al. 2012). We also include opacity due to Na and K (Burrows and Volobuyev, 2003; Gandhi and Madhusudhan, 2017). The bound-free and free-free cross sections of H^- are calculated using the prescriptions of Bell and Berrington (1987) and John (1988) (see also Arcangeli et al. 2018; Parmentier et al. 2018; Gandhi et al. 2020a).

We also consider the effect of vertical mixing in the GENESIS code. Spiegel et al. (2009) find that TiO is heavy enough to gravitationally settle if not kept aloft by mixing, and cold traps are known to deplete TiO if it is not replenished (e.g. Burrows et al., 2007; Spiegel et al., 2009). We use a simple mixing model in which the equilibrium abundance is added to a ‘quenched’ abundance in the range $0.1\text{-}10^{-3}$ bar. This ‘quenched’ value is taken to be the equilibrium abundance at 0.1 bar, where we assume that vertical mixing begins (e.g. Spiegel et al., 2009; Moses et al., 2013b). The resulting abundance profile is effectively equal to the larger of the equilibrium or quenched values.

Figure 3.4 shows the residuals between spectra of two otherwise identical models generated with each of the Toto and S98 cross sections with the P - T profile shown in the

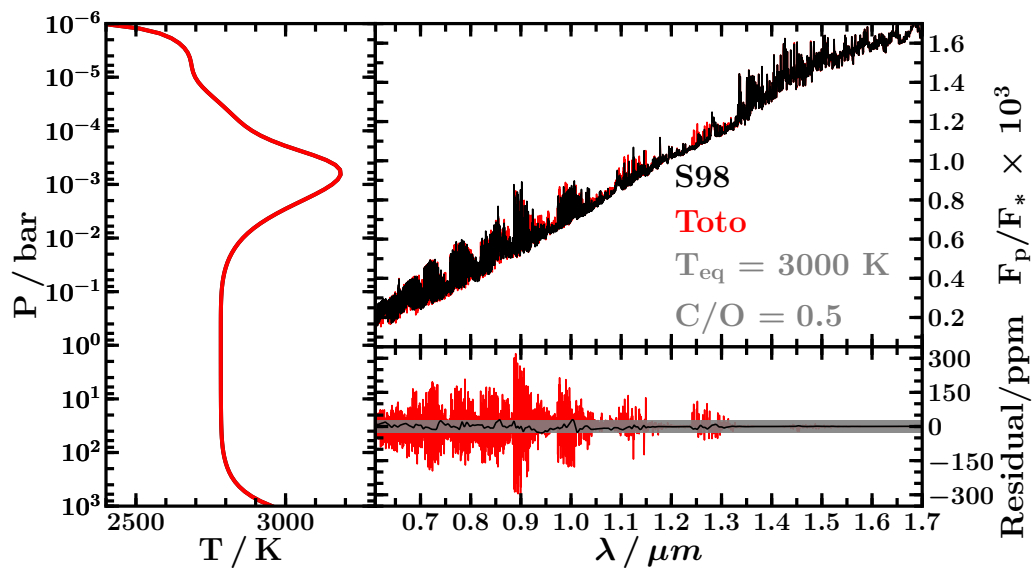


Fig. 3.4 Upper right panel: spectra for two model atmospheres with identical P - T profiles, chemical profiles, irradiation and planetary properties, but using the S98 (black) and TOTO (red) TiO cross sections. The planetary properties are those listed in Section 3.2 and the semi-major axis is adjusted such that the dayside equilibrium temperature is 3000 K. Lower right panel: the residuals between the two spectra (TOTO spectrum - S98 spectrum) at a resolution of $R \sim 10000$ (red) and smoothed with a Gaussian of width 2.3 nm (black) to represent the PSF of HST/WFC3. The atmospheric model used is self-consistent for the TOTO cross sections, and the P - T profile is shown in the left panel.

left panel. The P - T profile used is a self-consistent P - T profile generated using the TOTO line list assuming a dayside equilibrium temperature of 3000 K as well as equilibrium chemistry and vertical mixing as described above. Note that in this chapter, we define dayside equilibrium temperature as

$$T_{\text{eq}} = \left(\frac{f}{2}\right)^{1/4} \sqrt{\frac{R_s}{a}} T_{\text{eff}}, \quad (3.1)$$

(henceforth referred to as equilibrium temperature) where f is the fraction of incident irradiation which remains on the dayside, R_s and T_{eff} are the radius and effective temperature of the star, respectively, and a is the semi-major axis of the planet. Throughout this chapter we assume a value of $f = 1/2$ (i.e. full redistribution of incident radiation around the planet), unless otherwise stated, and a is chosen such that T_{eq} has the value quoted in each figure. For the incident stellar irradiation we use ATLAS model spectra (Kurucz, 1979; Castelli and Kurucz, 2003) and both the stellar and planetary properties we use are listed in Section 3.2.2.

The spectra in Figure 3.4 differ most in the optical range by up to a factor of 300 ppm. Intuitively, this is because TiO is primarily active in the optical range, and as such will have a larger impact on optical spectra. In the near-infrared, the two spectra differ by up to ~ 100 ppm. However, the differences in both the optical and near-infrared are only visible at higher spectral resolutions. When the two spectra are smoothed to a resolution similar to that of HST/WFC3, the residuals between them are of order ~ 25 ppm which is comparable to the signal-to-noise achievable with HST/WFC3. When interpreting emission spectra, choice of TiO line list is therefore most important at high resolutions.

In what follows, we choose to use the TOTO cross sections in our analysis of thermal inversions caused by TiO. In addition to the advantages discussed in Section 3.2.1, TOTO also has better completeness than previous line lists and takes advantage of more recent experimental data in fitting the DUO spectroscopic models (McKemmish et al., 2019).

3.3 Influence of Chemistry on Thermal Inversions

The thermal profile in a hot Jupiter atmosphere is dictated by the incident stellar irradiation and the sources of opacity in the atmosphere. In this section, we briefly investigate the relationship between atmospheric chemistry and temperature structure using a semi-analytic approach. A key component in determining the opacities is the abundance of each chemical species. We therefore begin by calculating equilibrium abundances for a range of chemical species as a function of temperature and C/O ratio using the HSC

CHEMISTRY software as described in Section 3.2.3. By considering radiative equilibrium, we then use these chemical abundances to explore the range of thermal solutions which are possible under various conditions. We vary the C/O ratio by using solar elemental abundances but varying the C abundance. The C/O ratio can alternatively be varied by changing the O abundance (e.g. Drummond et al., 2019). However, this would directly alter the abundances of TiO and other O-rich species, which we are primarily interested in in this study, so we opt to vary only the C abundance. In later sections, we also vary metallicity by keeping solar elemental ratios but scaling abundances by a constant factor.

Figure 3.5 shows the calculated equilibrium abundances for H₂O, CO and TiO as a function of C/O ratio and temperature. The HSC CHEMISTRY software includes the effects of condensation (we assume that condensed phases rain out) and thermal dissociation, which can be seen in the top panel of Figure 3.5 as the abundance of TiO decreases rapidly at temperatures below ~1750 K (condensation), and both TiO and H₂O are depleted at temperatures above ~3000 K (thermal dissociation). As expected, the abundances of both species drop by several orders of magnitude as the C/O ratio increases above unity, consistent with previous studies (Madhusudhan et al., 2011b; Madhusudhan, 2012; Moses et al., 2013b). In contrast, the CO abundance remains high across both low and high C/O ratios, and at cooler temperatures (~1300 K), CO abundance decreases as CH₄ takes over as the dominant carrier of carbon (Madhusudhan, 2012).

These abundances affect the temperature in a region of the atmosphere through the ratio of visible to infrared opacity, $\kappa_{\text{vis}}/\kappa_{\text{ir}}$ (Hubeny et al., 2003; Guillot, 2010; Hubeny, 2017). κ_{vis} determines the amount of incident radiation which can be absorbed, while κ_{ir} dictates the efficiency with which the gas is able to radiate away energy, both of which affect the steady-state temperature of the gas. These quantities are defined by:

$$\begin{aligned}\kappa_{\text{vis}} &= \frac{\int_0^\infty \kappa_\nu J_\nu d\nu}{\int_0^\infty J_\nu d\nu}, \\ \kappa_{\text{ir}} &= \frac{\int_0^\infty \kappa_\nu B_\nu d\nu}{\int_0^\infty B_\nu d\nu}.\end{aligned}\tag{3.2}$$

B_ν is the thermal emission of the gas (a Planck function of temperature T) and κ_ν is the opacity of the gas as a function of frequency, defined as:

$$\kappa_\nu = \sum_i \sigma_i n_i,$$

where the sum is over all species and σ_i , n_i are the cross section and number density of each species, respectively. J_ν is the zeroth moment of spectral intensity of incident

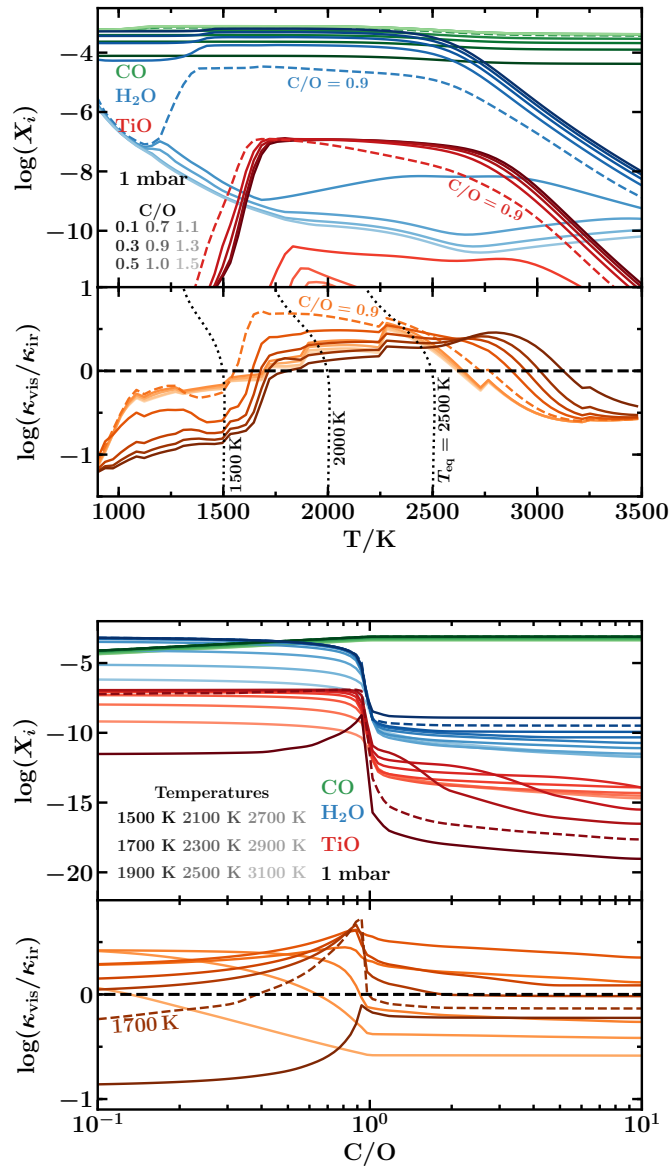


Fig. 3.5 Equilibrium abundances of TiO, H₂O and CO as a function of temperature (top panel) and C/O ratio (bottom panel), for a pressure of 1 mbar. In each plot, the lower section shows the log of the ratio of optical to infrared opacities, $\log(\kappa_{\text{vis}}/\kappa_{\text{ir}})$. Bold black dashed lines highlight $\kappa_{\text{vis}}/\kappa_{\text{ir}}=1$. Values of $\kappa_{\text{vis}}/\kappa_{\text{ir}} \gtrsim 1$ correspond to a thermal inversion in the atmosphere. In the upper panel, dotted black lines show $\kappa_{\text{vis}}/\kappa_{\text{ir}}$ as a function of photospheric temperature (temperature at an optical depth of 2/3), calculated using the P - T profile of Guillot (2010) and assuming equilibrium temperatures of $T_{\text{eq}} = 1500$ K, 2000 K and 2500 K, respectively. In the top (bottom) panels, different line colours indicate different values of the C/O ratio (temperature), with darker shades indicating smaller values as shown by the legend. In the top panel, dashed coloured lines correspond to C/O=0.9, while in the bottom panel dashed coloured lines correspond to a temperature of 1700 K. For these values, $\kappa_{\text{vis}}/\kappa_{\text{ir}}$ has the highest peak in each plot, respectively.

irradiation, $J_v = \frac{1}{2} \int_{-1}^1 I_{v\mu_\theta} d\mu_\theta$, where $I_{v\mu_\theta}$ is the spectral intensity of incident irradiation at an angle θ ($\mu_\theta = \cos\theta$) to the local normal.

The effect of $\kappa_{\text{vis}}/\kappa_{\text{ir}}$ on the atmospheric temperature gradient can be seen using the analytic P - T profile of Guillot (2010). This profile parameterises atmospheric temperature (T), as a function of optical depth (τ), intrinsic planetary temperature (T_{int}), dayside temperature and $\kappa_{\text{vis}}/\kappa_{\text{ir}}$. As such, $dT/d\tau$ can be calculated as a function of $\kappa_{\text{vis}}/\kappa_{\text{ir}}$. Assuming a negligible T_{int} , $dT/d\tau$ is negative (i.e. there is a thermal inversion) when $\kappa_{\text{vis}}/\kappa_{\text{ir}} > 1$, for all finite values of τ and dayside temperature (Guillot, 2010; Gandhi and Madhusudhan, 2019).

In Figure 3.5, we show $\kappa_{\text{vis}}/\kappa_{\text{ir}}$ as a function of C/O ratio and temperature. For simplicity, we use a single pressure of 1 mbar to represent the upper atmosphere. To calculate $\kappa_{\text{vis}}/\kappa_{\text{ir}}$, we include opacity contributions from TiO, H₂O, CH₄, NH₃, CO, CO₂, HCN, C₂H₂, Na, K, VO and CIA, using equilibrium chemical abundances from HSC CHEMISTRY. From Figure 3.5 (top panel), we see that $\kappa_{\text{vis}}/\kappa_{\text{ir}}$ only has values above unity for temperatures greater than ~ 1500 K. This suggests that thermal inversions caused by TiO can only occur for atmospheric temperatures above 1500 K. This temperature limit corresponds to C/O=0.9, while lower and higher C/O ratios begin to exceed $\kappa_{\text{vis}}/\kappa_{\text{ir}}$ only at higher temperatures. Larger values of $\kappa_{\text{vis}}/\kappa_{\text{ir}}$ coincide with larger values of TiO abundance, which is expected since TiO is a primary visible absorber in this scenario. Outside the range of large $\kappa_{\text{vis}}/\kappa_{\text{ir}}$, condensation and thermal dissociation of TiO both diminish its value at low and high temperatures, respectively. Na and K can also contribute significantly to the optical opacity, and hence thermal inversions, for $C/O \gtrsim 1$ (see also Mollière et al., 2015). For example, at $C/O \geq 1$, where TiO is strongly depleted, optical opacity due to Na and K results in $\kappa_{\text{vis}}/\kappa_{\text{ir}} > 1$ for temperatures greater than ~ 1750 K.

We can use $\kappa_{\text{vis}}/\kappa_{\text{ir}}$ as shown in figure 3.5 to broadly assess the feasibility of thermal inversions for a given T_{eq} . To do this, we again use the analytic temperature profile from Guillot (2010), setting $\tau = 2/3$ (i.e. corresponding to the photosphere) and assuming that intrinsic heat is negligible compared to the irradiation. For a chosen equilibrium temperature, this results in a relation between $\kappa_{\text{vis}}/\kappa_{\text{ir}}$ and photospheric temperature. This is shown by the dotted black lines in the upper panel of Figure 3.5 for three equilibrium temperatures (1500, 2000 and 2500 K). Solutions for the photospheric temperature occur at the intersection points between these lines and the values of $\kappa_{\text{vis}}/\kappa_{\text{ir}}$ calculated independently from the molecular opacities (coloured lines in lower section of upper panel in Figure 3.5). Where these intersections happen at $\kappa_{\text{vis}}/\kappa_{\text{ir}} > 1$, a thermal inversion is possible.

Figure 3.5 therefore shows that inversions start to become possible at temperatures in the range ~ 1500 - 2000 K, depending on the C/O ratio. For example, for C/O=0.9, thermal inversions are possible at equilibrium temperatures just above 1500 K, while for C/O \geq 1.0 equilibrium temperatures $\gtrsim 1750$ K are required. This is comparable to the equilibrium temperature at which Fortney et al. (2008) begin to see thermal inversions for a Sun-like host star (~ 1800 K). To fully understand the effects of equilibrium chemical abundances on the P - T profile of an atmosphere, we extend our analysis with full numerical atmospheric models in Section 3.5.

3.4 Metrics for Assessing Thermal Inversions

In this section, we assess metrics for inferring the presence and strength of thermal inversions in exoplanet atmospheres with solar-like compositions. A common way to do this involves comparing two photometric measurements, e.g. using the Spitzer IRAC 1 and IRAC 2 channels (e.g. Burrows et al., 2007; Knutson et al., 2010; Madhusudhan and Seager, 2010). Assessing the presence of a thermal inversion with two or more spectral or photometric bands requires at least one band which probes a high-opacity region of the spectrum and an opacity window which probes as little line opacity as possible, i.e. a spectral continuum. The continuum band probes deeper regions of the atmosphere while the high-opacity band probes higher up in the atmosphere. The difference in brightness temperature between these bands provides a measure of the temperature gradient in the photosphere. While a ‘perfect’ opacity window would contain no line opacity at all, this is not realistic. Furthermore, continuum opacity such as CIA opacity is itself wavelength dependent. Therefore, different continuum bands can have varying levels of both line opacity contamination and continuum opacity. A continuum band with less line opacity probes deeper into the atmosphere and therefore has the potential to probe a larger temperature contrast when compared to the ‘high-opacity’ band. Therefore, when looking for metrics to assess thermal inversions it is advantageous to consider the clearest possible continuum bands. For example, Stevenson (2016) use the J-band as a continuum compared to a water absorption band when quantifying absorption features in transmission spectra.

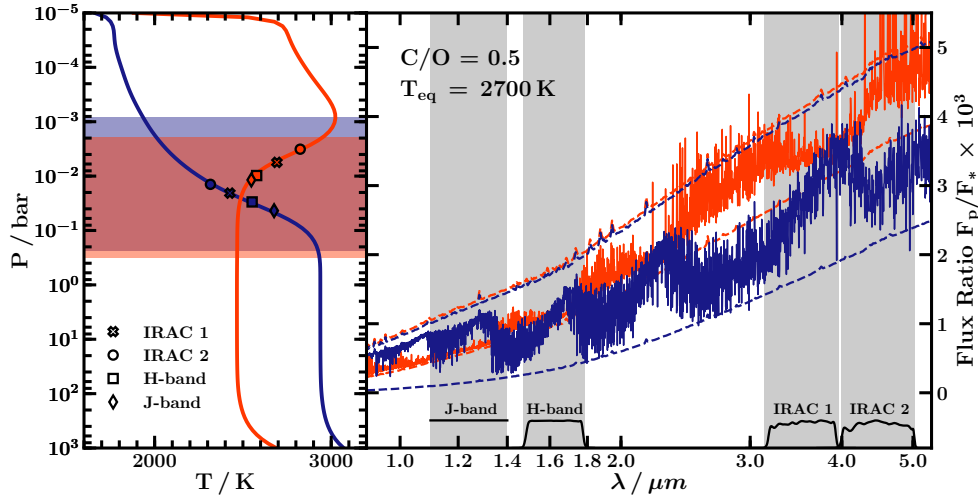


Fig. 3.6 Temperatures and pressures probed by the J-band, H-band, IRAC 1 and IRAC 2 photometric bands. Red and blue spectra in the right panel correspond to the P - T profiles of the same colour in the left panel; both are generated using the properties listed in Section 3.2 and the red spectrum includes TiO while the blue one does not. Markers in the left panel show the brightness temperatures (and corresponding pressures) of the IRAC 1, IRAC 2, H-band and J-band photometric points from each of the spectra, respectively. Each of these bands is shown by the grey shaded regions in the right panel and their transmission functions are shown in black. Blue and red shaded regions in the left panel show the pressure ranges of the photospheres for the blue and red P - T profiles, respectively.

The IRAC 1 and IRAC 2 channels (at $3.6 \mu\text{m}$ and $4.5 \mu\text{m}$, respectively) are commonly used to infer the presence of thermal inversions in hot Jupiters as the $3.6 \mu\text{m}$ band does not contain very strong molecular features for solar composition atmospheres while the $4.5 \mu\text{m}$ band probes a strong CO feature (e.g. Burrows et al., 2007; Knutson et al., 2009a; Madhusudhan and Seager, 2010). This property has also been used to construct colour-magnitude diagrams for exoplanets and brown dwarfs and to subsequently compare irradiated exoplanets to other types of sub-stellar object (Triaud, 2014; Triaud et al., 2014). For a hot Jupiter with solar composition and a thermal inversion, the brightness temperature contrast between the IRAC 2 and IRAC 1 channels, $T_{4.5\mu\text{m}} - T_{3.6\mu\text{m}}$, is expected to be positive. On the other hand, an atmosphere with solar composition but without a thermal inversion would be expected to have $T_{4.5\mu\text{m}} - T_{3.6\mu\text{m}} < 0$. However, in reality, the IRAC 1 band is not a perfect opacity window. In particular, it has contributions from CH_4 , H_2O and HCN (Madhusudhan, 2012). This is particularly evident for high C/O ratios close to 1 where CH_4 and HCN can have significant opacity contributions. Under such circumstances, an atmosphere without a thermal inversion can still have significantly

low flux in the IRAC 1 band due to CH_4 and/or HCN absorption compared to the IRAC 2 band with CO . This situation can give rise to a positive $T_{4.5\mu\text{m}} - T_{3.6\mu\text{m}}$ contrast which can mimic the behaviour of a thermal inversion (Section 3.5.2). Other photometric bands may therefore provide a better opacity window compared to the IRAC 1 channel, and planets with different chemistries may require different bands to probe the spectral continuum.

Here, we use theoretical models to assess metrics for temperature gradients in atmospheres with solar-like compositions. We calculate brightness temperatures using the method described by Garhart et al. (2020); for a spectral bin in the wavelength range $\lambda_{\text{min}} - \lambda_{\text{max}}$ and a normalised instrument sensitivity function ζ , the brightness temperature, T_b , is chosen such that

$$\int_{\lambda_{\text{min}}}^{\lambda_{\text{max}}} \pi \zeta B_{\lambda}(T_b) d\lambda = \frac{F_p}{F_s} \frac{R_s^2}{R_p^2} \times \int_{\lambda_{\text{min}}}^{\lambda_{\text{max}}} \pi \zeta I_s d\lambda, \quad (3.3)$$

where $\frac{F_p}{F_s}$ is the observed planet-star flux ratio in the photometric band, πI_s is the stellar surface flux (we use ATLAS model spectra: Kurucz (1979); Castelli and Kurucz (2003)) and R_p is the planetary radius.

We begin by investigating optimal continuum bands for hot Jupiter atmospheres of solar composition. In particular, we compare the H- and J-bands to the IRAC 1 band according to their performance as continuum bands for solar-composition spectra (see Figure 3.6). Both the H- and J-bands coincide with local minima in H_2O opacity so, for spectra dominated by H_2O , they should probe deeper regions of the atmosphere relative to bands which probe stronger features (Stevenson, 2016). We demonstrate this property here using two self-consistent atmospheric models for which the P - T profiles and spectra are shown in Figure 3.6. Both models are generated using the GENESIS self-consistent modelling code (Gandhi and Madhusudhan, 2017). The equilibrium chemical abundances are calculated using HSC CHEMISTRY assuming a C/O ratio of 0.5. The model shown in blue does not include TiO and has a non-inverted profile, while the model shown in red does include TiO and has a thermal inversion. For each model, we compute a simulated photometric measurement for each of the four bands mentioned above, and calculate the brightness temperature of each measurement. These temperatures are plotted over the P - T profiles in the left panel of Figure 3.6 and indicate which part of the photosphere is probed by each band.

We find that the H-band and J-band probe deeper atmospheric pressures compared to the IRAC 1 band for these models. This is clearly demonstrated in Figure 3.7, which shows optical depth as a function of wavelength and pressure in the atmosphere (i.e. altitude). The J-, H- and IRAC 1 bands all correspond to windows in opacity, where optical

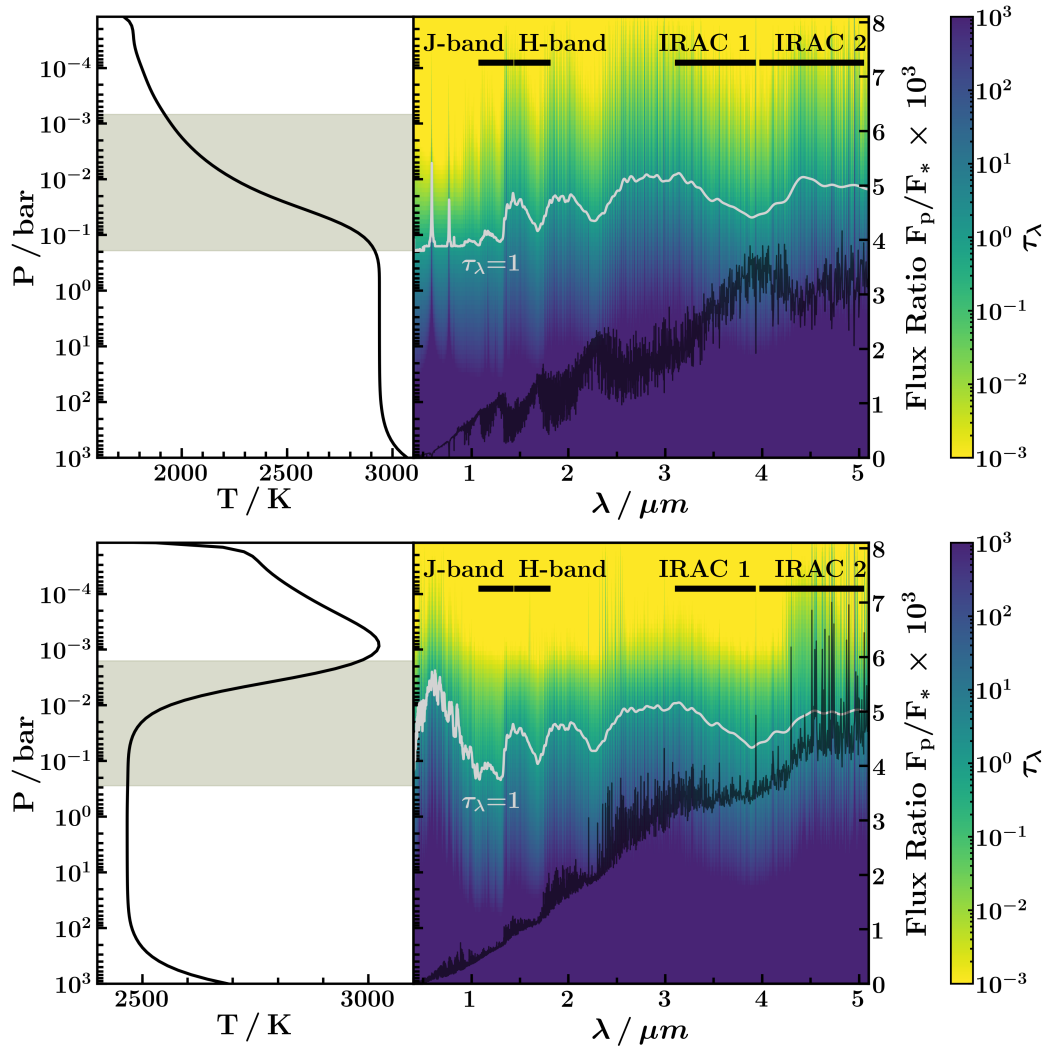


Fig. 3.7 Optical depth as a function of wavelength and pressure (i.e. altitude) in the atmosphere for the two P - T profiles shown in Figure 3.6. Left panels show the P - T profile with the photosphere (calculated as the extent of the $\tau=1$ surface) shaded in grey. In the right panels, the $\tau=1$ surface is shown as a function of wavelength and pressure by the grey line. Opacity windows, including the J-, H- and IRAC 1 bands occur where the optical depth reaches unity at deeper pressures. The emergent spectrum of the planet is shown in black. Horizontal black lines indicate the J-, H-, IRAC 1 and IRAC 2 bands.

depth reaches unity at deeper pressures. However, in the J- and H- bands, unit optical depth is reached at pressures ~ 1 order of magnitude greater than that for the IRAC 1 band. Figure 3.7 also shows that deeper pressures can be probed at higher spectral resolutions by sampling very narrow windows in opacity and avoiding contamination from higher-opacity regions. We demonstrate this concept in greater detail in appendix B.2 (see also de Kok et al. 2014). Despite this effect, wider photometric bands are still observationally favourable as they are less sensitive to small wavelength shifts in the detector.

Since, in the cases shown here, the J- and H- bands are better opacity windows than the IRAC 1 band, the brightness temperature contrasts between the IRAC 2 channel and the H-band ($T_{4.5\mu\text{m}} - T_{\text{H}}$) or between the IRAC 2 channel and the J-band ($T_{4.5\mu\text{m}} - T_{\text{J}}$) are greater than the contrast between the two IRAC channels ($T_{4.5\mu\text{m}} - T_{3.6\mu\text{m}}$). For both the inverted and non-inverted model P - T profiles, an inversion/non-inversion could be inferred based on the brightness temperatures of the IRAC 2 channel and any of the other three bands, since the IRAC 2 channel probes the shallowest pressures (highest altitudes) in both cases, corresponding to the hottest/coolest brightness temperature for the inverted/non-inverted profile. However, a larger brightness temperature contrast provides more information about the atmospheric temperature gradient and can potentially allow for a more robust inference of an inversion/non-inversion. In this case, the J-band would therefore be the best suited for comparison to the IRAC 2 band, as it probes deeper into the atmosphere. Although the H- and J-bands may not be optimal probes of the continuum for spectra which are not dominated by H_2O opacity, this demonstrates that it can be beneficial to consider bands other than the IRAC 1 channel when seeking to determine the presence of a thermal inversion based on photometric measurements alone. In Section 3.5, we extend this assessment to a wider range of C/O ratios, equilibrium temperatures, metallicities, gravities and stellar types.

3.5 Metrics as a function of planetary and host star properties

In this section, we use self-consistent models to investigate in detail how chemical composition, incident irradiation and gravity affect the strength of thermal inversions in hot Jupiters as well as the performance of temperature gradient metrics. We use the GENESIS code (Gandhi and Madhusudhan, 2017) to generate self-consistent model atmospheres and their spectra for various C/O ratios, equilibrium temperatures, metallicities, stellar types and gravities. The equilibrium chemical abundances are calculated with HSC CHEMISTRY, and we also include the effects of vertical mixing by quenching all chemical

abundances between 0.1 and 10^{-3} bar (see Section 3.2.3). In addition to vertical mixing, we also consider the redistribution of incident flux to the nightside of the planet. Following Garhart et al. (2020), we approximate the redistribution factor, f , as a step function where planets with $T_{\text{eq}} \leq 2500$ K transport 50% of incident flux to the nightside ($f = 1/2$), while planets with $T_{\text{eq}} > 2500$ K retain all incident energy on the dayside ($f = 1$) (see also Cowan and Agol, 2011).

Using these equilibrium models, we calculate P - T profiles and model spectra for a range of T_{eq} , C/O ratios, metallicities, stellar types and gravities. Since we are focusing on thermal inversions due to TiO, we explore C/O ratios ≤ 1 as TiO is significantly depleted at higher C/O ratios. The opacity sources we include in our models are those listed in Section 3.2.3. We note that other sources of optical opacity not considered here (e.g. atomic Fe and Mg, Lothringer and Barman 2019) can also cause thermal inversions, though we focus on thermal inversions due to TiO in the present work. We then use these models to explore temperature gradient as a function of these parameters, and compare different empirical metrics for assessing this gradient. In order to test the performance of the empirical metrics, we compare them to the true temperature gradient derived from the model P - T profiles. This is found by considering the temperature contrast across the photosphere, which we take to be in the range $1 - 10^{-3}$ bar. For highly irradiated atmospheres, it is well known that the temperature profile becomes isothermal in the high optical depth limit before becoming steeper again at even higher pressures (Guillot, 2010). Note that we are using an internal temperature of 100 K (i.e. the temperature corresponding to the internal flux emanating from the centre of the planet, which is equivalent to the effective temperature when no incident irradiation is present). Since this is much smaller than the irradiation temperature, the isotherm extends to the bottom of our computational domain and we do not see the steeper gradient. For the dayside of irradiated atmospheres such as those modelled here, the base of the photosphere coincides with the top of this isotherm in the lower atmosphere (e.g. Hubeny et al., 2003; Burrows et al., 2006b; Guillot, 2010). The temperature of the isotherm is therefore a consistent measure of the temperature at the bottom of the photosphere across all the models we consider. For profiles with a thermal inversion, the temperature contrast is defined as the maximum photospheric temperature minus the minimum temperature between the bottom of the photosphere (~ 1 bar) and the location of the temperature maximum. For profiles with no inversion, the contrast is defined as the minimum atmospheric temperature minus the temperature at the bottom of the photosphere (at 1 bar, i.e. the temperature of the isotherm). We consider a P - T profile to have a thermal inversion if the inversion strength is greater than 30 K. Maps of inversion strength as a function of C/O ratio and equilibrium temperature are shown in

Figures 3.8, 3.9 and 3.10 for varying metallicities, stellar host types and planetary surface gravities.

3.5.1 Inversion strength

The true temperature contrasts shown in the top rows of Figures 3.8, 3.9 and 3.10 show that a wide variety of P - T profiles are possible in this parameter space, including strong thermal inversions, isotherms and non-inverted profiles. This is in accordance with observations of hot Jupiters, which have revealed spectra with emission features (e.g. Haynes et al., 2015; Evans et al., 2017; Sheppard et al., 2017; Arcangeli et al., 2018), flat spectra (e.g. Swain et al., 2013; Cartier et al., 2017; Mansfield et al., 2018), and absorption features (e.g. Beatty et al., 2017b). We also plot contours of $\kappa_{\text{vis}}/\kappa_{\text{ir}} = 1$ (calculated at a nominal pressure of 1 mbar) in the top panels of Figure 3.8 to show the regions of parameter space expected to host thermal inversions (Section 3.3). Note however that these contours do not include effects due to vertical mixing and are only calculated at a single pressure, whereas thermal inversions can happen at different pressures for different cases. Nevertheless, the $\kappa_{\text{vis}}/\kappa_{\text{ir}} = 1$ contours roughly outline the regions of the parameter space where thermal inversions occur.

The models in Figures 3.8, 3.9 and 3.10 suggest that strong inversions are more likely to occur at higher C/O ratios in the C/O < 1 regime, as has been previously discussed in other works (e.g. Mollière et al., 2015; Gandhi and Madhusudhan, 2019). This is consistent with the trend seen in Section 3.3 and in the $\kappa_{\text{vis}}/\kappa_{\text{ir}} = 1$ contour that thermal inversions are possible for a C/O of 0.9 at a lower equilibrium temperature compared to other C/O ratios. In addition, for a C/O ratio of one, only weak thermal inversions or non-inverted profiles are seen in the models, consistent with the strong depletion of TiO at C/O=1 (Madhusudhan et al., 2011b). As discussed in Section 3.3, these thermal inversions are caused by optical opacity from Na and K (also see e.g., Mollière et al., 2015) as TiO abundance is strongly depleted for C/O \geq 1 (e.g., Madhusudhan, 2012).

Another clear trend is that for increasing metallicity, peak inversion strength occurs at higher T_{eq} (Figure 3.8). This is because TiO is depleted by condensation and thermal dissociation at relatively higher temperatures for higher metallicity (Figure B.3), so a higher equilibrium temperature is needed to obtain $\kappa_{\text{vis}}/\kappa_{\text{ir}}=1$ (see appendix B.3 and Mollière et al. (2015)). Furthermore, the strongest thermal inversions are stronger for high-metallicity models, as seen in Figure 3.8. Compared to variation in metallicity, changes in stellar type have a more subtle effect on thermal inversion strength in the parameter space tested here. However, Figure 3.9 does show that earlier stellar types can allow somewhat stronger thermal inversions, e.g. inversion strengths for a K7V host star are typically

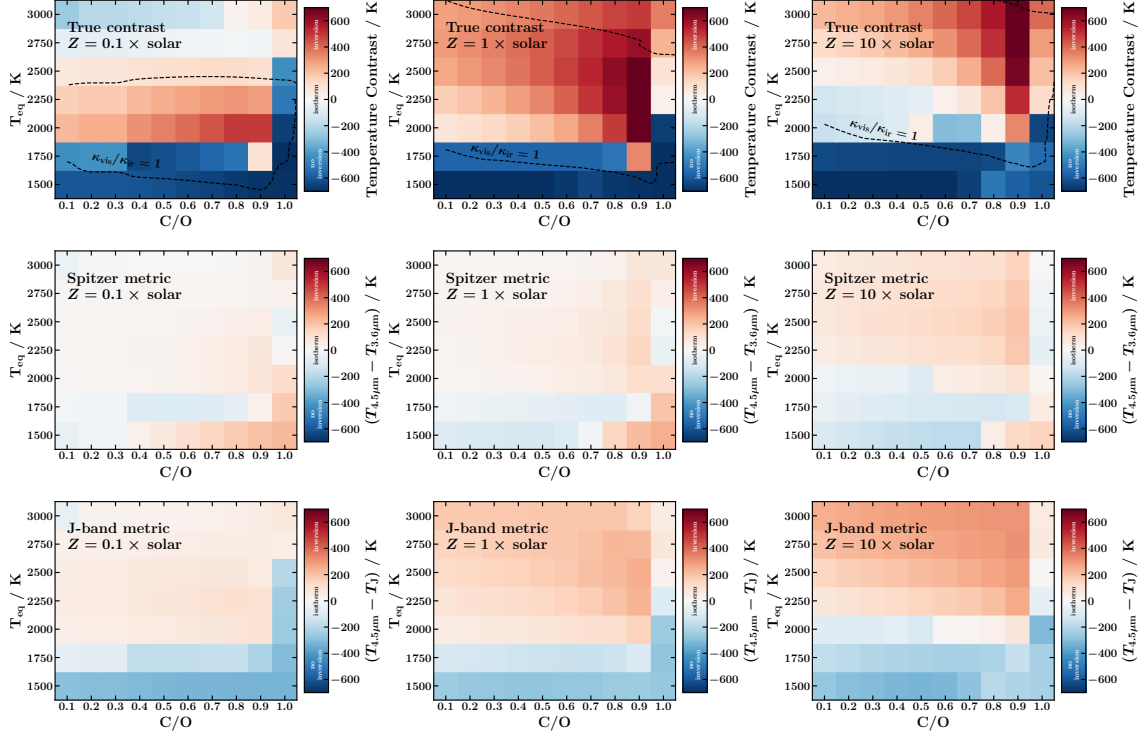


Fig. 3.8 Inversion maps showing the strength of the inversion/non-inversion of equilibrium P - T profiles as a function of equilibrium temperature and C/O ratio. Equilibrium P - T profiles are calculated as described in Section 3.2. Left, middle and right columns correspond to metallicities of 0.1, 1 and $10\times$ solar, respectively. Top row: colour scale shows temperature contrast within the pressure range $1\text{-}10^{-3}$ bar (see Section 3.5 for definition of the temperature contrast). Dashed black line shows contour of $\kappa_{\text{vis}}/\kappa_{\text{ir}} = 1$ at a pressure of 1 mbar (see Section 3.3). This predicts that models inside the contour should have thermal inversions, though note that this contour does not include effects due to vertical mixing and does not account for the fact that thermal inversions can happen at different pressures for different cases. Middle and bottom rows: performance of the Spitzer and J-band metrics throughout the parameter space. Colour scale shows brightness temperature contrasts between the IRAC 1 and IRAC 2 bands ($T_{4.5\mu\text{m}} - T_{3.6\mu\text{m}}$, middle row) and between the J-band and IRAC 2 band ($T_{4.5\mu\text{m}} - T_J$, bottom row). Positive (negative) values indicate a thermal inversion (non-inversion).

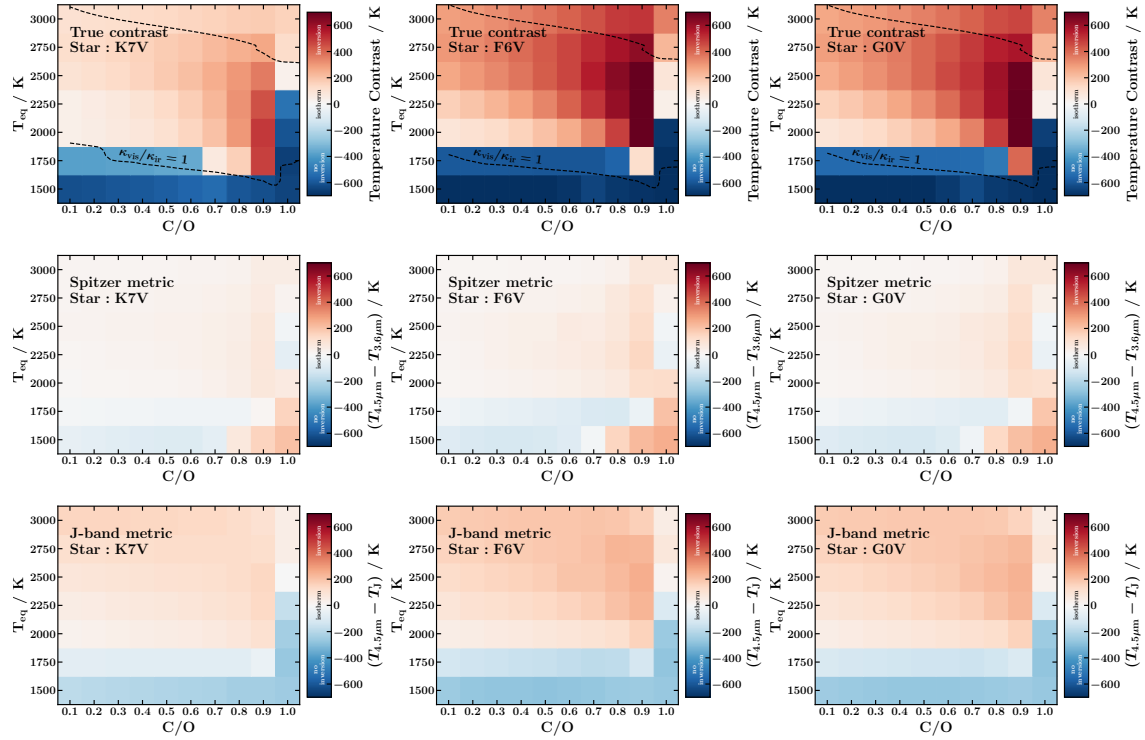


Fig. 3.9 Inversion strength as a function of equilibrium temperature, C/O ratio and stellar type of the host star. Left, middle and right columns correspond to the stellar types K7V, F6V and G0V, respectively. The stellar properties used for each stellar type are those of WASP-43, WASP-18 and HD 209458, respectively (Hellier et al., 2011; Southworth, 2012; Stassun et al., 2017). Colour scales show the same temperature contrasts as in Figure 3.8. Contours of $\kappa_{\text{vis}}/\kappa_{\text{ir}} = 1$ in the top row are calculated in the same way as for Figure 3.8 but using the appropriate host star temperature for each case.

weaker compared to F6V and G0V host stars in this parameter space (see also Lothringer and Barman, 2019). Furthermore, a later stellar type can allow thermal inversions to occur at lower equilibrium temperatures. In particular, for the K7V host star, thermal inversions start to become possible at 1750 K and C/O=0.7-0.8, which is not the case for the F6V and G0V host stars.

We also test the effect of increasing the planetary surface gravity in Figures 3.8 and 3.10. In the centre column of Figure 3.8, the surface gravity is chosen to be similar to WASP-12b ($\log(g/\text{cm}^{-2})=2.99$), while in Figure 3.10 we use a larger gravity similar to WASP-18b ($\log(g/\text{cm}^{-2})=4.26$). Between these two extremes, there are only minimal differences in inversion strength in the parameter space investigated here. One difference is that in the high-gravity case, slightly higher inversion strengths are typically found for lower T_{eq} and lower C/O ratio. There are also a few cases for which the high- and low-gravity

models disagree on the presence of a thermal inversion. However, the P - T profiles in these cases are in fact similar between the high- and low-gravity models, and the difference in inversion classification is due only to small differences between the profiles. Since the two gravities investigated here are extremes of the range expected for hot Jupiters, we conclude that gravity has a relatively small impact on inversion strength compared to factors such as metallicity. We also note that in our models, the gravity impacts the thermal profile only through the scale height and the fact that the photosphere is at higher pressure and therefore has greater pressure broadening of the chemical cross sections. However, a varying gravity could impact the gravitational settling of heavier species such as TiO, which we do not consider here (Beatty et al., 2017a).

3.5.2 Performance of metrics

We also use these models to test the performances of the Spitzer and J-band metrics discussed in Section 3.4. As discussed in Section 3.4, each of the photometric bands used by these metrics probes either a spectral feature (i.e. the IRAC 2 band) or a spectral window (e.g. the IRAC 1 and J-bands), allowing different pressures in the atmosphere to be probed. In Section 3.4, the efficacy of these bands in probing spectral features and windows was explored for a solar-like composition and a single equilibrium temperature. Here, we extend this analysis to a range of C/O ratios, equilibrium temperatures, metallicities, stellar types and gravities. Figure 3.8 shows brightness temperature contrasts for these metrics between equilibrium temperatures of 1500 K to 3000 K, for C/O ratios of 0.1-1.0 and for metallicities of 0.1, 1 and $10\times$ solar. The middle row of Figure 3.8 shows brightness temperature contrasts between the Spitzer IRAC 1 and IRAC 2 bands, $T_{4.5\mu\text{m}} - T_{3.6\mu\text{m}}$, while the bottom row shows the $T_{4.5\mu\text{m}} - T_{\text{J}}$ contrast. Similarly, these contrasts are shown for different stellar types (K7V, F6V and G0V) and planetary gravities in Figures 3.9 and 3.10, respectively.

Across the parameter space we explore, the IRAC 2 channel probes a CO spectral feature, as CO is abundant at all of the temperatures and C/O ratios modelled (Figure 3.5). However, the spectral features or windows probed by the IRAC 1 and J-bands can vary depending on chemistry. For example, the IRAC 1 band coincides with CH₄ and HCN opacity features. Therefore, for an atmosphere with high CH₄ and/or HCN abundance, the IRAC 1 band will no longer probe a spectral window and the performance of the Spitzer metric may not be optimal. This can be seen in Figures 3.8, 3.9 and 3.10 at low equilibrium temperatures ($T_{\text{eq}} \approx 1500$ K) and high C/O, where $T_{4.5\mu\text{m}} - T_{3.6\mu\text{m}}$ has positive values, despite the lack of thermal inversion in the models in this region of parameter space. Overall, the J-band metric provides a slightly better match to the true contrast

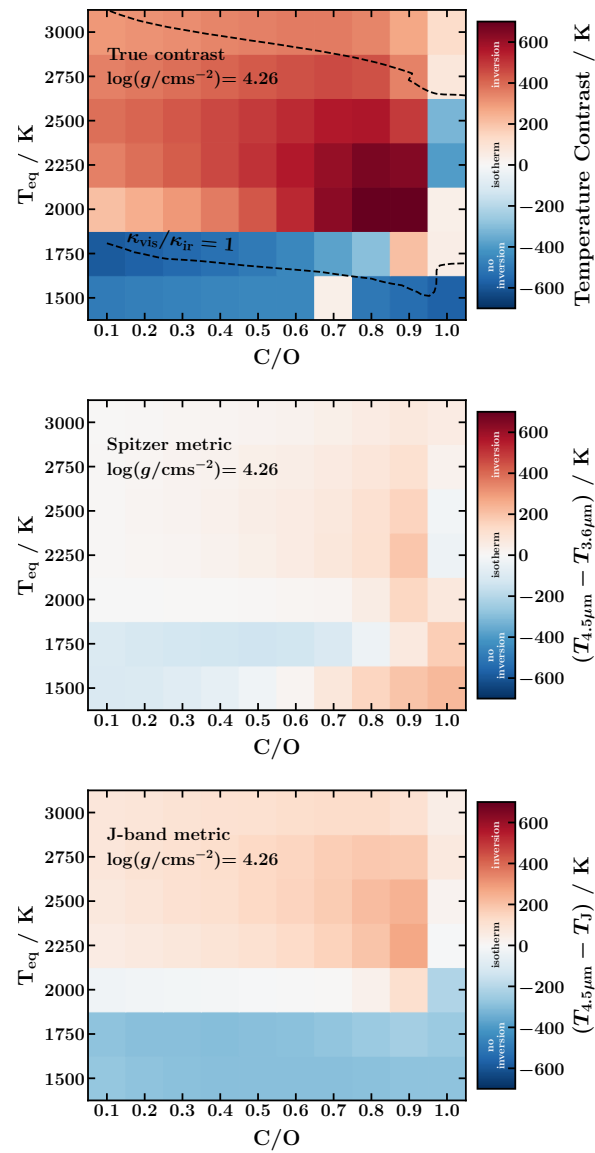


Fig. 3.10 Same as centre column of Figure 3.8 but for a planet with a higher gravity ($\log(g/\text{cm}^2)=4.26$, similar to WASP-18b, compared to $\log(g/\text{cm}^2)=2.99$ in Figure 3.8).

than the IRAC 1 band. However, since the J-band is chosen as a continuum relative to H₂O absorption, the J-band metric will not necessarily work for atmospheres that are water poor, e.g. for C/O > 1 or other compositions not considered here. We explore this phenomenon further in Section 3.5.3.

While the Spitzer and J-band metrics largely agree as to whether an inversion is present or not, there are two main exceptions to this trend. The first is at low equilibrium temperatures and high C/O, for reasons described above. The second is at $T_{\text{eq}} \sim 1750$ K where, for some C/O ratios, the J-band incorrectly infers a non-inversion. For example, this occurs with a K7V host star (Figure 3.9). Nevertheless, the two metrics agree for most T_{eq} and C/O ratios. This is consistent with the fact that our analysis is for oxygen-rich compositions where H₂O absorption dominates and the J-band and IRAC 1 band do indeed probe the continuum. Furthermore, where this agreement exists, the $T_{4.5\mu\text{m}} - T_{\text{J}}$ contrast is consistently larger than the $T_{4.5\mu\text{m}} - T_{3.6\mu\text{m}}$ contrast. This effect is visible in Figure 3.6 for a solar-like composition, and Figures 3.8, 3.9 and 3.10 confirm that it holds across the range of T_{eq} , C/O ratios, metallicities, stellar types and gravities explored here. This suggests that, as in Figure 3.6, the J-band is consistently probing deeper pressures than the IRAC 1 band. For an oxygen-rich atmosphere with a thermal inversion, one would therefore expect that $T_{\text{J}} < T_{3.6\mu\text{m}} < T_{4.5\mu\text{m}}$. Similarly, $T_{4.5\mu\text{m}} < T_{3.6\mu\text{m}} < T_{\text{J}}$ would be expected for an oxygen-rich atmosphere with no thermal inversion. In Section 3.5.3, we compare these brightness temperatures for hot Jupiters with spectral and photometric observations. By looking for outliers to this trend, we can therefore identify which planets have different chemistries or disequilibrium processes compared to those we consider in our models.

3.5.3 Comparison of data to models

While we have so far discussed photometric bands for assessing thermal inversions in oxygen-rich spectra, we now consider a more general approach by directly considering brightness temperatures probed by existing data. We do this by plotting the brightness temperatures of HST/WFC3 and Spitzer IRAC 1 and IRAC 2 observations for 7 planets (Figure 3.11). Here, we choose to use IRAC 1 and IRAC 2 brightness temperatures from Garhart et al. (2020) as they perform a uniform analysis across many Spitzer secondary eclipse observations. However, we note that Spitzer data for a given object can differ depending on the way it is analysed (e.g. Garhart et al. 2020 compared to Kreidberg et al. 2018).

As discussed in Section 3.5, oxygen-rich atmospheres are expected to have $T_{\text{J}} < T_{3.6\mu\text{m}} < T_{4.5\mu\text{m}}$ or $T_{4.5\mu\text{m}} < T_{3.6\mu\text{m}} < T_{\text{J}}$ for cases with and without a thermal inversion, respectively, and under the assumptions of our models (e.g. chemistry and prescriptions

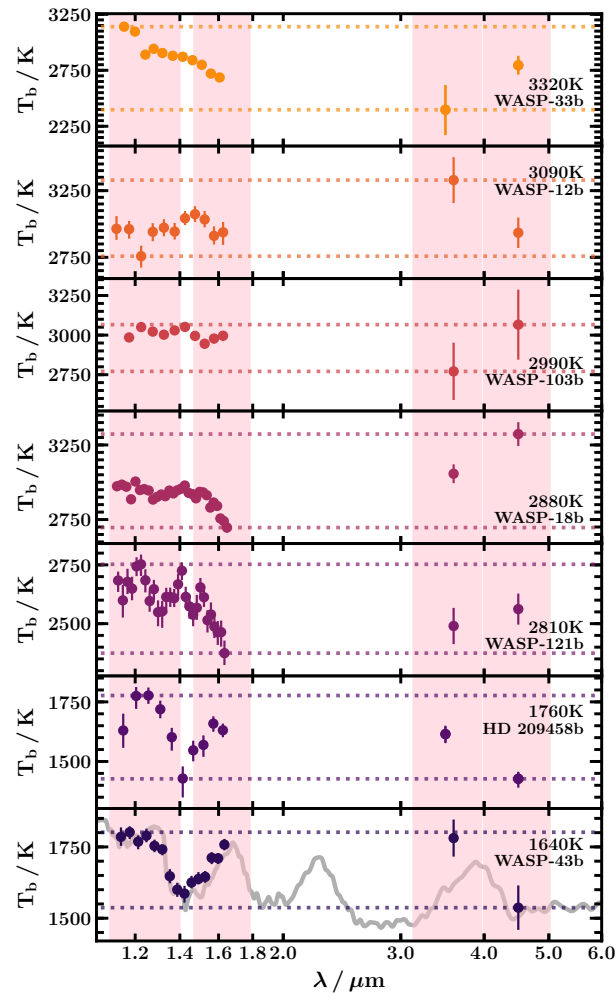


Fig. 3.11 Brightness temperatures probed by HST/WFC3 and Spitzer IRAC 1 and IRAC 2 data for seven planets, ordered by equilibrium temperature. Nominal equilibrium temperatures are calculated assuming dayside only redistribution and are labelled for each planet. The bottom panel shows the spectrum from Figure 3.6 which corresponds to a non-inverted P - T profile, for reference. Spitzer brightness temperatures for WASP-33b and HD 209458b are calculated using data from Deming et al. (2012) and Diamond-Lowe et al. (2014), respectively. Other Spitzer temperatures are from Garhart et al. (2020). HST brightness temperatures are calculated using spectra from Haynes et al. (2015) (WASP-33b) Kreidberg et al. (2014b) (WASP-43b), Evans et al. (2017) (WASP-121b), Sheppard et al. (2017) (WASP-18b), Kreidberg et al. (2018) (WASP-103b), Stevenson et al. (2014a) (WASP-12b) and Line et al. (2016) (HD 209458b). WASP-33b, WASP-18b, WASP-103b and WASP-121b are reported to have thermal inversions in the literature while WASP-12b, WASP-43b and HD 209458b have non-inverted profiles (see references above). Planetary and stellar properties used to calculate the brightness temperatures are from Collier Cameron et al. (2010); Collins et al. (2017); Gillon et al. (2014); Hellier et al. (2009); Southworth (2010, 2012); Delrez et al. (2016); Hellier et al. (2011); Gillon et al. (2012); Stassun et al. (2017).

for vertical mixing). Here, we investigate whether the planets in Figure 3.11 also exhibit this trend. To do this, we use HST/WFC3 brightness temperatures in the J-band as a proxy for J-band photometric brightness temperatures and compare these to Spitzer brightness temperatures. We also consider how this trend compares to inferences of thermal (non-)inversions from retrievals in the literature.

WASP-43b and HD 209458b are ideal cases to demonstrate the trend found in our models as they have water detections (Kreidberg et al., 2014b; Line et al., 2016), suggesting an oxygen-rich composition. Both planets have also been found not to host thermal inversions using retrieval techniques (Blecic et al., 2014; Kreidberg et al., 2014b; Stevenson et al., 2014a; Diamond-Lowe et al., 2014; Line et al., 2016). Therefore, we expect both planets to have $T_{4.5\mu\text{m}} < T_{3.6\mu\text{m}} < T_{\text{J}}$ as described above. Indeed, Figure 3.11 shows that this is the case. The HST/WFC3 brightness temperatures in the J-band are consistent with or hotter than that for IRAC 1 (within error bars), and both are higher than the IRAC 2 brightness temperature. WASP-18b shows the opposite trend, $T_{\text{J}} < T_{3.6\mu\text{m}} < T_{4.5\mu\text{m}}$, which would suggest a thermal inversion and indeed agrees with the inference of a thermal inversion by Sheppard et al. (2017). WASP-103b also has an inferred thermal inversion (Kreidberg et al., 2018). The brightness temperatures shown in Figure 3.11 are inconclusive as the errorbars on the Spitzer brightness temperatures are quite large, though note that Kreidberg et al. (2018) reduce the Spitzer data differently to Garhart et al. (2020).

In contrast, WASP-121b, WASP-12b and WASP-33b show evidence for different chemistries/disequilibrium processes to our models. WASP-121b has been inferred to host a thermal inversion (Evans et al., 2017), but has a high J-band brightness temperature relative to IRAC 1 and IRAC 2, which are consistent within the errorbars. Furthermore, for WASP-12b the J-band and IRAC 2 brightness temperatures are significantly lower than that for IRAC 1. In the case of WASP-33b, the opposite is true: the J-band and IRAC 2 brightness temperatures are both significantly higher than that for IRAC 1. Thus, all three planets show a different brightness temperature trend compared to our oxygen-rich models. This could be due to chemical species which we have not considered here (e.g. FeH, TiH), other chemical disequilibrium mechanisms, a C/O ratio greater than 1 or offsets between instruments that are not considered here. Ultimately, while photometric metrics for assessing temperature gradients provide a useful initial assessment, their dependence on chemistry and the inherent complexity of planetary atmospheres is such that atmospheric retrievals are needed to confidently assess the presence of a thermal inversion or lack thereof.

Another use for comparing brightness temperatures for observed spectra is to provide a quick and empirical lower limit on the photospheric temperature gradient in the atmosphere. The larger the contrast between the maximum and minimum measured

brightness temperatures, and the more precise they are, the stronger the constraints that can be placed on the photospheric temperature contrast. In particular, HST/WFC3 data can significantly improve the temperature contrasts determined with IRAC 1 and IRAC 2 data alone. For example, in the case of WASP-121b, the brightness temperature contrast based on the IRAC 1 and IRAC 2 measurements alone is $70 \text{ K} \pm 100 \text{ K}$, which is consistent with an isotherm. However, the range of brightness temperatures probed by the HST/WFC3 data is wider than that for the Spitzer data, and results in a temperature contrast of $380 \text{ K} \pm 70 \text{ K}$. Similarly, for WASP-33b, WASP-12b and WASP-18b, HST/WFC3 data also makes significant improvements to the brightness temperature contrast. Note that uncertainty in the host star temperature can affect the errors in these brightness temperatures. In the cases shown here, we find that the largest error contributions from the stellar temperature are comparable to those from the flux uncertainties alone (i.e. the errorbars shown in Figure 3.11) and therefore do not impact our assessment significantly. However, this effect should be treated rigorously for more detailed studies.

One of the reasons that the HST/WFC3 data help to place tighter constraints on some brightness temperature contrasts is that the signal-to-noise of the data is very good and results in tight constraints on brightness temperature. This is despite the fact that, as shown by the blackbody curves in Figure 3.6, a greater precision in flux is needed at shorter wavelengths for the same precision in brightness temperature. As a result, fairly precise spectral/photometric measurements are needed at shorter wavelengths in order to place tight constraints on brightness temperature. However, since the precision available with HST/WFC3 allows excellent brightness temperature precision (reaching $\sim 10 \text{ K}$ for some cases in Figure 3.11), this effect does not preclude shorter wavelengths from this type of analysis. When using observations from other instruments, however, it is important to consider how the uncertainties in the fluxes will correspond to uncertainty in brightness temperature, which will depend on the wavelength range of the observations.

While we have used examples with HST/WFC3 and Spitzer data here, this analysis can also be performed with other observations and at different wavelengths. It is important to note that when comparing brightness temperatures from different instruments (including the analysis above), systematic offsets between the instruments can bias the temperature contrast obtained. One way to test for and characterise such offsets is by performing an atmospheric retrieval which includes a freely-varying 'offset' parameter, which can then be retrieved from the data. Furthermore, future instruments such as the James Webb Space Telescope's (JWST's) NIRSpec will have much larger spectral ranges, allowing brightness temperatures to be measured across a wide range of wavelengths with the same instrument.

3.6 Summary and Discussion

In this chapter, we investigate the importance of TiO in the spectral appearance and temperature structures of hot Jupiter atmospheres. To this end, we first examine the importance of the accuracy of TiO line lists for determining its observable spectral signatures in transmission and emission spectra, both at low and high resolution. We further investigate the effect of TiO on the temperature structure of an atmosphere. To do this, we investigate the strength of thermal inversions as a function of C/O ratio, equilibrium temperature, metallicity, stellar type and gravity, considering TiO as the inversion-causing molecule. In addition, we assess the performance of temperature gradient metrics as a function of these parameters.

We begin by comparing the recent TOTO TiO line list (McKemmish et al., 2019) to those of Schwenke (1998) and Plez (2012) (sourced from Ryabchikova et al., 2015) (hereafter S98 and P12 line lists, respectively), focusing on the consequences for the interpretation of transmission, emission and high-resolution Doppler spectra. Interpretation of high-resolution Doppler spectra using cross-correlation methods relies on accurate line positions and sufficiently strong planetary spectral features. We assess the accuracy of line positions in the TOTO line list by considering the fraction of energy levels and transitions which are taken from experimental data. For example, at 2000 K, there are 4491 transitions with line intensities above 10^{-17} cm/molecule, of which 83% are from experimental data and have high accuracy. Furthermore, experimental data for the $\nu = 2$ and higher vibrational excitations of the B $^3\Pi$ state are needed to fill in the strong spectral bands which are currently calculated theoretically.

For both transmission and emission spectra we find that the differences between the TOTO and S98 line lists have the greatest impact on model spectra in the optical range. As a result, optical transmission spectra are strongly affected and the spectra generated with each line list can differ significantly depending on the spectral resolution (almost 1000 ppm at $R \sim 10^4$). Since thermal emission spectra of exoplanets are largely observed in the infrared spectral range, the differences between the TOTO and S98 line lists have a more subtle effect. For two model spectra generated with the same P - T profile but using each of the TiO line lists, the differences are only observable at higher resolutions (e.g. up to ~ 100 ppm at a resolution of $R \sim 10^4$ in the near-infrared).

Beyond the effects of TiO line lists, we also explore how TiO equilibrium chemistry can shape the thermal profile of an atmosphere. We investigate the equilibrium abundances of chemical species (calculated using the HSC CHEMISTRY software package) as a function of equilibrium temperature, T_{eq} , C/O ratio, metallicity, stellar host type and planetary surface

gravity. In turn, this allows an exploration of thermal inversions in this parameter space. Through semi-analytic considerations of radiative equilibrium, we find that thermal inversions can occur at the coolest equilibrium temperature for a C/O ratio of ~ 0.9 , consistent with previous studies (e.g. Mollière et al., 2015; Gandhi and Madhusudhan, 2019).

We further calculate self-consistent 1D model atmospheres and their spectra for a range of C/O ratios T_{eq} , metallicities, stellar types and gravities. We include the effects of vertical mixing, as well as the variation of the energy redistribution factor as a function of T_{eq} . These models confirm the trend found by our simple analysis by which thermal inversions happen at cooler T_{eq} at $C/O \approx 0.9$. Furthermore, the transition from non-inverted to inverted P - T profiles happens at the expected temperature range of ~ 1750 - 2000 K for models with solar-like composition, where TiO is known to condense. We also find that for higher-metallicity models, a higher equilibrium temperature is needed to cause a thermal inversion. Conversely, a later stellar type can result in thermal inversions occurring at cooler T_{eq} . We find that gravity has a smaller effect on thermal inversion strength compared to other parameters.

In order to characterise the strength of the inversions/non-inversions in our models, we assess a range of metrics based on the contrast in brightness temperature between two photometric bands. Although the brightness temperature contrast between Spitzer's IRAC 1 and IRAC 2 channels is commonly used as an indication of inversion strength (e.g. Burrows et al., 2007; Knutson et al., 2010; Madhusudhan and Seager, 2010), we find that in the case of H_2O -dominated spectra a stronger temperature contrast can be observed by comparing the IRAC 2 channel to the H-band or J-band. Furthermore, we find that for high C/O ratios and low equilibrium temperatures, the IRAC 1 band contains significant opacity from CH_4 and HCN and, as such, does not provide a good measure of the spectral continuum. In this regime, an atmosphere without a thermal inversion can have a larger IRAC 2 flux compared to the IRAC 1 flux, mimicking the signature of a thermal inversion for lower C/O ratios. Similarly, the J-band incorrectly infers a non-inversion at some C/O ratios for $T_{\text{eq}} \sim 1750$ K, for example with a later stellar host type. Therefore, neither metric works optimally across the whole parameter space considered. We investigate this for observed spectra by finding the brightness temperature contrasts between the WFC3 and Spitzer IRAC 1 and IRAC 2 bands for various planets. While our oxygen-rich models show the trend that the J-band is a clearer continuum band than the IRAC 1 band, several of these planets do not follow the same pattern. This is likely due to differences in chemistry and/or disequilibrium effects not considered in our models. Overall, we suggest that continuum opacity bands depend on the atmospheric chemistry and that

temperature gradient metrics should therefore be used with caution as a single metric does not necessarily apply to all atmospheric chemistries.

Thermal inversions and the role of TiO in producing them remains a key part in understanding hot Jupiter atmospheres and the processes which shape them. As exoplanetary atmospheric observations continue to improve, it will be necessary to use the highest-quality chemical cross-sections and understand the role of the many parameters which dictate the structure of an atmosphere in order to demystify these exotic worlds.

4

Cloud Scattering and Thermal Emission across the Hot Jupiter Regime

In this chapter we continue to explore the atmospheres of hot Jupiters, focusing in particular on their emission spectra and potential cloud scattering properties.¹ Optical photometric observations of hot Jupiter atmospheres can place important constraints on their scattering properties. In particular, recent TESS and HST secondary eclipse observations in the optical have the potential to provide important constraints on the presence of clouds in hot Jupiter atmospheres. In this chapter, we investigate the optical to near-infrared spectra of three hot Jupiters spanning a range of temperatures and gravities: KELT-1 b, WASP-18 b and WASP-43 b. We fit multi-band photometric observations of planet-star flux contrasts of these objects with model spectra using a self-consistent 1D atmospheric model. In all three cases, we find that the spectra can be explained by thermal emission alone, without the need for optical scattering from clouds.

4.1 Introduction

Clouds and hazes are important tracers of physical processes in exoplanet atmospheres, and can affect the energy budget of an atmosphere by scattering incident irradiation (e.g. Helling, 2019). In particular, the observational accessibility of hot Jupiter atmospheres makes these exoplanets excellent testing grounds for theories of cloud and haze processes. For example, as discussed in Chapter 1, transmission spectroscopy, secondary eclipse and phase curve observations of hot Jupiter atmospheres have revealed a range of cloud and

¹Parts of this work corresponding to KELT-1 b have been published in von Essen et al. (2021).

haze properties in a number of hot Jupiters (e.g. Demory et al., 2013; Evans et al., 2013; Parmentier et al., 2016; Sing et al., 2016; Gao et al., 2020).

In particular, optical phase curves and secondary eclipse photometry have commonly been used to place constraints on the scattering properties of these objects. Such observations of some hot Jupiters using Kepler photometry have suggested relatively high geometric albedos in the optical, which could be indicative of cloud scattering on their daysides (e.g. Demory et al., 2011b, 2013; Shporer et al., 2014). However, of the hot Jupiters with optical albedo estimates, the majority have been found to have fairly low optical albedos (e.g. Rowe et al., 2006, 2008; Angerhausen et al., 2015; Esteves et al., 2015; Bell et al., 2017; Hooton et al., 2018; Močnik et al., 2018; Shporer et al., 2019; Mallonn et al., 2019; Kane et al., 2020; Wong et al., 2020b). High-precision optical photometry with current facilities such as TESS (Ricker et al., 2015) and HST’s WFC3/UVIS instrument (Wakeford et al., 2020; Fraine et al., 2021) have the potential to provide important constraints on the albedos of hot Jupiters. TESS and the WFC3/UVIS F350LP filter operate in the $\sim 0.6\text{--}1\ \mu\text{m}$ and $\sim 0.35\text{--}0.82\ \mu\text{m}$ ranges, respectively, and are ideally suited to search for reflected light from exoplanet atmospheres (e.g. Shporer et al., 2019; Beatty et al., 2020; Fraine et al., 2021; von Essen et al., 2021). In particular, the growing population of exoplanets with TESS data is allowing comprehensive studies of atmospheric albedos across a range of exoplanets (e.g. Wong et al., 2020b).

While optical flux measurements can provide constraints on the scattering properties of an atmosphere, such inferences are also degenerate with the thermal emission of the hot Jupiter itself (e.g. Christiansen et al., 2010; Cowan and Agol, 2011; Demory et al., 2011a; Schwartz and Cowan, 2015). Infrared flux measurements can help to break this degeneracy by constraining the thermal and chemical properties of the dayside atmosphere, thereby distinguishing the thermal and reflected components of the measured optical flux (e.g. Demory et al., 2011b; Keating and Cowan, 2017; Wong et al., 2020a,b). In this chapter, we use self-consistent atmospheric models to interpret the optical to near-infrared spectra, including recent TESS and/or WFC3/UVIS secondary eclipse observations, of KELT-1 b, WASP-18 b and WASP-43 b. The bulk properties of these three objects are listed in Table 4.1.

KELT-1 b is a highly-irradiated brown dwarf with a mass of $\sim 27 M_J$, radius of $\sim 1.1 R_J$ and irradiation temperature of $\sim 2900\ \text{K}$ (Siverd et al., 2012). Existing Spitzer and ground-based observations have indicated a non-inverted temperature profile as well as day- and nightside temperatures of $2988\pm 60/2902\pm 74\ \text{K}$ and $1173_{-130}^{+175}\ \text{K}/1053_{-161}^{+230}\ \text{K}$, respectively, for the Spitzer $3.6\ \mu\text{m}$ and $4.5\ \mu\text{m}$ channels (Beatty et al., 2017a, 2019). This target therefore serves as an excellent probe for the high-temperature extreme of the highly-irradiated

Table 4.1 Planetary properties for KELT-1 b, WASP-18 b and WASP-43 b.

Planet	KELT-1 b¹	WASP-18 b²	WASP-43 b³
M_p/M_J	27.2	10.4	1.8
R_p/R_J	1.11	1.17	0.93
$\log(g/\text{cgs})$	4.7	4.3	3.7
T_{irr}/K	2880	2860	1640

References: 1. Siverd et al. (2012), 2. Southworth et al. (2009), 3. Hellier et al. (2011).

giant planet/brown dwarf regime. Recent work by Beatty et al. (2020) has also interpreted TESS secondary eclipse photometry of KELT-1 b, considering both clear and cloudy models for the dayside. They find that a cloudy model is better able to fit the TESS data, and we compare our models to theirs in Section 4.3.

WASP-18 b and WASP-43 b are hot Jupiters probing different temperature regimes. With an irradiation temperature of ~ 2900 K (Southworth et al., 2009), WASP-18 b serves as an excellent case study of a highly-irradiated hot Jupiter. In contrast to KELT-1 b, existing HST and Spitzer secondary eclipse data suggest that the atmosphere of WASP-18 b hosts a thermal inversion (Sheppard et al., 2017). It has also been suggested that H^- opacity may be contributing to the emission spectrum of WASP-18 b as a result of the photodissociation of H_2O (Arcangeli et al., 2018). However, Gandhi et al. (2020b) do not find evidence for H^- when performing a retrieval on existing HST and Spitzer data. Lying at the opposite end of the hot Jupiter temperature range, WASP-43 b has an irradiation temperature of ~ 1600 K (Hellier et al., 2011). Secondary eclipse observations with HST and Spitzer have revealed a non-inverted temperature profile for the dayside as well as a detection of H_2O (Blecic et al., 2014; Kreidberg et al., 2014b; Stevenson et al., 2017). WASP-43 b therefore represents an excellent target to contrast with KELT-1 b and WASP-18 b.

In what follows, we begin by describing the atmospheric model used in Section 4.2. We then interpret dayside and nightside emission observations of KELT-1 b in Section 4.3, and dayside secondary eclipse observations of WASP-43 b and WASP-18 b in Section 4.4. We summarise and discuss our results in Section 4.5.

4.2 Atmospheric Model

In this chapter, we self-consistently model the atmospheres of hot Jupiters across the ~ 1500 - 3000 K temperature range. To do this, we use the adaptation of the GENESIS self-consistent atmospheric model (Gandhi and Madhusudhan, 2017) used in Chapter 3. In particular, equilibrium chemical abundances are calculated using the HSC CHEMISTRY

(version 8) software package, though for simplicity we do not include the effects of vertical mixing here. Notably, HSC CHEMISTRY includes effects due to thermal dissociation and ionisation, which are relevant in the highly-irradiated daysides of KELT-1 b and WASP-18 b.

While the equilibrium chemistry calculation includes > 150 molecular, atomic, and ionic species, the species which typically dominate irradiated giant planet atmospheres are H₂O, CH₄, CO, CO₂, NH₃, HCN, C₂H₂, Na, K, TiO, VO, and H⁻, besides H₂ and He (e.g. Burrows and Sharp, 1999; Moses et al., 2013b; Madhusudhan et al., 2016; Arcangeli et al., 2018). We therefore include opacity due to these species in our atmospheric models, using cross-sections calculated as in Gandhi and Madhusudhan (2017) and Gandhi et al. (2020a) as well as line transition data from a variety of sources (see also Chapter 3), which include the HITEMP, HITRAN, and ExoMol databases (H₂O, CO and CO₂: Rothman et al. 2010, CH₄: Yurchenko et al. 2013; Yurchenko and Tennyson 2014, C₂H₂: Rothman et al. 2013; Gordon et al. 2017, NH₃: Yurchenko et al. 2011, HCN: Harris et al. 2006; Barber et al. 2014, TiO: McKemmish et al. 2019, VO: McKemmish et al. 2016, H₂-H₂ and H₂-He Collision-Induced Absorption: Richard et al. 2012). The Na and K opacities are calculated as in Burrows and Volobuyev (2003) and Gandhi and Madhusudhan (2017), while the H⁻ bound-free and free-free cross sections are calculated using the prescriptions of Bell and Berrington (1987) and John (1988) (see also Arcangeli et al. 2018; Parmentier et al. 2018; Gandhi et al. 2020a).

We use this self-consistent model to explore the contribution of thermal emission vs scattering that is required to explain the observed optical and infrared fluxes of KELT-1 b, WASP-18 b and WASP-43 b. In what follows, we explore models with different internal temperatures (T_{int}), metallicities and C/O ratios. We note that the degeneracy between the presence of clouds and the deep-atmosphere temperature profile has previously been explored in the context of non-irradiated brown dwarfs by Tremblin et al. (2015), who find that a reduced temperature gradient in the deep atmosphere can reproduce observed T-dwarf spectra without the need for clouds, as both effects mute the observed flux at bluer wavelengths. Here, we focus on strongly-irradiated objects for which a key indicator of clouds is optical scattering of incident irradiation, which is not the case for non-irradiated objects. In this highly-irradiated scenario, infrared data can help to constrain the atmospheric temperature profile and establish the contribution of thermal emission vs scattering required to explain the observed optical flux.

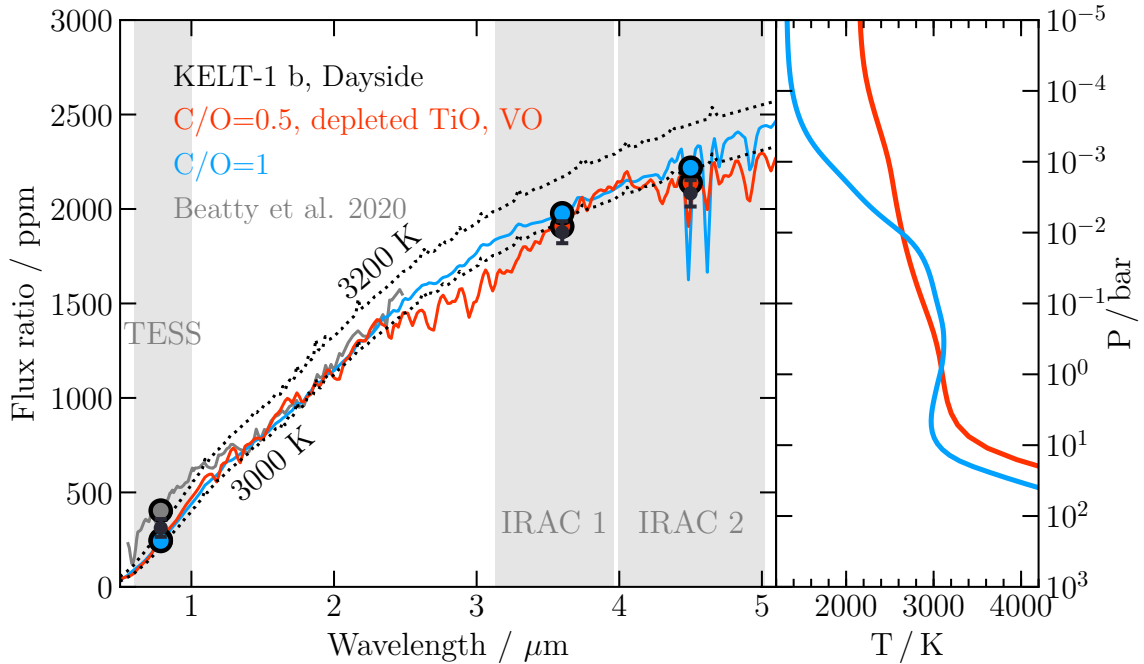


Fig. 4.1 Model dayside spectra (left) and pressure-temperature (P - T) profiles (right), assuming solar metallicity and an internal temperature of 1500 K. The red spectrum and P - T profile correspond to a $C/O=0.5$ and depleted TiO / VO (e.g. due to gravitational settling), while the blue model corresponds to a $C/O=1$. The black dashed lines correspond to blackbody spectra at 3000 and 3200 K. The cloudy, $T_{int}=1000$ K model from Beatty et al. (2020) is shown in grey for reference. Flux is shown in SI units ($Wsr^{-1}m^{-3}$). Data are shown by black points and error bars. Coloured circles show the binned model spectra. Vertical gray bands show the TESS and Spitzer bandpasses.

4.3 Modelling the Dayside and Nightside Emission of KELT-1 b

In this section, we self-consistently model the day- and nightside spectra of KELT-1 b and compare our models to secondary eclipse and phase curve observations from TESS and Spitzer. The Spitzer dayside and nightside fluxes used here are from Beatty et al. (2019). The TESS secondary eclipse data are described in von Essen et al. (2021) and included considerations of the primary and secondary eclipses, the phase curve, ellipsoidal variations, Doppler beaming and stellar activity. The secondary eclipse depth was found to be 304 ± 75 ppm, consistent with an independent analysis of the TESS data by Beatty et al. (2020), who derive a secondary eclipse depth of 371^{+47}_{-49} ppm.

In our self-consistent models, we consider a scenario with no energy redistribution, i.e. instant re-radiation corresponding to $f = -1/3$ in equation 1.10 (e.g., Burrows et al., 2008a). Given the extreme irradiation received by KELT-1 b, a low day-night energy redistribution efficiency is expected (Cowan and Agol, 2011). Therefore, we choose to explore models in the limit of no day-night energy redistribution for simplicity. We note, however, that recent studies find that H_2 dissociation and recombination may increase heat transport in highly-irradiated atmospheres (Bell and Cowan, 2018; Tan and Komacek, 2019; Mansfield et al., 2020). We also account for the internal heat flux emanating from KELT-1b, which is characterized by T_{int} . While the dayside temperature structure and spectrum are dominated by the irradiation, the nightside is dominated by the internal flux and energy advected from the dayside.

We are able to fit the dayside data using irradiated models with no redistribution (Figure 4.1). At the temperatures present in the dayside atmosphere, CO is expected to be a significant opacity source in the IRAC 2 band (Burrows and Sharp, 1999; Madhusudhan et al., 2016). However, since the brightness temperature in the IRAC 2 band is comparable to the IRAC 1 band and lower than the TESS band, this suggests the absence of a thermal inversion in the infrared photosphere, which is consistent with the findings of previous studies on KELT-1 b (Beatty et al., 2017a). A thermal inversion would instead cause a strong CO emission feature in the IRAC 2 band, which is not seen. In turn, a non-inverted temperature profile corresponds to a low optical/infrared opacity ratio (e.g., Hubeny et al., 2003; Guillot, 2010), for example, due to a depletion of optical absorbers such as TiO and VO. Such a depletion may be caused by the gravitational settling of TiO and VO due to their high mean-molecular weight (Spiegel et al., 2009) or increased efficiency of cold trap processes (Parmentier et al., 2013; Beatty et al., 2017a). We find that a model with solar metallicity and $C/O=0.5$ provides a good fit to the data if the abundances of TiO and VO are just 5% of those predicted under thermochemical equilibrium (within 1.4σ , 0.5σ , 0.8σ of the TESS, IRAC 1, and IRAC 2 points, respectively, see red spectrum in Figure 4.1). The continuum of the model spectrum is close to a blackbody spectrum at ~ 3000 K, with the decreasing temperature gradient resulting in a slight CO absorption feature in the IRAC 2 band.

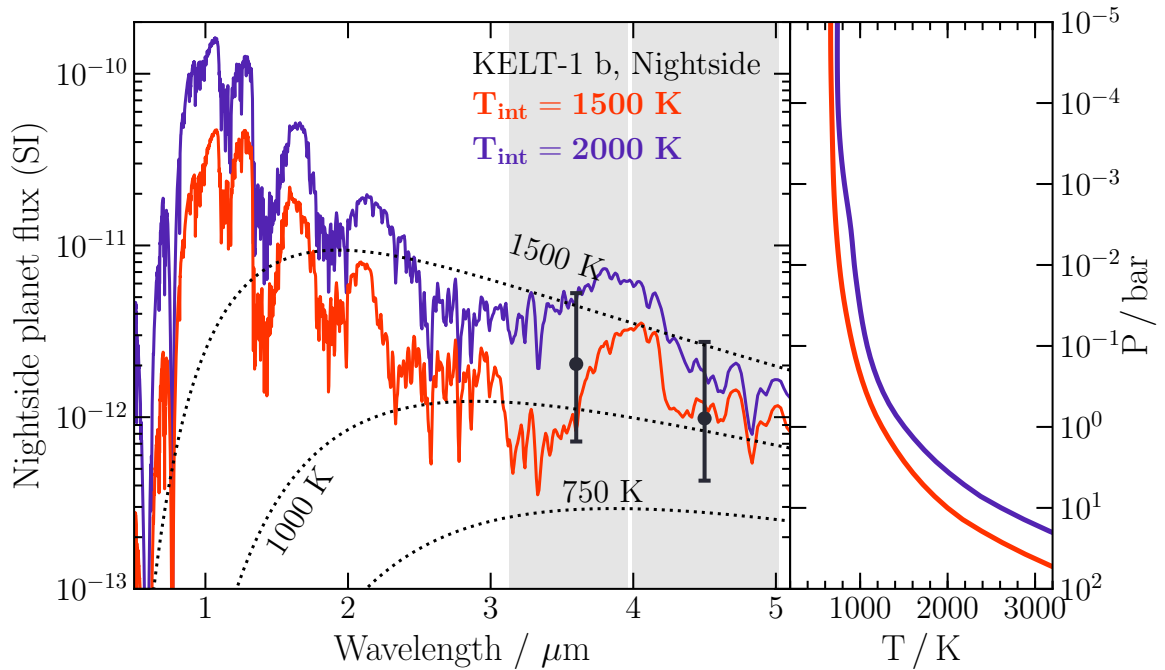


Fig. 4.2 Model nightside spectra (left) and pressure-temperature profiles (right) for KELT-1 b assuming internal temperatures of 1500 K (red lines) and 2000 K (purple lines). Dashed black lines correspond to blackbody spectra at 750, 1000 and 1500 K. Flux is shown in SI units ($\text{Wsr}^{-1}\text{m}^{-3}$). Data are shown by black points and error bars. Coloured circles show the binned model spectra. Vertical gray bands show the Spitzer IRAC 1 and IRAC 2 bandpasses.

An alternative scenario that involves depleted TiO and VO is that featuring a high C/O ratio (Madhusudhan et al., 2011a). We find that a model with solar metallicity in all elements except carbon and $\text{C/O}=1$ is able to fit the TESS, IRAC 1, and IRAC 2 data within 1.5σ , 1.7σ , and 1.9σ , respectively (blue spectrum in Figure 4.1). The photosphere in the $\sim 0.6\text{-}5\ \mu\text{m}$ range lies between $\sim 0.1\text{-}10$ bar, where the temperature profile is relatively isothermal. As a result, the emergent thermal emission spectrum is also close to a blackbody at ~ 3000 K. In this model, the atmospheric chemistry is still dominated by CO, which results in some absorption in the IRAC 2 band. We note that given the deep photosphere in KELT-1 b, thermal dissociation is less prevalent in the photosphere compared to lower-gravity hot Jupiters with shallower photospheres. We also note that, given the strong stellar irradiation, the dayside spectrum of KELT-1 b is not sensitive to internal temperatures below $\gtrsim 2000$ K. As a result, T_{int} is constrained only by the nightside data and we assume a value of $T_{\text{int}}=1500$ K for the dayside, consistent with the nightside data as discussed below. Note that if KELT-1 b were not irradiated, it would be expected to

have $T_{\text{int}} \sim 850$ K (Saumon and Marley, 2008; Beatty et al., 2019), and an even higher T_{int} may be consistent with its inflated radius (Siverd et al., 2012); see Section 4.5 for further discussion.

The dayside data can be explained by thermal emission alone, without the need for a high albedo, although the latter cannot be ruled out with current data. Figure 4.1 also shows the $T_{\text{int}}=1000$ K cloudy model from Beatty et al. (2020) (from their Figure 6) for reference. Our clear model is able to fit the TESS point slightly better than the Beatty et al. (2020) cloudy model, while the fit to the Spitzer data cannot be compared as their model is truncated at $2.5 \mu\text{m}$. Since the current data do not rule out a cloud-free atmosphere, further observations are needed to constrain whether clouds are present on the dayside of KELT-1 b. Indeed, a plausible solution may be a partially cloudy atmosphere, with contributions from both clear and cloudy regions. Future spectroscopic secondary eclipse or phase curve observations may provide more confident constraints on the presence of clouds in KELT-1 b's dayside.

We find that the Spitzer nightside brightness temperatures are consistent with a blackbody in the range ~ 1000 - 1500 K (within 1σ). Within the limit of no day-night redistribution, the data can be explained by non-irradiated self-consistent models with T_{int} in the range ~ 1500 - 2000 K (Figure 4.2). This places an upper limit of ~ 2000 K on T_{int} , as a smaller internal flux is permitted by the data if additional flux is advected from the dayside to the nightside. In the models shown in Figure 4.2, the absorption features in the $3.6 \mu\text{m}$ and $4.5 \mu\text{m}$ bands are due to CH_4 and CO , respectively. We assume a C/O ratio of 0.5, consistent with the dayside model shown in red in Figure 4.1. However, we note that the nightside data are not able to constrain chemical abundances and a range of C/O ratios and metallicities are consistent with the nightside observations. Furthermore, we note that since these models do not include energy advected from the dayside, solutions with lower T_{int} and greater day-night energy redistribution are also possible.

4.4 Modelling the Dayside Atmospheres of WASP-43 b and WASP-18 b

WASP-43 b and WASP-18 b represent opposite ends in temperature across the hot and ultra-hot Jupiter regimes. Therefore, they are good case studies for the comparative study of hot Jupiter atmospheres, including the presence of clouds and hazes. In this section, we model their dayside atmospheres in order to fit observed TESS, WFC3/UVIS and Spitzer secondary eclipse depths. The Spitzer data we use here are from Blečić et al. (2014) (for WASP-43 b) and Shepard et al. (2017) (for WASP-18 b). In the optical, we use the TESS

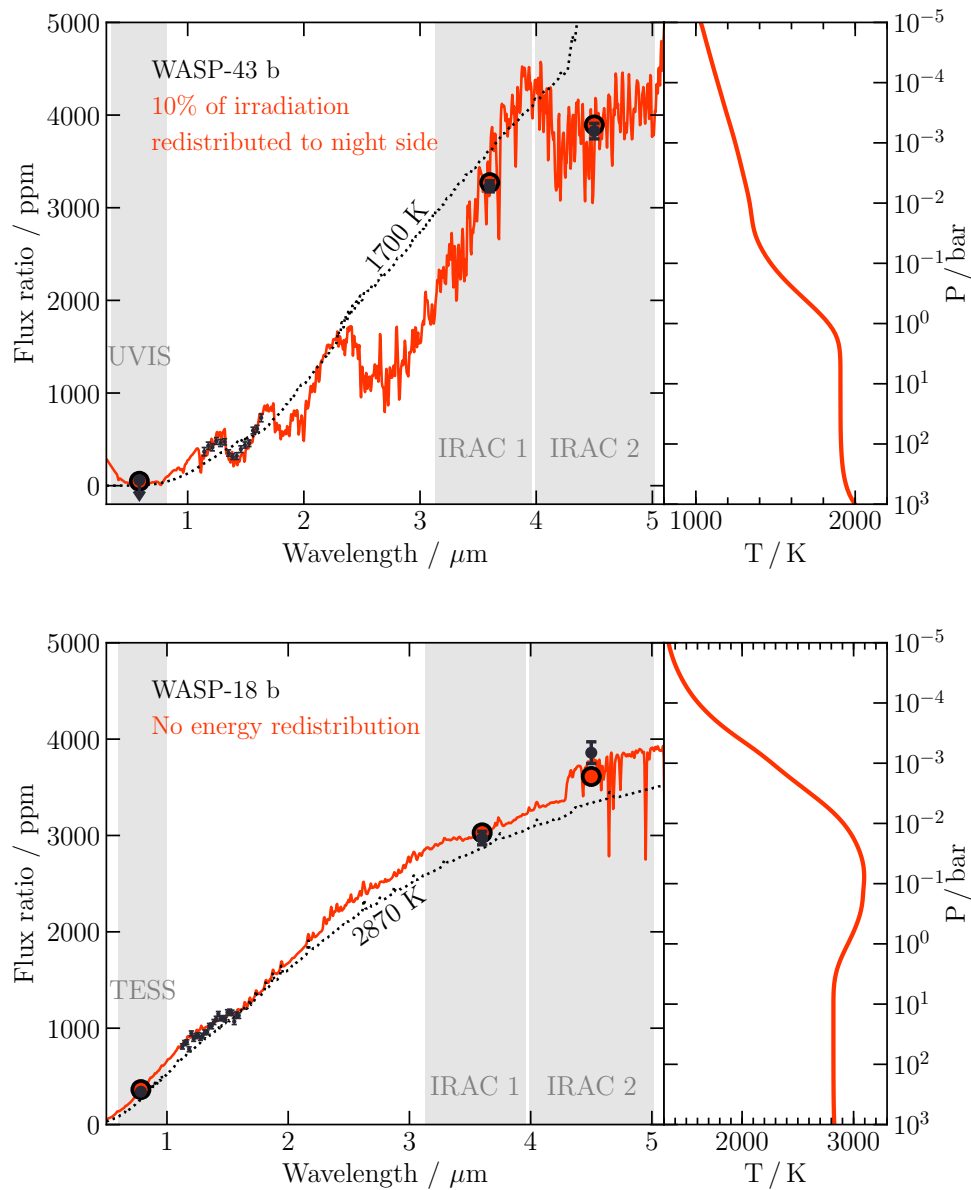


Fig. 4.3 Self-consistent temperature profiles and thermal emission spectra for the dayside atmospheres of WASP-43 b (top panel) and WASP-18 b (bottom panel). TESS, WFC3/UVIS and Spitzer observations (upper limits) are shown as black points and error bars (arrows), while the red circles show the binned model points. The Spitzer data for WASP-43 b and WASP-18 b are from Blečić et al. (2014) and Sheppard et al. (2017), respectively. The UVIS data for WASP-43 b is from Fraine et al. (2021), and the TESS data for WASP-18 b is from Shporer et al. (2019). Small black points and error bars show *HST*/WFC3 data for WASP-43 b (Kreidberg et al., 2014b) and WASP-18 b (Sheppard et al., 2017). The dashed black lines show blackbody spectra corresponding to the irradiation temperature, T_{irr} , for each planet (Equation 1.7).

secondary eclipse depth obtained by Shporer et al. (2019) for WASP-18 b, and the 3σ upper limit on the WFC3/UVIS eclipse depth obtained by Fraine et al. (2021) for WASP-43 b with the F350LP filter. The Spitzer, TESS and WFC3/UVIS secondary eclipse depths are shown in Figure 4.3.

We explore physically plausible models for WASP-43 b and WASP-18 b in order to explain their observed TESS and WFC3/UVIS occultation depths in the optical as well as their Spitzer IRAC dayside fluxes. Given the relatively high irradiation levels of both WASP-43 b and WASP-18 b, internal heat is not expected to noticeably affect the observable atmosphere. In our models, we therefore set the internal temperature to a nominal value of 100 K, similar to the internal temperature of Jupiter. The remaining free parameters which we vary are the C/O ratio, metallicity and the efficiency of day-night energy redistribution.

For WASP-43 b, we find that an atmospheric model with solar metallicity and C/O = 0.5 is able to fit the observed UVIS and Spitzer data if 10% of the energy incident on the dayside is transported to the nightside, i.e. $f = 0.1$ in Equation 1.10 (top panel of Figure 4.3). This is consistent with the inference of inefficient day-night energy redistribution by Gillon et al. (2012). This model fits the Spitzer data within the $\sim 1\sigma$ uncertainties, while models with more efficient day-night energy redistribution result in IRAC 1 and IRAC 2 brightness temperatures which are colder than what is observed.

This atmospheric model for WASP-43 b is dominated by H₂O and CO opacity, as expected for H₂-rich atmospheres at such temperatures (Burrows and Sharp, 1999; Madhusudhan et al., 2016). The IRAC 1 and IRAC 2 bands probe H₂O and CO absorption features, respectively. Meanwhile, the WFC3/UVIS band probes the spectral continuum and therefore corresponds to a higher brightness temperature relative to the Spitzer data. The model also agrees well with occultation data from the Hubble Space Telescope's Wide-Field Camera 3 (*HST*/WFC3; Kreidberg et al. 2014b), as shown in Figure 4.3. We further note that the UVIS upper limit is consistent with pure thermal emission, without the need for reflected light. This is consistent with the results of Fraine et al. (2021), who compare the WFC3/UVIS data to global circulation and cloud models.

In the case of WASP-18 b, we find that an atmospheric model with solar metallicity and C/O = 1 is able to fit the observed TESS and Spitzer data if there is no day-night energy redistribution and no energy redistribution on the dayside of the planet (i.e. instant re-radiation, as considered for KELT-1 b). The model is shown in the bottom panel of Figure 4.3 and is able to fit the TESS and Spitzer observations within the $\sim 2\sigma$ uncertainties.

This atmospheric model for WASP-18 b is also consistent with the findings of Sheppard et al. (2017), who infer a high C/O ratio based on occultation data from Spitzer and *HST*/WFC3. We further find that their *HST*/WFC3 data are in good agreement with our

self-consistent model (Figure 4.3). We note that the photometric TESS and Spitzer data are not significantly sensitive to the model C/O ratio, while the lack of H₂O absorption in the *HST*/WFC3 data is better fit by a higher C/O ratio. Consistent with Sheppard et al. (2017), Arcangeli et al. (2018) and Gandhi et al. (2020b), we find that a thermal inversion is required to explain the Spitzer data for WASP-18 b. In particular, the IRAC 2 data probes a CO emission feature and therefore has a higher brightness temperature than the TESS and IRAC 1 observations. Furthermore, we find that with this model, the TESS observation is readily explained by thermal emission alone, without the need for reflected light. This is consistent with the low albedo measurement of Shporer et al. (2019) for WASP-18 b using the TESS secondary eclipse.

4.5 Summary and Conclusions

We find that, despite the wide range of dayside temperatures and gravities probed by KELT-1 b, WASP-18 b and WASP-43 b, the dayside fluxes of these exoplanets can all be explained by thermal emission alone without the need for a high albedo due to clouds or hazes. Furthermore, in the cases of KELT-1 b and WASP-18 b, the high infrared fluxes observed can only be explained by assuming very inefficient energy redistribution; the presence of any optical scattering due to clouds/hazes would cool the dayside atmosphere and therefore be inconsistent with the infrared observations.

For KELT-1 b, WASP-18 b and WASP-43 b, we find that inefficient energy redistribution is required to explain the data, though more so for KELT-1 b and WASP-18 b. In particular, we find that 10% day-night energy redistribution can explain the observations of WASP-43 b, and no energy redistribution on the dayside (i.e. instant re-radiation) can explain the KELT-1 b and WASP-18 b observations. This is consistent with the observed trend of lower energy redistribution efficiencies for highly-irradiated hot Jupiters (Cowan and Agol, 2011). Consistent with previous works (Stevenson et al., 2014a; Sheppard et al., 2017), we find that non-inverted temperature profiles are required to explain the thermal emission spectra of KELT-1 b and WASP-43 b (Kreidberg et al., 2014b; Beatty et al., 2017a; Stevenson et al., 2017; Gandhi and Madhusudhan, 2018), while a thermal inversion is required for WASP-18 b (Sheppard et al., 2017; Arcangeli et al., 2018).

For KELT-1 b, the Spitzer nightside brightness temperatures place an upper limit of ~ 2000 K on the internal temperature of KELT-1 b. In the limit of no day-night redistribution, the nightside data can be explained using an atmospheric model with an internal temperature of ~ 1500 - 2000 K, somewhat higher than the ~ 850 K internal temperature expected for the brown dwarf (e.g. Saumon and Marley, 2008; Beatty et al., 2019) if it were

unaffected by the stellar irradiation and if the age of the host star (~ 2 Gyr, Siverd et al. 2012) is accurate. However, we note that some of the nightside flux which is being attributed to internal flux could potentially be contributed by day-night energy redistribution, which is not included explicitly in the nightside model. Alternatively, a high internal temperature could be linked to the inflated radius of KELT-1 b, which is larger than the radius expected for a field brown dwarf of the same mass (i.e. $\sim 1.1 R_J$ compared to $< 1 R_J$, Burrows et al. 1997; Baraffe et al. 2003; Siverd et al. 2012). An increased interior entropy, e.g. due to delayed cooling as a result of strong irradiation, could explain both the inflated radius and a higher internal temperature.

As the population of hot Jupiters with TESS and HST observations continues to grow, so too does our understanding of their atmospheric albedos. Furthermore, complementary infrared observations are essential in order to model and characterise these atmospheres in more detail. While optical occultation depths provide a measure of planetary geometric albedos, infrared spectra allow such albedos to be put into context, e.g. with atmospheric compositions and thermal profiles. Future, more precise observations of optical scattering and thermal emission from hot Jupiters could enable population-level studies with joint constraints on the temperature structures, compositions, and sources of scattering in their atmospheres.

5

Temperature Profiles and Emission Spectra of Mini-Neptune Atmospheres

Having focused on giant planets and sub-stellar objects in the previous chapters, we now transition to exploring lower-mass exoplanets, beginning with mini-Neptunes.¹ Atmospheric observations of mini-Neptunes orbiting M-dwarfs are beginning to provide constraints on their chemical and thermal properties, while also providing clues about their interiors and potential surfaces. With their relatively large scale heights and large planet-star contrasts, mini-Neptunes are currently ideal targets towards the goal of characterising temperate low-mass exoplanets. Understanding the thermal structures and spectral appearances of mini-Neptunes is important to understand various aspects of their atmospheres, including radiative/convective energy transport, boundary conditions for the interior, and their potential habitability. In the present study, we explore these aspects of mini-Neptunes using self-consistent models of their atmospheres. We begin by exploring the effects of irradiation, internal flux, metallicity, clouds and hazes on the atmospheric temperature profiles and thermal emission spectra of temperate mini-Neptunes. In particular, we investigate the impact of these properties on the radiative-convective boundary and the thermodynamic conditions in the lower atmosphere, which serves as the interface with the interior and/or a potential surface. Building on recent suggestions of habitability of the mini-Neptune K2-18 b, we find a range of physically-motivated atmospheric conditions that allow for liquid water under the H₂-rich atmospheres of such planets. We find that observations of thermal emission with JWST/MIRI spectrophotometry can place useful constraints on the habitability of temperate mini-Neptunes

¹This work has been published in Piette and Madhusudhan (2020b).

such as K2-18 b, and provide more detailed constraints on the chemical and thermal properties of warmer planets such as GJ 3470 b. Our results underpin the potential of temperate mini-Neptunes such as K2-18 b as promising candidates in the search for habitable exoplanets.

5.1 Introduction

Mini-Neptunes arguably represent optimal targets for atmospheric studies of temperate planets with potentially ‘habitable’ surfaces. By ‘habitable’ we mean thermodynamic conditions at which liquid water is possible on a planetary surface (e.g., Kasting et al., 1993; Meadows and Barnes, 2018) and at which life is known to survive on Earth, including extremophiles, i.e., at temperatures $\lesssim 400$ K and pressures $\lesssim 1250$ bar (e.g. Rothschild and Mancinelli 2001; Merino et al. 2019, see also Section 1.4.5). On the one hand, temperate rocky planets in the habitable-zone can host surfaces conducive to life (e.g. Yang et al., 2013; Koll and Abbot, 2016; Wolf et al., 2017; Lincowski et al., 2018; Meadows and Barnes, 2018) but their small radii and large atmospheric mean molecular weights make observations challenging (Barstow and Irwin, 2016; de Wit et al., 2018; Lustig-Yaeger et al., 2019). On the other hand, larger Neptune-size ice giants with H₂-rich atmospheres are ideal for atmospheric characterisation (e.g. Fraine et al., 2014; Wakeford et al., 2017) but the high pressures and temperatures in their deep atmospheres preclude habitable conditions. Temperate mini-Neptunes with the right mass and radius offer the potential for habitable conditions below the atmosphere (Madhusudhan et al., 2020), while their hydrogen-dominated atmospheres make them conducive for spectroscopic observations, similarly to ice giants (e.g., Kreidberg et al., 2014a; Chen et al., 2017a; Tsiaras et al., 2019; Benneke et al., 2019a; Benneke et al., 2019b).

Several studies have investigated the effects of various parameters on physical processes in H₂-rich atmospheres. For example, varying T_{int} changes the location of the radiative-convective boundary and the temperature structure in the lower atmosphere, with implications for chemical mixing and atmospheric circulation (Morley et al., 2017a; Carone et al., 2020; Thorngren et al., 2019). While atmospheric mixing through eddy diffusion in the radiative zone can homogenise the observable atmosphere (e.g. $P \lesssim 1$ bar; Moses et al. 2011), convection makes it more efficient to mix material from the deep atmosphere. Similarly, clouds and hazes with strong optical scattering can cool the atmosphere as they reflect incident stellar irradiation (e.g. Morley et al., 2015), which in turn can affect the surface and interior temperatures possible in such planets. The effects of other physical parameters on H₂-rich atmospheres of Neptunes/mini-Neptunes have

also been explored in previous works, such as metallicity (Spiegel et al., 2010) and UV flux (Moses et al., 2013a; Miguel and Kaltenegger, 2014). The effects of photospheric clouds and hazes on mini-Neptune atmospheric spectra have also been explored in detail (Howe and Burrows, 2012; Morley et al., 2013). Furthermore, Malik et al. (2019) recently used self-consistent atmospheric models to explore the occurrence of thermal inversions in both hydrogen-rich and higher-metallicity super-Earth atmospheres.

While habitability studies often focus on Earth-like terrestrial planets, this has also been explored for larger planets with H₂-rich atmospheres. Since a nominal definition of habitability requires the presence of liquid surface water (e.g. Meadows and Barnes, 2018), temperate conditions are required at the planetary surface to allow for habitability. For Earth-like rocky exoplanets, surface temperatures and pressures are regulated by their thin atmospheres dominated by gases such as N₂, H₂O and CO₂, which define the traditional habitable zone (e.g. Kasting et al., 1993; Kopparapu et al., 2017; Meadows et al., 2018; Meadows and Barnes, 2018). Recent studies have shown that H₂-dominated atmospheres on such planets could also cause a significant greenhouse effect (Stevenson, 1999; Pierrehumbert and Gaidos, 2011; Koll and Cronin, 2019), and can extend the traditional habitable-zone out to larger orbital separations. For example, Pierrehumbert and Gaidos (2011) argue for the habitability of such planets out to 1.5 AU for a 3 M_⊕ planet orbiting an early M Dwarf, which could be accessible by microlensing. However, atmospheric characterisation of such planets is challenging due to their larger orbital distances. In this study, we focus on planets with H₂-rich atmospheres in close-in orbits which are accessible with transit observations and consider the conditions under which their surfaces could be habitable.

While past studies of habitability under H₂-rich atmospheres have been focused on rocky super-Earths (e.g. Pierrehumbert and Gaidos, 2011; Seager et al., 2013), it is becoming evident that certain mini-Neptunes with H₂-rich atmospheres may also host habitable surfaces (Madhusudhan et al., 2020). Such mini-Neptunes must have masses and radii, i.e., bulk densities, that can allow a sufficiently low surface pressure for a H₂O layer under the H₂-rich atmosphere. Extremophiles on Earth are known to survive pressures as high as 1250 bar and temperatures up to 395 K (Merino et al., 2019). Therefore, a mini-Neptune with a surface pressure of $\lesssim 1000$ bar could potentially be habitable if its surface temperature is cool enough. As discussed in Section 1.4.3, Madhusudhan et al. (2020) find that this is the case for the habitable-zone mini-Neptune K2-18 b.

K2-18 b may therefore represent a Rosetta Stone for exoplanetary habitability, with the potential for both habitable conditions and detailed atmospheric characterisation with current and future facilities. Of course, unlike K2-18 b, not all mini-Neptunes are expected

to host habitable surfaces. Mini-Neptunes that are hotter and with lower bulk densities than K2-18b would lead to significantly higher temperatures and pressures, respectively, below their H₂-rich atmospheres that would be too high to be habitable. For example, GJ 1214 b, with similar mass and radius to K2-18 b but with an equilibrium temperature of ~500K, is expected to have super-critical H₂O beneath its atmosphere at temperatures un conducive to life (Rogers and Seager, 2010b). However, for planets such as K2-18b, a wide range of atmospheric parameters may allow for habitable conditions. Indeed, conditions even slightly hotter than K2-18b and a range of surface pressures may allow for habitability, as we explore in this study. K2-18b may, therefore, be the archetype for this class of planets, many more of which may be discovered by current and upcoming surveys.

In this study, we focus on three primary aspects of mini-Neptunes atmospheres. Firstly, we explore the temperature structures and spectral appearance of mini-Neptunes as a function of key atmospheric parameters, such as incident irradiation, internal flux, metallicity, and cloud/haze properties. In particular, we investigate the interplay between radiative and convective energy transport mechanisms in mini-Neptune atmospheres as a function of these parameters, with important implications for atmospheric composition and dynamics. Secondly, we investigate the implications of atmospheric temperature structures of mini-Neptunes on their surface conditions underneath the atmosphere and assess their potential habitability. Finally, we evaluate the observability of mini-Neptune atmospheres in thermal emission with JWST to characterise both potentially-habitable as well as warmer mini-Neptunes. In particular, we propose a simple metric to identify temperate mini-Neptunes which could potentially host habitable conditions, with a view to guiding follow-up observations. We demonstrate our results on some case studies, including the habitable-zone mini-Neptune K2-18 b and the warmer mini-Neptune GJ 3470 b.

In what follows, we begin by outlining our atmospheric model in Section 5.2. In Section 5.3, we then present a suite of self-consistent P - T profiles and emergent spectra exploring the atmospheric parameter space of mini-Neptunes using K2-18 b as a prototype. We further conduct a detailed study of the mini-Neptune K2-18 b in Section 5.4 with the specific goal of assessing the thermodynamic conditions at the base of the atmosphere and the potential for habitable conditions therein. In Section 5.5 we investigate the observability of mini-Neptunes, both temperate and warmer planets, with JWST in the mid-infrared. We conclude and discuss our findings in Section 5.6.

5.2 Atmospheric Model

We model the atmospheres of mini-Neptunes using an adaptation of the self-consistent atmospheric modeling framework GENESIS (Gandhi and Madhusudhan 2017; also used in Chapter 3). As described in Section 1.3.1, GENESIS self-consistently calculates the pressure-temperature (P - T) profile, the chemical profile and the spectrum of a plane-parallel atmosphere under assumptions of radiative-convective, hydrostatic, local thermodynamic and thermochemical equilibrium. In what follows, we discuss the model considerations and adaptations to GENESIS made in the present study, including radiative transfer, clouds/hazes, and comparisons with similar models in the literature.

5.2.1 Energy budget and radiative-convective equilibrium

Applying radiative-convective equilibrium to the model atmosphere involves balancing inward and outward energy transport in each layer of the atmosphere, as described in Section 1.2. In particular, the level of incident irradiation can be characterised by the irradiation temperature (Equation 1.7). In our model we assume that the incident irradiation is uniformly redistributed over the day-side plane parallel atmosphere. A significant amount of the incident irradiation is expected to be reflected back in the presence of strong optical scattering (e.g. due to clouds or hazes) as we consider in the present work. A fraction of the remnant irradiation that reaches the deeper atmosphere may be transported to the night-side depending on the location of the atmosphere-interior boundary. For example, in cases where the boundary occurs at low pressures, the day-night redistribution may take place in the interior, e.g., the H_2O layer, rather than the atmosphere. We, therefore, do not include any day-night atmospheric redistribution explicitly; we discuss this in Section 5.6.

The internal flux can be characterised by internal temperature, T_{int} . Values of T_{int} can depend on formation mechanisms, mass, composition, internal sources of heating and age, since a planet loses its initial energy from formation over time at a rate determined by its internal and atmospheric properties. Estimates of T_{int} can therefore be made using planetary evolution models (e.g. Valencia et al., 2013; Lopez and Fortney, 2014). In this chapter, we explore a wide range of plausible internal temperatures for mini-Neptunes. Valencia et al. (2013) find that for the mini-Neptune GJ 1214 b, T_{int} can be as high as 80 K/62 K if it has a water-rich/solar-like composition and a young age of 0.1 Gyr. Morley et al. (2017a) consider higher values of T_{int} ($\gtrsim 300$ K) for GJ 436b as this planet may be experiencing tidal heating. Conversely, the minimum possible value of T_{int} is 0 K. In this chapter, we explore the range $T_{\text{int}}=0$ -200 K. As discussed in Section 1.3.1, GENESIS uses

Rybicki's method to iteratively solve the equations of radiative-convective equilibrium given the boundary conditions from irradiation and internal heat (Hubeny and Mihalas, 2014; Gandhi and Madhusudhan, 2017). The internal heat flux, characterised by T_{int} , is therefore applied at the base of the model atmosphere, i.e. at 1000 bar in this chapter.

Note that we do not explicitly include the effects of a surface within our models. In Section 5.4, we consider how the thermodynamic conditions in the atmosphere would affect a H₂O surface if it were present at a given pressure. Since the surface pressures considered are deeper than the photosphere, we are effectively assuming that this surface behaves as a blackbody. In Section 5.4.3, we further consider the effects of H₂O evaporation from the surface by saturating the abundance of H₂O in the atmosphere.

5.2.2 Radiative transfer

Given a P - T profile and the opacity structure of an atmosphere, the radiation field of the atmosphere can be calculated using the radiative transfer equation (Equation 1.11). This procedure is necessary at two points in the calculation of the atmospheric model: (i) in the iterative solution of radiative-convective equilibrium, and (ii) in order to calculate the emergent spectrum of the planet once a converged, energy-balanced atmospheric model is found. For the solution of radiative-convective equilibrium, a fast radiative transfer solution is ideal as the calculation needs to be performed in each iteration. Furthermore, values of mean intensity are not directly needed from this solution; instead, Eddington factors ($f_v = K_v/J_v$, where $K_v = 1/2 \int_{-1}^1 \mu^2 I_v(\mu) d\mu$) are sufficient for the calculation of radiative equilibrium. On the other hand, calculation of the emergent spectrum requires accurate solutions for the mean intensity and is only calculated once, so need not be as fast. We therefore choose to use the Feautrier method (Feautrier, 1964) in the iterative solution of radiative-convective equilibrium, and the Discontinuous Finite Element (DFE) method (Castor et al., 1992) combined with Accelerated Lambda Iteration (ALI) for the calculation of the spectrum. Both methods are second-order accurate and provide direct solutions to the radiative transfer equation.

The Feautrier method solves radiative transfer under the assumption that the source function is isotropic. This is achieved by recasting equation 1.11 in terms of the symmetric and anti-symmetric averages of specific intensity, $j_v = (I_v(\mu) + I_v(-\mu))/2$ and $h_v = (I_v(\mu) - I_v(-\mu))/2$, respectively. This results in the Feautrier equation, $\mu^2 \frac{d^2 j_v}{d\tau_v^2} = j_v - S_v$. This equation is then solved using matrix methods as described in Hubeny and Mihalas (2014), and yields the desired Eddington factors which are used in the solution of radiative-convective equilibrium.

The DFE solution for radiative transfer divides the atmosphere into plane-parallel layers and solves for the specific intensity at the top and bottom of each layer, I_d^+ and I_d^- , respectively, for layer d . Crucially, a discontinuity between adjacent layers is allowed, i.e. $I_d^+ \neq I_{d+1}^-$, and it is this property which allows the method to be second-order accurate (Castor et al., 1992). The specific intensity for layer d , I_d is then given by a weighted average of I_d^+ and I_d^- . This formalism leads to the following recurrence relations for I_d^+ and I_d^- (dropping the ν subscript for clarity):

$$\begin{aligned} a_d I_{d+1}^- &= 2I_d^- + \Delta\tau_{d+1/2} S_d + b_d S_{d+1} \\ a_d I_d^+ &= 2(\Delta\tau_{d+1/2} + 1)I_d^- + b_d S_d - \Delta\tau_{d+1/2} S_{d+1/2}, \end{aligned}$$

where $a_d = \Delta\tau_{d+1/2}^2 + 2\Delta\tau_{d+1/2} + 2$, $b_d = \Delta\tau_{d+1/2}(\Delta\tau_{d+1/2} + 1)$ and $\Delta\tau_{d+1/2} = (\tau_{d+1} - \tau_d)/|\mu|$. When scattering is present, this method must be used iteratively, which can be done using ALI. The general principle of ALI methods is to write a matrix equation such as $I = \Lambda[S]$ as an iterative process, i.e. $I^{\text{new}} = \Lambda^*[S^{\text{new}}] + (\Lambda - \Lambda^*)[S^{\text{old}}]$ where Λ^* is an approximate operator chosen to minimise computation time and maximise convergence rate. Details of the implementation of ALI for the DFE method can be found in Hubeny (2017).

5.2.3 Chemistry, opacities and clouds/hazes

In this chapter, we consider opacity due to species in gas phase, hazes and clouds. The gas-phase species we include here are the main volatiles expected in hydrogen-rich atmospheres: H₂O, CH₄, NH₃, CO, CO₂, HCN and C₂H₂ (Madhusudhan, 2012; Moses et al., 2013b). We calculate their equilibrium abundances self-consistently with the P - T profile using the analytic method of Heng and Tsai (2016) in each iteration of the radiative-convective equilibrium solver. We also include opacity due to H₂-H₂ and H₂-He collision-induced absorption (CIA). The cross sections we use for these species are calculated from the HITEMP, HITRAN and ExoMol line list databases using the methods of Gandhi and Madhusudhan (2017) (H₂O, CO and CO₂: Rothman et al. 2010, CH₄: Yurchenko et al. 2013; Yurchenko and Tennyson 2014, C₂H₂: Rothman et al. 2013; Gordon et al. 2017, NH₃: Yurchenko et al. 2011, HCN: Harris et al. 2006; Barber et al. 2014, CIA: Richard et al. 2012).

In our models we also consider the phase transition of gaseous H₂O in the atmosphere into both the liquid and ice phases. When H₂O condenses to the liquid phase, we remove it from the atmosphere as precipitation. This ‘rainout’ happens if the H₂O mixing ratio is greater than the local saturation vapour pressure. In this case, we assume that any H₂O in excess of the saturation level rains out, and the remaining atmospheric H₂O vapour pressure is equal to the saturation vapour pressure in these regions. On the other hand, in

regions of the atmosphere where the temperature is below the freezing point, the H₂O is removed entirely from the gas phase and instead included as an ice cloud as described below.

We also include a simple prescription for hazes in our models. We assume that the haze is homogeneously distributed in the atmosphere and its opacity is of the form of an enhanced H₂ Rayleigh scattering; i.e. H₂ Rayleigh scattering boosted by a multiplicative factor. This allows us to explore the general effects of haze on model P - T profiles with a simple parameterisation. In order to compare the strength of our model hazes to more detailed studies, we look to the models of Howe and Burrows (2012) for GJ 1214 b. One of the best fit models presented by Howe and Burrows (2012) includes a tholin haze of density 100 cm^{-3} and particle size $0.1 \text{ }\mu\text{m}$, whose extinction has a λ^{-4} dependence at wavelengths $< 1 \text{ }\mu\text{m}$. The scattering opacity of this haze is equivalent to $\sim 1000\times$ the scattering opacity of H₂ Rayleigh scattering at 1 mbar and 300 K. In Section 5.3, we therefore explore haze opacities in the range 0 - $10,000\times$ H₂ Rayleigh scattering.

Our prescription for clouds involves cloud decks whose particle abundances decay exponentially with altitude above the cloud base given a cloud scale height, analogous to the condensate profiles of Ackerman and Marley (2001). Rather than parameterising the cloud scale height according to parameters such as f_{rain} as in Ackerman and Marley (2001), we choose for simplicity a nominal cloud scale height of $1/3$ of an atmospheric scale height, similar to Jovian ammonia clouds (e.g., Carlson et al. 1994; Brooke et al. 1998, see also Ackerman and Marley 2001). The base of the deck is fixed at a given pressure, which in Sections 5.4 and 5.5 we choose such that the temperature at the base of the cloud approximately coincides with the condensation temperature of the cloud species (e.g. see condensation curves of Morley et al., 2012). In Section 5.3, however, we independently explore the effect of cloud location on the P - T profile and therefore do not consider condensation temperature. We nominally assume a KCl composition to represent the effects of salt clouds, and also explore the effects of water ice clouds. In Section 5.4, we include KCl, ZnS and ice clouds wherever they are thermodynamically expected to occur.

We vary cloud opacity in our models by varying the abundance of the condensate species (i.e. varying metallicity). At the base of each cloud, we assume that all of the cloud species is in the condensed phase. For the salt clouds, the abundance of cloud particles is therefore determined by the abundance of the least-abundant element in the condensate species (e.g. Cl for KCl) and the particle size. Cloud particle sizes are known to vary depending on a range of physical factors which have been explored in detail in several works (e.g. Ackerman and Marley, 2001; Morley et al., 2014). For simplicity, throughout this chapter, we assume a nominal modal particle size of $0.33 \text{ }\mu\text{m}$ for the salt

clouds and use the cloud extinction cross sections given by Pinhas and Madhusudhan (2017). For ice clouds, the particle abundance at the base of the cloud depends on the H_2O abundance and the particle size (which can vary between models, see Section 5.4). We use the extinction cross sections for water ice from Budaj et al. (2015).

Above an ice cloud deck, the abundance of gaseous H_2O can depend on the presence of vertical mixing. For our model parameter exploration in Section 5.3, we freeze out all H_2O above the base of the water ice cloud deck (i.e. assuming a cold trap and no vertical mixing) to provide a uniform comparison between models with different ice cloud abundance, which is a free parameter. In reality, however, if a thermal inversion occurs it is possible that the temperature profile above the cloud deck is hotter than the freezing point. In such cases, it is conceivable that water vapour may be present above the cloud deck due to vertical mixing in the atmosphere; e.g., analogous to condensable species being lofted to upper regions in irradiated atmospheres (e.g., Parmentier et al., 2013). For example, if the temperature at 0.1 bar is 250 K and the temperature at 10^{-3} bar is 300 K, H_2O will be frozen out at 0.1 bar but H_2O vapour could still be present at 10^{-3} bar given sufficient vertical mixing. Therefore, we allow for this possibility when modeling the specific case studies in Sections 5.4 and 5.5, i.e., H_2O is only frozen out when it is expected to be in the ice phase, allowing it to come back to vapor phase higher up in the atmosphere if the temperature there is above the freezing point.

5.2.4 System parameters

In Section 5.3, we apply our model to a generic mini-Neptune to qualitatively assess the impacts of various atmospheric parameters on its P - T profile and spectrum. The planetary and host star parameters we choose to use for this test case are based on those of K2-18 b (Foreman-Mackey et al., 2015; Montet et al., 2015), and we use the values given by Cloutier et al. (2019b) and Benneke et al. (2019b). For the planetary parameters, we assume a radius of $2.61R_{\oplus}$ and log gravity of 3.094 (in cgs). For the stellar parameters, we assume a radius of $0.4445R_{\odot}$, log gravity of 4.836 (in cgs), temperature of 3457 K and an [Fe/H] metallicity of 0.12. We use a Kurucz stellar model for the stellar spectrum in our models (Kurucz, 1979; Castelli and Kurucz, 2003).

In Section 5.4, we calculate models specifically for K2-18 b using the same parameters as described above, and using its orbital separation to determine the irradiation temperature based on parameters from Benneke et al. (2019b). For K2-18 b, $T_{\text{irr}}=332$ K. We further estimate the internal temperature of K2-18 b based on existing estimates for GJ 1214 b (Charbonneau et al., 2009), which has a similar mass and radius to K2-18 b (Cloutier et al., 2019b; Benneke et al., 2019b). Valencia et al. (2013) find that for ages between ~ 1 -10

Gyr, considering both solar and water-rich atmospheric compositions, GJ 1214 b has an internal temperature in the range ~ 25 -50 K. We therefore calculate models for these two end-member values of T_{int} .

We also calculate models for GJ 3470 b (Bonfils et al., 2012) in Section 5.4, a planet with radius comparable to Neptune but of lower mass. For this, we use planetary and stellar properties from Awiphan et al. (2016). The planetary radius and log gravity are $4.57R_{\oplus}$ and 2.81 (in cgs), respectively, with a mass of $13.9 M_{\oplus}$, and semi-major axis of 0.0355 au. For the stellar parameters we use a radius of $0.547R_{\odot}$, log gravity of 4.695 (in cgs), effective temperature of 3600 K and an [Fe/H] metallicity of 0.2. The irradiation temperature of GJ 3470 b given these system parameters is 812 K. For the internal temperature, we use an intermediate value of 30 K (Valencia et al., 2013).

In Section 5.2.5, we also model GJ 1214 b for comparison with previous models in the literature. For these models, we use the stellar and planetary parameters of GJ 1214/GJ 1214 b from Harpsøe et al. (2013). The planetary radius and log gravity are $2.85R_{\oplus}$ and 2.88 (in cgs), respectively, and the semi-major axis is 0.0141 au. For the star we use a radius of $0.216R_{\odot}$, log gravity of 4.944 (in cgs), effective temperature of 3026 K and an [Fe/H] metallicity of 0.39.

The GENESIS models described above can be used to generate atmospheric models with arbitrary pressure and wavelength resolution. We choose to use 10000 wavelength points uniformly distributed between 0.4 and 50 μm and 100 depth layers log-uniformly distributed between pressures of 10^3 and 10^{-6} bar.

5.2.5 Model comparison

We compare our self-consistent forward model to three other examples of mini-Neptune models in the literature: Benneke et al. (2019b) and Scheucher et al. (2020) for K2-18b, and Morley et al. (2013) for GJ 1214 b. We use the same input parameters and model set-up as described in these works. The internal temperature is not specified for these models, so we choose to use $T_{\text{int}}=100$ K as this results in good agreement.

We first reproduce the model P - T profile of K2-18 b from figure 5 of Benneke et al. (2019b). We include opacity due to H_2O vapour, H_2 - H_2 and H_2 -He CIA and Rayleigh scattering due to H_2 . Following Benneke et al. (2019b), we assume an albedo of 0.3. We further assume uniform day-night redistribution of the incident flux, i.e., 50% of the incident irradiation, minus the reflected component, remains on the dayside. We use a H_2O abundance of $40\times$ the expected abundance for a solar composition in thermochemical equilibrium, i.e. approximately the best fitting value found by Benneke et al. (2019b) (their Fig. 4), which they use to calculate their model P - T profile. We also use the planetary and

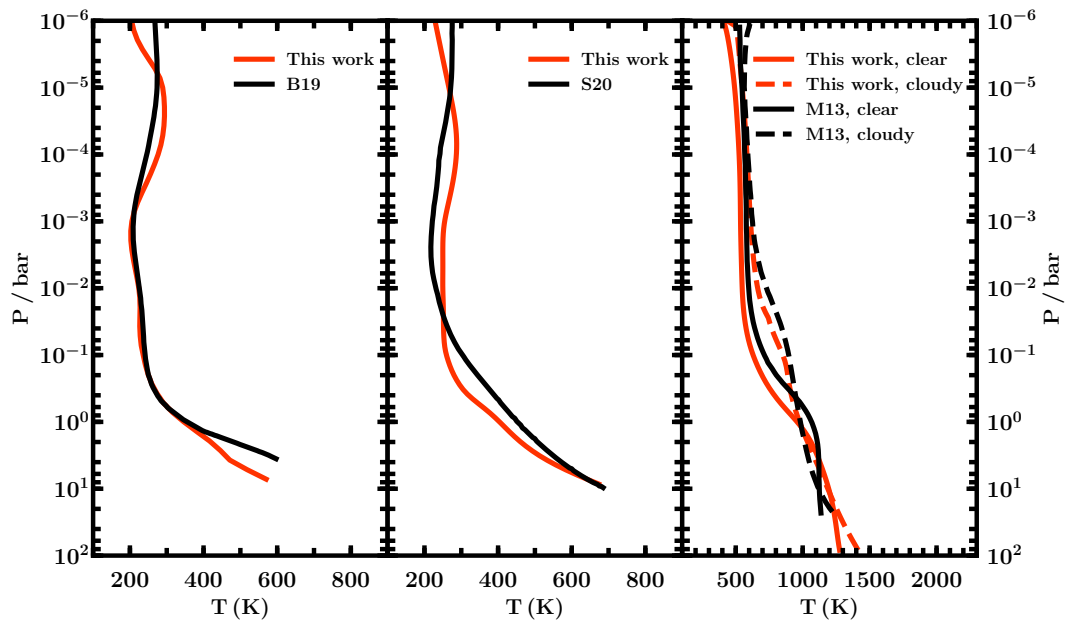


Fig. 5.1 Comparisons with model pressure-temperature profiles of mini-Neptunes in the literature. Left panel: comparison to the model for K2-18 b from figure 5 of Benneke et al. (2019b) (B19). Centre panel: comparison to the K2-18 b solar-metallicity model from figure 11 of Scheucher et al. (2020) (S20, case 6 in their table 6). Right panel: comparison to clear (solid lines) and cloudy (dashed lines) models for GJ 1214 b from Morley et al. (2013) (M13). See section 5.2.5 for details.

stellar parameters for K2-18 b/K2-18 given by Benneke et al. (2019b), which are also listed in Section 5.2.4. The left panel of Figure 5.1 shows the model from Benneke et al. (2019b) as well as our reproduction, which agrees very closely.

Note that the P - T profile of Benneke et al. (2019b) does not appear to explicitly include the effects of water ice clouds, despite having temperatures below the freezing point of H_2O . Instead, an albedo of 0.3 was assumed to remove the corresponding amount of incident flux at the top of the atmosphere. Our reproduction is, therefore, also cloud-free and assumes the same albedo treatment. We explore cloudy and hazy models of K2-18 b in Section 5.4.

We further reproduce the solar-metallicity P - T profile for K2-18 b from figure 11 of Scheucher et al. (2020) (case 6 in their table 6). Their model assumes equilibrium chemical abundances for an isotherm at 320 K, and this chemistry is kept fixed for the calculation of the P - T profile. We therefore include opacity due to H_2O , CH_4 and NH_3 in our reproduction (the dominant carriers of O, C and N, respectively, at this temperature) assuming fixed, constant-with-depth abundances corresponding to the equilibrium abundances expected at 320 K (i.e. mixing ratios of 10^{-3} , $10^{-3.3}$ and $10^{-3.9}$ for H_2O , CH_4 and NH_3 , respectively; see e.g., Woitke et al. 2018). We also include opacity due to H_2 - H_2 and H_2 -He CIA as well as H_2 Rayleigh scattering. Following Scheucher et al. (2020), we do not include any clouds or hazes in this model. We also assume uniform day-night energy redistribution. We also use the planetary and stellar parameters for K2-18 b/K2-18 given in Section 5.2.4. Both the model from Scheucher et al. (2020) and our reproduction of this are shown in the centre panel of Figure 5.1.

Our model and that of Scheucher et al. (2020) agree closely. Any differences between them may be due to differences in the treatment of radiative transfer and radiative-convective equilibrium, e.g., Scheucher et al. (2020) do not self-consistently consider convective flux. We further note that this P - T profile enters the ice phase of H_2O and should therefore include the presence of water ice clouds. We find in Section 5.4 that assessing the habitability of K2-18 b requires consideration of optical opacity in the atmosphere, e.g., clouds and/or hazes. As such, the cloud- and haze-free models of Scheucher et al. (2020) are limited in assessing the habitability of this planet.

We also use our model to reproduce a clear and a cloudy P - T profile for GJ 1214 b from figure 1 of Morley et al. (2013). We model a $1\times$ solar clear atmosphere and a $50\times$ solar cloudy atmosphere, both assuming that incident irradiation is redistributed on the dayside only (i.e. corresponding to the hotter P - T profiles in figure 1 of Morley et al. 2013). In both cases, we include opacity due to all of the volatile species discussed in Section 5.2.3. In the cloudy model, we also include KCl and ZnS clouds with base pressures of

0.025 and 0.158 bar, respectively. This is where the Morley et al. (2013) model crosses the condensation curves for each of these species and where the cloud bases are positioned in their model. We use a modal particle size of $38.6 \mu\text{m}$ for these clouds. Since the effective temperature of GJ 1214 is cooler than 3500 K, we are not able to use a spectral model from the Kurucz library as described above (which includes models with $T_{\text{eff}} \geq 3500 \text{ K}$) and instead use a model from the PHOENIX library (Husser et al., 2013) with the closest stellar parameters to GJ 1214, i.e. $T_{\text{eff}}=3000 \text{ K}$, $\log(g/\text{cgs})=5.0$ and $[\text{Fe}/\text{H}]=0.5$. Our models and those of Morley et al. (2013) are shown in the right panel of Figure 5.1. The models show good agreement and differ by $\lesssim 100 \text{ K}$, which may be due to differences in the stellar spectrum used.

5.3 Effects of Atmospheric Parameters

The temperature profiles of mini-Neptune atmospheres are determined by a range of atmospheric properties, including the internal flux, irradiation, and the opacity structure of the atmosphere, which are, therefore, key to understanding the various processes discussed above. In this section, we investigate the effects of these properties on the temperature structures and thermal emission spectra of mini-Neptune atmospheres. In particular, we explore the effects of internal temperature, irradiation, infrared opacity and cloud/haze properties, discussing how they impact the observability and physical processes of these atmospheres as well as consequences for modelling the interiors of mini-Neptunes.

We consider a fiducial model with $T_{\text{irr}}=350 \text{ K}$, $T_{\text{int}}=40 \text{ K}$ and $1 \times$ solar metallicity, and explore models in the range $T_{\text{irr}}=350\text{-}1000 \text{ K}$, $T_{\text{int}}=0\text{-}200 \text{ K}$ and metallicities of $0.1\text{-}100 \times$ solar. We present both clear and hazy/cloudy models, exploring haze opacities up to $1000 \times$ Rayleigh scattering (according to the parameterisation discussed in Section 5.2.3) and salt/water ice clouds with up to $100 \times$ solar metallicity. We discuss the P - T profiles and thermal emission spectra of these models in Sections 5.3.1 and 5.3.2, respectively.

5.3.1 Temperature profiles and energy transport

We begin by exploring how T_{int} , T_{irr} , metallicity, cloud/haze opacity and cloud type affect the thermal profiles of mini-Neptunes. Energy transport in a planetary atmosphere is governed by the boundary conditions at the top and bottom of the atmosphere, characterised by T_{irr} and T_{int} , respectively, and by the opacity profile which lies between them. In the upper, low-opacity, regions of the atmosphere, energy transport is primarily radiative,

an effect which is enhanced by strong incident irradiation. In the deeper, high-opacity layers, convective transport begins to dominate. Where the transition between the two regimes - the radiative-convective boundary - occurs depends on several factors including incident and intrinsic flux as well as optical and infrared opacity. Depending on the location of the radiative-convective boundary, the presence of convection can in turn impact atmospheric mixing and, therefore, the chemical homogeneity of the atmosphere.

Here, we investigate how the parameters listed above impact the thermal profile and energy transport mechanisms of an atmosphere by generating self-consistent P - T profiles, as described in Section 5.2, and independently varying each parameter in turn. Figure 5.2 shows model P - T profiles for which we vary the haze opacity (left panel) or cloud opacity (centre and right panels). In the centre and right panels, we place a KCl cloud at 10 bar and a H₂O ice cloud at 0.1 bar, respectively, to test the effects of different types of clouds. We test the effects of T_{int} , T_{irr} and metallicity in Figure 5.3, for both a clear atmosphere (upper panels) and a hazy one (lower panels). For each P - T profile, we also show the 1-30 μm photosphere, smoothed by a Gaussian of width 0.1 μm , to represent the pressures and temperatures probed by low-resolution infrared thermal emission observations. In what follows, we describe the effects of each of these parameters in turn on the atmospheric temperature profile.

Effect of clouds/hazes

Figure 5.2 shows the effects of hazes, high-altitude ice clouds and deeper salt clouds on the thermal profile of a mini-Neptune. Here the cloud/haze properties are varied according to the prescriptions described in section 5.2. For example, in the centre and right panels the abundance of cloud species is varied according to the metallicity specified, keeping the cloud scale heights and locations fixed. While in reality the cloud base location is driven by its condensation temperature, in this section we choose to only vary cloud opacity in order to independently demonstrate the structural effects that this has on the P - T profile. Note that, for the purpose of demonstration here, the abundance of water ice particles is varied independently of the gaseous H₂O abundance. The models in Figure 5.2 all assume $T_{\text{int}}=40$ K, $T_{\text{irr}}=350$ K and solar abundances of the gaseous species listed in Section 5.2.

Clouds and hazes both provide optical opacity which scatters incident irradiation and can therefore cool the atmosphere. This is shown clearly in the left and centre columns of Figure 5.2, as increasing the haze/KCl cloud abundance results in a cooler temperature profile. Ice clouds can also cool the atmosphere (right column of Figure 5.2), though very high opacity clouds can also warm the atmosphere by intercepting outgoing flux (Morley et al., 2014). Both the photospheric temperature and the temperature at deeper pressures

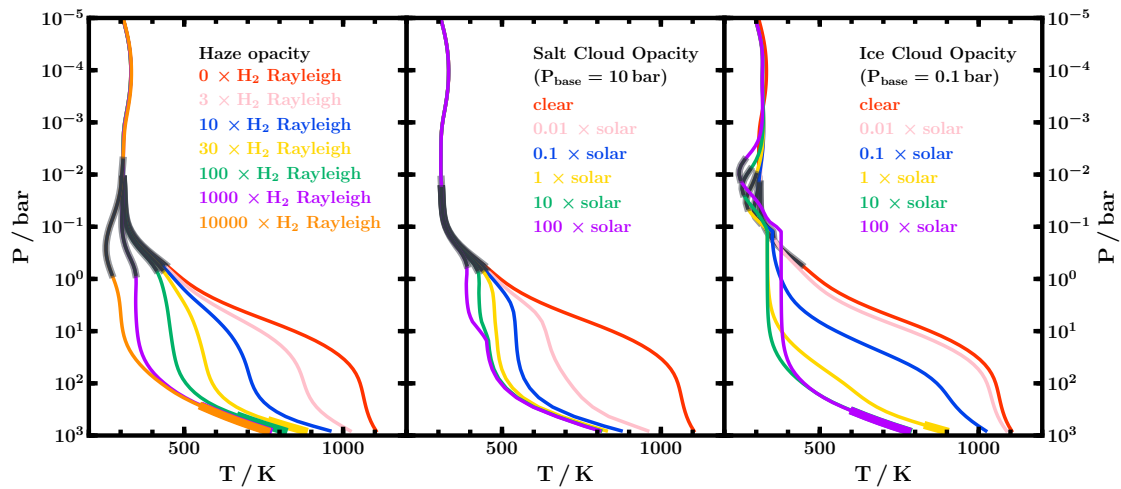


Fig. 5.2 P - T profiles for model atmospheres with varying haze and cloud opacities. Left panel shows effects of varying haze, which is included homogeneously throughout the atmosphere and implemented using an enhanced Rayleigh scattering prescription (see section 5.2.3). Centre and right panels show the effects of a KCl/water ice cloud deck, with the abundance of the cloud condensate parametrised by the metallicity, as described in section 5.2.3. For the salt/water ice clouds, the base of the cloud deck is at a pressure of 10 bar/0.1 bar and the modal particle size is $0.33 \mu\text{m}/4 \mu\text{m}$, respectively. We use a nominal cloud scale height of $1/3$ of an atmospheric scale height. For each model, $T_{\text{int}}=40 \text{ K}$, $T_{\text{irr}}=350 \text{ K}$ and the metallicity of the gaseous species in the atmosphere is $1 \times \text{solar}$. In each panel, the red profile denotes a clear atmosphere. Convective regions are shown by bold lines, and photospheres are shown by bold dark grey lines (see Section 5.3.1)

are affected by these effects, meaning that clouds and hazes are important components in understanding both the spectra and interiors of mini-Neptunes. Figure 5.2 also shows that stronger cloud/haze opacity typically results in a more isothermal temperature profile below the photosphere. This can impact the habitability of the planet as cooler, more habitable temperatures are maintained to higher pressures where a surface may occur. We discuss this further in Section 5.4.

The location of the radiative-convective boundary is also affected by the presence of clouds/hazes. As we discuss in Section 5.3.1, the boundary between the radiative and convective regions of the atmosphere is dependent on the incident irradiation, with weaker irradiation resulting in a shallower radiative-convective boundary. By scattering incident irradiation, clouds/hazes also raise this boundary to lower pressures. For example, in Figure 5.2, only the models with the strongest haze/cloud opacities have a radiative-convective boundary shallower than 1000 bar (i.e. the edge of the computational domain), and the boundary occurs at lower pressures for models with higher haze/cloud opacity.

Irradiation vs internal flux

As the boundary conditions at the top and bottom of the atmosphere, irradiation and internal flux compete in determining the location of the radiative-convective boundary. A high T_{irr} results in a larger region of the atmosphere being dominated by radiative transport, pushing the radiative-convective boundary deeper. Conversely, a hotter T_{int} pushes this boundary higher up. These effects can be seen in Figure 5.3, and are strongest for the hazy models in the lower left and lower centre panels. As T_{irr} decreases the temperature gradient at 1000 bar gradually becomes steeper, transitioning from almost isothermal at $T_{\text{irr}} = 1000$ K to an adiabatic gradient at $T_{\text{irr}} \leq 650$ K, when the radiative-convective boundary occurs within the computational domain.

As expected, T_{int} has the opposite effect. Models with higher T_{int} show significantly shallower radiative-convective boundaries, with the shallowest within this parameter space at ~ 1 bar for the model with $T_{\text{int}} = 200$ K. However, such a high value of T_{int} may be unlikely for a mini-Neptune (e.g. Valencia et al., 2013), though high T_{int} values have been considered for planets which may be affected by tidal heating (e.g. GJ 436b, Morley et al., 2017a). For models with $T_{\text{int}} \leq 100$ K the radiative-convective boundary is deeper than 10 bar. This suggests that intrinsic heat in mini-Neptunes may be insufficient to mix their atmospheres up to shallow pressures through convection unless they have significant haze/cloud opacities. Instead, eddy diffusion in the radiative regime or large-scale radiative-driven circulation may be a more likely mechanism for vertical mixing (e.g. Showman and Guillot, 2002).

While T_{irr} and T_{int} have strong effects on the radiative-convective boundary when haze is present, in the haze-free models their influence is reduced at the pressures investigated here. The upper left and centre panels in Figure 5.3 show that none of the T_{irr} or T_{int} values explored result in a radiative-convective boundary shallower than 1000 bar for a clear, haze-free model. Though the larger values of T_{int} explored do result in a higher temperature gradient at high pressures, this suggests that for the clear models in the parameter space explored here (i.e. $T_{\text{irr}} \gtrsim 350$ K), incident irradiation and radiative transport dominate the atmosphere up to pressures of at least 1000 bar.

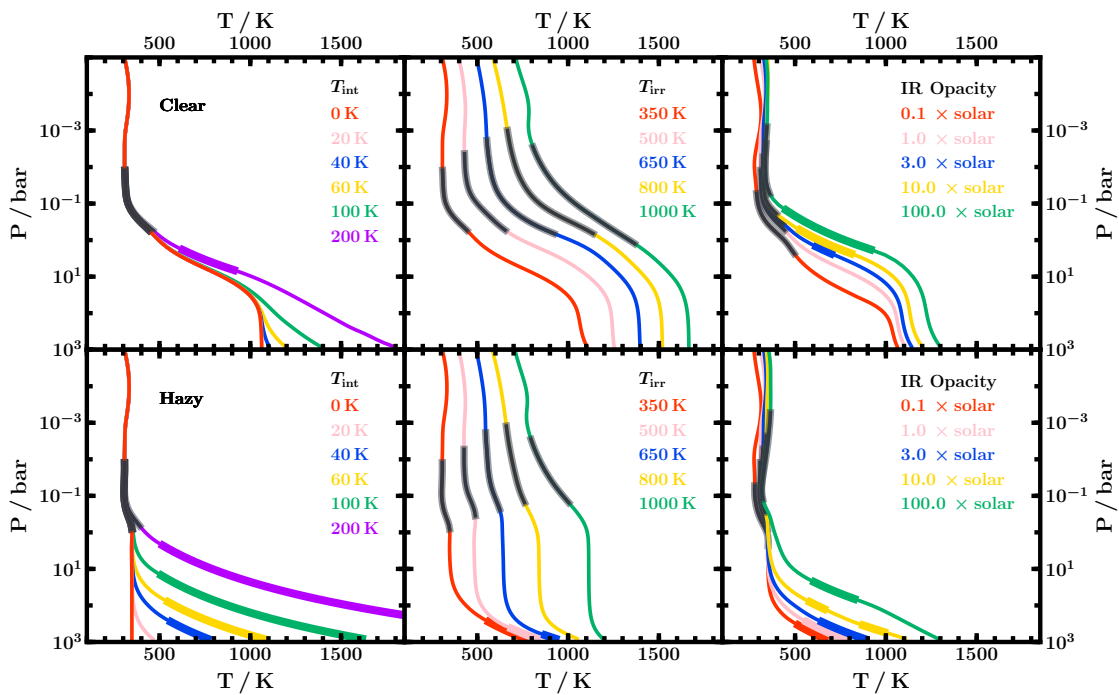


Fig. 5.3 Self-consistent atmospheric P - T profiles across a range of internal temperatures, irradiation temperatures and infrared opacities (parameterised by metallicity relative to solar abundances). Top three panels show P - T profiles for a clear atmosphere while lower panels include haze equivalent to $1000\times$ H_2 Rayleigh scattering. The fiducial values used for T_{int} , T_{irr} and infrared opacity are 40 K, 350 K and $1\times$ solar metallicity, respectively. Bold line segments indicate convective regions and photospheres are shown by bold dark grey lines (see Section 5.3.1).

Aside from the radiative-convective boundary, irradiation and internal flux also have significant effects on the temperature profile in general. As expected, a hotter T_{irr} translates the temperature profile to higher temperatures, and consequently the photospheric temperature is extremely sensitive to this parameter. In contrast, T_{int} only affects the deep-

est regions of the atmosphere and does not affect the photosphere unless it is extremely high (e.g. Morley et al., 2017a). The left and centre columns of Figure 5.3 also show that the temperatures at high pressures are strongly dependent on both T_{irr} and T_{int} , meaning that these properties are important to consider when using such models as boundary conditions for internal structure models.

Effect of infrared opacity

Infrared opacity is an important factor in determining energy transport, as it intercepts outgoing planetary flux. For planets with a cool stellar host whose spectrum peaks in the near-infrared, such as K2-18, the infrared opacity can also absorb incident irradiation. As a result, higher abundances of these infrared absorbers result in a hotter temperature profile. This can be seen in the right column of Figure 5.3, which shows P - T profiles for different infrared opacities, characterised by metallicity relative to solar elemental abundances. These P - T profiles also show that metallicity predominantly affects deeper regions of the atmosphere; the profiles are similar at low pressures and begin to diverge at $P \gtrsim 0.1$ bar. At these higher pressures, models with higher metallicity also exhibit convective zones as the increase in opacity reduces the efficiency of radiative transport. We also note that for models with very high IR opacity (e.g., $\gtrsim 100\times$ solar), the H_2O mixing ratio in the lower atmosphere can be close to saturated. We consider the rainout which can result from super-saturation in sections 5.4 and 5.5.

Since high infrared opacities result in hotter temperatures deep in the atmosphere, this property is an important factor both for boundary conditions in internal structure models and for considerations of habitability. However, the photosphere is not strongly affected by changes in infrared opacity. This is because an increase in infrared opacity effectively translates the P - T profile to lower pressures, while the photosphere of a higher-opacity model also occurs at lower pressures (Spiegel et al., 2010). As a result, the photospheres of the models in the right column of Figure 5.3 probe similar temperatures despite the differences in their infrared opacities.

5.3.2 Thermal Emission Spectra

In this section, we investigate the effects of internal temperature, irradiation, metallicity and clouds/hazes on the thermal emission spectra of mini-Neptunes. These emergent spectra are strongly sensitive to the atmospheric temperature profile, and are therefore impacted by the parameters listed above through their effects on the temperature profile. Figures 5.4 and 5.5 show thermal emission spectra corresponding to the P - T profiles in

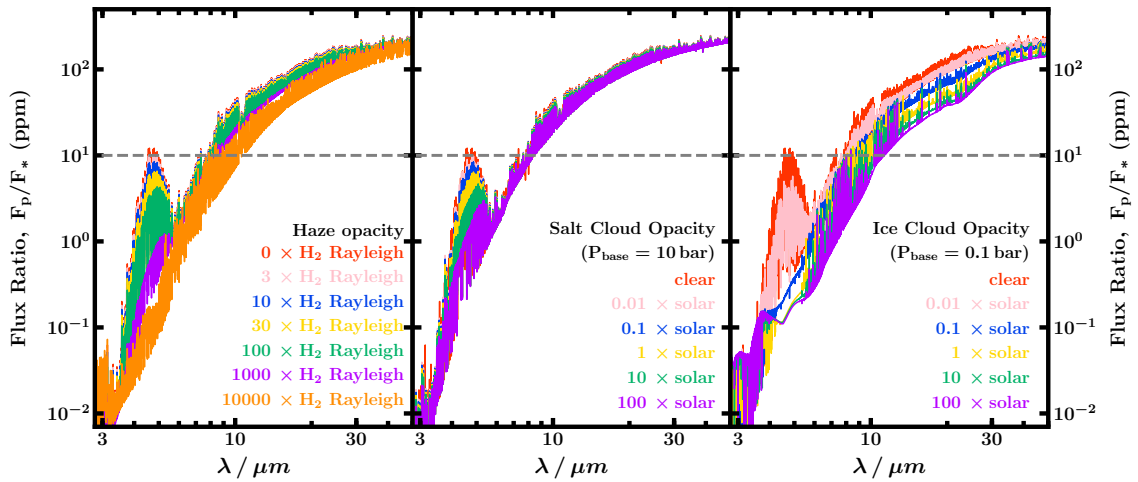


Fig. 5.4 Model thermal emission spectra corresponding to the P - T profiles in Figure 5.2. For each model, $T_{\text{int}}=40$ K, $T_{\text{irr}}=350$ K and the metallicity of the gaseous species in the atmosphere is $1 \times$ solar. We vary haze, salt cloud and water ice cloud opacities in the left, centre and right panels, respectively. The horizontal dashed grey lines show the 10 ppm level, which may be considered an optimistic precision achievable with JWST.

Figures 5.2 and 5.3, respectively. In each of these, a flux ratio of 10 ppm is shown by a dashed line to indicate an optimistic minimum uncertainty expected with JWST.

Clouds and hazes predominantly affect the spectrum at shorter wavelengths, as they reflect incident stellar irradiation which peaks in the optical. However, this reflected light is well below an optimistic 10 ppm uncertainty for JWST, and is, therefore, unlikely to be detectable for the temperate mini-Neptunes modelled here. Nevertheless, clouds and hazes can also affect the spectrum through their effects on the P - T profile. For example, high-altitude ice clouds significantly cool the photospheric temperature, which results in less emitted flux. In the case of hazes and deeper KCl clouds, stronger haze/cloud opacity results in a more isothermal P - T profile in the photosphere and weaker absorption features. This can be seen in the continuum peak at $\sim 5 \mu m$, which is smaller for models with stronger haze/KCl cloud opacity.

Although T_{irr} and T_{int} both play major roles in determining the P - T profile and radiative-convective boundary (Section 5.3.1), only T_{irr} has a significant effect on the observable spectrum. As T_{irr} translates the P - T profile to hotter/cooler temperatures, the emergent flux increases/decreases accordingly. However, T_{int} largely affects the P - T profile below the photosphere and does not impact the spectrum unless its value is sufficiently high. For the models shown here with $T_{\text{irr}}=350$ K, $T_{\text{int}}=200$ K is enough to affect the photosphere and result in a slightly higher continuum peak at $\sim 5 \mu m$. This is a stronger

effect for hazy models compared to clear ones (left column of Figure 5.5), though the haze also mutes the continuum feature. Estimates of T_{int} for mini-Neptunes will therefore rely on theoretical cooling models as this parameter will not be derivable from observed spectra unless it is very high.

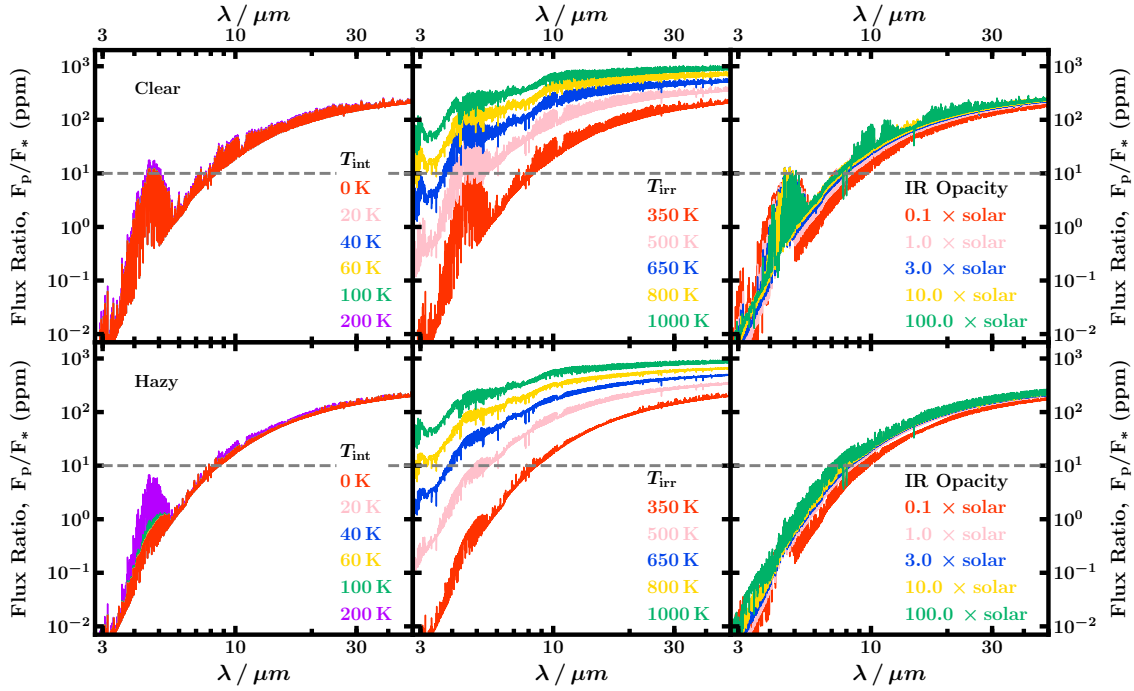


Fig. 5.5 Model thermal emission spectra corresponding to the P - T profiles in Figure 5.3, for varying T_{int} , T_{irr} and infrared opacity (left, centre and right columns, respectively). The fiducial values used for T_{int} , T_{irr} and infrared opacity are 40 K, 350 K and $1 \times$ solar metallicity, respectively. Top three panels show spectra for a clear atmosphere while lower panels include haze equivalent to $1000 \times$ H_2 Rayleigh scattering. The horizontal dashed grey lines show the 10 ppm level, which may be considered an optimistic precision achievable with JWST.

The right column of Figure 5.3 shows that metallicity does not have a strong effect on the observable spectrum, especially at longer wavelengths. As discussed by Spiegel et al. (2010), this is because the increase in temperature due to increased metallicity is balanced by the photosphere shifting to lower pressures. Furthermore, this shallower photosphere is also more isothermal, which weakens the strength of spectral features.

While each atmospheric parameter affects the observable spectrum to different extents, we note that all of the spectra in Figures 5.4 and 5.5 are well above 10 ppm at longer

wavelengths and should be observable with JWST. In Section 5.5, we discuss how JWST observations could help to constrain the conditions in atmospheres of mini-Neptunes.

5.4 Considerations for habitability

In the search for extrasolar habitability, planets in the habitable zones of M-dwarfs provide excellent targets thanks to their small host star radii and semi-major axes. Furthermore, mini-Neptunes have large atmospheric scale heights and planet/star size ratios, making them especially conducive to atmospheric characterisation. K2-18 b is a prime example of such a planet, and its atmosphere has been characterised through transmission spectroscopy, leading to a strong detection of water vapour (Benneke et al., 2019b; Tsiaras et al., 2019). Using the observed spectrum and bulk properties (mass and radius), Madhusudhan et al. (2020) placed joint constraints on the atmosphere and interior of K2-18b and found several solutions allowing for liquid water at habitable temperatures and pressures at its surface. The Transiting Exoplanet Survey Satellite (TESS) is expected to find more planets of this type, with several existing candidates and some already confirmed (e.g. Günther et al., 2019).

Traditional definitions of the habitable zone are typically designed for terrestrial planets with thin atmospheres (Kasting et al., 1993; Kopparapu et al., 2017; Meadows and Barnes, 2018), for which the equilibrium temperature can be comparable to the surface temperature. This is not the case for mini-Neptunes, which host H₂-rich envelopes and whose surfaces can occur at much deeper/higher pressures. Due to the greenhouse effect of H₂, the temperatures at these higher pressures can be significantly hotter than the equilibrium temperature of the planet (Pierrehumbert and Gaidos, 2011; Koll and Cronin, 2019). Habitability on mini-Neptunes therefore relies on physical processes which can counter this heating effect, such as clouds and hazes.

In this section, we explore atmospheric conditions under which K2-18 b could host liquid water on its surface at habitable temperatures and pressures. Liquid water on the surface is typically considered to be a nominal requirement for habitability (e.g. Meadows and Barnes, 2018). Furthermore, it is known that extremophiles on Earth are able to survive at temperatures up to 395 K and pressures up to 1250 bar (Merino et al., 2019). In what follows, we therefore refer to temperatures $\lesssim 395$ K at pressures $\lesssim 1250$ bar as habitable conditions. We begin by discussing the requirements for a liquid ocean in Section 5.4.1. Since the atmospheric H₂O abundance above an ocean can be a complex function of altitude (as seen on Earth, e.g., Pierrehumbert et al. 2006), we then explore

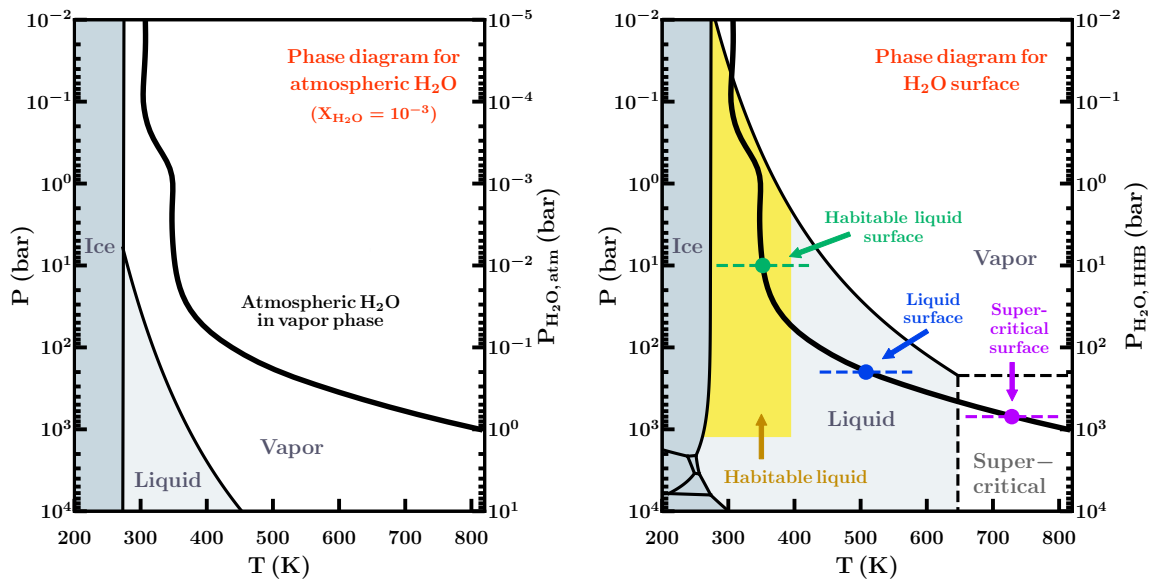


Fig. 5.6 Schematic of an atmospheric P - T profile (bold black lines) and the corresponding phases of the atmospheric H₂O (left panel) and of the 100% H₂O layer beneath the atmosphere (right panel). Left panel: background shows the phase diagram for the atmospheric H₂O assuming a fixed mixing ratio of 10⁻³. For the P - T profile shown here, the atmospheric H₂O is in the vapor phase throughout. Right panel: background shows the phase diagram for 100% H₂O, corresponding to the phase at the surface of the 100% H₂O layer beneath the atmosphere. The region of the liquid phase satisfying $P < 1000$ bar, $T < 395$ K is highlighted in yellow and corresponds to conditions known to be habitable for extremophiles on Earth (e.g. Merino et al., 2019). Depending on the location of the H₂O layer/H₂-rich atmosphere boundary (HHB), the surface of the H₂O layer in this example can be in the liquid phase (at habitable or inhabitable temperatures) or the supercritical phase. These scenarios are marked by the green, blue and purple dashed lines and circles, respectively. In both panels, the left y-axis (P) corresponds to the total atmospheric pressure while the right y-axes ($P_{\text{H}_2\text{O, atm}}$ and $P_{\text{H}_2\text{O, HHB}}$) show the partial pressure of H₂O in the atmosphere (left panel) and the total pressure of H₂O at the HHB (right panel), respectively. In the following figures, the H₂O phase diagram is always shown for the HHB, as shown in the right panel here.

atmospheric P - T profiles for two end-member scenarios: fixed metallicity in Section 5.4.2 and 100% relative humidity in Section 5.4.3.

5.4.1 Conditions for an ocean

An essential condition for the presence of a water ocean in a planet is the availability of a water reservoir beneath the atmosphere at the right thermodynamic conditions. Several works have explored the possibility of water oceans in super-Earths and water worlds with a large H_2O layer in the interior (e.g., Léger et al., 2004; Rogers and Seager, 2010b; Rogers et al., 2011; Zeng and Sasselov, 2013; Thomas and Madhusudhan, 2016) as well as ice giants with mixed-composition interiors that require sufficiently large H_2O mixing ratios at low photospheric temperatures (e.g., Wiktorowicz and Ingersoll, 2007). In the present work, we assume the presence of a water layer below the H_2 -rich atmosphere, following the recent constraints on the mini-Neptune K2-18b from Madhusudhan et al. (2020). Whether or not a liquid water ocean is possible below the atmosphere, thus, depends on the pressure-temperature conditions at the bottom of the atmosphere as we model here.

For K2-18b, Madhusudhan et al. (2020) find that the atmospheric mass fraction is between $\lesssim 10^{-6}$ and $\sim 6 \times 10^{-2}$, allowing surface pressures as low as ~ 1 bar for some atmospheric P - T profiles. In their interior model, a 100% H_2O layer exists below the atmosphere, similar to other models in the literature for super-Earths and mini-Neptunes (e.g. Nettelmann et al., 2011; Rogers et al., 2011; Valencia et al., 2013). As discussed in Section 5.1, not all mini-Neptunes would have masses and radii consistent with habitable pressures ($\lesssim 1000$ bar) below their H_2 -rich atmospheres. However, mini-Neptunes with bulk densities similar to or higher than K2-18 b could allow for habitable surface pressures.

In what follows, we use the term HHB, as in Madhusudhan et al. (2020), to denote the boundary between the H_2O surface and the H_2 -rich atmosphere, i.e., the pressure level where the atmosphere terminates and the 100% H_2O layer begins. Just above the HHB, the H_2O abundance is that of the atmosphere, i.e. lower than 100%. At the HHB and below, the H_2O abundance is 100%, i.e., in the water layer. Therefore, the phase of water can change across the HHB depending on the pressure and temperature conditions at the HHB; for example, from vapour in the atmosphere to liquid in the 100% H_2O layer below. To assess the phase of the 100% H_2O layer just below the HHB, we compare model atmospheric P - T profiles to the phase diagram of 100% H_2O (Fei et al., 1993; Wagner and Pruß, 2002; Seager et al., 2007; French et al., 2009; Sugimura et al., 2010; Thomas and Madhusudhan, 2016), as shown in the right panel of Figure 5.6. Note that this phase diagram does not correspond to the atmospheric H_2O , as the partial pressure of H_2O in the atmosphere is less than the total pressure (see left panel of Figure 5.6). Instead, at each pressure and temperature it

corresponds to the phase of H₂O at the surface of the 100% H₂O layer below assuming that the bottom of the atmosphere is at that pressure and temperature.

5.4.2 Effects of cloud/hazes, metallicity and T_{int}

In this section, we explore the effects of clouds, hazes, metallicity and internal temperature on the potential habitability of K2-18 b. For these models, we assume a fixed atmospheric metallicity informed by the transmission spectrum of K2-18 b, as described below. The assumed H₂O abundance is largely sub-saturated in these models, representing one extreme in relative humidity, which is known to be a complex function of many parameters on Earth (e.g. Pierrehumbert et al., 2006). We then explore models with a saturated H₂O abundance in Section 5.4.3.

Our model P - T profiles are shown in figures 5.7 and 5.8 and discussed further below. At any given pressure, P , in the P - T profile, the comparison to the H₂O phase diagram indicates the phase at the surface of the H₂O layer if the HHB occurred at that pressure (i.e., $P_{\text{HHB}} = P$), as shown in the right panel of Figure 5.6. Note that we do not assume a particular location for the HHB in our models. Instead, we calculate the atmospheric P - T profile up to 1000 bar, and see where the HHB would cross the H₂O phase diagram for different values of P_{HHB} . For example, if a model P - T profile crosses the liquid phase for 100% H₂O at 10 bar, this suggests that if the HHB were to occur at 10 bar, the surface of the 100% H₂O layer would be liquid.

Madhusudhan et al. (2020) show that $P_{\text{HHB}} \gtrsim 1$ bar for K2-18 b. That is, the surface between the atmosphere and the 100% H₂O layer can exist at pressures $\gtrsim 1$ bar. Therefore, atmospheric P - T profiles which intersect with the liquid H₂O phase at pressures $\gtrsim 1$ bar could allow for surface liquid water below the atmosphere at that pressure. Furthermore, if the P - T profile intersects the liquid phase at < 395 K, this liquid surface water would be at habitable temperatures. We reiterate that the phase diagram of H₂O shown here does not correspond to the phase of H₂O in the atmosphere. Instead, it corresponds to the phase of the 100% H₂O layer at the HHB, just below the atmosphere.

In order to generate atmospheric P - T profiles for K2-18 b, we use spectroscopic constraints on the atmospheric chemistry from Madhusudhan et al. (2020). Madhusudhan et al. (2020) find an atmospheric H₂O abundance of ~ 1 - $100\times$ solar, with no detection of any other species. We therefore include only H₂O in our models, varying its metallicity from 1 to $100\times$ solar. In all our models, we also include salt (KCl/ZnS) clouds and water ice clouds wherever they are thermochemically expected to occur (Section 5.2). Water ice cloud particle sizes can have a wide range of modal particle sizes (e.g. Morley et al., 2014); we tried a range of sizes and in the models presented here use particle sizes in the range

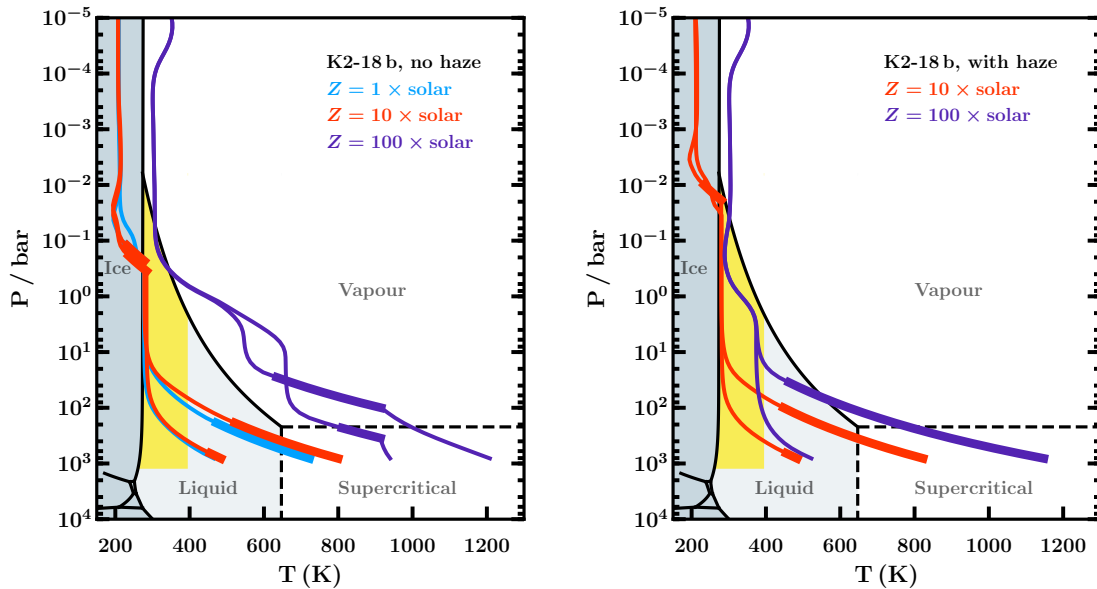


Fig. 5.7 Model dayside P - T profiles for K2-18 b, for a range of metallicities and internal temperatures, that could allow habitable conditions below the atmosphere. For each metallicity, the cooler/hotter profile at 1000 bar corresponds to $T_{\text{int}}=25$ K/50 K. Left panel: models with no haze. Models with $1\times$ and $10\times$ solar metallicity enter the water ice phase so we include ice clouds where they are thermodynamically required (cloud bases in the range 0.2-0.3 bar). The $100\times$ solar metallicity model has KCl and ZnS clouds in the deep atmosphere (cloud bases between 100 and 1000 bar). Right panel: models with hazes. The $10\times$ solar metallicity model with $T_{\text{int}}=25$ K has haze equivalent to $500\times$ H_2 Rayleigh scattering, while the other models have $1000\times$ H_2 Rayleigh scattering. Models with $10\times$ solar metallicity have water ice clouds (cloud bases in the range 0.01-0.03 bar). The phase diagram of H_2O is shown in the background, corresponding to the surface conditions of a 100% H_2O layer beneath the H_2 -rich atmosphere, i.e., at the HHB (see section 5.4 and right panel of Figure 5.6). The shaded yellow regions show habitable conditions in Earth's oceans, with $T < 395$ K and $P < 1250$ bar (Merino et al., 2019). Models passing through the yellow region could therefore potentially host habitable liquid water at the HHB.

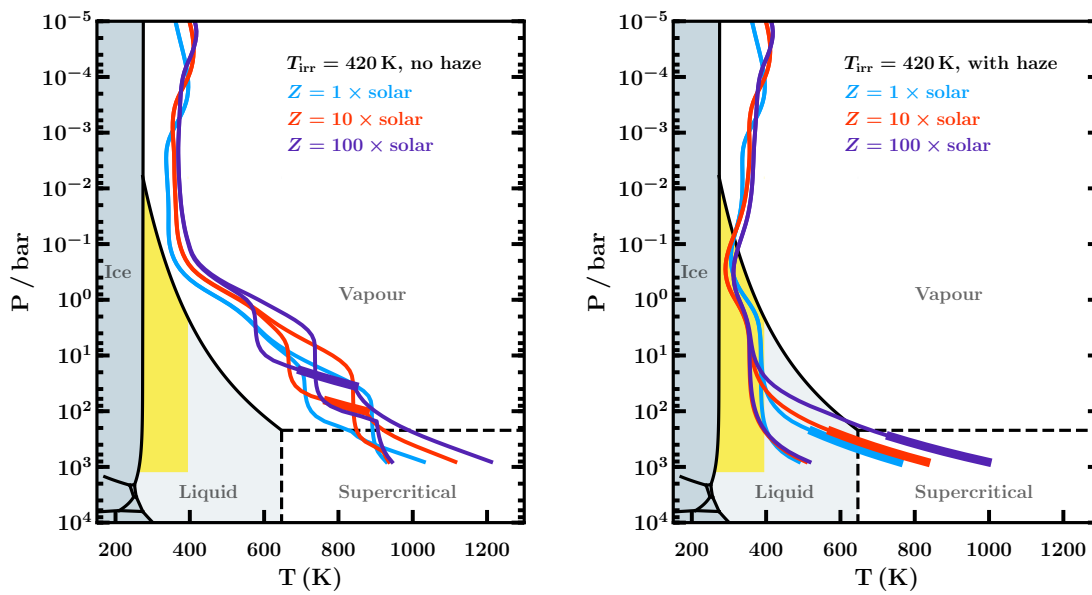


Fig. 5.8 Same as Figure 5.7, but for a planet resembling K2-18 b with an irradiation temperature of 420 K (i.e. receiving $\sim 2.5\times$ more incident flux). Left panel: models with no hazes. Each model includes KCl and ZnS clouds with cloud base pressures between 30 and 1000 bar. Right panel: models including hazes. $1\times$ solar models include haze equivalent to $3000\times$ H_2 Rayleigh scattering, while the other models have $10000\times$ H_2 Rayleigh scattering. Strong haze opacity is required for the P - T profiles to enter the shaded yellow region, where a H_2O surface beneath the atmosphere could host habitable liquid water.

1-3 μm . The base of each ice cloud is located approximately where the atmospheric H_2O enters the ice phase (as described in Section 5.2.3). In the models shown in Figure 5.7, the cloud bases lie in the range 0.01-0.2 bar. As described in Section 5.2, we calculate models for two end-member values of T_{int} : 25 and 50 K.

We find that a range of atmospheric conditions allow for habitability in K2-18 b. Madhusudhan et al. (2020) find habitable solutions for two atmospheric P - T profiles. Here, we explore a wider range of parameters and their impact on potential habitability. Figure 5.7 shows model P - T profiles for K2-18 b both with and without hazes (right and left panels, respectively). As expected, higher-metallicity models are hotter and host salt clouds in the lower atmosphere, while the low-metallicity models are cooler. The haze-free models with 1 and $10\times$ solar metallicity are sufficiently cool that ice clouds are present in the upper atmosphere, which further cools the deeper regions of the atmosphere (light blue and red lines in left panel of Figure 5.7, respectively). Higher-metallicity models with hazes also remain cool at high pressures (right panel of Figure 5.7). For both the hazy models and the haze-free 1 and $10\times$ solar models, a H_2O surface beneath the atmosphere could potentially host habitable liquid surface water if this surface occurs at the right pressure (see shaded yellow regions in figure 5.7).

We find that a planet resembling K2-18 b but with a higher irradiation temperature can also be potentially habitable. Figure 5.8 shows model P - T profiles for a planet like K2-18 b but with $T_{\text{irr}}=420$ K rather than 332 K (i.e., receiving $\sim 2.5\times$ more incident flux, achieved by decreasing the semi-major axis). With no hazes or ice clouds (left panel), these profiles reach high temperatures deep in the atmosphere. In this case, the models do not cross the ‘potentially habitable’ shaded yellow region. However, models with strong haze opacity (right panel) are significantly cooled such that habitable liquid water could exist at the surface of a H_2O layer beneath the atmosphere. Therefore, mini-Neptunes similar to but somewhat warmer than K2-18 b could also have the potential for habitability, although stronger optical opacity is needed to cool such planets sufficiently. We also note that throughout this chapter we have assumed no day-night redistribution of the incident radiation. Therefore, our habitability estimates are conservative. Allowing for efficient day-night redistribution could allow such planets at even higher T_{irr} to be potentially habitable. We discuss this further in section 5.6.

5.4.3 Effects of H_2O saturation

In this section, we explore models for K2-18 b for which the atmosphere is saturated with H_2O vapour, representing the upper extreme in relative humidity. We consider two surface pressures corresponding to the base of the atmosphere: $P_{\text{HIB}}=100$ bar (left panel of Figure

5.9) and $P_{\text{HHB}}=1$ bar (right panel of Figure 5.9). For each surface pressure, we consider a range of haze opacities and $T_{\text{int}}=25\text{-}50$ K to explore how these parameters affect the habitability of the ocean.

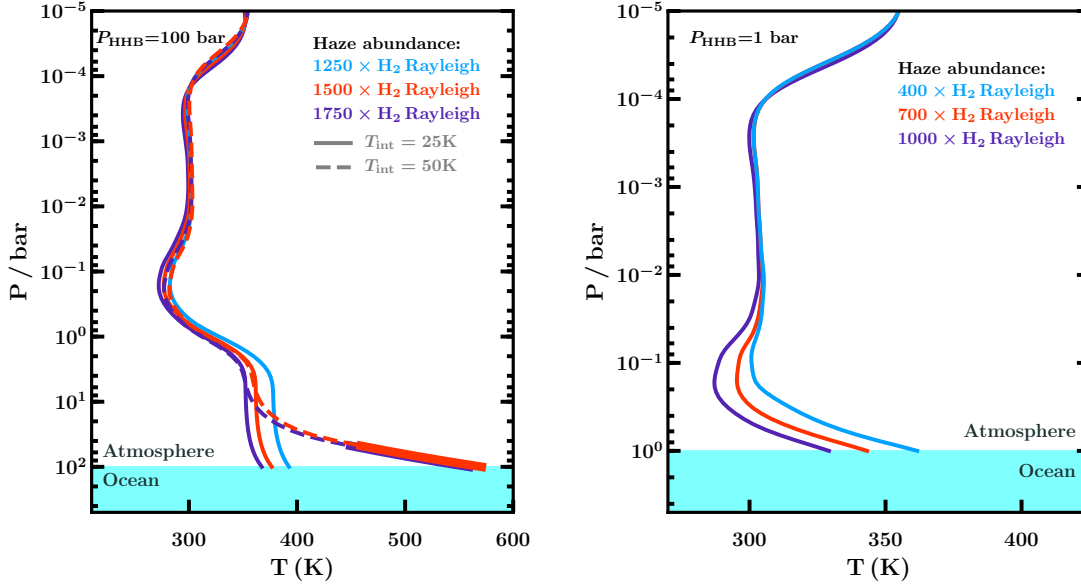


Fig. 5.9 Model dayside P - T profiles for K2-18 b with 100% relative humidity which allow for a liquid ocean at the surface. Surface temperatures below ~ 400 K could allow for habitable conditions for Earth-like aquatic life (e.g. Merino et al., 2019). Left panel: Models with an ocean-atmosphere boundary (HHB) at 100 bar and varying haze abundances and internal temperatures (see legend). Right panel: Models with the HHB at 1 bar and varying haze abundances; these P - T profiles are not sensitive to T_{int} between 25-50 K. The atmospheric H_2O abundance is fully saturated between the ocean surface and the cold trap (see section 5.4.3).

We assume the atmosphere to be 100% saturated between the ocean surface and the cold trap at higher altitudes. The mixing ratio of water vapor follows the saturation curve up to the cold trap where it reaches the minimum value in saturation for the corresponding temperature profile. The pressure level at this minimum is $\sim 0.1\text{-}0.3$ bar for most cases, but can be as deep as 20 bar for cases with $P_{\text{HHB}}=100$ bar and $T_{\text{int}}=50$ K. Beyond the cold trap the H_2O saturation vapour pressure begins to increase with altitude and the actual H_2O mixing ratio there depends on various factors including the efficiency of atmospheric mixing (e.g. Pierrehumbert et al., 2006). At altitudes beyond the cold trap (i.e., at lower pressures) we assume the H_2O mixing ratio to be constant at either the minimum value at the cold trap or $100\times$ solar, whichever is smaller. The maximum abundance of $100\times$ solar

is set by the upper-limit on the H₂O abundance at the photosphere (~1-100 mbar level) derived from the observed transmission spectrum of K2-18 b (Madhusudhan et al., 2020).

We note that in some cases, especially when the temperature structure is nearly isothermal in the lower atmosphere, a second cold trap can occur close to the ocean surface. Here, the saturation vapour pressure increases with altitude starting right at the surface of the ocean, before decreasing again higher up in the atmosphere and leading to the more conventional cold trap there as discussed above. For such “surface cold traps” we assume that atmospheric mixing easily overcomes the cold trap and causes the H₂O abundance to remain saturated in the lower atmosphere.

In Figure 5.9, we show models for which the surface of the 100% H₂O layer is in the liquid phase. For a surface pressure of 100 bar (left panel of Figure 5.9), we find several cases which allow for habitable temperatures at the ocean surface (i.e. $\lesssim 400$ K). In particular, models with $T_{\text{int}}=25$ K and haze abundances above $\sim 1250 \times \text{H}_2$ Rayleigh scattering satisfy this condition. Models with higher T_{int} and/or less haze have warmer surface temperatures but still allow for a liquid ocean. We note that since the definition of habitability used here is based solely on Earth-like life, these warmer temperatures do not preclude unknown life forms which may have adapted to more extreme conditions.

For a surface pressure of 1 bar (right panel of Figure 5.9), we find that even more solutions allow for habitable conditions at the ocean surface. Firstly, at these low pressures, a T_{int} in the range 25-50 K does not affect the P - T profile, allowing for more habitable cases. Secondly, much less haze is needed to achieve a habitable surface temperature ($\gtrsim 400 \times \text{H}_2$ Rayleigh scattering) as the atmosphere is thinner and has less greenhouse warming. We therefore find that despite the high relative humidity (i.e., 100% saturation) above the ocean, a range of surface pressures, haze opacities and T_{int} allow for potentially habitable conditions in planets like K2-18 b.

5.5 Observability

As we have shown above, mini-Neptunes such as K2-18 b could provide potential targets in the search for habitability in exoplanets. In particular, their observability with current and future facilities arguably makes them optimal targets for such studies. Recent observations of K2-18 b (Benneke et al., 2019b; Tsiaras et al., 2019) have already shown that current facilities are able to observe temperate mini-Neptunes with transmission spectroscopy. Furthermore, Madhusudhan et al. (2020) showed that for K2-18 b, a H₂O layer beneath the atmosphere could have a surface as shallow as ~1 bar and surface temperatures low enough for habitable liquid water. In this section, we investigate how thermal emission

spectra of such planets can be used to learn about their atmospheres and to place limits on their surface conditions. In particular, we explore how observations using JWST/MIRI (Rieke et al., 2015; Kalirai, 2018) can constrain both potentially habitable and warmer mini-Neptunes.

5.5.1 Constraints on habitability

In this section, we consider how atmospheric thermal emission observations can help to constrain the potential habitability of surface conditions in temperate mini-Neptunes similar to or smaller than K2-18 b (see Section 5.1). In particular, thermal emission spectra can provide information about the temperature in the photosphere. The P - T profiles in Figures 5.2 and 5.3 show that the photospheres of these atmospheres can extend as deep as ~ 0.1 -1 bar, while high-altitude clouds can raise the photosphere to shallower pressures. Below the photosphere, different P - T profiles can have a variety of gradients, from more isothermal profiles (e.g. due to ice clouds or haze) to relatively steep ones (e.g. due to high metallicity and/or low optical opacity), as demonstrated in Figure 5.7. Therefore, the photospheric temperature provides a lower limit to the temperature of a potential surface beneath the atmosphere. For example, if the brightness temperature of the atmosphere in an observed band is >400 K, the temperature at deeper pressures will be even higher, and habitable conditions are less likely. However, a photospheric temperature of ~ 300 K could allow habitable conditions if the P - T profile is isothermal below the photosphere, though a steeper temperature gradient could result in surface temperatures too high for habitability. For models with ice clouds, a high cloud opacity can result in the photosphere occurring at very low temperatures, e.g. $\lesssim 250$ K, while making the P - T profile isothermal below the cloud base and resulting in potentially habitable conditions at higher pressures. Observing such a low photospheric temperature, i.e. below the freezing point of H_2O , could therefore suggest the presence of such clouds and the possibility of a habitable surface.

For temperate mini-Neptunes with the potential for habitability, the emergent flux peaks in the mid-infrared ($\gtrsim 10 \mu\text{m}$), and is therefore more easily observable at these wavelengths. Figures 5.4 and 5.5 show that the spectrum of a planet with irradiation temperature ~ 350 K typically exceeds 10 ppm for wavelengths $\gtrsim 10 \mu\text{m}$. Assuming optimistic uncertainties of ~ 10 ppm, JWST observations in the mid-infrared (i.e. using MIRI) will be able to characterise these cool atmospheres and place limits on their habitability. Another advantage of this wavelength range is that the spectrum in the mid-infrared is predominantly sensitive to irradiation temperature, and is less sensitive to composition (see Section 5.3.2). This can be seen in Figures 5.4 and 5.5, where model spectra with

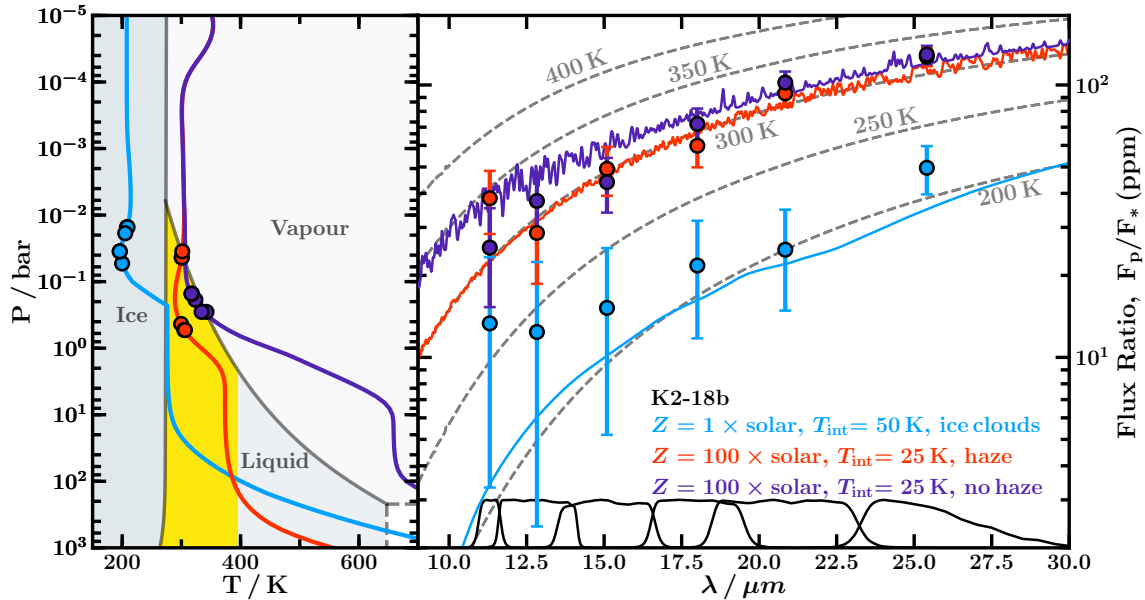


Fig. 5.10 Observability of temperate and potentially habitable mini-Neptunes with JWST/MIRI. Left: Model P - T profiles for K2-18 b with varying metallicities (1 and $100\times$ solar) and internal temperatures ($T_{\text{int}}=25$ and 50 K). Clouds are included wherever they are thermodynamically expected (see Figure 5.7 for details). Phase diagram for 100% H_2O shows the phase that a water layer would have at the boundary between the H_2 -rich atmosphere and H_2O interior (HHB). The yellow region highlights pressures and temperatures where this water would be liquid and habitable. The coloured circles denote brightness temperatures in different JWST/MIRI photometric bands described in the right panel. Right: Model spectra corresponding to the P - T profiles in the left panel. Simulated photometric data from the JWST/MIRI filters at wavelengths $>10 \mu\text{m}$ are shown for each spectrum (coloured circles, see Section 5.5), with best-case error bars of 10 ppm. The brightness temperatures for the central unperturbed value of each photometric point are plotted on the corresponding P - T profile in the left panel, showing the depths probed by each measurement. Sensitivity curves for each filter are shown in black. Grey dashed lines show blackbody curves corresponding to planetary temperatures of 200, 250, 300, 350 and 400 K.

different metallicities converge at longer wavelengths. The mid-infrared spectrum is therefore optimal for determining the temperature in the photosphere, regardless of its chemistry.

For a planet with mass and radius low enough for habitable surface pressures (e.g. K2-18 b), the photospheric temperature measured in the mid-infrared can therefore provide a quick metric for assessing whether a mini-Neptune could potentially host habitable conditions, and can rule out atmospheres which are likely too hot for habitability. Promising candidates can then be investigated further, e.g. using transmission spectroscopy to infer chemical compositions. Photometry provides an ideal way to measure this metric. In what follows, we explore how JWST/MIRI photometry can be used to measure photospheric temperature and distinguish potentially habitable planets from those which are too hot.

5.5.2 JWST for mini-Neptune habitability

JWST/MIRI will allow both photometric and spectroscopic observations beyond $10\ \mu\text{m}$, where potentially habitable mini-Neptunes can most easily be observed. Here, we assess how MIRI photometry can be used to constrain the photospheric temperatures of such planets. To do this, we simulate photometric data with the six MIRI photometric bands which probe wavelengths above $10\ \mu\text{m}$ (F1130W-F2550W; Rieke et al. 2015; Bouchet et al. 2015) for a range of model atmospheres. The simulated photometric data are calculated by binning each model spectrum according to the instrument spectral response (Glasse et al., 2015). We assume best-case error bars of 10 ppm, which is a reasonable estimate for JWST photometry considering that the Hubble Space Telescope (HST) WFC3 spectrum of K2-18 b is known to a precision of ~ 25 ppm at $R\sim 40$ (Benneke et al., 2019b; Tsiaras et al., 2019). Figure 5.10 shows these data alongside the P - T profiles for each model. For each photometric point, we also calculate the brightness temperature probed (using equation 3.3) and indicate this on the corresponding P - T profile; this gives an indication of the pressure being probed by each data point.

Figure 5.10 shows the brightness temperatures corresponding to the six photometric bands and the pressures which they probe for each P - T profile. In particular, for the model with ice clouds, the pressures probed are limited by the high optical depth of the cloud and are shallower than 0.01 bar. Conversely, for the warmest models with no ice clouds, the photometric points probe deeper than 0.1 bar. In all three cases, the brightness temperatures of the photometric points are cooler than the temperatures at higher pressures, where a surface could be expected to exist (e.g. $\gtrsim 1$ bar, Madhusudhan et al. 2020). As such, the photometric data can provide a lower limit on the temperature of such a surface.

Figure 5.10 also shows that profiles whose photospheric temperatures differ by ~ 100 K can easily be distinguished using MIRI photometry beyond $10 \mu\text{m}$. Brightness temperatures $\gtrsim 300$ K (e.g. for the warmer models in Figure 5.10) correspond to several tens - ~ 100 ppm, which can be measured precisely if the error bars are ~ 10 ppm. Brightness temperatures of ~ 200 - 250 K (e.g. for the coolest model in Figure 5.10) can also be measured precisely using the longer-wavelength MIRI filters ($\gtrsim 17.5 \mu\text{m}$), and can easily be distinguished from the warmer models. Indeed, the brightness temperature of this cooler model (~ 200 K) can be constrained to within < 50 K using the F2550W filter ($25.5 \mu\text{m}$) and assuming 10 ppm uncertainties. As such, MIRI photometry provides a way to place lower limits on surface temperature and to rule out atmospheres which are likely too hot to host habitable surfaces. Furthermore, a non-detection with the longest-wavelength MIRI photometric band (F2550W) could suggest a very cool photospheric temperature and motivate further observations as habitable temperatures could be present deeper in the atmosphere.

While we have used K2-18 b as a case study, these results also apply to similar planets around other M-dwarfs. Given the photospheric temperature of a planet, the observed flux ratio depends on the effective temperature of the star and is higher for cooler stars. Since K2-18 is an M2.5 V star, this case study provides a conservative estimate of the observability of mini-Neptunes orbiting M-dwarfs; later types can result in stronger signals.

5.5.3 JWST for warmer mini-Neptunes

Mid-infrared atmospheric observations can also be used to constrain the chemical and thermal properties of warmer mini-Neptunes. While these planets may not host habitable surfaces, their higher temperatures allow more detailed observations and constraints on their properties. In turn, such constraints can provide boundary conditions for internal structure models or give clues about their formation. Furthermore, since cooler mini-Neptunes are less suited to chemical characterisation with thermal emission, their warmer counterparts may help to constrain the dayside compositions of mini-Neptunes as a population. In this section, we investigate the observability of warm mini-Neptunes with JWST/MIRI using GJ 3470 b as a case study.

To model GJ 3470 b, we use the bulk properties given in Section 5.2.4 and spectroscopic atmospheric constraints from Benneke et al. (2019a). Benneke et al. (2019a) find a significant detection of H_2O and constrain its abundance to be that expected from a solar metallicity atmosphere with an uncertainty of roughly ± 1 dex. They also infer the presence of CO and/or CO_2 from the emission spectrum of the planet observed with Spitzer IRAC 1 and IRAC 2. However, since both of these species result in absorption

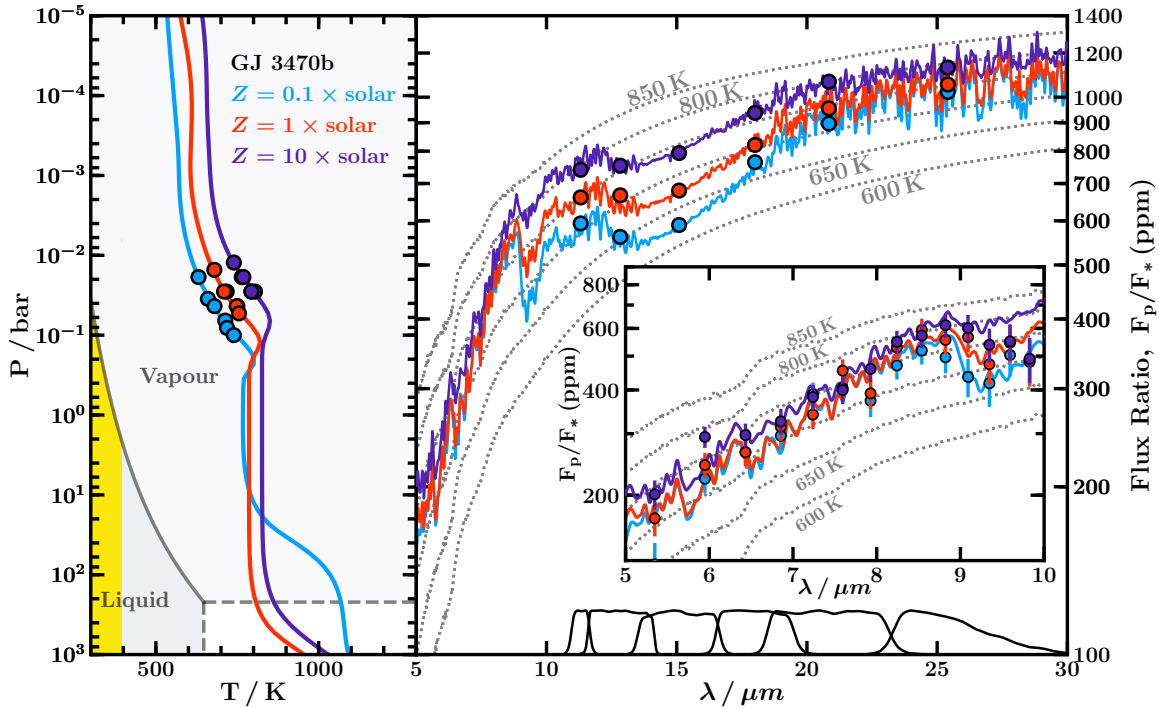


Fig. 5.11 Observability of thermal emission from warm mini-Neptunes with JWST/MIRI. Left panel: model P - T profiles for GJ 3470 b with varying metallicities (0.1, 1 and $10 \times$ solar) and $T_{\text{int}}=30$ K (see Section 5.5.3). Phase diagram shows the phase of a 100% H_2O layer at the HHB, as in Figure 5.10. The coloured circles denote brightness temperatures in different JWST/MIRI photometric bands described in the right panel. Right panel: Spectra corresponding to these P - T profiles, with simulated MIRI photometry data (coloured circles, see Section 5.5). Brightness temperatures for the central value of each photometric point are plotted on the corresponding P - T profile in the left panel. We assume error bars of 10 ppm, which are smaller than the data symbols. Sensitivity curves for each MIRI filter used are shown in black, as in Figure 5.10. Inset: Enlarged view of spectra in the range 5-10 μm . Simulated MIRI LRS data, generated using PandExo (Batalha et al., 2017), are shown as coloured circles and error bars. Dashed grey lines show blackbody curves for planetary temperatures of 600, 650, 700, 750, 800 and 850 K.

features in the IRAC 2 4.5 μm bandpass, their abundances are degenerate with each other and form a knee-like degeneracy. We therefore do not vary the abundances of CO and CO₂ in our models and use the median mixing ratios inferred by Benneke et al. (2019a), i.e. $10^{-3.04}$ and $10^{-2.71}$, respectively, as the enhancement of one would merely lead to the depletion of the other. Benneke et al. (2019a) further infer a depletion of CH₄ and NH₃ in GJ 3470 b, so we omit these species from our models. Since the abundances of CO and CO₂ relative to H₂O are significantly higher than expected from equilibrium chemistry, we choose to use constant-with-depth abundances for these three species. We also include KCl and ZnS clouds as described in Section 5.2, with cloud bases at 0.3 bar. The P - T profiles and spectra for these models are shown in Figure 5.11. As in Figure 5.10, we also show simulated MIRI photometry assuming uncertainties of 10 ppm, which allows high signal-to-noise measurements of the emergent flux and photospheric temperature.

Figure 5.5 shows that a model spectrum with $T_{\text{irr}}=800$ K exceeds an optimistic uncertainty of 10 ppm at wavelengths greater than ~ 3 μm . In this wavelength range, the MIRI Low Resolution Spectroscopy (LRS) and Medium Resolution Spectroscopy (MRS) can be used to observe the thermal emission from these planets. In Figure 5.11, we show simulated MIRI LRS data for the model spectra of GJ 3470 b. We simulate this data using PandExo (Batalha et al., 2017) for the MIRI LRS slitless mode. For the error bars we assume a single eclipse, and the data are binned by a factor of 10. Absorption features due to H₂O, CH₄, CO₂ and HCN are present in this spectral range and, using retrieval analyses, abundances of these species could be inferred from such spectra. For example, a strong absorption feature is visible at ~ 9 -10 μm . In addition to chemical information, the emission spectrum can also be used to constrain the P - T profile of the planet. In the examples shown in Figure 5.11, the spectra probe pressures within the range ~ 0.01 -0.1 bar, meaning that the temperature profile in this range could be inferred using retrieval techniques.

5.6 Discussion & Conclusions

Mini-Neptunes in the habitable zones of M-dwarfs can provide an excellent opportunity to study temperate exoplanets and their potential habitability. In particular, Madhusudhan et al. (2020) showed that the mass, radius and atmospheric properties of the habitable-zone mini-Neptune K2-18 b allow it to have a H₂O surface beneath the atmosphere with a surface pressure as low as ~ 1 bar, potentially with habitable conditions. In this study, we explore the effects of a range of atmospheric parameters on the thermal profiles and spectra of such planets. We investigate three primary aspects of mini-Neptune atmospheres: (i) the diversity of atmospheric temperature structures, with implications

for energy transport, chemistry and their emergent spectra, (ii) thermodynamic conditions deep in the atmosphere, which impact the potential for habitability as well as boundary conditions for internal structure models, and (iii) their observability with thermal emission spectra, including constraints on potential habitability.

We begin by exploring the diversity of temperature structures and emission spectra of mini-Neptunes as a function of several atmospheric parameters. The parameters we consider are irradiation temperature, internal temperature, metallicity and cloud/haze properties. We find that for typical internal temperatures of mini-Neptunes, the radiative-convective boundary occurs well below the photosphere. As a result, vertical mixing in the photosphere is more likely to be caused by eddy mixing rather than convection. We also find that strong optical opacity due to clouds/hazes can result in an isothermal temperature structure beneath the photosphere, which can maintain cool temperatures to high pressures, with implications for habitability on deep surfaces. For all of the models we consider, which have irradiation temperatures ≥ 350 K, we further find that the emergent spectra are above the 10 ppm level at wavelengths $> 10 \mu\text{m}$. This means that the emission spectra of such mini-Neptunes could be observable with JWST/MIRI, which we discuss below.

We also apply our atmospheric model to the habitable-zone mini-Neptune K2-18 b to assess its atmospheric conditions and potential habitability. We consider a range of physically-motivated thermal profiles by varying metallicity, internal temperature and haze abundance. We compare our P - T profiles to the phase diagram of water in order to assess the phase that a H_2O surface would have given a particular surface pressure. We find that many of our models intersect the liquid or supercritical phases at pressures $\gtrsim 1$ bar, suggesting that liquid or supercritical surface water could be possible on this planet for a range of atmospheric conditions. This has implications for internal structure models of mini-Neptunes as the equation of state of H_2O is strongly temperature-dependent for phases other than ice (Thomas and Madhusudhan, 2016; Madhusudhan et al., 2020).

We also explore atmospheric models for K2-18 b which allow liquid surface water at habitable temperatures and pressures, i.e. $T \lesssim 395$ K and $P \lesssim 1250$ bar, corresponding to the most extreme temperature and pressure conditions habitable for extremophiles on Earth (Merino et al., 2019). Madhusudhan et al. (2020) model the atmosphere and interior of K2-18 b and find that, for two atmospheric P - T profiles, solutions with habitable liquid water at the surface are possible. Here, we explore a variety of atmospheric models for K2-18 b spanning a range of metallicities, internal temperatures and haze opacities and find several solutions which allow habitable liquid water at the surface. We also consider a hypothetical planet resembling K2-18 b but with $T_{\text{irr}}=420$ K rather than 332 K (i.e., receiving

$\sim 2.5\times$ more incident flux). We find that, despite its hotter irradiation temperature, several model solutions for this planet also allow liquid surface water at habitable temperatures and pressures. In these scenarios, stronger optical scattering is needed to sufficiently cool a planetary surface. These results suggest that mini-Neptunes throughout the traditionally-defined habitable zone could potentially host habitable conditions, depending on their atmospheric properties and surface pressures.

In our current models, optical scattering due to clouds/hazes is necessary to cool the lower atmosphere to habitable temperatures. In principle, some of the dayside energy may also be redistributed to the nightside, thereby cooling the dayside atmosphere. Here, we have conservatively assumed that any redistribution of the stellar irradiation from the dayside to the nightside occurs in the interior, below the atmosphere. In principle, where the interior-atmosphere boundary is deep enough, the day-night energy redistribution can occur in the atmosphere, as is known to occur in irradiated gas giants (Showman et al., 2009). In the context of 1-D models, such an effect can be modeled by an artificial energy sink in the dayside atmosphere (e.g. Burrows et al., 2008a). If energy is removed from the day-side at pressures $\lesssim 1000$ bar, this could contribute to cooling the atmosphere at habitable pressures, thereby increasing the chances of habitable conditions in our models. As such, our estimates for habitable conditions in the present work may be conservative. Including such an effect may also mean that less optical opacity is required for habitable conditions to be possible. This can be explored in future work, alongside more complex prescriptions for clouds and hazes, in order to understand the potential habitability of mini-Neptunes in greater detail.

We further note that our current models do not include the effects of water condensation on convection and the temperature profile. Latent heat released by the condensation of water is known to make convection easier in some circumstances (e.g. Pierrehumbert, 2010), resulting in a more isothermal ‘moist’ adiabat. Conversely, in atmospheres where the background gas is lighter than the condensing species (e.g. H_2O condensation in a H_2 -rich atmosphere), condensation can inhibit both moist and double-diffusive convection and result in a super-adiabatic temperature gradient (e.g. Guillot, 1995; Leconte et al., 2017; Friedson and Gonzales, 2017). The ways in which these effects can shape the energy transport and P - T profiles in H_2 -rich atmospheres are not yet fully understood, though future missions to Uranus or Neptune may help to elucidate this Guillot (2019).

Finally, we consider the observability of mini-Neptune thermal emission with JWST, including observable signatures of potentially habitable conditions. We find that photometry with JWST/MIRI could be used to measure the photospheric temperatures of mini-Neptunes such as K2-18 b down to ~ 200 K assuming 10 ppm error bars. Based on

our models, we find that photospheric temperatures below the freezing point of H₂O suggest the presence of ice clouds and could be a sign of temperate conditions below the atmosphere. Photospheric temperatures of $\sim 300\text{-}400$ K can also be a sign of habitable conditions below the atmosphere, though this depends on the temperature gradient at higher pressures. This gradient is driven by several factors including infrared opacity and the presence of hazes/clouds. However, photospheric temperatures $\gtrsim 400$ K typically imply even hotter, and therefore non-habitable, conditions at higher pressures.

Our models therefore show that MIRI photometry can provide a simple way to establish whether a mini-Neptune such as K2-18 b could potentially host habitable conditions, guiding follow-up observations. For example, transmission spectroscopy could provide more detailed chemical constraints which in turn could be used to provide further insight into the habitability of the planet (e.g. Seager et al., 2013; Bains et al., 2014; Meadows and Barnes, 2018). In addition to temperate, potentially-habitable mini-Neptunes, we also explore the observability of warmer mini-Neptunes with JWST and find that MIRI low resolution spectroscopy could be used to constrain their chemical compositions and thermal profiles.

Our results show that mini-Neptunes similar to or smaller than K2-18 b, whose masses and radii allow for habitable surface pressures, could potentially host habitable conditions beneath their H₂-rich envelopes for a wide range of atmospheric parameters. Since these planets are more easily observable than temperate terrestrial planets, they arguably represent optimal targets for the study of habitability in exoplanets. Furthermore, JWST/MIRI could provide initial constraints on the habitability of such mini-Neptunes.

6

Atmospheric Retrieval of Rocky Exoplanets in Thermal Emission

Having explored giant planet and mini-Neptune atmospheres in previous chapters, we now arrive at the low-mass end of the exoplanet mass range: rocky exoplanets¹. As observational capabilities continue to improve, the characterisation of rocky exoplanet atmospheres is becoming possible. Unlike more massive exoplanets, rocky exoplanets can host a range of secondary, high-mean-molecular-weight atmospheric compositions, which in turn may be indicative of the planet's evolutionary history and surface/interior processes. While the small scale heights of such atmospheres make their characterisation more challenging, emission spectroscopy is a promising technique to place constraints on their chemical and thermal properties as it is less sensitive to the atmospheric scale height compared to transmission spectroscopy.

In this chapter, we present HyDRo, an atmospheric retrieval framework for thermal emission spectra of rocky exoplanets. HyDRo does not make prior assumptions about the background atmospheric composition (e.g. H₂-rich, as previous emission retrievals have assumed), and can therefore be used to interpret spectra of secondary atmospheres with unknown compositions. We use HyDRo to assess the chemical constraints which can be placed on rocky exoplanet atmospheres using JWST. Firstly, we identify the best currently-known rocky exoplanet candidates for spectroscopic observations in thermal emission with JWST, finding > 30 known rocky exoplanets whose thermal emission will be detectable by JWST/MIRI in fewer than 10 eclipses at $R \sim 10$. We then consider the observations required to characterise the atmospheres of three promising rocky exoplanets across the

¹This work has been submitted for publication in Piette, Madhusudhan & Mandell (submitted to MNRAS).

~400-800 K equilibrium temperature range: Trappist-1 b, GJ 1132 b, and LHS 3844 b. Considering a range of CO₂- to H₂O-rich atmospheric compositions, we find that as few as 8 eclipses of LHS 3844 b or GJ 1132 b with MIRI will be able to place important constraints on the chemical compositions of their atmospheres, including confident detections of CO₂ and H₂O in the case of a cloud-free, Venus-like composition. Similarly, 30 eclipses with MIRI/LRS can allow detections of a cloud-free CO₂-rich or CO₂-H₂O atmosphere on Trappist-1b. HyDRo will be able to place important atmospheric constraints on rocky exoplanets with JWST, providing clues about their geochemical environments.

6.1 Introduction

With the upcoming James Webb Space Telescope (JWST), the next frontier of atmospheric characterisation of exoplanets will turn towards smaller and cooler planets, including rocky exoplanets potentially hosting terrestrial-like secondary atmospheres (e.g. Greene et al., 2016; Lustig-Yaeger et al., 2019; Turbet et al., 2020). In this chapter, we report a new retrieval framework designed to analyse the thermal emission spectra of rocky exoplanets. We further use this framework to assess the ideal targets and observations needed to make important new constraints on rocky exoplanet atmospheric chemistry.

Thermal emission spectroscopy offers an exceptional opportunity to characterise secondary, high- μ atmospheres on rocky exoplanets. While the small scale heights of such atmospheres can be prohibitive for transmission spectroscopy (e.g. Lustig-Yaeger et al., 2019), thermal emission spectroscopy is highly sensitive to atmospheric temperature gradients and molecular absorption. The mid-infrared wavelength range is particularly advantageous in the study of secondary atmospheres given the abundance of molecular features in this range (e.g. Deming et al., 2009; Greene et al., 2016; Madhusudhan, 2019). Furthermore, the signal-to-noise ratio (S/N) achievable for secondary eclipse observations is maximised in the mid-infrared. JWST's Mid-Infrared Instrument (MIRI), with a spectral range of ~5-28 μ m, will therefore provide an unprecedented opportunity to investigate rocky exoplanet atmospheres including their chemical and thermal conditions.

Atmospheric retrievals have revolutionised atmospheric characterisation of exoplanets in the past decade (Madhusudhan, 2018) and will be critical to provide detailed constraints on rocky exoplanet atmospheres. To date, such retrievals have typically been applied to hydrogen-rich atmospheres (e.g. Lee et al., 2012; Line et al., 2013; Waldmann et al., 2015; Wakeford et al., 2017; Gandhi and Madhusudhan, 2018; Barstow et al., 2020) and do not consider secondary atmospheric compositions dominated by non-H species. However, Benneke and Seager (2012) report an agnostic chemical abundance parameterisation

which does not assume a dominant atmospheric component a priori, and has been tested in the context of transmission spectroscopy (Benneke and Seager, 2012, 2013). By using the centred-log-ratio transformation, the parameterisation applies an identical prior probability distribution to each chemical species in the retrieval, allowing it to constrain the compositions of secondary atmospheres.

In this chapter, we present the first atmospheric retrieval framework for the thermal emission spectra of rocky exoplanets. The framework utilises the HyDRA emission retrieval framework of Gandhi and Madhusudhan (2018) and the chemical abundance parameterisation of Benneke and Seager (2012). It includes a range of opacity sources expected in secondary atmospheres, for example allowing for Venus-like and H₂O-dominated compositions. We further identify a large sample of optimal rocky exoplanet candidates for atmospheric characterisation in thermal emission with JWST MIRI. Focusing on three case studies, we use the new retrieval framework to investigate the chemical detections which can be made using JWST MIRI. In particular, we consider a hierarchy of science cases which can be used to systematically confirm/exclude increasingly complex atmospheric states.

In what follows, we describe the new retrieval framework in Section 6.2.1. In Section 6.2.2, we outline the self-consistent atmospheric model used to model rocky exoplanet thermal emission spectra, and use such a model in Section 6.2.3 to validate the retrieval framework. We identify optimal rocky exoplanet candidates for atmospheric characterisation in Section 6.3, and in Section 6.4 we investigate the observability of CO₂ and H₂O in three of the best targets for characterization with MIRI in different temperature regimes: LHS 3844 b, GJ 1132 b and Trappist-1 b. We discuss further considerations in Section 6.5 and present our conclusions in Section 6.6.

6.2 Retrieval Framework & Atmospheric Model

We describe here the HyDRA retrieval framework, adapted for use with rocky planets whose primary atmospheric constituent is unknown (Section 6.2.1). To test this framework and to provide predictions and observability strategies for JWST, we calculate self-consistent atmospheric models for known rocky planets, and simulate their observed thermal emission spectra with JWST in Sections 6.2.3 and 6.4. These atmospheric models and simulated data are described in Section 6.2.2.

Table 6.1 Prior probability distributions for the P - T profile parameters (see also Madhusudhan and Seager 2009, Gandhi and Madhusudhan 2018).

Parameter	Prior Distribution	Range
$\alpha_1/\text{K}^{-1/2}$	uniform	0.02 – 1
$\alpha_2/\text{K}^{-1/2}$	uniform	0.02 – 1
$T_{100\text{mb}}/\text{K}$	uniform	100 – 2500
P_1/bar	log-uniform	10^{-5} – 100
P_2/bar	log-uniform	10^{-5} – 100
P_3/bar	log-uniform	10^{-2} – 100

6.2.1 Retrieval Framework

In this chapter, we build on the HyDRA retrieval framework (Gandhi and Madhusudhan 2018, see also Section 1.3.2) and adapt it for use with rocky planets. As in Gandhi and Madhusudhan (2018), we use the 6-parameter P - T profile of Madhusudhan and Seager (2009), which we find to be successful in retrieving the self-consistently derived temperature profiles of rocky exoplanets (Sections 6.2.3 and 6.4). The priors we use for each of the P - T profile parameters are shown in Table 6.1. These priors allow for both inverted and non-inverted temperature profiles in order to span the wide range of temperature gradients which can exist in the dayside atmosphere. We also use the PYMULTINEST Nested Sampling Bayesian parameter estimation algorithm (Skilling, 2006; Feroz et al., 2009; Buchner et al., 2014), as described in Section 1.3.2.

To date, HyDRA and adaptations thereof have been used to retrieve the thermal emission spectra of H_2 -dominated atmospheres, including hot Jupiters and brown dwarfs (Gandhi and Madhusudhan 2018; Gandhi et al. 2019, see also Chapter 2). For these cases, the retrieval implicitly assumes that the background molecule is H_2 . In the case of rocky exoplanet atmospheres, however, the primary constituent of the atmosphere is unknown and a background molecule cannot be assumed. This motivates several adaptations to the retrieval framework, which are described in Sections 6.2.1 and 6.2.1 below. Unlike giant planets and brown dwarfs, rocky planets also have the potential to host little or no atmosphere at all due to atmospheric escape processes (e.g. Kreidberg et al., 2019). In Section 6.2.1, we discuss how the Bayesian evidences of rocky exoplanet retrievals can be used to statistically assess the presence of an atmosphere, as well as to calculate the detection significance for specific chemical species. We further validate the HyDRO retrieval framework in Section 6.2.3 by applying it to simulated data for Trappist-1 b.

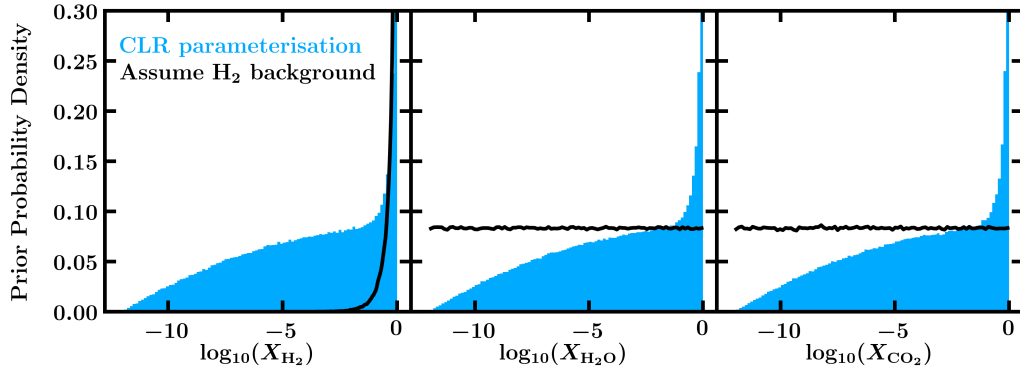


Fig. 6.1 Prior probability densities for log chemical abundances using the centred-log-ratio (CLR) parameterisation (blue) or assuming a H_2 -dominated composition and log-normal priors for the other species (black). The CLR parameterisation results in identical priors for all species, without assuming a fixed background species.

Chemical abundance parameterisation

In retrievals of H_2 -dominated atmospheres, the abundances of trace gases are typically included as parameters with a log-uniform prior. The mixing ratio of H_2 , X_{H_2} , is then calculated given the constraint that all mixing ratios, X_i , must sum to one, i.e.

$$\sum_{i=1}^n X_i = 1 \quad (6.1)$$

where n is the number of chemical species in the model. This treatment results in a different prior for the mixing ratio of the background molecule (in this case X_{H_2}) relative to the mixing ratios of the other species. This is shown in Figure 6.1; in particular, the prior for X_{H_2} is heavily skewed to higher values relative to the other chemical species. While appropriate for giant planets and brown dwarfs, these priors would result in biased results for low-mass exoplanets whose primary atmospheric constituent is unknown.

Benneke and Seager (2012) proposed an alternative parameterisation for the chemical mixing ratios in exoplanets with unknown dominant atmospheric constituents, and applied it to retrievals of transmission spectra of super-Earths. This parameterisation avoids the issues described above by using the centred-log-ratio (CLR) transformation, which is commonly used in the geological sciences to interpret compositional data (e.g. Pawlowsky-Glahn and Egozcue, 2006). Here, we adopt this method for retrievals of thermal emission spectra. As described by Benneke and Seager (2012), the transformed ‘CLR’

parameters for each of the n chemical species included in the model, ξ_i , are given by

$$\xi_i = \ln \frac{X_i}{g(\mathbf{x})}, \quad (6.2)$$

where

$$g(\mathbf{x}) = \exp \left(\frac{1}{n} \sum_{i=1}^n \ln X_i \right). \quad (6.3)$$

The ξ_i parameters are then sampled by the Bayesian parameter estimation algorithm assuming uniform priors. In principle, ξ_i can vary between $-\infty$ and $+\infty$, corresponding to mixing ratios between 0 and 1. However, in practice, the chemical species have vanishing effects on the model spectrum once very small abundances are reached. For a given assumed minimum mixing ratio, p_{\min} , the corresponding maximum possible mixing ratio for a given species is $1 - p_{\min}(n - 1)$, following equation 6.1. For the ξ_i parameters, these limits translate to

$$\frac{1}{n} [\ln(p_{\min}) - \ln(1 - np_{\min})]$$

for the lower bound of the uniform prior, and

$$\frac{n-1}{n} [\ln(1 - np_{\min}) - \ln(p_{\min})]$$

for the upper bound. In this chapter, we choose to use $p_{\min} = 10^{-12}$, as in Benneke and Seager (2012). Once the ξ_i parameters have been sampled from this prior, they can be transformed back into mixing ratios (following equations 6.1, 6.2 and 6.3), and used to calculate the model spectrum:

$$X_i = \frac{e^{\xi_i}}{\sum_{j=1}^n e^{\xi_j}}.$$

The CLR parameterisation results in identical priors for the mixing ratios of each chemical species in the model, as shown in Figure 6.1. These priors are spiked towards higher abundances given the necessity that at least one species must have a large abundance (as noted by Benneke and Seager 2012). The resulting parameter space therefore considers all chemical species in the model equally, allowing any of them to be the dominant atmospheric species.

Atmospheric opacity

Since rocky exoplanet atmospheres may be dominated by high mean-molecular-weight (high- μ) species, it is important to include all relevant sources of opacity for such species, including collision-induced absorption (CIA) and Rayleigh scattering. In our models, we

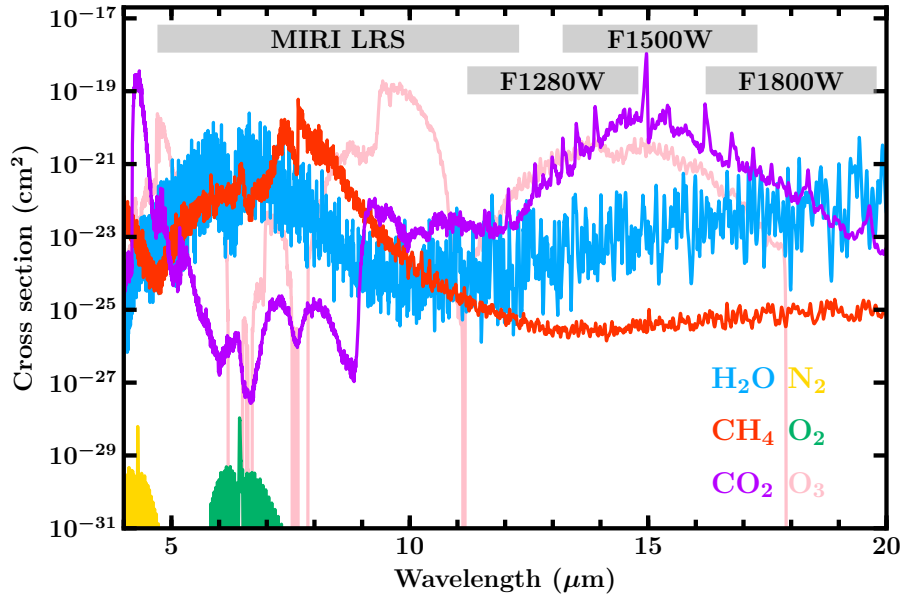


Fig. 6.2 Important sources of opacity in the mid-infrared for secondary atmospheres, at a pressure of 1 bar and temperature of 500 K. The wavelength ranges of MIRI LRS and the MIRI F1280W, F1500W and F1800W photometric bands are shown by thick grey lines.

therefore include the latest CO_2 - CO_2 and N_2 - N_2 CIA opacities from the HITRAN database (Karman et al., 2019), as well as H_2 - H_2 CIA opacity Richard et al. (2012). We further include Rayleigh scattering due to CO_2 , H_2O and H_2 (e.g. Malik et al., 2019). We note that the CIA data currently available is limited in temperature and wavelength. In this work, we therefore assume no CIA opacity outside the wavelength ranges available, and set the opacity at temperatures outside the given limits to those at the boundaries (see also Welbanks and Madhusudhan, 2021). Given the wide range of temperatures known for rocky exoplanets, future work will be required to more accurately assess the role of CIA opacity on their atmospheric spectra.

We also include molecular opacity due to species expected to be important in rocky planet atmospheres which also have spectral features in the JWST/MIRI spectral range (~ 5 - $30 \mu\text{m}$), i.e. CO_2 , H_2O , CH_4 , O_2 , O_3 , and N_2 (e.g. Hu et al., 2012b; Gaillard and Scaillet, 2014; Herbort et al., 2020). These species are known to be important in the atmospheres of the solar system terrestrial planets and/or may dominate the atmospheres of rocky exoplanets in the temperature range considered here, i.e. $T_{\text{eq}} \sim 400 - 800 \text{ K}$ (e.g. Herbort et al., 2020; Hu et al., 2020; Thompson et al., 2021; Wunderlich et al., 2021). While CO is also thought to be important in such atmospheres, it does not have significant features in the MIRI spectral range and we therefore exclude it from our present retrievals. In order to

simulate a realistic, agnostic retrieval analysis, we include all of the opacity sources listed here in each of the retrievals in this work, regardless of the ‘true’ input composition.

The molecular cross sections for the species we include are calculated as described in Gandhi and Madhusudhan (2017) using line lists from the ExoMol, HITEMP and HITRAN databases (CO₂ and H₂O: Rothman et al. 2010, CH₄: Yurchenko et al. 2013; Yurchenko and Tennyson 2014, O₂ and O₃: Rothman et al. (2013), N₂: Barklem and Collet 2016; Western et al. 2018). As discussed in Gandhi and Madhusudhan (2017), these cross sections are pressure broadened using the parameters for air broadening. Ideally, the pressure broadening would reflect the true composition of the atmosphere for each atmospheric model computed in the retrieval. However, given the wide range of possible atmospheric compositions for rocky exoplanets, this approach would be very cumbersome (e.g. Scheucher et al., 2020) and computationally expensive in the context of an atmospheric retrieval, in which a wide range of compositions is explored. Furthermore, the relevant line broadening coefficients are not all currently known (e.g. Wordsworth and Pierrehumbert, 2013). Further work on the pressure broadening of molecular opacities in rocky exoplanet atmospheres will be needed in order to improve these models and retrievals in the future.

Figure 6.2 shows the molecular opacities included in the retrieval as a function of wavelength, as well as the spectral coverage of JWST/MIRI’s Low Resolution Spectroscopy (LRS) mode and three of MIRI’s photometric bands. Some species have overlapping molecular absorption in the MIRI spectral range and may potentially lead to degeneracies in the retrieved abundances, depending on the data quality and spectral coverage. For example, H₂O and CH₄ have a somewhat similar cross section profile in the MIRI LRS spectral range. Similarly, CO₂ and O₃ both have strong features at $\sim 9 \mu\text{m}$. In Section 6.4, we consider atmospheric compositions ranging from CO₂-rich to H₂-O-rich, and find that H₂O and CO₂ can both be detected in the thermal emission spectrum despite these degeneracies.

Atmospheric detections

The Bayesian evidence of a retrieved model fit can be used to statistically and robustly compare different retrieval models (e.g. Trotta, 2008). The Nested Sampling algorithm used in HyDRo calculates the Bayesian evidence of the retrieved model fit and therefore allows such comparisons to be made, as described in Section 1.3.2. Bayesian model comparison is commonly used to assess the statistical significance of molecular detections by comparing retrieval models which include/exclude a certain molecule (e.g. Benneke and Seager, 2013; Gandhi and Madhusudhan, 2018). Here, we consider how such model

comparison can be used to assess the presence of an atmosphere by comparing models with/without the presence of molecular features.

The presence of an atmosphere on a transiting exoplanet can be inferred in several ways (e.g. Koll et al., 2019; Mansfield et al., 2019), including the detection of absorption features in its thermal emission spectrum. In order to calculate the significance of such an atmospheric detection, we compare each of our retrievals in Sections 6.2.3 and 6.4 to a featureless blackbody retrieval model, whose only parameter is the surface temperature. The resulting Bayes factor (Equation 1.16) therefore indicates the confidence with which atmospheric absorption is detected. We note that surface reflection may lead to a bare planet having spectral features despite the lack of an atmosphere (e.g. Hu et al., 2012a). However, such features are typically expected to be small; comparison to a blackbody spectrum thus provides a good first-order estimate of whether an atmosphere is present.

6.2.2 Self-Consistent Atmospheric Model & Simulated Data

In order to test the observability of known rocky exoplanets, we first use self-consistent 1D atmospheric models to simulate their thermal emission spectra and then use `HyDRo` to assess the observations needed for robust chemical detections. We use an adaptation of the `GENESIS` self-consistent atmospheric model (Gandhi and Madhusudhan 2017, see also Chapters 1.3.1, 3 and 5) to do this. As described in Chapter 5, we use the Feautrier method (Feautrier, 1964) in the iterative solution of radiative-convective equilibrium, and the Discontinuous Finite Element method (Castor et al., 1992) combined with Accelerated Lambda Iteration for the final calculation of the spectrum.

At the base of the atmosphere, we assume a surface pressure of 10 bar and a small internal flux corresponding to an internal temperature of 10 K, i.e. somewhat comparable to the internal temperatures of the terrestrial planets in the solar system (e.g. Zharkov, 1983; Davies and Davies, 2010; Parro et al., 2017). The planetary surfaces considered in this work lie deeper than the photosphere, and we therefore assume for simplicity that they behave as blackbodies. The atmosphere is assumed to be in steady state, therefore we do not explicitly include chemical fluxes from the surface, though the atmospheric compositions we consider may be the result of surface processes such as outgassing.

We model the stellar irradiation for GJ 1132 b using a Kurucz stellar model (Kurucz, 1979; Castelli and Kurucz, 2003) corresponding to the stellar properties listed in Table 6.2. For the stellar spectra of Trappist-1 and LHS 3844, however, we use `PHOENIX` models (Husser et al., 2013) as their effective temperatures (~ 2500 K and ~ 3000 K, respectively) are significantly below the coolest temperature considered in the Kurucz models (3500 K).

We further assume full day-night energy redistribution, i.e. a flux redistribution factor of $f = 0.5$ in Equation 1.10 (or $f=0.25$ according to the notation of Burrows et al. (2008a)).

In Section 6.4, we focus on three key atmospheric compositions ranging from CO₂-rich to H₂O rich. These are: (i) a Venus-like composition with 97% CO₂, 2.9% N₂ and 0.1% H₂O by volume, (ii) a 50% CO₂, 50% H₂O composition (by volume) and (iii) a 100% H₂O composition. We include molecular opacity from each of these species as well as CO₂-CO₂ and N₂-N₂ CIA, and Rayleigh scattering due to CO₂ and H₂O (see Section 6.2.1). For simplicity, we assume constant-with-depth chemical abundances. We note that a range of other species (e.g. NH₃, HCN, SO₂ or H₂S) may also be present in rocky exoplanet atmospheres, for example due to photochemistry or outgassing (e.g. Moses, 2014; Herbot et al., 2020; Thompson et al., 2021; Wunderlich et al., 2021; Yu et al., 2021). However, for simplicity we focus here on CO₂/H₂O-dominated compositions. For each of the planets modelled in Sections 6.2.3 and 6.4, we list the planetary and stellar parameters used in Table 6.2.

From the model thermal emission spectra calculated using GENESIS, we simulate both MIRI LRS spectra and MIRI photometry. For the MIRI LRS spectra, we bin the model spectrum to the pixel resolution and convolve it to a resolution of $R \sim 100$ (i.e. close to the instrument resolution) using a Gaussian kernel. The Gaussian kernel has fixed full width at half maximum (FWHM), chosen such that $\text{FWHM} = \lambda/100$ at the centre of the MIRI LRS spectral range, i.e. at $\lambda = 8.5 \mu\text{m}$. We calculate the uncertainties on the simulated LRS data using PANDEXO (Batalha et al., 2017) using a noise floor of 20 ppm at native resolution, and add this as random Gaussian noise to the simulated data. For the simulated MIRI photometry, we bin the spectra using the instrument response functions for each band (Glasse et al., 2015) and assume nominal single-eclipse uncertainties of 100 ppm, i.e. a conservative estimate of the uncertainties expected for the targets considered in Section 6.4 (see e.g. Lustig-Yaeger et al. 2019). As with the simulated MIRI LRS data, we add this uncertainty as random Gaussian noise to the simulated photometry data. In this chapter, we use the bands in the range $\sim 12 - 20 \mu\text{m}$, i.e. F1280W, F1500W and F1800W, as these probe opacity due to CO₂ and H₂O, as shown in Figure 6.2.

6.2.3 Validation of Retrieval Framework

We validate the retrieval framework by applying it to simulated data for Trappist-1 b. We further compare our results to Lustig-Yaeger et al. (2019), who have assessed the atmospheric observability of the Trappist-1 planets. We model the spectrum of Trappist-1 b assuming a Venus-like composition and simulate its MIRI LRS spectrum, as described in Section 6.2.2. We simulate data uncertainties assuming 30 eclipses. The self-consistent

Table 6.2 Planetary and stellar parameters for the rocky exoplanets modelled in this chapter. Values in parentheses are those used when data is unavailable or rounded values used for a PHOENIX stellar model in the case of Trappist-1 and LHS 3844 b. Stellar K magnitudes are from 2MASS (Cutri et al., 2003b).

Planet	Trappist-1 b	GJ 1132 b	LHS 3844 b
$R_p (R_\oplus)$	1.086	1.130	1.303
$M_p (M_\oplus)$	0.85	1.66	2.25*
$T_{\text{eq}} (\text{K})$	400	585	807
a (au)	0.01111	0.0153	0.00622
$R_s (R_\odot)$	0.117	0.2105	0.189
$T_{\text{eff}} (\text{K})$	2559 (2500)	3270	3036 (3000)
$\log(g_s/\text{cgs})$	5.2 (5.0)	4.881	5.06
[Fe/H]	0.04 (0.0)	-0.12	(0.0)
K mag	10.296	8.322	9.145
Refs	1	2,3,4	5

* Calculated mass assuming an Earth-like composition.

References: 1. Gillon et al. (2017b), 2. Bonfils et al. (2018), 3. Southworth et al. (2017), 4. Berta-Thompson et al. (2015), 5. Vanderspek et al. (2019).

temperature profile and thermal emission spectrum obtained (including simulated data) are shown in Figure 6.3. Note that the simulated MIRI LRS data shown in Figure 6.3 have been binned for clarity, but the data used for the retrieval are at the native resolution.

The retrieved spectrum and temperature profile are also shown in Figure 6.3, alongside the posterior distributions for the chemical abundances in the model. Both CO_2 and H_2O (the only spectrally active species in the self-consistent model) are detected with strong statistical confidence, at 5.51σ and 4.90σ , respectively. Correspondingly, the retrieved spectrum is able to fit the CO_2 absorption feature at $\sim 9 \mu\text{m}$ as well as the broad absorption feature due to H_2O around $\sim 6 \mu\text{m}$. This result is consistent with Lustig-Yaeger et al. (2019), who find that ~ 30 eclipses with MIRI LRS are able to significantly rule out a featureless emission spectrum for Trappist-1 b, in the case of a clear 10 bar CO_2 atmosphere.

We further find that the retrieval is able to accurately fit the photospheric temperature profile with very good precision, within $\sim 200 \text{ K}$ at 2σ . The retrieved P - T profile in Figure 6.3 is able to reproduce the ‘true’ input temperature profile to within 2σ throughout the atmosphere, with a tighter fit at photospheric pressures and larger uncertainty outside the photospheric range (as expected, since these regions have little effect on the observable spectrum). Thermal emission observations of rocky exoplanets therefore have the potential to place exquisite constraints on the thermodynamic conditions in their atmospheres.

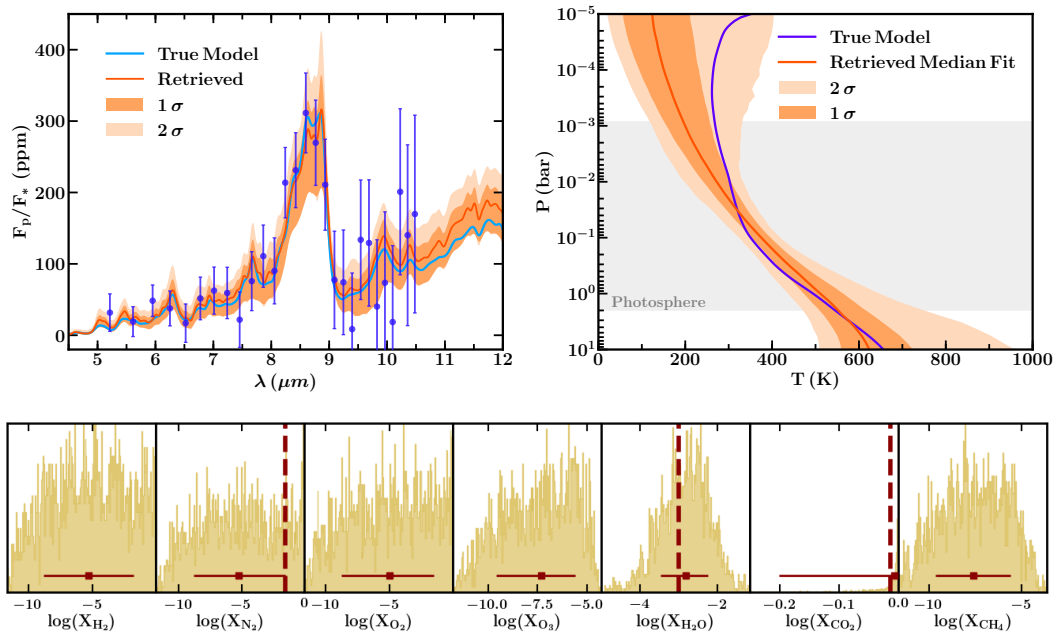


Fig. 6.3 Retrieved emission spectrum, temperature profile and chemical abundances for simulated data of Trappist-1 b, assuming a Venus-like composition. The data are simulated for 30 MIRI LRS eclipses. *Top left*: self-consistently modelled ‘true’ spectrum for Trappist-1 b (blue line) and corresponding simulated MIRI LRS data (purple markers and error bars). The median retrieved spectrum and $1\sigma/2\sigma$ contours are shown by the orange line and dark/light orange shading, respectively. *Top right*: self-consistent ‘true’ temperature profile (purple line) and median retrieved temperature profile and $1\sigma/2\sigma$ contours (orange line and dark/light orange shading, respectively). The shaded grey region shows the range of the 5-20 μm photosphere assuming $R\sim 100$. *Bottom*: Retrieved posteriors for the chemical abundances. ‘True’ input values are shown by vertical dashed lines. Maroon markers and error bars show the median retrieved abundances with 1σ error bars. CO_2 and H_2O are detected at 5.55σ and 4.07σ statistical significance, respectively.

6.3 Target Selection

In this Section, we evaluate the observability of known rocky exoplanets in thermal emission, and identify optimal candidates for atmospheric characterisation. Since the planet-star contrast is greater at longer wavelengths, we specifically assess the planets' observability in the mid-infrared with MIRI LRS, i.e. in the spectral range 5-12 μm . We begin by considering all known exoplanets in the NASA Exoplanet Archive² with masses $< 10M_{\oplus}$ and radii $< 2R_{\oplus}$ whose stars have K magnitudes < 13 . We further include LHS 3844 b, which does not have a measured mass but represents an ideal target for rocky exoplanet characterisation.

In order to identify optimal targets for thermal emission observations, we first assess these targets by considering their planetary and stellar spectra to be blackbodies. For the planetary temperature, we nominally calculate the equilibrium temperature of the planet assuming zero albedo and full day-night redistribution, i.e.

$$T_p = \sqrt{\frac{R_s}{2a}} T_{\text{eff}},$$

where R_s and T_{eff} are the stellar radius and effective temperature, respectively, and a is the semi-major axis. We then calculate the planet-star flux ratio for each system,

$$\frac{F_p}{F_s} = \frac{R_p^2 B_{\lambda}(T_p)}{R_s^2 B_{\lambda}(T_{\text{eff}})},$$

where R_p is the planetary radius and B_{λ} is the Planck function. We filter the targets according to F_p/F_s in three steps:

1. Filter out any targets for which $F_p/F_s < 10$ ppm at 12 μm
2. Recalculate F_p/F_s using a Phoenix spectrum for the star (still assuming a blackbody spectrum for the planet), and use PANDEXO (Batalha et al., 2017) to calculate the uncertainty in the MIRI LRS spectrum.
3. Calculate the number of eclipses needed, $E_{S/N=3}$, to achieve a signal-to-noise (S/N) of 3 anywhere in the MIRI LRS range assuming a resolution of $R \sim 10$. We use $E_{S/N=3}$ as a metric for the observability of the target.

By evaluating $E_{S/N=3}$ at a resolution of $R \sim 10$, this metric quantifies the spectroscopic observability of rocky exoplanets and indicates which planets may be amenable to at-

²exoplanetarchive.ipac.caltech.edu

atmospheric characterisation. Since CO₂ and H₂O have broad prominent features in the MIRI LRS spectral range, $R \sim 10$ is a suitable resolution to identify the presence of such species in the atmospheres of rocky exoplanets (e.g. see Figure 6.5). For example, we find that the promising rocky exoplanet target GJ 1132 b has $E_{S/N=3}=1.32$, and in Section 6.4 we show that 8 secondary eclipses with MIRI LRS are sufficient to constrain a CO₂-rich atmosphere. Conversely, fewer eclipses would be required to make photometric detections of the planetary thermal emission, e.g. as discussed by Koll et al. (2019).

Figure 6.4 shows the observability of the resulting population of rocky exoplanets as a function of their stellar and planetary parameters. As expected, hotter and larger planets are typically more observable than cooler, smaller ones. Furthermore, the number of eclipses required to achieve $S/N=3$ with MIRI LRS increases with host star K magnitude. This suggests that the two main obstacles for observing rocky planet atmospheres in thermal emission are the level of thermal emission from the planet itself (which affects the measured signal) and the brightness of the host star (which impacts the observational uncertainty). With MIRI LRS, the thermal emission from several hot rocky exoplanets will be observable in fewer than 10 eclipses at $R \sim 10$. However, the characterisation of temperate rocky planet atmospheres will require either more observing time, greater sensitivity than that expected of MIRI, or brighter targets.

We find 33 rocky exoplanets whose thermal emission will be detectable with $S/N=3$ at $R \sim 10$ in fewer than 10 secondary eclipses (Table C.1). One of the most observable of these is LHS 3844 b; with an equilibrium temperature of ~ 800 K, it is the only planet in this sample cooler than 1000 K with $E_{S/N=3} < 1$. In the intermediate-temperature regime, GJ 1132 b represents an excellent target and is the only exoplanet cooler than 600 K with $E_{S/N=3} < 4$. The coolest exoplanet among these 26 targets is LTT 1445 A b, which has an equilibrium temperature of 438 K. With $E_{S/N=3}=7.2$, LTT 1445 A b therefore represents a unique opportunity to probe rocky exoplanets close to the temperate regime.

Our results are consistent with the findings of Koll et al. (2019), who use the emission spectroscopy metric (ESM) of Kempton et al. (2018) to characterise the observability of rocky exoplanets. Concurrent with the trend found in Figure 6.4, they find that the observability of rocky exoplanets in thermal emission typically increases with equilibrium temperature. They also predict that TESS will find ~ 19 exoplanets with radius $< 1.5R_{\oplus}$ and an ESM greater than that of GJ 1132 b (which is considered to be an optimal rocky exoplanet candidate for atmospheric characterisation, e.g. Morley et al. 2017b). By considering known exoplanets with masses $< 10M_{\oplus}$ and radii $< 2R_{\oplus}$, we find in this chapter that at least 14 known exoplanets are more observable than GJ 1132 b according to our observability metric. These include the 3 known planets identified by Koll et al.

(2019) as having an ESM greater than that of GJ 1132 b, i.e. HD 213885 b, LHS 3844 b and 55 Cnc e.

In Section 6.4, we perform a more detailed analysis of the three promising targets Trappist-1 b, GJ 1132 b, and LHS 3844 b. These planets each represent ideal targets for their respective equilibrium temperatures, which span the temperate to hot regimes ($\sim 400\text{-}800$ K). We note that the estimated number of eclipses calculated here for a S/N of 3 is not exact due to the assumption of blackbody spectra, and characterises the ease with which thermal emission from the planet can be observed rather than the number of eclipses required to make chemical detections. However, this analysis does provide a simple metric to assess ideal targets for characterising rocky exoplanet atmospheres, and can guide more detailed evaluations such as those in Section 6.4. Indeed, this simple analysis shows that a large number of known rocky exoplanets are suitable targets for atmospheric characterisation in thermal emission with JWST.

6.4 Results

We investigate the observability of key molecular species in rocky exoplanet atmospheres using three promising candidates as case studies: Trappist-1 b, GJ 1132 b and LHS 3844 b, which span the $\sim 400\text{-}800$ K equilibrium temperature range (Berta-Thompson et al., 2015; Gillon et al., 2016; VanderSpek et al., 2019). In particular, we consider three different atmospheric compositions including a Venus-like atmosphere, a 50% CO₂/50% H₂O atmosphere and a 100% H₂O atmosphere (see Section 6.2.2). For each planet and atmospheric composition, we first model the thermal emission spectrum and simulate JWST MIRI data, as described in Section 6.2.2. The model spectra for each case study are shown in Figures 6.5 and 6.6, including simulated MIRI data. We then perform atmospheric retrievals on this simulated data and assess the detection significances of the key molecular species in each case, as detailed in Section 6.2.1. We assume full day-night energy redistribution for all our models as this provides a conservative estimate of the observations required to make chemical detections; less efficient heat redistribution would result in a hotter day-side and a deeper secondary eclipse. However, we note that LHS 3844 b's observed phase curve has a strong day-night contrast which likely indicates inefficient day-night heat transport and a hotter day-side than assumed here. The observability estimates we provide here are therefore conservative.

For each of the atmospheres investigated here, we take a hierarchical approach by considering four key science cases to be addressed, in order of increasing scientific complexity:

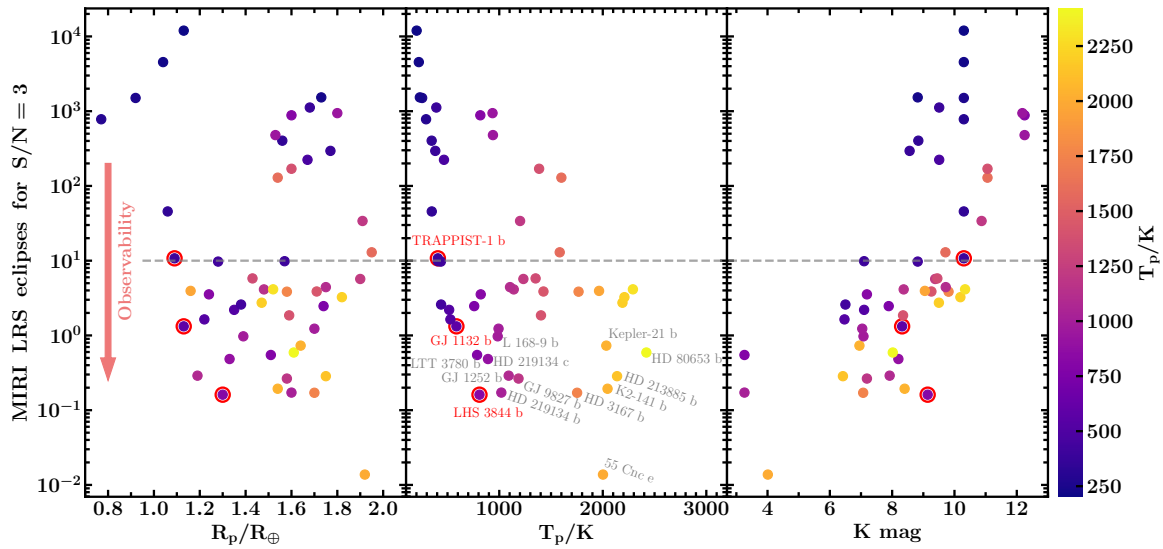


Fig. 6.4 Observability of known rocky planets in thermal emission as a function of planet radius (R_p , left panel), equilibrium temperature (T_p , centre panel) and K magnitude of the host star (right panel). Observability is defined as the number of secondary eclipses with MIRI LRS required to detect the thermal emission of the planet, F_p/F_s , at $S/N=3$ assuming a resolution of $R\sim 10$. Note that non-integer numbers of eclipses would need to be rounded up as partial transits would not contribute as much to the S/N . The targets shown here are chosen such that $F_p/F_s > 10$ ppm in the MIRI LRS spectral range (i.e $5\text{--}12\ \mu\text{m}$). In each panel, the markers for each planet are coloured according to planet equilibrium temperature (see colourbar). The case studies LHS 3844 b, GJ 1132 b and Trappist-1 b are circled in red in each panel, for reference. The horizontal dashed line denotes 10 eclipses required with MIRI LRS for a $S/N=3$. The planets below this line represent optimal targets for atmospheric characterisation in thermal emission with JWST MIRI, and their properties are listed in Table C.1.

1. **Comparison to a bare rock with no energy redistribution:** A solid, bare rocky surface is expected to be significantly hotter than an atmosphere with energy redistribution, and may be observationally distinguished from an atmosphere with efficient energy redistribution (Koll et al., 2019). We consider whether the simulated data are enough to rule out this hot bare rock scenario, indicating energy redistribution e.g. due to an atmosphere or magma ocean.
2. **Presence of spectral features:** Can the observations statistically rule out a black-body spectrum? If so, the presence of absorption or emission features confirms the presence of an atmosphere and an atmospheric temperature gradient.
3. **Detection of CO₂:** CO₂ has a sharp spectral feature at $\sim 9 \mu\text{m}$ (Figure 6.2) which can be observed in MIRI LRS spectra. CO₂ is therefore one of the easiest molecules to detect in this spectral range for the range of atmospheric compositions considered in this chapter.
4. **Detection of H₂O:** With sufficient spectral precision, H₂O can be detected and its atmospheric abundance can be measured.

In what follows, we investigate these four science cases for each planet and atmospheric composition. The retrieved thermal emission spectra, temperature profiles and posterior probability distributions for the chemical abundances are shown for each case investigated in Figures 6.6, 6.7 and 6.8, respectively. Table 6.3 further shows the detection significances obtained for each of these cases.

6.4.1 Case Study: LHS 3844 b

LHS 3844 b is a highly-irradiated rocky planet orbiting a nearby M-dwarf, with a dayside temperature of $\sim 1000 \text{ K}$ (Kreidberg et al., 2019; Vanderspek et al., 2019). Recent phase curve observations of the planet have revealed a strong day-night temperature contrast and no hotspot shift, ruling out the possibility of an atmosphere with pressure $\gtrsim 10 \text{ bar}$ (Kreidberg et al., 2019). Recent observations of LHS 3844 b with transmission spectroscopy are further inconsistent with a clear, H₂-rich atmosphere of pressure $\gtrsim 0.1 \text{ bar}$ and suggest either a high- μ atmosphere, a H₂-rich atmosphere with high-altitude clouds (cloud-top pressures $< 0.1 \text{ bar}$) or no atmosphere at all (Diamond-Lowe et al., 2020).

Thermal emission spectroscopy will be required to assess the presence of an atmosphere on LHS 3844 b. Even in the case of a high- μ atmosphere, which can be prohibitive for transmission spectroscopy, the thermal emission spectrum is sensitive to molecular absorption/emission features. Here, we assess whether observations with JWST/MIRI could

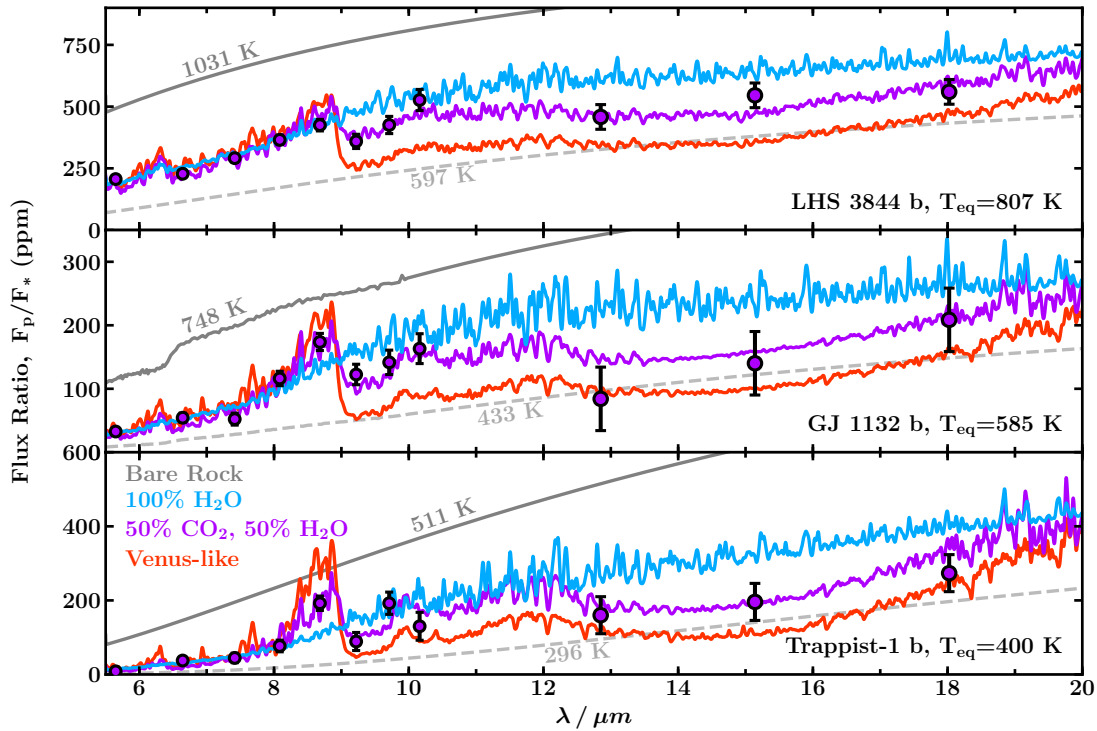


Fig. 6.5 Thermal emission spectra for LHS 3844 b, GJ 1132 b and Trappist-1 b assuming Venus-like (red lines), 50% CO₂/50% H₂O (purple lines) or 100% H₂O (blue lines) compositions. Blackbody spectra corresponding to the temperature expected for a bare rock with no energy redistribution are also shown by solid grey lines. Dashed grey lines show blackbody spectra corresponding to the equilibrium temperature expected for a Venus-like Bond albedo of 0.7. Data points and error bars show simulated MIRI LRS data and photometric data in the F1280W, F1500W and F1800W bandpasses. The error bars assume 20 MIRI LRS eclipses for LHS 3844 b and GJ 1132 b, and 80 eclipses for Trappist-1 b. Note that the LRS data are binned for clarity. The photometric points have error bars of 50 ppm for all three targets, corresponding to ~4 eclipses each.

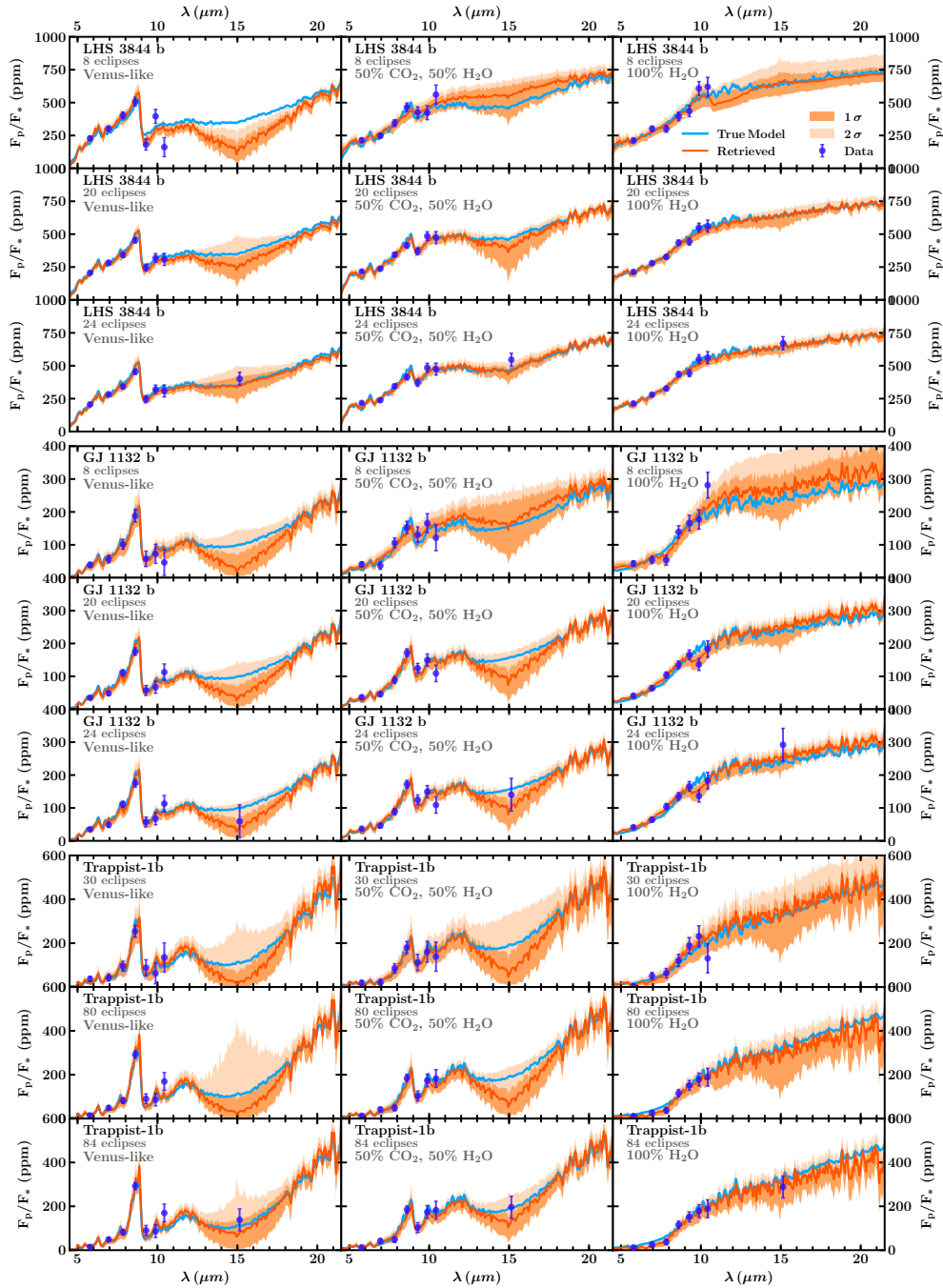


Fig. 6.6 Retrieved thermal emission spectra for LHS 3844 b (top three rows), GJ 1132 b (middle three rows) and Trappist-1 b (bottom three rows) for the simulated data described in section 6.4 assuming a Venus-like, 50% CO₂/50% H₂O or 100% H₂O composition (left, centre and right columns, respectively). Dark orange lines show the median retrieved spectrum, while dark and light orange shaded regions show 1 σ and 2 σ confidence intervals. Purple points and error bars show simulated MIRI LRS and photometric data, as described in Section 6.4. The light blue line shows the ‘true’ input spectrum.

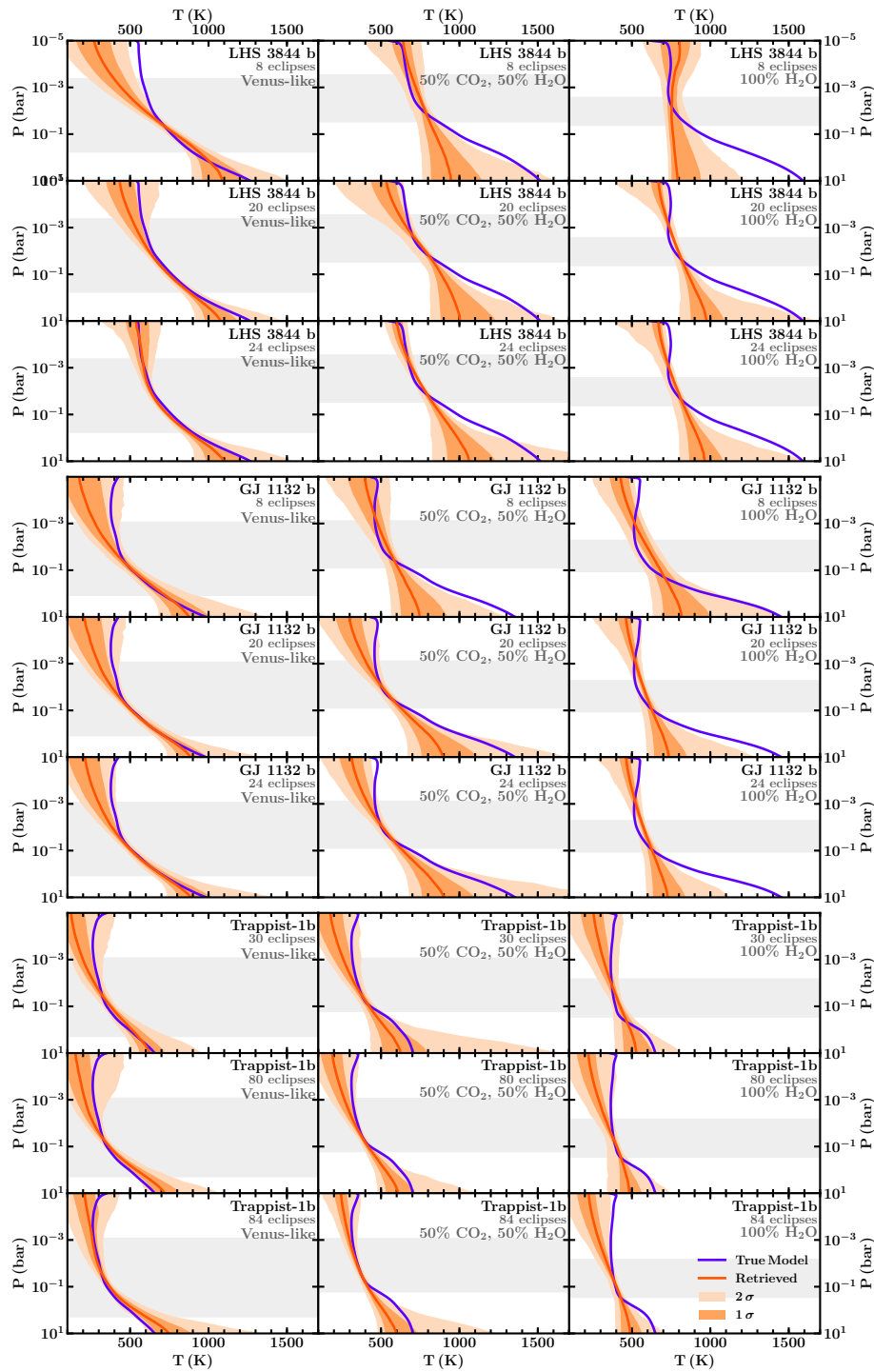


Fig. 6.7 Retrieved temperature profiles for LHS 3844 b (top three rows), GJ 1132 b (middle three rows) and Trappist-1 b (bottom three rows) for the simulated data described in section 6.4 assuming a Venus-like, 50% CO₂/50% H₂O or 100% H₂O composition (left, centre and right columns, respectively). Dark orange lines show the median retrieved temperature profile, while dark and light orange shaded regions show 1σ and 2σ confidence intervals. Purple lines show the ‘true’ input temperature profile. Shaded grey regions show the range of the 5-20μm photosphere assuming R~100.

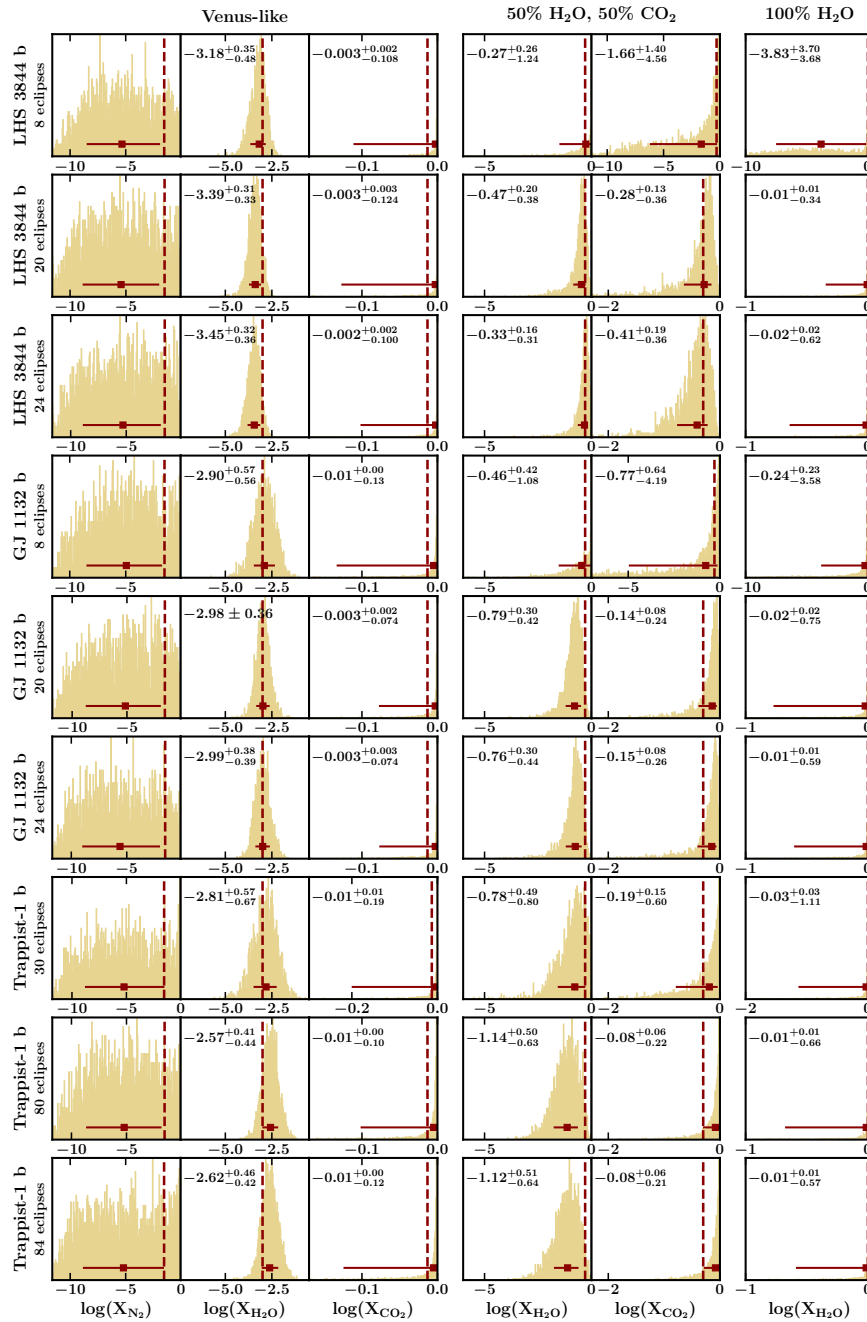


Fig. 6.8 Posterior probability distributions for the species present in each simulated data model (Venus-like: left three columns; 50% H₂O/50% CO₂: 4th and 5th columns; 100% H₂O: right column). Note that the retrieval model includes all the species discussed in Section 6.2.1, but species not present in the simulated data are not constrained. Posteriors are shown for the case studies LHS 3844 b (top three rows), GJ 1132 b (middle three rows) and Trappist-1 b (bottom three rows) for the simulated data described in section 6.4. ‘True’ input values are shown by vertical dashed lines. Median retrieved abundances and 1 σ uncertainties are shown by maroon markers and error bars, and quoted for the H₂O and CO₂ posteriors. The abundance of N₂ is unconstrained in the Venus-like case due to its lack of spectral features in the wavelength range considered.

constrain the presence of an atmosphere on LHS 3844 b assuming a cloud-free Venus-like, 50% CO₂/50% H₂O and 100% H₂O composition. For this case study we consider three observing strategies: (i) a shorter observing time strategy with 8 MIRI LRS eclipses, (ii) a longer strategy with 20 MIRI LRS eclipses and (iii) a strategy with 20 MIRI LRS eclipses plus 4 eclipses with the MIRI imager F1500W photometric band. The simulated spectra and data are shown in the top panel of Figure 6.5 and the top three rows of Figure 6.6.

From Figure 6.5, it is clear that the uncertainties on the data using 20 MIRI LRS eclipses and/or the photometry allow the Venus-like, 50% CO₂/50% H₂O and 100% H₂O compositions to be distinguished, especially at wavelengths $\gtrsim 9 \mu\text{m}$. For the longer observing time strategies, the data also significantly deviate from a blackbody spectrum for all three compositions considered; for example, the sharp CO₂ feature at $\sim 9 \mu\text{m}$ can easily be distinguished for the Venus-like and 50% CO₂/50% H₂O models. For the shortest observing time strategy of 8 MIRI LRS eclipses, the Venus-like case can also clearly be distinguished from a blackbody spectrum. A bare-rock surface (assuming no energy redistribution, grey spectrum in the top panel of Figure 6.5) is also evidently rejected by the simulated data for all compositions and observing strategies. We note, however, that this simulated data assumes efficient day-night energy distribution, which is not expected for LHS 3844 b as discussed above.

For each atmospheric composition considered, we perform an atmospheric retrieval on the simulated MIRI data described above. The retrieved spectra, temperature profiles and posterior probability distributions for the chemical abundances are shown in the top three rows of Figures 6.6, 6.7 and 6.8, respectively, for each case. The ‘true’ input spectra are retrieved within the 2σ uncertainties for all three atmospheric compositions, within the spectral range of the data. The retrieved abundances of H₂O and CO₂ are also retrieved within the 2σ uncertainties. Furthermore, the temperature profile of each atmosphere is accurately retrieved within the $\sim 2\sigma$ uncertainties in the photosphere. Outside the photosphere, the observed spectrum does not contain information about the temperature profile and it is therefore expected that the retrieved temperature profile may deviate in this range.

We further evaluate the confidence with which the data reject a blackbody spectrum and the confidence with which CO₂ and H₂O are detected, as described above and in Section 6.2.1. With only 8 MIRI LRS eclipses, we find that CO₂ and H₂O can confidently be detected in the Venus-like case, with detection significances of 5.55σ and 4.07σ , respectively (Table 6.3). Furthermore, while the 50% H₂O/50% CO₂ and 100% H₂O cases are more challenging to characterise with only 8 eclipses, a blackbody spectrum can be rejected at $\lesssim 3\sigma$ for the 100% H₂O composition. 8 MIRI LRS eclipses are therefore sufficient

to characterise a cloud-free Venus-like composition on LHS 3844 b, or to tentatively detect atmospheric absorption (i.e. reject a blackbody spectrum) in the case of a 100% H₂O atmosphere.

For the two longer observing time strategies, i.e. with at least 20 MIRI LRS eclipses, stronger constraints can be obtained for all three compositions considered. For both the Venus-like and 50% H₂O/50% CO₂ cases, we find that CO₂ and H₂O can be detected with $> 4\sigma$ significance. The 100% H₂O composition remains more challenging to characterise, but these longer observing time strategies do allow a blackbody spectrum to be rejected at a higher confidence of $> 4\sigma$, compared to the 8 eclipse strategy. 20 MIRI LRS eclipses are therefore sufficient to characterise cloud-free, CO₂-rich compositions for LHS 3844 b, or to confidently detect atmospheric absorption in the case of a 100% H₂O atmosphere. We note that the addition of the four photometric eclipses does not significantly improve the retrieved constraints beyond what is achieved with 20 MIRI LRS eclipses alone. Furthermore, for all three observing strategies considered here, the abundances of CO₂ and H₂O (when detected) can be measured to within $\lesssim 0.5$ dex across the compositions we have considered here, i.e. comparable to the precision achieved for chemical abundances in hot Jupiters to date (e.g Sheppard et al., 2017; Welbanks et al., 2019).

6.4.2 Case Study: GJ 1132 b

GJ 1132 b is a small rocky exoplanet with an equilibrium temperature of ~ 600 K (Berta-Thompson et al., 2015). Thanks to its nearby host star and large planet-star size contrast, this planet is an ideal candidate for thermal emission spectroscopy of warm rocky planets (Morley et al., 2017b). To date, atmospheric observations of GJ 1132 b using transmission spectroscopy have revealed a relatively flat spectrum, consistent with a high- μ atmosphere (Southworth et al., 2017; Diamond-Lowe et al., 2018). Thermal emission spectroscopy will be needed to confirm the presence of this atmosphere and to establish its chemical composition. Here, we consider the JWST/MIRI observations needed to constrain the presence and chemical composition of an atmosphere on GJ 1132 b assuming a Venus-like, 50% CO₂/50% H₂O or 100% H₂O composition.

In order to characterise the observability of GJ 1132 b, we investigate the same three observing strategies used above for LHS 3844 b, i.e.: (i) 8 eclipses with MIRI LRS, (ii) 20 eclipses with MIRI LRS, (iii) 20 eclipses with MIRI LRS plus 4 eclipses with the F1500W photometric band. The simulated spectra and data for both cases are shown in Figure 6.5 and the middle three rows of Figure 6.6, respectively. For all three observing strategies, the data are clearly distinguishable from the solid bare-rock scenario with no energy redistribution (grey spectrum in Figure 6.5). For the Venus-like composition, the observational

uncertainties for each strategy are further sufficient to distinguish the strong CO₂ feature at $\sim 9 \mu\text{m}$. The retrieved spectra, temperature profiles and posterior distributions for each composition and observing strategy are shown in the middle three rows of Figures 6.6, 6.7 and 6.8, respectively.

With the assumption of 8 MIRI LRS eclipses, we find that the Venus-like composition is confidently constrained, with 4.70σ and 4.42σ detections of CO₂ and H₂O, respectively (Table 6.3). CO₂ and H₂O are not detected for the 50% CO₂/50% H₂O and 100% H₂O compositions using this strategy, but in the 100% H₂O case a blackbody spectrum is nevertheless rejected at $> 4\sigma$. The spectra are retrieved to within the 2σ uncertainties in the spectral range of the data, while the temperature profiles are also retrieved to within 2σ in the photosphere. Likewise, the abundances of CO₂ and H₂O are accurately retrieved to within the 2σ uncertainties. For the Venus-like case, the abundances of CO₂ and H₂O are constrained within < 0.6 dex. This relatively short observing time strategy would therefore be suitable for determining whether GJ 1132 b is a cloud-free exo-Venus, or to detect atmospheric absorption in the case of a 100% H₂O composition.

For the longer observing time strategies, i.e. using 20 MIRI LRS eclipses, we find that $\gtrsim 3\sigma$ detections of both CO₂ and H₂O can be made across all three atmospheric compositions. In particular, confident, $4 - 8\sigma$ detections of these species can be made in the Venus-like and 50% CO₂/50% H₂O cases. The 100% H₂O case is slightly more challenging to characterise, allowing $\sim 3\sigma$ detections of H₂O with these observing strategies. As with LHS 3844 b, we note that the addition of four eclipses with the F1500W filter on top of the 20 MIRI LRS eclipses does not significantly improve the atmospheric constraints which are made. The spectra and temperature profiles are all retrieved to within 2σ , while the abundances of CO₂ and H₂O are accurately retrieved within 2σ uncertainties of $\lesssim 0.75$ dex. We therefore conclude that these longer observing time strategies would be able to characterise the atmosphere of GJ 1132 b across a range of CO₂- and H₂O-rich compositions, including determining the abundances of these two species. Given the importance of CO₂ and H₂O in geochemical processes, such constraints would be invaluable in determining the possible atmospheric origins of GJ 1132 b.

6.4.3 Case Study: Trappist-1 b

The Trappist-1 system (Gillon et al., 2016, 2017b) is currently the most promising system of terrestrial-like exoplanets for atmospheric characterisation (Turbet et al., 2020). Thanks to the host star's small radius ($0.117 R_{\odot}$) and low effective temperature (2559 K), the secondary eclipse depths of the Trappist-1 planets are favourable despite the small planetary sizes and low planetary temperatures. In particular, Trappist-1 b is the warmest

planet in this system, with an equilibrium temperature of 400 K, and represents an excellent candidate for atmospheric characterisation of a temperate exoplanet in thermal emission. Meanwhile, transmission spectroscopy observations have already begun to place constraints on the atmosphere of Trappist-1 b. de Wit et al. (2016) rule out a clear, H₂-rich atmosphere at $> 10\sigma$ and note that while a H₂-rich atmosphere with high-altitude clouds/hazes is allowed by the data, this is an unlikely scenario given the relatively low irradiation level of Trappist-1 b. Conversely, Bourrier et al. (2017) find a marginal decrease in the Lyman- α flux of Trappist-1 during the transits of planets b and c, which may indicate the presence of extended hydrogen exospheres. However, this effect could also be caused by stellar activity. A secondary atmosphere on Trappist-1b therefore remains a promising possibility, and we investigate the observability of a Venus-like, 50% CO₂/50% H₂O and 100% H₂O atmosphere.

Compared to LHS 3844 b and GJ 1132 b, Trappist-1 b's relatively small planetary radius and cooler temperature results in a lower S/N and the need for longer observation times. Here, we consider three observation strategies: (i) 30 eclipses with MIRI LRS, (ii) 80 eclipses with MIRI LRS, and (iii) 80 eclipses with MIRI LRS plus 4 eclipses with the F1500W photometric band. The bottom panel of Figure 6.5 shows the simulated spectra for Trappist-1 b across the CO₂-rich to H₂O-rich compositions considered here, while the bottom three rows of Figure 6.6 show the simulated data and retrieved spectra. For all three observational strategies, the data are clearly distinguishable from the bare-rock scenario with no energy redistribution. Furthermore, for the Venus-like composition, the sharp CO₂ feature at $\sim 9 \mu\text{m}$ can be distinguished by eye, consistent with the confident detections of CO₂ in these retrievals.

Assuming 30 MIRI LRS eclipses, we find that CO₂ and H₂O can be detected in both the Venus-like and 50% CO₂/50% H₂O cases (Table 6.3). The Venus-like composition is most confidently constrained, with 5.5σ and 4.9σ detections of CO₂ and H₂O, respectively, while the 50% CO₂/50% H₂O composition leads to $\lesssim 3\sigma$ detections of these species. However, in the 100% H₂O case the simulated data are consistent with a blackbody and spectral features are not detected with statistical significance. Nevertheless, for all three compositions the retrieval framework fits the true spectrum and photospheric P - T profile within 2σ uncertainties (Figure 6.7). This 30-eclipse strategy would therefore be ideal to characterise (or rule out) clear, CO₂-dominated atmospheric compositions on Trappist-1 b.

Using a longer observing time of 80–84 eclipses, we find that the Venus-like and 50% CO₂/50% H₂O compositions are readily characterised, allowing ~ 4 – 10σ detections of CO₂ and H₂O (Table 6.3). The 100% H₂O composition is more challenging to characterise, though a blackbody spectrum is nevertheless rejected by the data at $\sim 4\sigma$ with both of

Table 6.3 Detection significances for CO₂ and H₂O given different atmospheric compositions and observing strategies for LHS 3844 b, GJ 1132 b and Trappist-1 b (see Section 6.4). The confidence level at which the data eliminates a blackbody spectrum is also shown for each case (columns labelled ‘non-BB’). The number of eclipses with MIRI LRS and MIRI photometry assumed for each case are shown in italics. Confidence levels below 2 σ are not shown.

Planet	Venus			50% H ₂ O/50% CO ₂			100% H ₂ O	
	CO ₂	H ₂ O	non-BB	CO ₂	H ₂ O	non-BB	H ₂ O	non-BB
LHS 3844 b								
<i>8 LRS</i>	5.55	4.07	8.37	–	2.52	2.28	–	2.93
<i>20 LRS</i>	7.06	5.32	10.59	3.87	5.02	4.86	2.74	4.20
<i>20 LRS, 4 F1500W</i>	6.95	5.20	11.00	3.61	4.72	4.45	2.82	4.50
GJ 1132 b								
<i>8 LRS</i>	4.70	4.42	5.69	–	2.68	2.31	–	4.38
<i>20 LRS</i>	7.62	6.91	8.75	4.35	4.53	5.03	3.18	3.20
<i>20 LRS, 4 F1500W</i>	8.05	6.90	9.20	4.76	5.05	5.33	2.96	3.20
Trappist-1 b								
<i>30 LRS</i>	5.51	4.90	5.82	2.89	3.40	3.02	2.31	2.47
<i>80 LRS</i>	9.09	9.60	11.06	4.40	4.68	4.75	2.50	4.08
<i>80 LRS, 4 F1500W</i>	9.79	9.57	11.73	4.86	4.70	4.98	2.65	3.90

these observing strategies. For all three compositions, the spectra, temperature profiles and the abundances of CO₂ and H₂O are retrieved within the 2 σ uncertainties. Similar to the retrievals for LHS 3844 b and GJ 1132 b, we note that these results are very similar for both the observing strategies with and without the photometry, suggesting that the MIRI LRS data is driving these detections. 80 eclipses using MIRI LRS are therefore sufficient to confidently characterise cloud-free CO₂-rich compositions for Trappist-1 b, and to detect the presence of atmospheric absorption in the case of a water-rich composition. Furthermore, we find that the abundances of CO₂ and H₂O are constrained to within excellent 1- σ uncertainties of < 0.7 dex, where these species are detected.

6.5 Discussion

In Section 6.4, we have shown that rocky exoplanet atmospheres across a wide range of temperatures (~400-800 K) can be characterised in thermal emission with JWST/MIRI, including confident detections of atmospheric absorption by CO₂ and H₂O. Here, we begin by discussing the calculation of detection significances and key subtleties which can arise. Having focused on cloud- and haze-free atmospheric compositions in previous sections,

we also discuss the impact which clouds and hazes may have on the characterisation of rocky exoplanet atmospheres. We further discuss the implications of 3D effects and methods to account for these.

6.5.1 Degeneracies & Detection Significances

When considering detection significances, it is useful to understand the role of model complexity in determining the Bayesian evidence. As described in Section 6.2.1, the confidence of a molecular detection can be assessed by comparing the Bayesian evidences of two retrievals including/excluding the molecule(s) in question. Similarly, the confidence with which a blackbody spectrum can be rejected can be assessed by comparing the Bayesian evidences of retrievals with a full atmospheric model vs. only a single temperature (i.e. a blackbody model). However, these Bayesian evidences encapsulate not only the fit to the spectrum but also the complexity of the model. For example, if a 10-parameter model results in the same goodness of fit as a 5-parameter model, the 5-parameter model will have a higher Bayesian evidence as it has a lower model complexity.

When calculating the detection significance of a single molecule, the models compared only have a difference of one parameter (i.e. the models are identical apart from the presence of one molecule), and so the detection significance calculated from this comparison is a fairly good measure of ‘goodness of fit’ as the model complexities are comparable. However, when the ‘full model’ is compared to a blackbody model, there is a significant difference in model complexity (i.e. 13 parameters for the full model vs 1 parameter for the blackbody). This means that the full model is penalised for its complexity relative to the blackbody model, and the blackbody spectrum may be rejected at a lower significance than expected. That is, the poor fit from a blackbody model may be compensated for by the simplicity of the model.

An alternative way to assess how confidently a blackbody model can be rejected is to compare this model to a ‘core parameters’ model. This ‘core parameters’ model is based on the full atmospheric model, but includes only the species for which there is evidence in the data. For example, if H₂O and CO₂ are detected in the data (using the full model) but no other species are detected, the ‘core parameters’ model would include only H₂O and CO₂ (as well as the usual temperature profile parameterisation). This effectively strips down the full model to the components which are necessary to fit the data, without including unnecessary parameters. Thus, when compared to the blackbody model, the ‘core parameters’ model is not penalised by unnecessary parameters, and instead the difference in model complexity is more representative of the complexity required to fit the data. For example, in the 50% CO₂/50% H₂O case for Trappist-1 b with 30 MIRI LRS

eclipses, comparing the blackbody model to the ‘core parameters’ model results in a 3.65σ rejection of the blackbody, whereas a comparison to the full model results in a 3.02σ rejection. Note that all detection significances shown in Table 6.3 use a comparison with the full model.

Ultimately, it is important to understand how the models used can affect the confidence with which a blackbody spectrum can be rejected. In cases with very strong molecular detections, a blackbody can be rejected with high confidence even when compared to the full model. In more marginal cases, however, it may be necessary to consider how model complexity affects this metric.

6.5.2 Impact of Clouds and Hazes

Clouds and hazes can have significant effects on the temperature profiles and thermal emission spectra of low-mass exoplanets (e.g. Morley et al. 2015, see also Chapter 5). So far in this chapter we have considered clear atmospheres, and we now discuss how clouds and hazes may affect the atmospheric characterisation of rocky exoplanets. While optical scattering from clouds and hazes is not directly visible in infrared observations, it has the effect of cooling the atmosphere and results in a more isothermal temperature profile. This can lead to a smaller planetary flux and muted spectral features, as demonstrated in Chapter 5 for mini-Neptunes. However, while cloudy atmospheres may provide challenges for chemical detections, secondary eclipse observations can still constrain atmospheric properties above the cloud deck, including the photospheric temperature.

For the case studies LHS 3844 b, GJ 1132 b and Trappist-1 b, we consider the observability of the atmosphere given strong optical scattering from clouds and hazes. Figure 6.5 shows blackbody spectra for each of these planets at an equilibrium temperature which assumes a Venus-like Bond albedo of 0.7 and full day-night energy redistribution (light grey dashed lines). For LHS 3844 b, this spectrum would be detectable at $>3\sigma$ with MIRI LRS in 8 eclipses (e.g. for the resolution shown in Figure 6.6) or in any of the F1280W, F1500W or F1800W bands in four eclipses. While spectral features may not necessarily be distinguishable due to the cloud opacity, the photospheric temperature could be constrained from such a detection. GJ 1132 b has a lower S/N ratio but would be detectable at $>3\sigma$ with 20 MIRI LRS eclipses (e.g. at the resolution shown in Figure 6.5). Trappist-1 b would be more challenging to detect with MIRI LRS, but four eclipses in any of the F1280W, F1500W or F1800W bands could be sufficient to detect the atmosphere and measure its photospheric temperature.

We therefore conclude that the atmospheres of LHS 3844 b, GJ 1132 b and Trappist-1 b would be observable with MIRI even in the case of an extreme, Venus-like Bond

albedo. Furthermore, a measurement of the photospheric temperature in this case would allow a joint constraint on the Bond albedo and day-night energy redistribution of the planet, which are degenerate in determining the dayside equilibrium temperature. For example, a photospheric temperature of ~ 430 K for GJ 1132 b would suggest a high Bond albedo of $\sim 0.7/0.85$, assuming efficient day-night energy redistribution/no day-night energy redistribution, respectively. In between the clear and Venus-like albedo cases, more moderate clouds and hazes may result in muted spectral features that can still be characterised using spectral retrieval analysis. JWST/MIRI observations of such rocky exoplanets will therefore place important constraints on their atmospheric properties, regardless of the presence of clouds and hazes.

6.5.3 3D effects

3-dimensional effects are known to impact thermal emission observations of exoplanet atmospheres, especially those which are tidally-locked (e.g. Showman et al., 2009; Knutson et al., 2007; Demory et al., 2016a; Kreidberg et al., 2019). While efficient day-night energy redistribution can act to homogenise the dayside atmosphere, dayside temperature and/or compositional inhomogeneities can have observable effects on the secondary eclipse spectrum of the atmosphere (e.g. Feng et al., 2020; Taylor et al., 2020; Cubillos et al., 2021). For rocky exoplanets, a higher equilibrium temperature and/or lower surface pressure typically leads to less efficient day-night energy redistribution (Koll and Abbot, 2016), with redistribution becoming efficient at surface pressures of $O(1)$ bar (Koll, 2019). Therefore, the degree of longitudinal variation on the daysides of rocky exoplanets may vary considerably between different targets, depending on their atmospheric properties. In cases of more extreme inhomogeneity, it has been demonstrated for hot Jupiters that 1D retrievals can result in biased results, depending on the signal-to-noise ratio of the data (e.g. Feng et al., 2020; Taylor et al., 2020; Cubillos et al., 2021). It is therefore useful to place the results of 1D atmospheric secondary eclipse retrievals into context, e.g. using multi-dimensional retrievals (e.g. Feng et al., 2016, 2020; Taylor et al., 2020) or with complementary phase curve observations. Nevertheless, 1D retrievals can provide a valuable first glimpse into the dayside atmospheres of rocky exoplanets.

Ultimately, phase curve observations are required to deconstruct the longitudinal structure of an exoplanet atmosphere. Several methods exist to extract longitudinal information from such observations (e.g. Feng et al., 2016, 2020; Irwin et al., 2020; Cubillos et al., 2021). In particular, Cubillos et al. (2021) present a new approach in which a 1D retrieval is applied to each ‘slice’ in a longitudinally-deconstructed phase curve, applying it to the phase curve of the hot Jupiter WASP-43 b. Such an approach could be used to

apply other 1D retrieval frameworks to phase curve observations, for example to apply HyDRo to phase curves of rocky exoplanets.

6.6 Conclusions

In this chapter, we develop the first atmospheric retrieval framework, HyDRo, for thermal emission spectra of rocky exoplanets. This framework is able to retrieve the chemical composition of the atmosphere without assuming a particular background species, using the centered-log-ratio chemical abundance parameterisation of Benneke and Seager (2012). The method is therefore ideally suited for determining the chemistry of secondary atmospheres, with implications for the study of exo-geology. The retrieval framework is further able to constrain the atmospheric temperature profile, providing important information about the thermal properties and potential surface conditions of the planet.

In order to test the retrieval framework, we generate self-consistent atmospheric models and simulated JWST MIRI data for a range of irradiation conditions and atmospheric compositions. To do this, we adapt the GENESIS self-consistent atmospheric model (Gandhi and Madhusudhan 2017, see also Chapters 3 and 5) for non-H₂ rich compositions. We first test the case of Trappist-1 b assuming a Venus-like composition and find that ~30 secondary eclipses with MIRI LRS result in a confident CO₂ detection, consistent with previous studies (Lustig-Yaeger et al., 2019). The retrieval framework is able to accurately constrain the atmospheric chemical compositions and temperature profile to within 2σ , validating the method.

We then identify optimal rocky exoplanet candidates for atmospheric characterisation with JWST using a simple observability metric. The mid-infrared is an ideal spectral range for such efforts given the relatively higher signal-to-noise ratio (S/N) in secondary eclipse as well as strong spectral features from prominent molecules such as H₂O and CO₂. We therefore rank the observability of known rocky exoplanets by considering the number of eclipses required with MIRI LRS to detect the thermal emission spectrum at S/N=3 at a resolution of $R \sim 10$, $E_{S/N=3}$. This resolution is chosen as a nominal metric for the spectroscopic observability of rocky exoplanets, which is relevant for the chemical characterisation of their atmospheres. As expected, host star brightness, planetary radius and planetary temperature play key roles in determining observability. While brighter host stars result in smaller observational uncertainties, larger planetary radii and temperatures result in a greater signal for a given stellar radius and temperature.

We find that at least 33 known rocky exoplanets should have detectable thermal emission signatures with MIRI LRS at S/N=3 and a resolution of $R \sim 10$, in fewer than 10 eclipses.

Of these, 14 are more observable than GJ 1132 b, which is considered to be an optimal target for rocky exoplanet atmospheric characterisation (Morley et al., 2017b). In particular, we find that LHS 3844 b, GJ 1132 b and Trappist-1 b each represent ideal candidates for the hot (~ 1000 K), warm (~ 600 K) and temperate (~ 300 - 400 K) regimes, respectively. We therefore focus on these case studies to assess the observability of secondary atmospheres across this range of irradiation conditions.

We investigate the observational strategies required to characterise a range of CO₂-rich to H₂O-rich atmospheres in LHS 3844 b, GJ 1132 b and Trappist-1 b. In particular, we consider four key science cases in order of scientific complexity which may be addressed by thermal emission observations of these atmospheres: (i) Is the spectrum consistent with a hot, bare rock surface (assuming no heat redistribution, as investigated by Koll et al. 2019)? (ii) Are spectral features detected in the spectrum, confirming atmospheric absorption? i.e. Can a blackbody be ruled out by the data? (iii) Is CO₂ confidently detected in the spectrum, e.g. using the prominent spectral feature at $\sim 9 \mu\text{m}$? (iv) Is H₂O confidently detected?

We investigate the confidence with which these science cases can be addressed for a Venus-like, 50% CO₂/50% H₂O or 100% H₂O atmosphere for the case studies LHS 3844 b, GJ 1132 b and Trappist-1 b. For LHS 3844 b, we find that 8 MIRI LRS eclipses are sufficient to confidently characterise a cloud-free Venus-like composition, leading to $> 4\sigma$ detections of CO₂ and H₂O. Alternatively, 20 eclipses with MIRI LRS allow both a Venus-like and 50% CO₂/50% H₂O composition to be confidently characterised, while a blackbody spectrum would be significantly rejected (at $> 4\sigma$) in the case of a 100% H₂O composition, indicating atmospheric absorption. Furthermore, in the cases where CO₂ and H₂O are detected, their abundances can be constrained within ~ 0.5 dex, i.e. comparable to the precision currently achieved for hot Jupiters (e.g. Sheppard et al., 2017; Welbanks et al., 2019).

For GJ 1132 b, we find that 8 eclipses with MIRI LRS allow $> 4\sigma$ detections of CO₂ and H₂O for the Venus-like composition, and can rule out a blackbody spectrum for a 100% H₂O composition. Meanwhile, a longer observing time strategy of 20 MIRI LRS eclipses allows $\gtrsim 3\sigma$ detections of CO₂ and H₂O across the CO₂- to H₂O-dominated compositions considered here. Furthermore, in the cases where CO₂ and H₂O are detected, their abundances are constrained to within 1σ uncertainties of $\lesssim 0.75$ dex.

In the case of Trappist-1 b, we find that a Venus-like composition could be readily characterised with 30 MIRI LRS eclipses, consistent with previous studies (Lustig-Yaeger et al., 2019). In particular, we find that $\sim 5\sigma$ detections of CO₂ and H₂O would be possible for a Venus-like composition and that, in the case of a 50% CO₂/50% H₂O composition, H₂O could be detected at $\sim 3\sigma$. We also consider a longer observing time strategy of

80 eclipses with MIRI LRS, and find that this leads to $> 4\sigma$ detections of CO₂ and H₂O across the Venus-like and 50% CO₂/50% H₂O compositions, while a blackbody spectrum is rejected at $> 4\sigma$ in the case of a 100% H₂O composition. For both of these observing strategies, the abundances of CO₂ and H₂O (in the cases where they are detected) are constrained to within a $1-\sigma$ precision of < 0.7 dex.

In addition to the chemical constraints described above, we find that the photospheric temperature profiles of LHS 3844 b, GJ 1132 b and Trappist-1 b are all accurately retrieved within the 2σ uncertainties, with temperature constraints as tight as ~ 100 K in some cases. The observing strategies described above for each of these planets may therefore provide an unprecedented view into the thermal conditions on these rocky worlds. We further note that for the longer observing time strategies investigated, an additional 4 eclipses with the F1500W photometry band do not contribute significantly to the constraints achieved with the MIRI LRS data alone. Therefore, a MIRI LRS-only observing strategy may be ideal for the initial characterisation of rocky exoplanets such as these.

The temperature profiles we explore in this chapter are for clear atmospheres, though we note that clouds and hazes may affect the temperature profile and resulting thermal emission spectrum. For example, optical scattering from clouds and hazes can result in somewhat muted spectral features (e.g. Morley et al., 2015). For the case studies LHS 3844 b, GJ 1132 b and Trappist-1 b, we find that photospheric temperatures could nevertheless be measured with MIRI LRS and/or MIRI photometry in the case of a high, Venus-like Bond albedo of 0.7. Such a measurement could allow the Bond albedo of the planet to be estimated, and very cool photospheric temperatures (i.e. high Bond albedos) may suggest the presence of clouds/hazes. Thermal emission observations will therefore provide a unique opportunity to probe the conditions in cloudy, rocky exoplanet atmospheres.

The characterisation of rocky exoplanet atmospheres arguably represents the next frontier in exoplanet science. We have shown here that secondary eclipse observations with JWST/MIRI will be able to place important constraints on the atmospheric chemistry of rocky exoplanets and potential geochemical signatures through molecules such as H₂O and CO₂. Furthermore, we find that >30 known rocky exoplanets are suitable candidates for dayside atmospheric characterisation with JWST/MIRI. Thermal emission spectroscopy offers an unparalleled opportunity to characterise secondary atmospheres, whose small scale heights can be prohibitive in transmission spectroscopy, and will be an essential tool to characterise exo-geology in the near future.

Conclusions and Future Directions

In this thesis, I have explored a diversity of radiative and thermal properties of exoplanetary atmospheres across the mass range. My investigation has focused on the emission spectra of such atmospheres and how these relate to their thermal and chemical properties and physicochemical processes. In this pursuit, I have explored important considerations for atmospheric retrievals of emission spectra, and used self-consistent models to investigate the interplay between different physical processes in various exoplanet atmospheres. From poorly-irradiated sub-stellar objects to hot Jupiters, mini-Neptunes and rocky exoplanets, a diverse range of chemical compositions and temperature structures can influence the observable radiative properties of these atmospheres, as well as their surface/interior conditions. In what follows, I summarise the main conclusions of this thesis and describe future directions in this area.

7.1 Poorly-Irradiated Giant Exoplanets and Sub-Stellar Objects

In Chapter 2, I explored important considerations for the atmospheric retrieval of isolated and sub-stellar objects using high-precision spectra. Thermal emission from brown dwarfs can currently be observed with higher precision compared to giant exoplanets. Brown dwarfs therefore represent excellent analogues to study atmospheric processes in the low-irradiation regime, and can help us to prepare for future, high-precision observations of giant exoplanets. In particular, I considered two key developments for such retrievals: (i) a new temperature profile parameterisation, and (ii) a method to incorporate model

uncertainty into the retrieval. I then incorporated these considerations into the existing HyDRA retrieval framework (Gandhi and Madhusudhan, 2018) and tested this on both simulated and real T-dwarf emission spectra.

I began by investigating the temperature profiles of non-irradiated atmospheres and their effects on the observed emission spectra. Given the steep temperature profiles typical in such atmospheres, small changes in the temperature gradient can result in significant changes to the emergent thermal emission spectrum. I therefore proposed a new temperature profile parameterisation which allows enough flexibility for the temperature gradient to be accurately retrieved. Furthermore, this parameterisation is designed to mitigate numerical artefacts (e.g. unphysical oscillations) commonly encountered in retrievals of high-precision brown dwarf emission spectra. This is achieved by parameterising the temperature profile according to the changes, ΔT_i , in temperature across 6 vertical layers in the atmosphere. The priors on these ΔT_i are chosen such that temperature increases with pressure (as expected in the low-irradiation regime), which prevents large, unphysical oscillations.

Given the high precision of the data considered, model uncertainty contributes a significant source of error in the retrieval. I therefore quantified the uncertainty in the model due to spatial and spectral resolution, and found that by balancing model accuracy with computational expense a model uncertainty of $\sim 8\%$ could be achieved. However, this 8% is only due to the vertical and spectral resolution effects investigated, and other effects could add additional uncertainty. I therefore added a ‘tolerance’ parameter, x_{tol} , to the retrieval framework, which allows unknown model and/or data uncertainties to be retrieved and propagated into the posterior probability distributions of the other model parameters. Unlike other such parameters in the literature, I limited the lower bound on the prior of x_{tol} to be the minimum known model uncertainty, i.e. $\sim 8\%$ in this case. This ensured that the known model uncertainty is factored into the posterior probability distributions of all the model parameters.

Following these developments, I tested the new retrieval framework on both simulated and real HST/WFC3 emission spectra of T-dwarfs. The simulated data was based on the properties of the T-dwarf Gl 570D (Burgasser et al., 2000; Line et al., 2015), and the retrieval was able to accurately determine the temperature profile and chemical abundances in the atmosphere. Notably, the abundances of H_2O and CH_4 (i.e the dominant species shaping the near-infrared spectra of T-dwarfs) were constrained to a precision of ~ 0.1 dex, which is a significant improvement compared to the ~ 0.5 dex precisions currently achievable for hot Jupiters. I also applied the retrieval framework to the HST/WFC3 spectrum of the T5 dwarf 2MASS J2339+1352 (Buenzli et al., 2014). The retrieval was able to fit the data

accurately, and the retrieved temperature profile was consistent with the range of effective temperatures expected for an isolated T5 dwarf. Furthermore, the chemical abundances of H_2O and CH_4 were retrieved to a precision of ~ 0.1 dex, as with the simulated retrieval. This demonstrates that brown dwarfs provide an excellent opportunity to study hydrogen-rich atmospheres in the low-irradiation regime.

7.2 Hot Jupiters

In Chapters 3 and 4, I explored the emission spectra and temperature profiles of hot Jupiters. In Chapter 3, I first investigated metrics for inferring thermal inversions, as well as the sensitivity of atmospheric observations to TiO opacity (which can cause thermal inversions in hot Jupiters). I then used self-consistent atmospheric models to determine whether optical scattering from clouds/hazes is required to explain the optical to infrared spectra of three hot Jupiters spanning a wide range in temperature and gravity.

TiO has long been suggested to be the cause of thermal inversions in the atmospheres of hot Jupiters, and has been detected in some cases. However, such detections rely on the accuracy of the TiO opacities used to interpret the data. The new TOTO line list for TiO was recently reported, and in Chapter 3 I investigated the impact of this new line list relative to a previous line list on both emission and transmission spectra at low and high resolution. I found that high-resolution observations are sensitive to the differences between the line lists.

Following this, I also investigated the performance of photometric thermal inversion metrics as a function of equilibrium temperature, C/O ratio, metallicity, gravity and spectral type of the stellar host. To do this, I used an adaptation of the GENESIS self-consistent atmospheric model (Gandhi and Madhusudhan, 2017) which considers equilibrium chemistry as well as vertical mixing of chemical species. I found that the propensity for thermal inversions due to TiO peaks at $\text{C/O} \sim 0.9$, consistent with previous works. Using these self-consistent temperature profiles and thermal emission spectra, I assessed the performance of thermal inversion metrics against the ‘true’ model temperature profile. A common metric for inferring thermal inversions is the difference in brightness temperature between the Spitzer IRAC 1 and IRAC 2 bands. However, I found that this metric can be misleading for high C/O ratios and lower equilibrium temperatures ($\lesssim 2000$ K) due to CH_4 and HCN opacity increasing in the IRAC 1 band. A metric based on the J-band and IRAC 2 band performs significantly better, though it is important to note that all metrics are sensitive to the underlying chemistry of the atmosphere in question.

In Chapter 4, I modelled the temperature profiles and emission spectra of three hot Jupiters in order to interpret their observed optical to infrared spectra: KELT-1 b, WASP-18 b and WASP-43 b. Recent optical observations of these targets provide a window into their optical scattering properties, with a high optical albedo indicative of cloud and/or haze in the atmosphere. However, I find that the TESS and/or WFC3/UVIS observations for these three planets, alongside existing Spitzer observations, are consistent with pure thermal emission without the need for cloud or haze scattering. In particular, the high infrared fluxes observed suggest that these atmospheres have very inefficient day-night energy redistribution, especially in the cases of KELT-1 b and WASP-18 b. Any scattering of incident irradiation due to clouds or hazes would cool the dayside and result in lower infrared fluxes, excluding the possibility of significant cloud/haze cover on the daysides of these hot Jupiters.

7.3 Mini-Neptunes

In Chapter 5, I investigated the temperature profiles and thermal emission spectra of mini-Neptunes. To do this, I used an adaptation of the GENESIS self-consistent atmospheric model, to which I added opacity due to clouds and hazes. This work was motivated by the recent characterisation of the atmosphere and interior of K2-18 b, a mini-Neptune in the habitable zone of its host star. Madhusudhan et al. (2020) found that K2-18 b could potentially host liquid water beneath its atmosphere; in Chapter 5 I therefore investigated how the atmospheric properties of such exoplanets could impact potential surface conditions and atmospheric observations of such exoplanets.

I began by exploring the effects of various atmospheric parameters on the temperature profiles and thermal emission spectra of mini-Neptunes. I found that optical scattering from clouds and hazes can significantly cool the atmosphere and also result in more isothermal temperature profiles, with cool temperatures extending to deeper pressures where a surface could potentially be present. Meanwhile, the internal temperature principally affects the deeper atmosphere. While a high internal temperature does not typically affect the photospheric temperature (or, therefore, thermal emission observations), it can significantly heat up the atmosphere at deeper pressures. Therefore, the thermal conditions at a deep surface in a mini-Neptune may be sensitive to the internal temperature.

While the atmospheric conditions much deeper than the photosphere do not directly impact the thermal emission spectrum, constraints on the photospheric properties can provide insights into the deeper atmosphere. For example, the photospheric temperature determines the continuum level of the spectrum and can therefore be determined

observationally. A cool photospheric temperature alongside an inference of strong cloud or haze scattering (e.g. from muted spectral features, or constrained from transmission spectroscopy) could therefore be suggestive of a cool, isothermal temperature profile with temperate conditions even beneath the photosphere. I also showed in Chapter 5 that photometric observations with JWST/MIRI could constrain the photospheric temperature of a K2-18 b-like exoplanet, even for a photosphere as cool as ~ 200 K.

Motivated by the possibility of a liquid water surface on K2-18 b, I also investigated the atmospheric conditions which could lead to such temperate surface conditions. Using K2-18 b as a case study, I explored models with a range of atmospheric metallicities, internal temperatures and haze abundances. I found that scenarios with low metallicity and/or strong enough haze could result in habitable surface conditions, given a sufficiently shallow surface pressure (i.e. $\lesssim 1000$ bar). I also found this to be true for a planet similar to K2-18 b but with an irradiation temperature which is ~ 100 K hotter, although a greater haze abundance is required to achieve these conditions. Furthermore, since a liquid water ocean could be expected to increase the atmospheric water vapour abundance due to evaporation, I also considered an end-member scenario in which the atmosphere is saturated with H_2O . Despite the increased greenhouse effect, I found that this scenario still allows for habitable surface conditions if haze is present in the atmosphere. These results show that mini-Neptunes, whose large atmospheric scale heights make them conducive for characterisation, may represent ideal targets in the search for exoplanet habitability.

7.4 Rocky Exoplanets

In Chapter 6, I presented a new retrieval framework for the emission spectra of rocky exoplanets, `HyDRo`. `HyDRo` is based on the `HyDRA` retrieval framework (Gandhi and Madhusudhan, 2018), and is adapted to include opacity sources expected to be important in secondary atmospheres with high mean molecular weight. Furthermore, while giant exoplanet retrievals typically assume a hydrogen-rich composition, the chemical abundance parameterisation in `HyDRo` does not assume a dominant chemical species. Therefore, the chemical compositions of rocky exoplanet atmospheres, whose dominant species are not known a priori, can be retrieved. I tested the new retrieval framework on the simulated JWST/MIRI spectrum of Trappist-1 b, and found that the spectrum, temperature profile and chemical composition of the atmosphere were accurately retrieved.

Motivated by the potential for rocky exoplanet characterisation in thermal emission with JWST, I further investigated the observability of known rocky exoplanets. I found that 33 known exoplanets with masses $< 10M_{\oplus}$ and radii $< 2R_{\oplus}$ have atmospheres whose

thermal emission will be detectable in fewer than 10 eclipses with MIRI/LRS (assuming a resolution of $R \sim 10$). Among these, GJ 1132 b and LHS 3844 b represent excellent case studies probing the warm to hot regimes (~ 600 - 800 K). I also found that Trappist-1 b would require just over 10 eclipses with MIRI/LRS for an atmospheric detection, making it an excellent case study for the temperate regime (~ 400 K).

Beyond the detection of an atmosphere, I used `HyDRo` to estimate the chemical and thermal atmospheric constraints which could be obtained for Trappist-1 b, GJ 1132 b and LHS 3844 b using JWST/MIRI. In particular, I explored a range of atmospheric compositions including a cloud-free Venus-like case, a 50%CO₂/50%H₂O composition and a 100% H₂O composition. For the Venus-like atmosphere, I found that as few as 8 eclipses of LHS 3844 b with MIRI/LRS would be sufficient to detect CO₂ and H₂O at $\gtrsim 4\sigma$ significance. Meanwhile, 20 eclipses with MIRI/LRS are sufficient to detect CO₂ and H₂O at $\gtrsim 4\sigma$ for both the Venus-like and 50%CO₂/50%H₂O compositions. For GJ 1132 b, 8 MIRI/LRS eclipses allow both CO₂ and H₂O to be detected in the case of a cloud-free Venus-like atmosphere (at 4.70σ and 4.42σ , respectively). Alternatively, a longer observing time involving 20 MIRI/LRS eclipses allows $> 3\sigma$ detections of CO₂ and H₂O across the CO₂-rich to H₂O-rich compositions. For Trappist-1 b, I found that 30 eclipses with MIRI/LRS were enough to confidently detect CO₂ and H₂O in the Venus-like case, consistent with previous estimates (e.g. Lustig-Yaeger et al. 2019). Furthermore, 80 eclipses with MIRI/LRS allow CO₂ and H₂O to be detected to $\gtrsim 4\sigma$ for the Venus-like and 50%CO₂/50%H₂O compositions.

Thermal emission observations provide an excellent way to characterise the atmospheres of rocky exoplanet atmospheres, as their typically small scale heights can be prohibitive for transmission spectroscopy. Furthermore, thermal emission spectra can provide excellent constraints on the thermal profiles of these atmospheres. Indeed, for the case studies described above, `HyDRo` was consistently able to retrieve the photospheric temperature profile within the 1σ uncertainties. Overall, these results demonstrate that JWST/MIRI will be able to place unprecedented constraints on the atmospheric properties of rocky exoplanets.

7.5 Future Directions

As both observational and modelling capabilities continue to expand, so too does our understanding of the diverse and exotic landscape of exoplanet atmospheres. Moving forwards, the characterisation of increasingly detailed planetary processes will become possible. In particular, cloud processes across the exoplanetary mass range are yet to

be fully understood. For example, retrievals of cloudy brown dwarf atmospheres have been shown to be challenging (Burningham et al., 2017); future work will therefore be needed to characterise the properties of clouds in brown dwarfs. Furthermore, continued observations with TESS will add to the population of hot Jupiters with optical albedo measurements, allowing a broader understanding of cloud formation across this regime.

Recent developments have shown that the field of exoplanet atmospheres is rapidly progressing towards the characterisation of smaller and cooler exoplanets. For example, observations of mini-Neptunes such as K2-18 b (Benneke et al., 2019b; Tsiaras et al., 2019) and GJ 1214 b (Kreidberg et al., 2014a) are beginning to shed light on the chemical compositions and cloud properties in this regime. Furthermore, rocky exoplanets represent a new frontier in the characterisation of exoplanet atmospheres. Despite the significant challenges in observing the atmospheres of small exoplanets, current observations have already begun to place the first constraints on their atmospheric properties (e.g. Demory et al., 2016b; de Wit et al., 2016; Southworth et al., 2017; Kreidberg et al., 2019). JWST will be instrumental in providing further insights into such low-mass exoplanets. Its high S/N and broad infrared spectral range will allow the detection of a wide range of molecular species (e.g. Madhusudhan, 2019), shedding light on the diversity of both primary and secondary atmospheric compositions. Robust atmospheric retrieval frameworks will also be needed to confidently interpret these observations. The HyDRo framework presented in this thesis provides an initial step in this direction for thermal emission spectra, and future work in this area will include developments such as the capability to constrain cloud and haze properties.

Across the regime of low-mass exoplanets, interactions between the atmosphere and interior offer an enticing opportunity to constrain the atmospheric, surface and interior physics of these exotic worlds in tandem. For example, from rocky exoplanets to mini-Neptunes, a wide variety of surface and formation processes can affect the composition and thickness of the atmosphere. These include the accretion of volatiles, surface outgassing and dissolution of the atmosphere into a magma ocean (e.g. Elkins-Tanton and Seager, 2008; Rogers et al., 2011; Kite et al., 2016, 2020). Larger sub-Neptunes may not even host a defined surface/interior boundary, and the extent of their atmosphere-interior mixing is unknown. Conversely, the atmosphere and its energy transport mechanisms play a key role in determining the thermodynamic conditions of the surface and interior. For example, the pressure and temperature at the surface can affect outgassing rates (Gaillard and Scaillet, 2014) or the phase of the surface (Chapter 5).

Understanding these varied processes and their interplay will require both theoretical developments and laboratory experiments in order to push the boundaries of our knowl-

edge beyond the geologies, atmospheric compositions and cloud/haze physics seen in the solar system. Such studies are already underway, including laboratory haze experiments (e.g. Hörst et al., 2018; Moran et al., 2020; Vuitton et al., 2021), outgassing studies (e.g. Elkins-Tanton and Seager, 2008; Thompson et al., 2021) and studies of magma-atmosphere and ocean-atmosphere interactions (e.g. Kite et al., 2016, 2020; Hu and Delgado Diaz, 2019). Future work will explore such properties in more detail and investigate their observable signatures. Furthermore, increasingly precise constraints on the chemical compositions and thermal properties of such atmospheres (e.g. with JWST) will allow the first detections of such signatures. The rich diversity of physical and chemical processes in the low-mass regime promises to expand our understanding of planetary physics, and to ultimately place our own planet into the broader context of the exoplanet population.

References

- Ackerman, A. S. and Marley, M. S. (2001). Precipitating Condensation Clouds in Substellar Atmospheres. *ApJ*, 556(2):872–884.
- Agúndez, M., Parmentier, V., Venot, O., Hersant, F., and Selsis, F. (2014a). Pseudo 2D chemical model of hot-Jupiter atmospheres: application to HD 209458b and HD 189733b. *A&A*, 564:A73.
- Agúndez, M., Venot, O., Selsis, F., and Iro, N. (2014b). The Puzzling Chemical Composition of GJ 436b's Atmosphere: Influence of Tidal Heating on the Chemistry. *ApJ*, 781(2):68.
- Allard, N. F., Spiegelman, F., and Kielkopf, J. F. (2007). Study of the K-H₂ quasi-molecular line satellite in the potassium resonance line. *A&A*, 465:1085–1091.
- Allard, N. F., Spiegelman, F., and Kielkopf, J. F. (2016). K-H₂ line shapes for the spectra of cool brown dwarfs. *A&A*, 589:A21.
- Allard, N. F., Spiegelman, F., Leininger, T., and Molliere, P. (2019). New study of the line profiles of sodium perturbed by H₂. *A&A*, 628:A120.
- Allart, R., Bourrier, V., Lovis, C., Ehrenreich, D., et al. (2018). Spectrally resolved helium absorption from the extended atmosphere of a warm Neptune-mass exoplanet. *Science*, 362(6421):1384–1387.
- Almenara, J. M., Díaz, R. F., Bonfils, X., and Udry, S. (2016). Absolute densities, masses, and radii of the WASP-47 system determined dynamically. *A&A*, 595:L5.
- Amundsen, D. S., Baraffe, I., Tremblin, P., Manners, J., et al. (2014). Accuracy tests of radiation schemes used in hot Jupiter global circulation models. *A&A*, 564:A59.
- Amundsen, D. S., Mayne, N. J., Baraffe, I., Manners, J., et al. (2016). The UK Met Office global circulation model with a sophisticated radiation scheme applied to the hot Jupiter HD 209458b. *A&A*, 595:A36.
- Amundsen, D. S., Tremblin, P., Manners, J., Baraffe, I., and Mayne, N. J. (2017). Treatment of overlapping gaseous absorption with the correlated-k method in hot Jupiter and brown dwarf atmosphere models. *A&A*, 598:A97.
- Angelo, I. and Hu, R. (2017). A Case for an Atmosphere on Super-Earth 55 Cancri e. *AJ*, 154(6):232.

- Angerhausen, D., DeLarme, E., and Morse, J. A. (2015). A Comprehensive Study of Kepler Phase Curves and Secondary Eclipses: Temperatures and Albedos of Confirmed Kepler Giant Planets. *PASP*, 127(957):1113.
- Apai, D., Radigan, J., Buenzli, E., Burrows, A., et al. (2013). HST Spectral Mapping of L/T Transition Brown Dwarfs Reveals Cloud Thickness Variations. *ApJ*, 768:121.
- Arcangeli, J., Désert, J.-M., Line, M. R., Bean, J. L., et al. (2018). H⁻ Opacity and Water Dissociation in the Dayside Atmosphere of the Very Hot Gas Giant WASP-18b. *ApJL*, 855:L30.
- Asplund, M., Grevesse, N., Sauval, A. J., and Scott, P. (2009). The Chemical Composition of the Sun. *Annual Review of Astronomy and Astrophysics*, 47:481–522.
- Astudillo-Defru, N., Cloutier, R., Wang, S. X., Teske, J., et al. (2020). A hot terrestrial planet orbiting the bright M dwarf L 168-9 unveiled by TESS. *A&A*, 636:A58.
- Astudillo-Defru, N. and Rojo, P. (2013). Ground-based detection of calcium and possibly scandium and hydrogen in the atmosphere of HD 209458b. *A&A*, 557:A56.
- Atreya, S. K., Crida, A., Guillot, T., Lunine, J. I., et al. (2018). *The Origin and Evolution of Saturn, with Exoplanet Perspective*, page 5. Cambridge University Press.
- Awiphan, S., Kerins, E., Pichadee, S., Komonjinda, S., et al. (2016). Transit timing variation and transmission spectroscopy analyses of the hot Neptune GJ3470b. *MNRAS*, 463(3):2574–2582.
- Bains, W., Seager, S., and Zsom, A. (2014). Photosynthesis in hydrogen-dominated atmospheres. *Life (Basel, Switzerland)*, 4:716–744.
- Baraffe, I., Chabrier, G., and Barman, T. (2008). Structure and evolution of super-Earth to super-Jupiter exoplanets. I. Heavy element enrichment in the interior. *A&A*, 482(1):315–332.
- Baraffe, I., Chabrier, G., Barman, T. S., Allard, F., and Hauschildt, P. H. (2003). Evolutionary models for cool brown dwarfs and extrasolar giant planets. The case of HD 209458. *A&A*, 402:701–712.
- Barber, R. J., Strange, J. K., Hill, C., Polyansky, O. L., et al. (2014). ExoMol line lists - III. An improved hot rotation-vibration line list for HCN and HNC. *MNRAS*, 437:1828–1835.
- Barklem, P. S. and Collet, R. (2016). Partition functions and equilibrium constants for diatomic molecules and atoms of astrophysical interest. *A&A*, 588:A96.
- Barman, T. S., Hauschildt, P. H., and Allard, F. (2005). Phase-Dependent Properties of Extrasolar Planet Atmospheres. *ApJ*, 632(2):1132–1139.
- Barman, T. S., Konopacky, Q. M., Macintosh, B., and Marois, C. (2015). Simultaneous Detection of Water, Methane, and Carbon Monoxide in the Atmosphere of Exoplanet HR8799b. *ApJ*, 804(1):61.
- Barman, T. S., Macintosh, B., Konopacky, Q. M., and Marois, C. (2011). Clouds and Chemistry in the Atmosphere of Extrasolar Planet HR8799b. *ApJ*, 733(1):65.

- Barragán, O., Gandolfi, D., Dai, F., Livingston, J., et al. (2018). K2-141 b. A 5- M_{\oplus} super-Earth transiting a K7 V star every 6.7 h. *A&A*, 612:A95.
- Barros, S. C. C., Almenara, J. M., Deleuil, M., Diaz, R. F., et al. (2014). Revisiting the transits of CoRoT-7b at a lower activity level. *A&A*, 569:A74.
- Barstow, J. K. (2021). The curse of clouds. *Astronomy and Geophysics*, 62(1):1.36–1.42.
- Barstow, J. K., Aigrain, S., Irwin, P. G. J., and Sing, D. K. (2017). A Consistent Retrieval Analysis of 10 Hot Jupiters Observed in Transmission. *ApJ*, 834:50.
- Barstow, J. K., Changeat, Q., Garland, R., Line, M. R., et al. (2020). A comparison of exoplanet spectroscopic retrieval tools. *MNRAS*, 493(4):4884–4909.
- Barstow, J. K. and Irwin, P. G. J. (2016). Habitable worlds with JWST: transit spectroscopy of the TRAPPIST-1 system? *MNRAS*, 461(1):L92–L96.
- Basri, G. and Brown, M. E. (2006). Planetesimals to brown dwarfs: What is a planet? *Annual Review of Earth and Planetary Sciences*, 34(1):193–216.
- Batalha, N. E., Mandell, A., Pontoppidan, K., Stevenson, K. B., et al. (2017). Pan-dExo: A Community Tool for Transiting Exoplanet Science with JWST & HST. *PASP*, 129(6):064501.
- Bean, J. L., Miller-Ricci Kempton, E., and Homeier, D. (2010). A ground-based transmission spectrum of the super-Earth exoplanet GJ 1214b. *Nature*, 468(7324):669–672.
- Beatty, T. G., Madhusudhan, N., Pogge, R., Chung, S. M., et al. (2017a). The Broadband and Spectrally Resolved H-band Eclipse of KELT-1b and the Role of Surface Gravity in Stratospheric Inversions in Hot Jupiters. *AJ*, 154:242.
- Beatty, T. G., Madhusudhan, N., Tsiaras, A., Zhao, M., et al. (2017b). Evidence for Atmospheric Cold-trap Processes in the Noninverted Emission Spectrum of Kepler-13Ab Using HST/WFC3. *AJ*, 154(4):158.
- Beatty, T. G., Marley, M. S., Gaudi, B. S., Colón, K. D., et al. (2019). Spitzer Phase Curves of KELT-1b and the Signatures of Nightside Clouds in Thermal Phase Observations. *AJ*, 158(4):166.
- Beatty, T. G., Wong, I., Fetherolf, T., Line, M. R., et al. (2020). The TESS Phase Curve of KELT-1b Suggests a High Dayside Albedo. *AJ*, 160(5):211.
- Bell, K. L. and Berrington, K. A. (1987). Free-free absorption coefficient of the negative hydrogen ion. *Journal of Physics B Atomic Molecular Physics*, 20(4):801–806.
- Bell, T. J. and Cowan, N. B. (2018). Increased Heat Transport in Ultra-hot Jupiter Atmospheres through H_2 Dissociation and Recombination. *ApJL*, 857(2):L20.
- Bell, T. J., Nikolov, N., Cowan, N. B., Barstow, J. K., et al. (2017). The Very Low Albedo of WASP-12b from Spectral Eclipse Observations with Hubble. *ApJL*, 847(1):L2.
- Ben-Jaffel, L. and Ballester, G. E. (2013). Hubble Space Telescope detection of oxygen in the atmosphere of exoplanet HD 189733b. *A&A*, 553:A52.

- Ben-Yami, M., Madhusudhan, N., Cabot, S. H. C., Constantinou, S., et al. (2020). Neutral Cr and V in the Atmosphere of Ultra-hot Jupiter WASP-121 b. *ApJL*, 897(1):L5.
- Benneke, B., Knutson, H. A., Lothringer, J., Crossfield, I. J. M., et al. (2019a). A sub-Neptune exoplanet with a low-metallicity methane-depleted atmosphere and Mie-scattering clouds. *Nature Astronomy*, 3(9):813–821.
- Benneke, B. and Seager, S. (2012). Atmospheric Retrieval for Super-Earths: Uniquely Constraining the Atmospheric Composition with Transmission Spectroscopy. *ApJ*, 753(2):100.
- Benneke, B. and Seager, S. (2013). How to Distinguish between Cloudy Mini-Neptunes and Water/Volatile-dominated Super-Earths. *ApJ*, 778(2):153.
- Benneke, B., Wong, I., Piaulet, C., Knutson, H. A., et al. (2019b). Water Vapor and Clouds on the Habitable-zone Sub-Neptune Exoplanet K2-18b. *ApJL*, 887(1):L14.
- Berta, Z. K., Charbonneau, D., Désert, J.-M., Miller-Ricci Kempton, E., et al. (2012). The Flat Transmission Spectrum of the Super-Earth GJ1214b from Wide Field Camera 3 on the Hubble Space Telescope. *ApJ*, 747(1):35.
- Berta-Thompson, Z. K., Irwin, J., Charbonneau, D., Newton, E. R., et al. (2015). A rocky planet transiting a nearby low-mass star. *Nature*, 527(7577):204–207.
- Biller, B. A. and Bonnefoy, M. (2018). *Exoplanet Atmosphere Measurements from Direct Imaging*, page 101. Springer International Publishing AG.
- Birkby, J. L. (2018). *Spectroscopic Direct Detection of Exoplanets*, page 16. Springer International Publishing AG.
- Birkby, J. L., de Kok, R. J., Brogi, M., de Mooij, E. J. W., et al. (2013). Detection of water absorption in the day side atmosphere of HD 189733 b using ground-based high-resolution spectroscopy at $3.2\mu\text{m}$. *MNRAS*, 436:L35–L39.
- Birkby, J. L., de Kok, R. J., Brogi, M., Schwarz, H., and Snellen, I. A. G. (2017). Discovery of Water at High Spectral Resolution in the Atmosphere of 51 Peg b. *AJ*, 153(3):138.
- Blecic, J., Dobbs-Dixon, I., and Greene, T. (2017). The Implications of 3D Thermal Structure on 1D Atmospheric Retrieval. *ApJ*, 848:127.
- Blecic, J., Harrington, J., Madhusudhan, N., Stevenson, K. B., et al. (2014). Spitzer Observations of the Thermal Emission from WASP-43b. *ApJ*, 781(2):116.
- Bond, J. C., Laretta, D. S., and O'Brien, D. P. (2010). Making the Earth: Combining dynamics and chemistry in the Solar System. *Icarus*, 205:321–337.
- Bonfils, X., Almenara, J. M., Cloutier, R., Wünsche, A., et al. (2018). Radial velocity follow-up of GJ1132 with HARPS. A precise mass for planet b and the discovery of a second planet. *A&A*, 618:A142.
- Bonfils, X., Gillon, M., Udry, S., Armstrong, D., et al. (2012). A hot Uranus transiting the nearby M dwarf GJ 3470. Detected with HARPS velocimetry. Captured in transit with TRAPPIST photometry. *A&A*, 546:A27.

- Bonnefoy, M., Zurlo, A., Baudino, J. L., Lucas, P., et al. (2016). First light of the VLT planet finder SPHERE. IV. Physical and chemical properties of the planets around HR8799. *A&A*, 587:A58.
- Borucki, W. J. (2018). *Space Missions for Exoplanet Science: Kepler/K2*, page 80. Springer International Publishing AG.
- Bouchet, P., García-Marín, M., Lagage, P. O., Amiaux, J., et al. (2015). The Mid-Infrared Instrument for the James Webb Space Telescope, III: MIRIM, The MIRI Imager. *PASP*, 127(953):612.
- Bouchy, F., Udry, S., Mayor, M., Moutou, C., et al. (2005). ELODIE metallicity-biased search for transiting Hot Jupiters. II. A very hot Jupiter transiting the bright K star HD 189733. *A&A*, 444(1):L15–L19.
- Bourrier, V., Ehrenreich, D., Wheatley, P. J., Bolmont, E., et al. (2017). Reconnaissance of the TRAPPIST-1 exoplanet system in the Lyman- α line. *A&A*, 599:L3.
- Bourrier, V. and Lecavelier des Etangs, A. (2018). *Characterizing Evaporating Atmospheres of Exoplanets*, page 148. Springer International Publishing AG.
- Bourrier, V., Lecavelier des Etangs, A., Dupuy, H., Ehrenreich, D., et al. (2013). Atmospheric escape from HD 189733b observed in H I Lyman- α : detailed analysis of HST/STIS September 2011 observations. *A&A*, 551:A63.
- Boutle, I. A., Mayne, N. J., Drummond, B., Manners, J., et al. (2017). Exploring the climate of Proxima B with the Met Office Unified Model. *A&A*, 601:A120.
- Bowler, B. P. and Nielsen, E. L. (2018). *Occurrence Rates from Direct Imaging Surveys*, page 155. Springer International Publishing AG.
- Brogi, M., de Kok, R. J., Albrecht, S., Snellen, I. A. G., et al. (2016). Rotation and Winds of Exoplanet HD 189733 b Measured with High-dispersion Transmission Spectroscopy. *ApJ*, 817(2):106.
- Brogi, M., de Kok, R. J., Birkby, J. L., Schwarz, H., and Snellen, I. A. G. (2014). Carbon monoxide and water vapor in the atmosphere of the non-transiting exoplanet HD 179949 b. *A&A*, 565:A124.
- Brogi, M., Snellen, I. A. G., de Kok, R. J., Albrecht, S., et al. (2012). The signature of orbital motion from the dayside of the planet τ Boötis b. *Nature*, 486:502–504.
- Brogi, M., Snellen, I. A. G., de Kok, R. J., Albrecht, S., et al. (2013). Detection of Molecular Absorption in the Dayside of Exoplanet 51 Pegasi b? *ApJ*, 767(1):27.
- Brooke, T. Y., Knacke, R. F., Encrenaz, T., Drossart, P., et al. (1998). Models of the ISO 3- μ m Reflection Spectrum of Jupiter. *Icarus*, 136(1):1–13.
- Buchner, J., Georgakakis, A., Nandra, K., Hsu, L., et al. (2014). X-ray spectral modelling of the AGN obscuring region in the CDFS: Bayesian model selection and catalogue. *A&A*, 564:A125.

- Budaj, J., Kocifaj, M., Salmeron, R., and Hubeny, I. (2015). Tables of phase functions, opacities, albedos, equilibrium temperatures, and radiative accelerations of dust grains in exoplanets. *MNRAS*, 454(1):2–27.
- Buenzli, E., Apai, D., Radigan, J., Morley, C., et al. (2013). Probing the Heterogeneous Cloud Structure of Variable Brown Dwarfs with HST. In *Protostars and Planets VI Posters*.
- Buenzli, E., Apai, D., Radigan, J., Reid, I. N., and Flateau, D. (2014). Brown Dwarf Photospheres are Patchy: A Hubble Space Telescope Near-infrared Spectroscopic Survey Finds Frequent Low-level Variability. *ApJ*, 782:77.
- Burgasser, A. J. (2011). The Brown Dwarf-Exoplanet Connection. In Beaulieu, J. P., Dieters, S., and Tinetti, G., editors, *Molecules in the Atmospheres of Extrasolar Planets*, volume 450 of *Astronomical Society of the Pacific Conference Series*, page 113.
- Burgasser, A. J., Geballe, T. R., Leggett, S. K., Kirkpatrick, J. D., and Golimowski, D. A. (2006). A Unified Near-Infrared Spectral Classification Scheme for T Dwarfs. *ApJ*, 637:1067–1093.
- Burgasser, A. J., Kirkpatrick, J. D., Brown, M. E., Reid, I. N., et al. (2002). The Spectra of T Dwarfs. I. Near-Infrared Data and Spectral Classification. *ApJ*, 564(1):421–451.
- Burgasser, A. J., Kirkpatrick, J. D., Cutri, R. M., McCallon, H., et al. (2000). Discovery of a Brown Dwarf Companion to Gliese 570ABC: A 2MASS T Dwarf Significantly Cooler than Gliese 229B. *ApJL*, 531:L57–L60.
- Burgasser, A. J., Kirkpatrick, J. D., Liebert, J., and Burrows, A. (2003). The Spectra of T Dwarfs. II. Red Optical Data. *ApJ*, 594:510–524.
- Burningham, B., Marley, M. S., Line, M. R., Lupu, R., et al. (2017). Retrieval of atmospheric properties of cloudy L dwarfs. *MNRAS*, 470:1177–1197.
- Burrows, A., Budaj, J., and Hubeny, I. (2008a). Theoretical Spectra and Light Curves of Close-in Extrasolar Giant Planets and Comparison with Data. *ApJ*, 678(2):1436–1457.
- Burrows, A., Heng, K., and Nampaisarn, T. (2011). The Dependence of Brown Dwarf Radii on Atmospheric Metallicity and Clouds: Theory and Comparison with Observations. *ApJ*, 736(1):47.
- Burrows, A., Hubbard, W. B., Lunine, J. I., and Liebert, J. (2001). The theory of brown dwarfs and extrasolar giant planets. *Reviews of Modern Physics*, 73(3):719–765.
- Burrows, A., Hubeny, I., Budaj, J., Knutson, H. A., and Charbonneau, D. (2007). Theoretical Spectral Models of the Planet HD 209458b with a Thermal Inversion and Water Emission Bands. *ApJL*, 668:L171–L174.
- Burrows, A., Ibgui, L., and Hubeny, I. (2008b). Optical Albedo Theory of Strongly Irradiated Giant Planets: The Case of HD 209458b. *ApJ*, 682:1277–1282.
- Burrows, A., Marley, M., Hubbard, W. B., Lunine, J. I., et al. (1997). A Nongray Theory of Extrasolar Giant Planets and Brown Dwarfs. *ApJ*, 491:856–875.

- Burrows, A. and Sharp, C. M. (1999). Chemical Equilibrium Abundances in Brown Dwarf and Extrasolar Giant Planet Atmospheres. *ApJ*, 512:843–863.
- Burrows, A., Sudarsky, D., and Hubeny, I. (2006a). L and T Dwarf Models and the L to T Transition. *ApJ*, 640:1063–1077.
- Burrows, A., Sudarsky, D., and Hubeny, I. (2006b). Theory for the Secondary Eclipse Fluxes, Spectra, Atmospheres, and Light Curves of Transiting Extrasolar Giant Planets. *ApJ*, 650:1140–1149.
- Burrows, A. and Volobuyev, M. (2003). Calculations of the Far-Wing Line Profiles of Sodium and Potassium in the Atmospheres of Substellar-Mass Objects. *ApJ*, 583:985–995.
- Cabot, S. H. C., Madhusudhan, N., Hawker, G. A., and Gandhi, S. (2019). On the robustness of analysis techniques for molecular detections using high-resolution exoplanet spectroscopy. *MNRAS*, 482(4):4422–4436.
- Carlson, B. E., Lacy, A. A., and Rossow, W. B. (1994). Belt-zone variations in the Jovian cloud structure. *J. Geophys. Res.*, 99(E7):14623–14658.
- Carone, L., Baeyens, R., Mollière, P., Barth, P., et al. (2020). Equatorial retrograde flow in WASP-43b elicited by deep wind jets? *MNRAS*, 496(3):3582–3614.
- Cartier, K. M. S., Beatty, T. G., Zhao, M., Line, M., et al. (2017). Near-infrared Emission Spectrum of WASP-103b Using Hubble Space Telescope/Wide Field Camera 3. *AJ*, 153:34.
- Casasayas-Barris, N., Pallé, E., Nowak, G., Yan, F., et al. (2017). Detection of sodium in the atmosphere of WASP-69b. *A&A*, 608:A135.
- Casasayas-Barris, N., Pallé, E., Yan, F., Chen, G., et al. (2018). Na I and H α absorption features in the atmosphere of MASCARA-2b/KELT-20b. *A&A*, 616:A151.
- Castelli, F. and Kurucz, R. L. (2003). New Grids of ATLAS9 Model Atmospheres. In Piskunov, N., Weiss, W. W., and Gray, D. F., editors, *Modelling of Stellar Atmospheres*, volume 210 of *IAU Symposium*, page A20.
- Castor, J. I., Dykema, P. G., and Klein, R. I. (1992). A New Scheme for Multidimensional Line Transfer. II. ETLA Method in One Dimension with Application to Iron K alpha Lines. *ApJ*, 387:561.
- Chabrier, G., Johansen, A., Janson, M., and Rafikov, R. (2014). Giant Planet and Brown Dwarf Formation. *Protostars and Planets VI*, pages 619–642.
- Chachan, Y., Knutson, H. A., Gao, P., Kataria, T., et al. (2019). A Hubble PanCET Study of HAT-P-11b: A Cloudy Neptune with a Low Atmospheric Metallicity. *AJ*, 158(6):244.
- Charbonneau, D., Berta, Z. K., Irwin, J., Burke, C. J., et al. (2009). A super-Earth transiting a nearby low-mass star. *Nature*, 462(7275):891–894.
- Charbonneau, D., Brown, T. M., Latham, D. W., and Mayor, M. (2000). Detection of Planetary Transits Across a Sun-like Star. *ApJL*, 529(1):L45–L48.

- Charbonneau, D., Brown, T. M., Noyes, R. W., and Gilliland, R. L. (2002). Detection of an Extrasolar Planet Atmosphere. *ApJ*, 568(1):377–384.
- Chauvin, G., Desidera, S., Lagrange, A. M., Vigan, A., et al. (2017). Discovery of a warm, dusty giant planet around HIP 65426. *A&A*, 605:L9.
- Chen, G., Guenther, E. W., Pallé, E., Nortmann, L., et al. (2017a). The GTC exoplanet transit spectroscopy survey. V. A spectrally-resolved Rayleigh scattering slope in GJ 3470b. *A&A*, 600:A138.
- Chen, G., Pallé, E., Nortmann, L., Murgas, F., et al. (2017b). The GTC exoplanet transit spectroscopy survey. VI. Detection of sodium in WASP-52b’s cloudy atmosphere. *A&A*, 600:L11.
- Chen, G., Pallé, E., Welbanks, L., Prieto-Arranz, J., et al. (2018). The GTC exoplanet transit spectroscopy survey. IX. Detection of haze, Na, K, and Li in the super-Neptune WASP-127b. *A&A*, 616:A145.
- Chilcote, J., Pueyo, L., De Rosa, R. J., Vargas, J., et al. (2017). 1-2.4 μm Near-IR Spectrum of the Giant Planet β Pictoris b Obtained with the Gemini Planet Imager. *AJ*, 153(4):182.
- Christiansen, J. L., Ballard, S., Charbonneau, D., Madhusudhan, N., et al. (2010). Studying the Atmosphere of the Exoplanet HAT-P-7b Via Secondary Eclipse Measurements with EPOXI, Spitzer, and Kepler. *ApJ*, 710(1):97–104.
- Christiansen, J. L., Vanderburg, A., Burt, J., Fulton, B. J., et al. (2017). Three’s Company: An Additional Non-transiting Super-Earth in the Bright HD 3167 System, and Masses for All Three Planets. *AJ*, 154(3):122.
- Cloutier, R., Astudillo-Defru, N., Bonfils, X., Jenkins, J. S., et al. (2019a). Characterization of the L 98-59 multi-planetary system with HARPS. Mass characterization of a hot super-Earth, a sub-Neptune, and a mass upper limit on the third planet. *A&A*, 629:A111.
- Cloutier, R., Astudillo-Defru, N., Doyon, R., Bonfils, X., et al. (2019b). Confirmation of the radial velocity super-Earth K2-18c with HARPS and CARMENES. *A&A*, 621:A49.
- Cloutier, R., Eastman, J. D., Rodriguez, J. E., Astudillo-Defru, N., et al. (2020a). A Pair of TESS Planets Spanning the Radius Valley around the Nearby Mid-M Dwarf LTT 3780. *AJ*, 160(1):3.
- Cloutier, R., Rodriguez, J. E., Irwin, J., Charbonneau, D., et al. (2020b). TOI-1235 b: A Keystone Super-Earth for Testing Radius Valley Emergence Models around Early M Dwarfs. *AJ*, 160(1):22.
- Collier Cameron, A., Guenther, E., Smalley, B., McDonald, I., et al. (2010). Line-profile tomography of exoplanet transits - II. A gas-giant planet transiting a rapidly rotating A5 star. *MNRAS*, 407(1):507–514.
- Collins, K. A., Kielkopf, J. F., and Stassun, K. G. (2017). Transit Timing Variation Measurements of WASP-12b and Qatar-1b: No Evidence Of Additional Planets. *AJ*, 153(2):78.

- Colón, K. D., Ford, E. B., Redfield, S., Fortney, J. J., et al. (2012). Probing potassium in the atmosphere of HD 80606b with tunable filter transit spectrophotometry from the Gran Telescopio Canarias. *MNRAS*, 419(3):2233–2250.
- Cooper, C. S. and Showman, A. P. (2006). Dynamics and Disequilibrium Carbon Chemistry in Hot Jupiter Atmospheres, with Application to HD 209458b. *ApJ*, 649(2):1048–1063.
- Cowan, N. B. and Agol, E. (2011). The Statistics of Albedo and Heat Recirculation on Hot Exoplanets. *ApJ*, 729(1):54.
- Cowan, N. B., Machalek, P., Croll, B., Shekhtman, L. M., et al. (2012). Thermal Phase Variations of WASP-12b: Defying Predictions. *ApJ*, 747(1):82.
- Crossfield, I. J. M., Barman, T., Hansen, B. M. S., Tanaka, I., and Kodama, T. (2012). Re-evaluating WASP-12b: Strong Emission at 2.315 μm , Deeper Occultations, and an Isothermal Atmosphere. *ApJ*, 760:140.
- Crossfield, I. J. M., Dragomir, D., Cowan, N. B., Daylan, T., et al. (2020). Phase Curves of Hot Neptune LTT 9779b Suggest a High-metallicity Atmosphere. *ApJL*, 903(1):L7.
- Crossfield, I. J. M., Hansen, B. M. S., Harrington, J., Cho, J. Y. K., et al. (2010). A New 24 μm Phase Curve for ν Andromedae b. *ApJ*, 723(2):1436–1446.
- Crouzet, N., McCullough, P. R., Deming, D., and Madhusudhan, N. (2014). Water Vapor in the Spectrum of the Extrasolar Planet HD 189733b. II. The Eclipse. *ApJ*, 795(2):166.
- Császár, A. G., Czakó, G., Furtenbacher, T., and Mátyus, E. (2007). An active database approach to complete rotational–vibrational spectra of small molecules. *Annu. Rep. Comput. Chem.*, 3:155–176.
- Cubillos, P. E., Keating, D., Cowan, N. B., Vos, J. M., et al. (2021). Longitudinally Resolved Spectral Retrieval (ReSpect) of WASP-43b. *ApJ*, 915(1):45.
- Cushing, M. C., Kirkpatrick, J. D., Gelino, C. R., Griffith, R. L., et al. (2011). The Discovery of Y Dwarfs using Data from the Wide-field Infrared Survey Explorer (WISE). *ApJ*, 743:50.
- Cushing, M. C., Marley, M. S., Saumon, D., Kelly, B. C., et al. (2008). Atmospheric Parameters of Field L and T Dwarfs. *ApJ*, 678:1372–1395.
- Cushing, M. C., Roellig, T. L., Marley, M. S., Saumon, D., et al. (2006). A Spitzer Infrared Spectrograph Spectral Sequence of M, L, and T Dwarfs. *ApJ*, 648:614–628.
- Cutri, R. M., Skrutskie, M. F., van Dyk, S., Beichman, C. A., et al. (2003a). VizieR Online Data Catalog: 2MASS All-Sky Catalog of Point Sources (Cutri+ 2003). *VizieR Online Data Catalog*, page II/246.
- Cutri, R. M., Skrutskie, M. F., van Dyk, S., Beichman, C. A., et al. (2003b). *2MASS All Sky Catalog of point sources*. NASA/IPAC Infrared Science Archive.
- Dahn, C. C., Harris, H. C., Vrba, F. J., Guetter, H. H., et al. (2002). Astrometry and Photometry for Cool Dwarfs and Brown Dwarfs. *AJ*, 124:1170–1189.

- Dai, F., Masuda, K., Winn, J. N., and Zeng, L. (2019). Homogeneous Analysis of Hot Earths: Masses, Sizes, and Compositions. *ApJ*, 883(1):79.
- Damasso, M., Zeng, L., Malavolta, L., Mayo, A., et al. (2019). So close, so different: characterization of the K2-36 planetary system with HARPS-N. *A&A*, 624:A38.
- Davies, J. H. and Davies, D. R. (2010). Earth's surface heat flux. *Solid Earth*, 1(1):5–24.
- de Kok, R. J., Birkby, J., Brogi, M., Schwarz, H., et al. (2014). Identifying new opportunities for exoplanet characterisation at high spectral resolution. *A&A*, 561:A150.
- de Wit, J., Wakeford, H. R., Gillon, M., Lewis, N. K., et al. (2016). A combined transmission spectrum of the Earth-sized exoplanets TRAPPIST-1 b and c. *Nature*, 537(7618):69–72.
- de Wit, J., Wakeford, H. R., Lewis, N. K., Delrez, L., et al. (2018). Atmospheric reconnaissance of the habitable-zone Earth-sized planets orbiting TRAPPIST-1. *Nature Astronomy*, 2:214–219.
- Deeg, H. J. and Alonso, R. (2018). *Transit Photometry as an Exoplanet Discovery Method*, page 117. Springer International Publishing AG.
- Delrez, L., Madhusudhan, N., Lendl, M., Gillon, M., et al. (2018). High-precision multiwavelength eclipse photometry of the ultra-hot gas giant exoplanet WASP-103 b. *MNRAS*, 474:2334–2351.
- Delrez, L., Santerne, A., Almenara, J. M., Anderson, D. R., et al. (2016). WASP-121 b: a hot Jupiter close to tidal disruption transiting an active F star. *MNRAS*, 458(4):4025–4043.
- Deming, D., Fraine, J. D., Sada, P. V., Madhusudhan, N., et al. (2012). Infrared Eclipses of the Strongly Irradiated Planet WASP-33b, and Oscillations of Its Host Star. *ApJ*, 754(2):106.
- Deming, D. and Knutson, H. A. (2020). Highlights of exoplanetary science from Spitzer. *Nature Astronomy*, 4:453–466.
- Deming, D., Seager, S., Winn, J., Miller-Ricci, E., et al. (2009). Discovery and Characterization of Transiting Super Earths Using an All-Sky Transit Survey and Follow-up by the James Webb Space Telescope. *PASP*, 121(883):952.
- Deming, D., Wilkins, A., McCullough, P., Burrows, A., et al. (2013). Infrared Transmission Spectroscopy of the Exoplanets HD 209458b and XO-1b Using the Wide Field Camera-3 on the Hubble Space Telescope. *ApJ*, 774:95.
- Demory, B.-O., de Wit, J., Lewis, N., Fortney, J., et al. (2013). Inference of Inhomogeneous Clouds in an Exoplanet Atmosphere. *ApJL*, 776(2):L25.
- Demory, B.-O., Gillon, M., de Wit, J., Madhusudhan, N., et al. (2016a). A map of the large day-night temperature gradient of a super-Earth exoplanet. *Nature*, 532(7598):207–209.
- Demory, B. O., Gillon, M., Deming, D., Valencia, D., et al. (2011a). Detection of a transit of the super-Earth 55 Cancri e with warm Spitzer. *A&A*, 533:A114.
- Demory, B.-O., Gillon, M., Madhusudhan, N., and Queloz, D. (2016b). Variability in the super-Earth 55 Cnc e. *MNRAS*, 455(2):2018–2027.

- Demory, B.-O., Seager, S., Madhusudhan, N., Kjeldsen, H., et al. (2011b). The High Albedo of the Hot Jupiter Kepler-7 b. *ApJL*, 735(1):L12.
- Diamond-Lowe, H., Berta-Thompson, Z., Charbonneau, D., and Kempton, E. M. R. (2018). Ground-based Optical Transmission Spectroscopy of the Small, Rocky Exoplanet GJ 1132b. *AJ*, 156(2):42.
- Diamond-Lowe, H., Charbonneau, D., Malik, M., Kempton, E. M. R., and Beletsky, Y. (2020). Optical Transmission Spectroscopy of the Terrestrial Exoplanet LHS 3844b from 13 Ground-based Transit Observations. *AJ*, 160(4):188.
- Diamond-Lowe, H., Stevenson, K. B., Bean, J. L., Line, M. R., and Fortney, J. J. (2014). New Analysis Indicates No Thermal Inversion in the Atmosphere of HD 209458b. *ApJ*, 796(1):66.
- Dobbs-Dixon, I. and Agol, E. (2013). Three-dimensional radiative-hydrodynamical simulations of the highly irradiated short-period exoplanet HD 189733b. *MNRAS*, 435(4):3159–3168.
- Dorn, C., Noack, L., and Rozel, A. B. (2018). Outgassing on stagnant-lid super-Earths. *A&A*, 614:A18.
- Dressing, C. D. and Charbonneau, D. (2015). The Occurrence of Potentially Habitable Planets Orbiting M Dwarfs Estimated from the Full Kepler Dataset and an Empirical Measurement of the Detection Sensitivity. *ApJ*, 807(1):45.
- Dressing, C. D., Charbonneau, D., Dumusque, X., Gettel, S., et al. (2015). The Mass of Kepler-93b and The Composition of Terrestrial Planets. *ApJ*, 800(2):135.
- Drummond, B., Carter, A. L., Hébrard, E., Mayne, N. J., et al. (2019). The carbon-to-oxygen ratio: implications for the spectra of hydrogen-dominated exoplanet atmospheres. *MNRAS*, 486(1):1123–1137.
- Drummond, B., Hébrard, E., Mayne, N. J., Venot, O., et al. (2020). Implications of three-dimensional chemical transport in hot Jupiter atmospheres: Results from a consistently coupled chemistry-radiation-hydrodynamics model. *A&A*, 636:A68.
- Drummond, B., Mayne, N. J., Manners, J., Baraffe, I., et al. (2018b). The 3D Thermal, Dynamical, and Chemical Structure of the Atmosphere of HD 189733b: Implications of Wind-driven Chemistry for the Emission Phase Curve. *ApJ*, 869(1):28.
- Drummond, B., Mayne, N. J., Manners, J., Carter, A. L., et al. (2018a). Observable Signatures of Wind-driven Chemistry with a Fully Consistent Three-dimensional Radiative Hydrodynamics Model of HD 209458b. *ApJL*, 855(2):L31.
- Drummond, B., Tremblin, P., Baraffe, I., Amundsen, D. S., et al. (2016). The effects of consistent chemical kinetics calculations on the pressure-temperature profiles and emission spectra of hot Jupiters. *A&A*, 594:A69.
- Dumusque, X., Turner, O., Dorn, C., Eastman, J. D., et al. (2019). Hot, rocky and warm, puffy super-Earths orbiting TOI-402 (HD 15337). *A&A*, 627:A43.

- Dupuy, T. J. and Liu, M. C. (2012). The Hawaii Infrared Parallax Program. I. Ultracool Binaries and the L/T Transition. *ApJS*, 201(2):19.
- Durisen, R. H., Boss, A. P., Mayer, L., Nelson, A. F., et al. (2007). Gravitational Instabilities in Gaseous Protoplanetary Disks and Implications for Giant Planet Formation. In Reipurth, B., Jewitt, D., and Keil, K., editors, *Protostars and Planets V*, page 607.
- Ehrenreich, D. (2015). A giant cloud of hydrogen escaping the warm Neptune-mass planet GJ 436b. In *AAS/Division for Extreme Solar Systems Abstracts*, volume 47 of *AAS/Division for Extreme Solar Systems Abstracts*, page 200.01.
- Elkins-Tanton, L. T. and Seager, S. (2008). Ranges of Atmospheric Mass and Composition of Super-Earth Exoplanets. *ApJ*, 685(2):1237–1246.
- Elser, S., Meyer, M. R., and Moore, B. (2012). On the origin of elemental abundances in the terrestrial planets. *Icarus*, 221:859–874.
- Espinoza, N., Brahm, R., Henning, T., Jordán, A., et al. (2020). HD 213885b: a transiting 1-d-period super-Earth with an Earth-like composition around a bright ($V = 7.9$) star unveiled by TESS. *MNRAS*, 491(2):2982–2999.
- Espinoza, N., Rackham, B. V., Jordán, A., Apai, D., et al. (2019). ACCESS: a featureless optical transmission spectrum for WASP-19b from Magellan/IMACS. *MNRAS*, 482(2):2065–2087.
- Esteves, L. J., De Mooij, E. J. W., and Jayawardhana, R. (2015). Changing Phases of Alien Worlds: Probing Atmospheres of Kepler Planets with High-precision Photometry. *ApJ*, 804(2):150.
- Evans, T. M., Pont, F., Sing, D. K., Aigrain, S., et al. (2013). The Deep Blue Color of HD 189733b: Albedo Measurements with Hubble Space Telescope/Space Telescope Imaging Spectrograph at Visible Wavelengths. *ApJL*, 772(2):L16.
- Evans, T. M., Sing, D. K., Kataria, T., Goyal, J., et al. (2017). An ultrahot gas-giant exoplanet with a stratosphere. *Nature*, 548:58–61.
- Evans, T. M., Sing, D. K., Wakeford, H. R., Nikolov, N., et al. (2016). Detection of H₂O and Evidence for TiO/VO in an Ultra-hot Exoplanet Atmosphere. *ApJL*, 822(1):L4.
- Feautrier, P. (1964). Sur la resolution numerique de l'equation de transfert. *Comptes Rendus Academie des Sciences (serie non specifique)*, 258:3189.
- Fei, Y., Mao, H., and Hemley, R. J. (1993). Thermal expansivity, bulk modulus, and melting curve of h₂o–ice vii to 20 gpa. *The Journal of Chemical Physics*, 99(7):5369–5373.
- Feng, Y. K., Line, M. R., and Fortney, J. J. (2020). 2D Retrieval Frameworks for Hot Jupiter Phase Curves. *AJ*, 160(3):137.
- Feng, Y. K., Line, M. R., Fortney, J. J., Stevenson, K. B., et al. (2016). The Impact of Non-uniform Thermal Structure on the Interpretation of Exoplanet Emission Spectra. *ApJ*, 829(1):52.

- Feroz, F., Hobson, M. P., and Bridges, M. (2009). MULTINEST: an efficient and robust Bayesian inference tool for cosmology and particle physics. *MNRAS*, 398:1601–1614.
- Fischer, D. A., Anglada-Escude, G., Arriagada, P., Baluev, R. V., et al. (2016). State of the Field: Extreme Precision Radial Velocities. *PASP*, 128(964):066001.
- Fischer, D. A., Howard, A. W., Laughlin, G. P., Macintosh, B., et al. (2014). Exoplanet Detection Techniques. *Protostars and Planets VI*, pages 715–737.
- Foreman-Mackey, D., Montet, B. T., Hogg, D. W., Morton, T. D., et al. (2015). A Systematic Search for Transiting Planets in the K2 Data. *ApJ*, 806(2):215.
- Fortney, J. J., Cooper, C. S., Showman, A. P., Marley, M. S., and Freedman, R. S. (2006a). The Influence of Atmospheric Dynamics on the Infrared Spectra and Light Curves of Hot Jupiters. *ApJ*, 652:746–757.
- Fortney, J. J., Lodders, K., Marley, M. S., and Freedman, R. S. (2008). A Unified Theory for the Atmospheres of the Hot and Very Hot Jupiters: Two Classes of Irradiated Atmospheres. *ApJ*, 678:1419–1435.
- Fortney, J. J., Marley, M. S., and Barnes, J. W. (2007). Planetary Radii across Five Orders of Magnitude in Mass and Stellar Insolation: Application to Transits. *ApJ*, 659(2):1661–1672.
- Fortney, J. J., Saumon, D., Marley, M. S., Lodders, K., and Freedman, R. S. (2006b). Atmosphere, Interior, and Evolution of the Metal-rich Transiting Planet HD 149026b. *ApJ*, 642(1):495–504.
- Fossati, L., Haswell, C. A., Froning, C. S., Hebb, L., et al. (2010). Metals in the Exosphere of the Highly Irradiated Planet WASP-12b. *ApJL*, 714(2):L222–L227.
- Fraine, J., Deming, D., Benneke, B., Knutson, H., et al. (2014). Water vapour absorption in the clear atmosphere of a Neptune-sized exoplanet. *Nature*, 513(7519):526–529.
- Fraine, J., Mayorga, L. C., Stevenson, K. B., Lewis, N. K., et al. (2021). The Dark World: A Tale of WASP-43b in Reflected Light with HST WFC3/UVIS. *AJ*, 161(6):269.
- French, M., Mattsson, T. R., Nettelmann, N., and Redmer, R. (2009). Equation of state and phase diagram of water at ultrahigh pressures as in planetary interiors. *PhRvB*, 79(5):054107.
- Fressin, F., Torres, G., Charbonneau, D., Bryson, S. T., et al. (2013). The False Positive Rate of Kepler and the Occurrence of Planets. *ApJ*, 766(2):81.
- Fridlund, M., Gaidos, E., Barragán, O., Persson, C. M., et al. (2017). K2-111 b - a short period super-Earth transiting a metal poor, evolved old star. *A&A*, 604:A16.
- Friedson, A. J. and Gonzales, E. J. (2017). Inhibition of ordinary and diffusive convection in the water condensation zone of the ice giants and implications for their thermal evolution. *Icarus*, 297:160–178.
- Frustagli, G., Poretti, E., Milbourne, T., Malavolta, L., et al. (2020). An ultra-short period rocky super-Earth orbiting the G2-star HD 80653. *A&A*, 633:A133.

- Fulton, B. J., Petigura, E. A., Howard, A. W., Isaacson, H., et al. (2017). The California-Kepler Survey. III. A Gap in the Radius Distribution of Small Planets. *AJ*, 154:109.
- Furtenbacher, T. and Császár, A. G. (2012). MARVEL: measured active rotational-vibrational energy levels. II. Algorithmic improvements. *JQSRT*, 113:929–935.
- Furtenbacher, T., Császár, A. G., and Tennyson, J. (2007). MARVEL: measured active rotational-vibrational energy levels. *JMS*, 245:115–125.
- Gaia Collaboration, Brown, A. G. A., Vallenari, A., Prusti, T., et al. (2018). Gaia Data Release 2. Summary of the contents and survey properties. *A&A*, 616:A1.
- Gaillard, F. and Scaillet, B. (2014). A theoretical framework for volcanic degassing chemistry in a comparative planetology perspective and implications for planetary atmospheres. *Earth and Planetary Science Letters*, 403:307–316.
- Gandhi, S., Brogi, M., Yurchenko, S. N., Tennyson, J., et al. (2020a). Molecular cross-sections for high-resolution spectroscopy of super-Earths, warm Neptunes, and hot Jupiters. *MNRAS*, 495(1):224–237.
- Gandhi, S. and Madhusudhan, N. (2017). genesis: new self-consistent models of exoplanetary spectra. *MNRAS*, 472:2334–2355.
- Gandhi, S. and Madhusudhan, N. (2018). Retrieval of exoplanet emission spectra with HyDRA. *MNRAS*, 474:271–288.
- Gandhi, S. and Madhusudhan, N. (2019). New avenues for thermal inversions in atmospheres of hot Jupiters. *MNRAS*, 485(4):5817–5830.
- Gandhi, S., Madhusudhan, N., Hawker, G., and Piette, A. (2019). HyDRA-H: Simultaneous Hybrid Retrieval of Exoplanetary Emission Spectra. *AJ*, 158(6):228.
- Gandhi, S., Madhusudhan, N., and Mandell, A. (2020b). H- and Dissociation in Ultra-hot Jupiters: A Retrieval Case Study of WASP-18b. *AJ*, 159(5):232.
- Gao, P., Marley, M. S., and Ackerman, A. S. (2018). Sedimentation Efficiency of Condensation Clouds in Substellar Atmospheres. *ApJ*, 855(2):86.
- Gao, P., Thorngren, D. P., Lee, G. K. H., Fortney, J. J., et al. (2020). Aerosol composition of hot giant exoplanets dominated by silicates and hydrocarbon hazes. *Nature Astronomy*, 4:951–956.
- Garcia Munoz, A. and Isaak, K. G. (2015). Probing exoplanet clouds with optical phase curves. *Proceedings of the National Academy of Science*, 112(44):13461–13466.
- Garhart, E., Deming, D., Mandell, A., Knutson, H. A., et al. (2020). Statistical Characterization of Hot Jupiter Atmospheres Using Spitzer’s Secondary Eclipses. *AJ*, 159(4):137.
- Geballe, T. R., Saumon, D., Golimowski, D. A., Leggett, S. K., et al. (2009). Spectroscopic Detection of Carbon Monoxide in Two Late-Type T Dwarfs. *ApJ*, 695:844–854.
- Geballe, T. R., Saumon, D., Leggett, S. K., Knapp, G. R., et al. (2001). Infrared Observations and Modeling of One of the Coolest T Dwarfs: Gliese 570D. *ApJ*, 556:373–379.

- Gillon, M., Anderson, D. R., Collier-Cameron, A., Delrez, L., et al. (2014). WASP-103 b: a new planet at the edge of tidal disruption. *A&A*, 562:L3.
- Gillon, M., Demory, B.-O., Van Grootel, V., Motalebi, E., et al. (2017a). Two massive rocky planets transiting a K-dwarf 6.5 parsecs away. *Nature Astronomy*, 1:0056.
- Gillon, M., Jehin, E., Lederer, S. M., Delrez, L., et al. (2016). Temperate Earth-sized planets transiting a nearby ultracool dwarf star. *Nature*, 533(7602):221–224.
- Gillon, M., Triaud, A. H. M. J., Demory, B.-O., Jehin, E., et al. (2017b). Seven temperate terrestrial planets around the nearby ultracool dwarf star TRAPPIST-1. *Nature*, 542(7642):456–460.
- Gillon, M., Triaud, A. H. M. J., Fortney, J. J., Demory, B. O., et al. (2012). The TRAPPIST survey of southern transiting planets. I. Thirty eclipses of the ultra-short period planet WASP-43 b. *A&A*, 542:A4.
- Ginzburg, S., Schlichting, H. E., and Sari, R. (2018). Core-powered mass-loss and the radius distribution of small exoplanets. *MNRAS*, 476(1):759–765.
- Glasse, A., Rieke, G. H., Bauwens, E., García-Marín, M., et al. (2015). The Mid-Infrared Instrument for the James Webb Space Telescope, IX: Predicted Sensitivity. *PASP*, 127(953):686.
- Golimowski, D. A., Leggett, S. K., Marley, M. S., Fan, X., et al. (2004). L' and M' Photometry of Ultracool Dwarfs. *AJ*, 127:3516–3536.
- Gordon, I. E., Rothman, L. S., Hill, C., Kochanov, R. V., et al. (2017). The HITRAN2016 molecular spectroscopic database. *JQSRT*, 203:3–69.
- Goyal, J. M., Mayne, N., Drummond, B., Sing, D. K., et al. (2020). A library of self-consistent simulated exoplanet atmospheres. *MNRAS*, 498(4):4680–4704.
- Gravity Collaboration, Nowak, M., Lacour, S., Mollière, P., et al. (2020). Peering into the formation history of β Pictoris b with VLTI/GRAVITY long-baseline interferometry. *A&A*, 633:A110.
- Gray, D. F. (1976). *The observation and analysis of stellar photospheres*. Wiley.
- Greene, T. P., Line, M. R., Montero, C., Fortney, J. J., et al. (2016). Characterizing Transiting Exoplanet Atmospheres with JWST. *ApJ*, 817(1):17.
- Guenther, E. W., Barragán, O., Dai, F., Gandolfi, D., et al. (2017). K2-106, a system containing a metal-rich planet and a planet of lower density. *A&A*, 608:A93.
- Guillot, T. (1995). Condensation of Methane, Ammonia, and Water and the Inhibition of Convection in Giant Planets. *Science*, 269(5231):1697–1699.
- Guillot, T. (2010). On the radiative equilibrium of irradiated planetary atmospheres. *A&A*, 520:A27.
- Guillot, T. (2019). Uranus and Neptune are key to understand planets with hydrogen atmospheres [White paper]. *arXiv e-prints*, page arXiv:1908.02092.

- Günther, M. N., Pozuelos, F. J., Dittmann, J. A., Dragomir, D., et al. (2019). A super-Earth and two sub-Neptunes transiting the nearby and quiet M dwarf TOI-270. *Nature Astronomy*, 3:1099–1108.
- Gupta, A. and Schlichting, H. E. (2019). Sculpting the valley in the radius distribution of small exoplanets as a by-product of planet formation: the core-powered mass-loss mechanism. *MNRAS*, 487(1):24–33.
- Hammond, M. and Pierrehumbert, R. T. (2017). Linking the Climate and Thermal Phase Curve of 55 Cancri e. *ApJ*, 849(2):152.
- Hansen, B. M. S. (2008). On the Absorption and Redistribution of Energy in Irradiated Planets. *ApJS*, 179(2):484–508.
- Hardegree-Ullman, K. K., Cushing, M. C., Muirhead, P. S., and Christiansen, J. L. (2019). Kepler Planet Occurrence Rates for Mid-type M Dwarfs as a Function of Spectral Type. *AJ*, 158(2):75.
- Harpsoe, K. B. W., Hardis, S., Hinse, T. C., Jørgensen, U. G., et al. (2013). The transiting system GJ1214: high-precision defocused transit observations and a search for evidence of transit timing variation. *A&A*, 549:A10.
- Harrington, J., Hansen, B. M., Luszcz, S. H., Seager, S., et al. (2006). The Phase-Dependent Infrared Brightness of the Extrasolar Planet ν Andromedae b. *Science*, 314(5799):623–626.
- Harrington, J., Himes, M. D., Cubillos, P. E., Blečić, J., et al. (2021). An Open-Source Bayesian Atmospheric Radiative Transfer (BART) Code: I. Design, Tests, and Application to Exoplanet HD 189733 b. *arXiv e-prints*, page arXiv:2104.12522.
- Harris, G. J., Tennyson, J., Kaminsky, B. M., Pavlenko, Y. V., and Jones, H. R. A. (2006). Improved HCN/HNC linelist, model atmospheres and synthetic spectra for WZ Cas. *MNRAS*, 367:400–406.
- Harrison, J. H. D., Bonsor, A., and Madhusudhan, N. (2018). Polluted white dwarfs: constraints on the origin and geology of exoplanetary material. *MNRAS*, 479:3814–3841.
- Haswell, C. A., Fossati, L., Ayres, T., France, K., et al. (2012). Near-ultraviolet Absorption, Chromospheric Activity, and Star-Planet Interactions in the WASP-12 system. *ApJ*, 760(1):79.
- Hawker, G. A., Madhusudhan, N., Cabot, S. H. C., and Gandhi, S. (2018). Evidence for Multiple Molecular Species in the Hot Jupiter HD 209458b. *ApJL*, 863(1):L11.
- Haynes, K., Mandell, A. M., Madhusudhan, N., Deming, D., and Knutson, H. (2015). Spectroscopic Evidence for a Temperature Inversion in the Dayside Atmosphere of Hot Jupiter WASP-33b. *ApJ*, 806:146.
- He, C., Hörst, S. M., Lewis, N. K., Yu, X., et al. (2018). Photochemical Haze Formation in the Atmospheres of Super-Earths and Mini-Neptunes. *AJ*, 156(1):38.

- Hebb, L., Collier-Cameron, A., Loeillet, B., Pollacco, D., et al. (2009). WASP-12b: The Hottest Transiting Extrasolar Planet Yet Discovered. *ApJ*, 693(2):1920–1928.
- Helled, R. and Bodenheimer, P. (2010). Metallicity of the massive protoplanets around HR 8799 If formed by gravitational instability. *Icarus*, 207(2):503–508.
- Hellier, C., Anderson, D. R., Collier Cameron, A., Gillon, M., et al. (2009). An orbital period of 0.94 days for the hot-Jupiter planet WASP-18b. *Nature*, 460(7259):1098–1100.
- Hellier, C., Anderson, D. R., Collier Cameron, A., Gillon, M., et al. (2011). WASP-43b: the closest-orbiting hot Jupiter. *A&A*, 535:L7.
- Helling, C. (2019). Exoplanet Clouds. *Annual Review of Earth and Planetary Sciences*, 47:583–606.
- Helling, C., Dehn, M., Woitke, P., and Hauschildt, P. H. (2008). Consistent Simulations of Substellar Atmospheres and Nonequilibrium Dust Cloud Formation. *ApJL*, 675(2):L105.
- Helling, C., Lee, G., Dobbs-Dixon, I., Mayne, N., et al. (2016). The mineral clouds on HD 209458b and HD 189733b. *MNRAS*, 460(1):855–883.
- Heng, K., Hayek, W., Pont, F., and Sing, D. K. (2012). On the effects of clouds and hazes in the atmospheres of hot Jupiters: semi-analytical temperature-pressure profiles. *MNRAS*, 420(1):20–36.
- Heng, K. and Tsai, S.-M. (2016). Analytical Models of Exoplanetary Atmospheres. III. Gaseous C-H-O-N Chemistry with Nine Molecules. *ApJ*, 829:104.
- Heng, K., Wyttenbach, A., Lavie, B., Sing, D. K., et al. (2015). A Non-isothermal Theory for Interpreting Sodium Lines in Transmission Spectra of Exoplanets. *ApJL*, 803(1):L9.
- Henry, G. W., Marcy, G. W., Butler, R. P., and Vogt, S. S. (2000). A Transiting “51 Peg-like” Planet. *ApJL*, 529(1):L41–L44.
- Herbort, O., Woitke, P., Helling, C., and Zerkle, A. (2020). The atmospheres of rocky exoplanets. I. Outgassing of common rock and the stability of liquid water. *A&A*, 636:A71.
- Hill, C., Yurchenko, S. N., and Tennyson, J. (2013). Temperature-dependent molecular absorption cross sections for exoplanets and other atmospheres. *Icarus*, 226(2):1673–1677.
- Hoeijmakers, H. J., de Kok, R. J., Snellen, I. A. G., Brogi, M., et al. (2015). A search for TiO in the optical high-resolution transmission spectrum of HD 209458b: Hindrance due to inaccuracies in the line database. *A&A*, 575:A20.
- Hooton, M. J., Watson, C. A., de Mooij, E. J. W., Gibson, N. P., and Kitzmann, D. (2018). A Ground-based Near-ultraviolet Secondary Eclipse Observation of KELT-9b. *ApJL*, 869(2):L25.
- Hörst, S. M., He, C., Lewis, N. K., Kempton, E. M. R., et al. (2018). Haze production rates in super-Earth and mini-Neptune atmosphere experiments. *Nature Astronomy*, 2:303–306.

- Howe, A. R. and Burrows, A. S. (2012). Theoretical Transit Spectra for GJ 1214b and Other “Super-Earths”. *ApJ*, 756(2):176.
- Hu, R. and Delgado Diaz, H. (2019). Stability of Nitrogen in Planetary Atmospheres in Contact with Liquid Water. *ApJ*, 886(2):126.
- Hu, R., Ehlmann, B. L., and Seager, S. (2012a). Theoretical Spectra of Terrestrial Exoplanet Surfaces. *ApJ*, 752(1):7.
- Hu, R., Peterson, L., and Wolf, E. T. (2020). O₂- and CO-rich Atmospheres for Potentially Habitable Environments on TRAPPIST-1 Planets. *ApJ*, 888(2):122.
- Hu, R., Seager, S., and Bains, W. (2012b). Photochemistry in Terrestrial Exoplanet Atmospheres. I. Photochemistry Model and Benchmark Cases. *ApJ*, 761(2):166.
- Hubeny, I. (2017). Model atmospheres of sub-stellar mass objects. *MNRAS*, 469:841–869.
- Hubeny, I. and Burrows, A. (2007). A Systematic Study of Departures from Chemical Equilibrium in the Atmospheres of Substellar Mass Objects. *ApJ*, 669:1248–1261.
- Hubeny, I., Burrows, A., and Sudarsky, D. (2003). A Possible Bifurcation in Atmospheres of Strongly Irradiated Stars and Planets. *ApJ*, 594:1011–1018.
- Hubeny, I. and Mihalas, D. (2014). *Theory of Stellar Atmospheres*. Princeton University Press.
- Huitson, C. M., Sing, D. K., Vidal-Madjar, A., Ballester, G. E., et al. (2012). Temperature-pressure profile of the hot Jupiter HD 189733b from HST sodium observations: detection of upper atmospheric heating. *MNRAS*, 422(3):2477–2488.
- Husser, T.-O., Wende-von Berg, S., Dreizler, S., Homeier, D., et al. (2013). A new extensive library of PHOENIX stellar atmospheres and synthetic spectra. *A&A*, 553:A6.
- Irwin, L. N. (2018). *Exotic Forms of Life on Other Worlds*, page 161. Springer International Publishing AG.
- Irwin, P. G. J., Parmentier, V., Taylor, J., Barstow, J., et al. (2020). 2.5D retrieval of atmospheric properties from exoplanet phase curves: application to WASP-43b observations. *MNRAS*, 493(1):106–125.
- Irwin, P. G. J., Teanby, N. A., de Kok, R., Fletcher, L. N., et al. (2008). The NEMESIS planetary atmosphere radiative transfer and retrieval tool. *JQSRT*, 109:1136–1150.
- Jansen, T. and Kipping, D. (2020). Detection of the phase curve and occultation of WASP-100b with TESS. *MNRAS*, 494(3):4077–4089.
- Janson, M., Brandt, T. D., Kuzuhara, M., Spiegel, D. S., et al. (2013). Direct Imaging Detection of Methane in the Atmosphere of GJ 504 b. *ApJL*, 778(1):L4.
- Jensen, A. G., Redfield, S., Endl, M., Cochran, W. D., et al. (2012). A Detection of H α in an Exoplanetary Exosphere. *ApJ*, 751(2):86.

- John, T. L. (1988). Continuous absorption by the negative hydrogen ion reconsidered. *A&A*, 193(1-2):189–192.
- Kalirai, J. (2018). Scientific discovery with the James Webb Space Telescope. *Contemporary Physics*, 59(3):251–290.
- Kane, S. R., Fetherolf, T., and Hill, M. L. (2020). The Dark Planets of the WASP-47 Planetary System. *AJ*, 159(4):176.
- Karman, T., Gordon, I. E., van der Avoird, A., Baranov, Y. I., et al. (2019). Update of the HITRAN collision-induced absorption section. *Icarus*, 328:160–175.
- Kasting, J. F., Whitmire, D. P., and Reynolds, R. T. (1993). Habitable Zones around Main Sequence Stars. *Icarus*, 101(1):108–128.
- Kataria, T., Sing, D. K., Lewis, N. K., Visscher, C., et al. (2016). The Atmospheric Circulation of a Nine-hot-Jupiter Sample: Probing Circulation and Chemistry over a Wide Phase Space. *ApJ*, 821(1):9.
- Keating, D. and Cowan, N. B. (2017). Revisiting the Energy Budget of WASP-43b: Enhanced Day-Night Heat Transport. *ApJL*, 849(1):L5.
- Kempton, E. M. R., Bean, J. L., Louie, D. R., Deming, D., et al. (2018). A Framework for Prioritizing the TESS Planetary Candidates Most Amenable to Atmospheric Characterization. *PASP*, 130(993):114401.
- Khalafinejad, S., von Essen, C., Hoeijmakers, H. J., Zhou, G., et al. (2017). Exoplanetary atmospheric sodium revealed by orbital motion. Narrow-band transmission spectroscopy of HD 189733b with UVES. *A&A*, 598:A131.
- Kirkpatrick, J. D. (2005). New Spectral Types L and T. *ARA&A*, 43:195–245.
- Kite, E. S., Fegley, Bruce, J., Schaefer, L., and Ford, E. B. (2020). Atmosphere Origins for Exoplanet Sub-Neptunes. *ApJ*, 891(2):111.
- Kite, E. S., Fegley, Bruce, J., Schaefer, L., and Gaidos, E. (2016). Atmosphere-interior Exchange on Hot, Rocky Exoplanets. *ApJ*, 828(2):80.
- Kitzmann, D., Heng, K., Oreshenko, M., Grimm, S. L., et al. (2020). Helios-r2: A New Bayesian, Open-source Retrieval Model for Brown Dwarfs and Exoplanet Atmospheres. *ApJ*, 890(2):174.
- Knutson, H. A., Benneke, B., Deming, D., and Homeier, D. (2014a). A featureless transmission spectrum for the Neptune-mass exoplanet GJ436b. *Nature*, 505(7481):66–68.
- Knutson, H. A., Charbonneau, D., Allen, L. E., Burrows, A., and Megeath, S. T. (2008). The 3.6–8.0 μm Broadband Emission Spectrum of HD 209458b: Evidence for an Atmospheric Temperature Inversion. *ApJ*, 673:526–531.
- Knutson, H. A., Charbonneau, D., Allen, L. E., Fortney, J. J., et al. (2007). A map of the day-night contrast of the extrasolar planet HD 189733b. *Nature*, 447(7141):183–186.

- Knutson, H. A., Charbonneau, D., Burrows, A., O'Donovan, F. T., and Mandushev, G. (2009a). Detection of A Temperature Inversion in the Broadband Infrared Emission Spectrum of TrES-4. *ApJ*, 691(1):866–874.
- Knutson, H. A., Charbonneau, D., Cowan, N. B., Fortney, J. J., et al. (2009b). The 8 μm Phase Variation of the Hot Saturn HD 149026b. *ApJ*, 703(1):769–784.
- Knutson, H. A., Charbonneau, D., Cowan, N. B., Fortney, J. J., et al. (2009c). Multi-wavelength Constraints on the Day-Night Circulation Patterns of HD 189733b. *ApJ*, 690(1):822–836.
- Knutson, H. A., Dragomir, D., Kreidberg, L., Kempton, E. M. R., et al. (2014b). Hubble Space Telescope Near-IR Transmission Spectroscopy of the Super-Earth HD 97658b. *ApJ*, 794(2):155.
- Knutson, H. A., Howard, A. W., and Isaacson, H. (2010). A Correlation Between Stellar Activity and Hot Jupiter Emission Spectra. *ApJ*, 720:1569–1576.
- Knutson, H. A., Lewis, N., Fortney, J. J., Burrows, A., et al. (2012). 3.6 and 4.5 μm Phase Curves and Evidence for Non-equilibrium Chemistry in the Atmosphere of Extrasolar Planet HD 189733b. *ApJ*, 754(1):22.
- Koll, D. D. B. (2019). A Scaling Theory for Atmospheric Heat Redistribution on Rocky Exoplanets. *arXiv e-prints*, page arXiv:1907.13145.
- Koll, D. D. B. and Abbot, D. S. (2016). Temperature Structure and Atmospheric Circulation of Dry Tidally Locked Rocky Exoplanets. *ApJ*, 825(2):99.
- Koll, D. D. B. and Cronin, T. W. (2019). Hot Hydrogen Climates Near the Inner Edge of the Habitable Zone. *ApJ*, 881(2):120.
- Koll, D. D. B., Malik, M., Mansfield, M., Kempton, E. M. R., et al. (2019). Identifying Candidate Atmospheres on Rocky M Dwarf Planets via Eclipse Photometry. *ApJ*, 886(2):140.
- Komacek, T. D. and Showman, A. P. (2016). Atmospheric Circulation of Hot Jupiters: Dayside-Nightside Temperature Differences. *ApJ*, 821(1):16.
- Komacek, T. D. and Tan, X. (2018). Effects of Dissociation/Recombination on the Day-Night Temperature Contrasts of Ultra-hot Jupiters. *Research Notes of the American Astronomical Society*, 2(2):36.
- Konopacky, Q. M., Barman, T. S., Macintosh, B. A., and Marois, C. (2013). Detection of Carbon Monoxide and Water Absorption Lines in an Exoplanet Atmosphere. *Science*, 339:1398–1401.
- Kopparapu, R. k., Wolf, E. T., Arney, G., Batalha, N. E., et al. (2017). Habitable Moist Atmospheres on Terrestrial Planets near the Inner Edge of the Habitable Zone around M Dwarfs. *ApJ*, 845(1):5.
- Kosiarek, M. R., Blunt, S., López-Morales, M., Crossfield, I. J. M., et al. (2019). K2-291b: A Rocky Super-Earth in a 2.2 day Orbit. *AJ*, 157(3):116.

- Kramida, A., Yu. Ralchenko, Reader, J., and NIST ASD Team (2019). NIST Atomic Spectra Database (ver. 5.7.1), [Online]. Available: <https://physics.nist.gov/asd> [2017, April 9]. National Institute of Standards and Technology, Gaithersburg, MD.
- Kreidberg, L. (2018). *Exoplanet Atmosphere Measurements from Transmission Spectroscopy and Other Planet Star Combined Light Observations*, page 100. Springer International Publishing AG.
- Kreidberg, L., Bean, J. L., Désert, J.-M., Benneke, B., et al. (2014a). Clouds in the atmosphere of the super-Earth exoplanet GJ1214b. *Nature*, 505(7481):69–72.
- Kreidberg, L., Bean, J. L., Désert, J.-M., Line, M. R., et al. (2014b). A Precise Water Abundance Measurement for the Hot Jupiter WASP-43b. *ApJL*, 793:L27.
- Kreidberg, L., Koll, D. D. B., Morley, C., Hu, R., et al. (2019). Absence of a thick atmosphere on the terrestrial exoplanet LHS 3844b. *Nature*, 573(7772):87–90.
- Kreidberg, L., Line, M. R., Parmentier, V., Stevenson, K. B., et al. (2018). Global Climate and Atmospheric Composition of the Ultra-hot Jupiter WASP-103b from HST and Spitzer Phase Curve Observations. *AJ*, 156:17.
- Kurucz, R. L. (1979). Model atmospheres for G, F, A, B, and O stars. *ApJS*, 40:1–340.
- Lagrange, A. M. (2014). Direct imaging of exoplanets. *Philosophical Transactions of the Royal Society of London Series A*, 372(2014):20130090–20130090.
- Lagrange, A. M., Bonnefoy, M., Chauvin, G., Apai, D., et al. (2010). A Giant Planet Imaged in the Disk of the Young Star β Pictoris. *Science*, 329(5987):57.
- Lam, K. W. F., Santerne, A., Sousa, S. G., Vigan, A., et al. (2018). K2-265 b: a transiting rocky super-Earth. *A&A*, 620:A77.
- Lavie, B., Mendonça, J. M., Mordasini, C., Malik, M., et al. (2017). HELIOS-RETRIEVAL: An Open-source, Nested Sampling Atmospheric Retrieval Code; Application to the HR 8799 Exoplanets and Inferred Constraints for Planet Formation. *AJ*, 154:91.
- Leconte, J., Forget, F., and Lammer, H. (2015). On the (anticipated) diversity of terrestrial planet atmospheres. *Experimental Astronomy*, 40(2-3):449–467.
- Leconte, J., Selsis, F., Hersant, F., and Guillot, T. (2017). Condensation-inhibited convection in hydrogen-rich atmospheres. Stability against double-diffusive processes and thermal profiles for Jupiter, Saturn, Uranus, and Neptune. *A&A*, 598:A98.
- Lee, E., Dobbs-Dixon, I., Helling, C., Bognar, K., and Woitke, P. (2016). Dynamic mineral clouds on HD 189733b. I. 3D RHD with kinetic, non-equilibrium cloud formation. *A&A*, 594:A48.
- Lee, J. M., Fletcher, L. N., and Irwin, P. G. J. (2012). Optimal estimation retrievals of the atmospheric structure and composition of HD 189733b from secondary eclipse spectroscopy. *MNRAS*, 420(1):170–182.
- Lee, J.-M., Heng, K., and Irwin, P. G. J. (2013). Atmospheric Retrieval Analysis of the Directly Imaged Exoplanet HR 8799b. *ApJ*, 778(2):97.

- Léger, A., Selsis, F., Sotin, C., Guillot, T., et al. (2004). A new family of planets? “Ocean-Planets”. *Icarus*, 169(2):499–504.
- Leggett, S. K., Golimowski, D. A., Fan, X., Geballe, T. R., et al. (2002). Infrared Photometry of Late-M, L, and T Dwarfs. *ApJ*, 564:452–465.
- Lewis, N. K., Showman, A. P., Fortney, J. J., Marley, M. S., et al. (2010). Atmospheric Circulation of Eccentric Hot Neptune GJ436b. *ApJ*, 720(1):344–356.
- Lincowski, A. P., Meadows, V. S., Crisp, D., Robinson, T. D., et al. (2018). Evolved Climates and Observational Discriminants for the TRAPPIST-1 Planetary System. *ApJ*, 867(1):76.
- Line, M. R., Fortney, J. J., Marley, M. S., and Sorahana, S. (2014a). A Data-driven Approach for Retrieving Temperatures and Abundances in Brown Dwarf Atmospheres. *ApJ*, 793:33.
- Line, M. R., Knutson, H., Wolf, A. S., and Yung, Y. L. (2014b). A Systematic Retrieval Analysis of Secondary Eclipse Spectra. II. A Uniform Analysis of Nine Planets and their C to O Ratios. *ApJ*, 783:70.
- Line, M. R., Liang, M. C., and Yung, Y. L. (2010). High-temperature Photochemistry in the Atmosphere of HD 189733b. *ApJ*, 717(1):496–502.
- Line, M. R., Marley, M. S., Liu, M. C., Burningham, B., et al. (2017). Uniform Atmospheric Retrieval Analysis of Ultracool Dwarfs. II. Properties of 11 T dwarfs. *ApJ*, 848:83.
- Line, M. R., Stevenson, K. B., Bean, J., Desert, J.-M., et al. (2016). No Thermal Inversion and a Solar Water Abundance for the Hot Jupiter HD 209458b from HST/WFC3 Spectroscopy. *AJ*, 152(6):203.
- Line, M. R., Teske, J., Burningham, B., Fortney, J. J., and Marley, M. S. (2015). Uniform Atmospheric Retrieval Analysis of Ultracool Dwarfs. I. Characterizing Benchmarks, Gl 570D and HD 3651B. *ApJ*, 807:183.
- Line, M. R., Wolf, A. S., Zhang, X., Knutson, H., et al. (2013). A Systematic Retrieval Analysis of Secondary Eclipse Spectra. I. A Comparison of Atmospheric Retrieval Techniques. *ApJ*, 775(2):137.
- Lines, S., Mayne, N. J., Boule, I. A., Manners, J., et al. (2018). Simulating the cloudy atmospheres of HD 209458 b and HD 189733 b with the 3D Met Office Unified Model. *A&A*, 615:A97.
- Linsky, J. L., Yang, H., France, K., Froning, C. S., et al. (2010). Observations of Mass Loss from the Transiting Exoplanet HD 209458b. *ApJ*, 717(2):1291–1299.
- Lodders, K. and Fegley, B. (2002). Atmospheric Chemistry in Giant Planets, Brown Dwarfs, and Low-Mass Dwarf Stars. I. Carbon, Nitrogen, and Oxygen. *Icarus*, 155(2):393–424.
- Lodieu, N., Hambly, N. C., and Cross, N. J. G. (2021). Exploring the planetary-mass population in the Upper Scorpius association. *MNRAS*, 503(2):2265–2279.
- Lopez, E. D. and Fortney, J. J. (2014). UNDERSTANDING THE MASS-RADIUS RELATION FOR SUB-NEPTUNES: RADIUS AS a PROXY FOR COMPOSITION. *The Astrophysical Journal*, 792(1):1.

- López-Morales, M., Haywood, R. D., Coughlin, J. L., Zeng, L., et al. (2016). Kepler-21b: A Rocky Planet Around a $V = 8.25$ Magnitude Star. *AJ*, 152(6):204.
- Lothringer, J. D. and Barman, T. (2019). The Influence of Host Star Spectral Type on Ultra-hot Jupiter Atmospheres. *ApJ*, 876(1):69.
- Lothringer, J. D., Barman, T., and Koskinen, T. (2018). Extremely Irradiated Hot Jupiters: Non-oxide Inversions, H^- Opacity, and Thermal Dissociation of Molecules. *ApJ*, 866:27.
- Louden, T. and Wheatley, P. J. (2015). Spatially Resolved Eastward Winds and Rotation of HD 189733b. *ApJL*, 814(2):L24.
- Luhman, K. L. (2012). The Formation and Early Evolution of Low-Mass Stars and Brown Dwarfs. *ARA&A*, 50:65–106.
- Luque, R., Pallé, E., Kossakowski, D., Dreizler, S., et al. (2019). Planetary system around the nearby M dwarf GJ 357 including a transiting, hot, Earth-sized planet optimal for atmospheric characterization. *A&A*, 628:A39.
- Lustig-Yaeger, J., Meadows, V. S., and Lincowski, A. P. (2019). The Detectability and Characterization of the TRAPPIST-1 Exoplanet Atmospheres with JWST. *AJ*, 158(1):27.
- MacDonald, R. J. and Madhusudhan, N. (2017). HD 209458b in new light: evidence of nitrogen chemistry, patchy clouds and sub-solar water. *MNRAS*, 469(2):1979–1996.
- Macintosh, B., Graham, J. R., Barman, T., De Rosa, R. J., et al. (2015). Discovery and spectroscopy of the young jovian planet 51 Eri b with the Gemini Planet Imager. *Science*, 350:64–67.
- Madhusudhan, N. (2012). C/O Ratio as a Dimension for Characterizing Exoplanetary Atmospheres. *ApJ*, 758:36.
- Madhusudhan, N. (2018). *Atmospheric Retrieval of Exoplanets*, page 104. Springer International Publishing AG.
- Madhusudhan, N. (2019). Exoplanetary Atmospheres: Key Insights, Challenges, and Prospects. *ARA&A*, 57:617–663.
- Madhusudhan, N., Agúndez, M., Moses, J. I., and Hu, Y. (2016). Exoplanetary Atmospheres—Chemistry, Formation Conditions, and Habitability. *SSRv*, 205:285–348.
- Madhusudhan, N., Amin, M. A., and Kennedy, G. M. (2014a). Toward Chemical Constraints on Hot Jupiter Migration. *ApJL*, 794:L12.
- Madhusudhan, N., Crouzet, N., McCullough, P. R., Deming, D., and Hedges, C. (2014b). H_2O Abundances in the Atmospheres of Three Hot Jupiters. *ApJL*, 791(1):L9.
- Madhusudhan, N., Harrington, J., Stevenson, K. B., Nymeyer, S., et al. (2011a). A high C/O ratio and weak thermal inversion in the atmosphere of exoplanet WASP-12b. *Nature*, 469:64–67.
- Madhusudhan, N., Lee, K. K. M., and Mousis, O. (2012). A Possible Carbon-rich Interior in Super-Earth 55 Cancri e. *ApJL*, 759(2):L40.

- Madhusudhan, N., Mousis, O., Johnson, T. V., and Lunine, J. I. (2011b). Carbon-rich Giant Planets: Atmospheric Chemistry, Thermal Inversions, Spectra, and Formation Conditions. *ApJ*, 743:191.
- Madhusudhan, N., Nixon, M. C., Welbanks, L., Piette, A. A. A., and Booth, R. A. (2020). The interior and atmosphere of the habitable-zone exoplanet k2-18b. *The Astrophysical Journal*, 891(1):L7.
- Madhusudhan, N. and Seager, S. (2009). A Temperature and Abundance Retrieval Method for Exoplanet Atmospheres. *ApJ*, 707:24–39.
- Madhusudhan, N. and Seager, S. (2010). On the Inference of Thermal Inversions in Hot Jupiter Atmospheres. *ApJ*, 725:261–274.
- Maldonado, J. and Villaver, E. (2017). Searching for chemical signatures of brown dwarf formation. *A&A*, 602:A38.
- Malik, M., Grosheintz, L., Mendonça, J. M., Grimm, S. L., et al. (2017). HELIOS: An Open-source, GPU-accelerated Radiative Transfer Code for Self-consistent Exoplanetary Atmospheres. *AJ*, 153(2):56.
- Malik, M., Kempton, E. M. R., Koll, D. D. B., Mansfield, M., et al. (2019). Analyzing Atmospheric Temperature Profiles and Spectra of M Dwarf Rocky Planets. *ApJ*, 886(2):142.
- Mallonn, M., Köhler, J., Alexoudi, X., von Essen, C., et al. (2019). Low albedos of hot to ultra-hot Jupiters in the optical to near-infrared transition regime. *A&A*, 624:A62.
- Mandell, A. M., Haynes, K., Sinukoff, E., Madhusudhan, N., et al. (2013). Exoplanet Transit Spectroscopy Using WFC3: WASP-12 b, WASP-17 b, and WASP-19 b. *ApJ*, 779(2):128.
- Mansfield, M., Bean, J. L., Line, M. R., Parmentier, V., et al. (2018). An HST/WFC3 Thermal Emission Spectrum of the Hot Jupiter HAT-P-7b. *AJ*, 156(1):10.
- Mansfield, M., Bean, J. L., Stevenson, K. B., Komacek, T. D., et al. (2020). Evidence for H₂ Dissociation and Recombination Heat Transport in the Atmosphere of KELT-9b. *ApJL*, 888(2):L15.
- Mansfield, M., Kite, E. S., Hu, R., Koll, D. D. B., et al. (2019). Identifying Atmospheres on Rocky Exoplanets through Inferred High Albedo. *ApJ*, 886(2):141.
- Marcy, G. W. and Butler, R. P. (2000). Planets Orbiting Other Suns. *PASP*, 112(768):137–140.
- Marley, M. and Robinson, T. (2015). On the cool side: Modeling the atmospheres of brown dwarfs and giant planets. *Annual Review of Astronomy and Astrophysics*, 53(1):279–323.
- Marley, M. S., Fortney, J. J., Hubickyj, O., Bodenheimer, P., and Lissauer, J. J. (2007). On the Luminosity of Young Jupiters. *ApJ*, 655(1):541–549.
- Marley, M. S., Seager, S., Saumon, D., Lodders, K., et al. (2002). Clouds and Chemistry: Ultracool Dwarf Atmospheric Properties from Optical and Infrared Colors. *ApJ*, 568:335–342.

- Marois, C., Macintosh, B., Barman, T., Zuckerman, B., et al. (2008). Direct Imaging of Multiple Planets Orbiting the Star HR 8799. *Science*, 322:1348.
- Marois, C., Zuckerman, B., Konopacky, Q. M., Macintosh, B., and Barman, T. (2010). Images of a fourth planet orbiting HR 8799. *Nature*, 468:1080–1083.
- Mayne, N. J., Baraffe, I., Acreman, D. M., Smith, C., et al. (2014). The unified model, a fully-compressible, non-hydrostatic, deep atmosphere global circulation model, applied to hot Jupiters. ENDGame for a HD 209458b test case. *A&A*, 561:A1.
- Mayne, N. J., Debras, F., Baraffe, I., Thuburn, J., et al. (2017). Results from a set of three-dimensional numerical experiments of a hot Jupiter atmosphere. *A&A*, 604:A79.
- Mayor, M. and Queloz, D. (1995). A Jupiter-mass companion to a solar-type star. *Nature*, 378:355–359.
- McCullough, P. and MacKenty, J. (2012). Considerations for using Spatial Scans with WFC3. Space Telescope WFC Instrument Science Report.
- McCullough, P. R., Crouzet, N., Deming, D., and Madhusudhan, N. (2014). Water Vapor in the Spectrum of the Extrasolar Planet HD 189733b. I. The Transit. *ApJ*, 791(1):55.
- McKemmish, L. K., Masseron, T., Hoeijmakers, H. J., Perez-Mesa, V., et al. (2019). ExoMol Molecular linelists - XXXIII. The spectrum of Titanium Oxide. *MNRAS*, 488:2836–2854.
- McKemmish, L. K., Yurchenko, S. N., and Tennyson, J. (2016). ExoMol line lists - XVIII. The high-temperature spectrum of VO. *MNRAS*, 463(1):771–793.
- Meadows, V. S., Arney, G. N., Schwieterman, E. W., Lustig-Yaeger, J., et al. (2018). The Habitability of Proxima Centauri b: Environmental States and Observational Discriminants. *Astrobiology*, 18(2):133–189.
- Meadows, V. S. and Barnes, R. K. (2018). *Factors Affecting Exoplanet Habitability*, page 57. Springer International Publishing AG.
- Menou, K. (2012). Thermo-resistive Instability of Hot Planetary Atmospheres. *ApJL*, 754(1):L9.
- Menou, K. and Rauscher, E. (2009). Atmospheric Circulation of Hot Jupiters: A Shallow Three-Dimensional Model. *ApJ*, 700(1):887–897.
- Ment, K., Dittmann, J. A., Astudillo-Defru, N., Charbonneau, D., et al. (2019). A Second Terrestrial Planet Orbiting the Nearby M Dwarf LHS 1140. *AJ*, 157(1):32.
- Merino, N., Aronson, H. S., Bojanova, D. P., Feyhl-Buska, J., et al. (2019). Living at the extremes: Extremophiles and the limits of life in a planetary context. *Frontiers in Microbiology*, 10:780.
- Miguel, Y. and Kaltenegger, L. (2014). Exploring Atmospheres of Hot Mini-Neptunes and Extrasolar Giant Planets Orbiting Different Stars with Application to HD 97658b, WASP-12b, CoRoT-2b, XO-1b, and HD 189733b. *ApJ*, 780(2):166.

- Miller-Ricci Kempton, E., Zahnle, K., and Fortney, J. J. (2012). The Atmospheric Chemistry of GJ 1214b: Photochemistry and Clouds. *ApJ*, 745(1):3.
- Mohanty, S., Basri, G., Jayawardhana, R., Allard, F., et al. (2004a). Measuring Fundamental Parameters of Substellar Objects. I. Surface Gravities. *ApJ*, 609:854–884.
- Mohanty, S., Jayawardhana, R., and Basri, G. (2004b). Measuring Fundamental Parameters of Substellar Objects. II. Masses and Radii. *ApJ*, 609:885–905.
- Mollière, P., Stolker, T., Lacour, S., Otten, G. P. P. L., et al. (2020). Retrieving scattering clouds and disequilibrium chemistry in the atmosphere of HR 8799e. *A&A*, 640:A131.
- Mollière, P., van Boekel, R., Dullemond, C., Henning, T., and Mordasini, C. (2015). Model Atmospheres of Irradiated Exoplanets: The Influence of Stellar Parameters, Metallicity, and the C/O Ratio. *ApJ*, 813:47.
- Montet, B. T., Morton, T. D., Foreman-Mackey, D., Johnson, J. A., et al. (2015). Stellar and Planetary Properties of K2 Campaign 1 Candidates and Validation of 17 Planets, Including a Planet Receiving Earth-like Insolation. *ApJ*, 809(1):25.
- Moran, S. E., Hörst, S. M., Batalha, N. E., Lewis, N. K., and Wakeford, H. R. (2018). Limits on Clouds and Hazes for the TRAPPIST-1 Planets. *AJ*, 156(6):252.
- Moran, S. E., Hörst, S. M., Vuitton, V., He, C., et al. (2020). Chemistry of Temperate Super-Earth and Mini-Neptune Atmospheric Hazes from Laboratory Experiments. *The Planetary Science Journal*, 1(1):17.
- Moriarty, J., Madhusudhan, N., and Fischer, D. (2014). Chemistry in an Evolving Protoplanetary Disk: Effects on Terrestrial Planet Composition. *ApJ*, 787:81.
- Morley, C. V., Fortney, J. J., Kempton, E. M. R., Marley, M. S., et al. (2013). Quantitatively Assessing the Role of Clouds in the Transmission Spectrum of GJ 1214b. *ApJ*, 775(1):33.
- Morley, C. V., Fortney, J. J., Marley, M. S., Visscher, C., et al. (2012). Neglected Clouds in T and Y Dwarf Atmospheres. *ApJ*, 756(2):172.
- Morley, C. V., Fortney, J. J., Marley, M. S., Zahnle, K., et al. (2015). Thermal Emission and Reflected Light Spectra of Super Earths with Flat Transmission Spectra. *ApJ*, 815(2):110.
- Morley, C. V., Knutson, H., Line, M., Fortney, J. J., et al. (2017a). Forward and Inverse Modeling of the Emission and Transmission Spectrum of GJ 436b: Investigating Metal Enrichment, Tidal Heating, and Clouds. *AJ*, 153(2):86.
- Morley, C. V., Kreidberg, L., Rustamkulov, Z., Robinson, T., and Fortney, J. J. (2017b). Observing the Atmospheres of Known Temperate Earth-sized Planets with JWST. *ApJ*, 850(2):121.
- Morley, C. V., Marley, M. S., Fortney, J. J., Lupu, R., et al. (2014). Water Clouds in Y Dwarfs and Exoplanets. *ApJ*, 787(1):78.
- Moses, J. I. (2014). Chemical kinetics on extrasolar planets. *Philosophical Transactions of the Royal Society of London Series A*, 372(2014):20130073–20130073.

- Moses, J. I., Fouchet, T., Bézard, B., Gladstone, G. R., et al. (2005). Photochemistry and diffusion in Jupiter's stratosphere: Constraints from ISO observations and comparisons with other giant planets. *Journal of Geophysical Research: Planets*, 110(E8).
- Moses, J. I., Line, M. R., Visscher, C., Richardson, M. R., et al. (2013a). Compositional Diversity in the Atmospheres of Hot Neptunes, with Application to GJ 436b. *ApJ*, 777(1):34.
- Moses, J. I., Madhusudhan, N., Visscher, C., and Freedman, R. S. (2013b). Chemical Consequences of the C/O Ratio on Hot Jupiters: Examples from WASP-12b, CoRoT-2b, XO-1b, and HD 189733b. *ApJ*, 763:25.
- Moses, J. I., Visscher, C., Fortney, J. J., Showman, A. P., et al. (2011). Disequilibrium Carbon, Oxygen, and Nitrogen Chemistry in the Atmospheres of HD 189733b and HD 209458b. *ApJ*, 737:15.
- Močnik, T., Hellier, C., and Southworth, J. (2018). WASP-104b is Darker Than Charcoal. *AJ*, 156(2):44.
- Mugnai, L. V., Modirrousta-Galian, D., Edwards, B., Changeat, Q., et al. (2021). ARES V: No Evidence For Molecular Absorption in the HST WFC3 Spectrum of GJ 1132 b. *arXiv e-prints*, page arXiv:2104.01873.
- Nettelmann, N., Fortney, J. J., Kramm, U., and Redmer, R. (2011). Thermal Evolution and Structure Models of the Transiting Super-Earth GJ 1214b. *ApJ*, 733(1):2.
- Nikolov, N., Sing, D. K., Fortney, J. J., Goyal, J. M., et al. (2018). An absolute sodium abundance for a cloud-free 'hot Saturn' exoplanet. *Nature*, 557(7706):526–529.
- Nikolov, N., Sing, D. K., Gibson, N. P., Fortney, J. J., et al. (2016). VLT FORS2 Comparative Transmission Spectroscopy: Detection of Na in the Atmosphere of WASP-39b from the Ground. *ApJ*, 832(2):191.
- Nikolov, N., Sing, D. K., Pont, F., Burrows, A. S., et al. (2014). Hubble Space Telescope hot Jupiter transmission spectral survey: a detection of Na and strong optical absorption in HAT-P-1b. *MNRAS*, 437(1):46–66.
- Noll, K. S., Geballe, T. R., and Marley, M. S. (1997). Detection of Abundant Carbon Monoxide in the Brown Dwarf Gliese 229B. *ApJL*, 489:L87–L90.
- Nugroho, S. K., Kawahara, H., Masuda, K., Hirano, T., et al. (2017). High-resolution Spectroscopic Detection of TiO and a Stratosphere in the Day-side of WASP-33b. *AJ*, 154:221.
- Öberg, K. I., Murray-Clay, R., and Bergin, E. A. (2011). The Effects of Snowlines on C/O in Planetary Atmospheres. *ApJL*, 743(1):L16.
- Oreshenko, M., Lavie, B., Grimm, S. L., Tsai, S.-M., et al. (2017). Retrieval Analysis of the Emission Spectrum of WASP-12b: Sensitivity of Outcomes to Prior Assumptions and Implications for Formation History. *ApJL*, 847(1):L3.
- Owen, J. E., Shaikhislamov, I. F., Lammer, H., Fossati, L., and Khodachenko, M. L. (2020). Hydrogen Dominated Atmospheres on Terrestrial Mass Planets: Evidence, Origin and Evolution. *SSRv*, 216(8):129.

- Owen, J. E. and Wu, Y. (2017). The Evaporation Valley in the Kepler Planets. *ApJ*, 847(1):29.
- Parmentier, V. and Crossfield, I. J. M. (2018). *Exoplanet Phase Curves: Observations and Theory*, page 116. Springer International Publishing AG.
- Parmentier, V., Fortney, J. J., Showman, A. P., Morley, C., and Marley, M. S. (2016). Transitions in the Cloud Composition of Hot Jupiters. *ApJ*, 828(1):22.
- Parmentier, V. and Guillot, T. (2014). A non-grey analytical model for irradiated atmospheres. I. Derivation. *A&A*, 562:A133.
- Parmentier, V., Line, M. R., Bean, J. L., Mansfield, M., et al. (2018). From thermal dissociation to condensation in the atmospheres of ultra hot Jupiters: WASP-121b in context. *A&A*, 617:A110.
- Parmentier, V., Showman, A. P., and Lian, Y. (2013). 3D mixing in hot Jupiters atmospheres. I. Application to the day/night cold trap in HD 209458b. *A&A*, 558:A91.
- Parro, L. M., Jiménez-Díaz, A., Mansilla, F., and Ruiz, J. (2017). Present-day heat flow model of Mars. *Scientific Reports*, 7:45629.
- Pasek, M. A., Milsom, J. A., Ciesla, F. J., Lauretta, D. S., et al. (2005). Sulfur chemistry with time-varying oxygen abundance during Solar System formation. *Icarus*, 175:1–14.
- Patrascu, A. T., Yurchenko, S. N., and Tennyson, J. (2015). ExoMol molecular line lists - IX. The spectrum of AlO. *MNRAS*, 449:3613–3619.
- Patten, B. M., Stauffer, J. R., Burrows, A., Marengo, M., et al. (2006). Spitzer IRAC Photometry of M, L, and T Dwarfs. *ApJ*, 651:502–516.
- Pawłowsky-Glahn, V. and Egozcue, J. J. (2006). Compositional data and their analysis: an introduction. *Geological Society of London Special Publications*, 264(1):1–10.
- Perez-Becker, D. and Showman, A. P. (2013). Atmospheric Heat Redistribution on Hot Jupiters. *ApJ*, 776(2):134.
- Persson, C. M., Fridlund, M., Barragán, O., Dai, F., et al. (2018). Super-Earth of 8 M_{\oplus} in a 2.2-day orbit around the K5V star K2-216. *A&A*, 618:A33.
- Pierrehumbert, R., Brogniez, H., and Roca, R. (2006). *On the relative humidity of the Earth's atmosphere*, page 143–185. Princeton Univ. Press, Princeton, N. J.
- Pierrehumbert, R. and Gaidos, E. (2011). Hydrogen Greenhouse Planets Beyond the Habitable Zone. *ApJL*, 734(1):L13.
- Pierrehumbert, R. T. (2010). *Principles of Planetary Climate*. Cambridge University Press.
- Piette, A. A. A. and Madhusudhan, N. (2020a). Considerations for atmospheric retrieval of high-precision brown dwarf spectra. *MNRAS*, 497(4):5136–5154.
- Piette, A. A. A. and Madhusudhan, N. (2020b). On the Temperature Profiles and Emission Spectra of Mini-Neptune Atmospheres. *arXiv e-prints*, page arXiv:2009.11290.

- Piette, A. A. A., Madhusudhan, N., McKemmish, L. K., Gandhi, S., et al. (2020). Assessing spectra and thermal inversions due to TiO in hot Jupiter atmospheres. *MNRAS*, 496(3):3870–3886.
- Pinhas, A. and Madhusudhan, N. (2017). On signatures of clouds in exoplanetary transit spectra. *MNRAS*, 471(4):4355–4373.
- Pinhas, A., Madhusudhan, N., Gandhi, S., and MacDonald, R. (2019). H₂O abundances and cloud properties in ten hot giant exoplanets. *MNRAS*, 482(2):1485–1498.
- Pinhas, A., Rackham, B. V., Madhusudhan, N., and Apai, D. (2018). Retrieval of planetary and stellar properties in transmission spectroscopy with AURA. *MNRAS*, 480(4):5314–5331.
- Plez, B. (1998). A new TiO line list. *A&A*, 337:495–500.
- Pont, F., Sing, D. K., Gibson, N. P., Aigrain, S., et al. (2013). The prevalence of dust on the exoplanet HD 189733b from Hubble and Spitzer observations. *MNRAS*, 432(4):2917–2944.
- Pueyo, L. (2018). *Direct Imaging as a Detection Technique for Exoplanets*, page 10. Springer International Publishing AG.
- Rauscher, E. and Menou, K. (2010). Three-dimensional Modeling of Hot Jupiter Atmospheric Flows. *ApJ*, 714(2):1334–1342.
- Redfield, S., Endl, M., Cochran, W. D., and Koesterke, L. (2008). Sodium Absorption from the Exoplanetary Atmosphere of HD 189733b Detected in the Optical Transmission Spectrum. *ApJL*, 673(1):L87.
- Rice, K., Malavolta, L., Mayo, A., Mortier, A., et al. (2019). Masses and radii for the three super-Earths orbiting GJ 9827, and implications for the composition of small exoplanets. *MNRAS*, 484(3):3731–3745.
- Richard, C., Gordon, I., Rothman, L., Abel, M., et al. (2012). New section of the hitran database: Collision-induced absorption (cia). *Journal of Quantitative Spectroscopy and Radiative Transfer*, 113(11):1276 – 1285. Three Leaders in Spectroscopy.
- Ricker, G. R., Winn, J. N., Vanderspek, R., Latham, D. W., et al. (2015). Transiting Exoplanet Survey Satellite (TESS). *Journal of Astronomical Telescopes, Instruments, and Systems*, 1:014003.
- Rieke, G. H., Wright, G. S., Böker, T., Bouwman, J., et al. (2015). The Mid-Infrared Instrument for the James Webb Space Telescope, I: Introduction. *PASP*, 127(953):584.
- Robinson, T. D. and Catling, D. C. (2012). An Analytic Radiative-Convective Model for Planetary Atmospheres. *ApJ*, 757(1):104.
- Robinson, T. D. and Catling, D. C. (2014). Common 0.1bar tropopause in thick atmospheres set by pressure-dependent infrared transparency. *Nature Geoscience*, 7(1):12–15.
- Rodler, F., Kürster, M., and Barnes, J. R. (2013). Detection of CO absorption in the atmosphere of the hot Jupiter HD 189733b. *MNRAS*, 432(3):1980–1988.

- Roellig, T. L., Van Cleve, J. E., Sloan, G. C., Wilson, J. C., et al. (2004). Spitzer Infrared Spectrograph (IRS) Observations of M, L, and T Dwarfs. *ApJS*, 154(1):418–421.
- Rogers, L. A. (2015). Most 1.6 Earth-radius Planets are Not Rocky. *ApJ*, 801(1):41.
- Rogers, L. A., Bodenheimer, P., Lissauer, J. J., and Seager, S. (2011). Formation and Structure of Low-density exo-Neptunes. *ApJ*, 738(1):59.
- Rogers, L. A. and Seager, S. (2010a). A Framework for Quantifying the Degeneracies of Exoplanet Interior Compositions. *ApJ*, 712(2):974–991.
- Rogers, L. A. and Seager, S. (2010b). Three Possible Origins for the Gas Layer on GJ 1214b. *ApJ*, 716(2):1208–1216.
- Rothman, L. S., Gordon, I. E., Babikov, Y., Barbe, A., et al. (2013). The HITRAN2012 molecular spectroscopic database. *JQSRT*, 130:4–50.
- Rothman, L. S., Gordon, I. E., Barber, R. J., Dothe, H., et al. (2010). HITEMP, the high-temperature molecular spectroscopic database. *JQSRT*, 111:2139–2150.
- Rothschild, L. J. and Mancinelli, R. L. (2001). Life in extreme environments. *Nature*, 409(6823):1092–1101.
- Rowe, J. F., Matthews, J. M., Seager, S., Kuchnig, R., et al. (2006). An Upper Limit on the Albedo of HD 209458b: Direct Imaging Photometry with the MOST Satellite. *ApJ*, 646(2):1241–1251.
- Rowe, J. F., Matthews, J. M., Seager, S., Miller-Ricci, E., et al. (2008). The Very Low Albedo of an Extrasolar Planet: MOST Space-based Photometry of HD 209458. *ApJ*, 689(2):1345–1353.
- Ryabchikova, T., Piskunov, N., Kurucz, R. L., Stempels, H. C., et al. (2015). A major upgrade of the VALD database. *PhyS*, 90(5):054005.
- Salz, M., Czesla, S., Schneider, P. C., Nagel, E., et al. (2018). Detection of He I $\lambda 10830$ Å absorption on HD 189733 b with CARMENES high-resolution transmission spectroscopy. *A&A*, 620:A97.
- Samland, M., Mollière, P., Bonnefoy, M., Maire, A. L., et al. (2017). Spectral and atmospheric characterization of 51 Eridani b using VLT/SPHERE. *A&A*, 603:A57.
- Santerne, A., Brugger, B., Armstrong, D. J., Adibekyan, V., et al. (2018). An Earth-sized exoplanet with a Mercury-like composition. *Nature Astronomy*, 2:393–400.
- Saumon, D., Geballe, T. R., Leggett, S. K., Marley, M. S., et al. (2000). Molecular Abundances in the Atmosphere of the T Dwarf GL 229B. *ApJ*, 541:374–389.
- Saumon, D. and Marley, M. S. (2008). The Evolution of L and T Dwarfs in Color-Magnitude Diagrams. *ApJ*, 689:1327–1344.
- Saumon, D., Marley, M. S., Cushing, M. C., Leggett, S. K., et al. (2006). Ammonia as a Tracer of Chemical Equilibrium in the T7.5 Dwarf Gliese 570D. *ApJ*, 647:552–557.

- Scalo, J., Kaltenegger, L., Segura, A. G., Fridlund, M., et al. (2007). M Stars as Targets for Terrestrial Exoplanet Searches And Biosignature Detection. *Astrobiology*, 7(1):85–166.
- Scheucher, M., Wunderlich, F., Grenfell, J. L., Godolt, M., et al. (2020). Consistently Simulating a Wide Range of Atmospheric Scenarios for K2-18b with a Flexible Radiative Transfer Module. *ApJ*, 898(1):44.
- Schneider, A. C., Greco, J., Cushing, M. C., Kirkpatrick, J. D., et al. (2016). A Proper Motion Survey Using the First Sky Pass of NEOWISE-reactivation Data. *ApJ*, 817(2):112.
- Schwartz, J. C. and Cowan, N. B. (2015). Balancing the energy budget of short-period giant planets: evidence for reflective clouds and optical absorbers. *MNRAS*, 449(4):4192–4203.
- Schwenke, D. W. (1998). Opacity of TiO from a coupled electronic state calculation parametrized by AB initio and experimental data. *Faraday Discussions*, 109:321.
- Seager, S. (2010). *Exoplanet Atmospheres: Physical Processes*. Princeton University Press.
- Seager, S., Bains, W., and Hu, R. (2013). Biosignature Gases in H₂-dominated Atmospheres on Rocky Exoplanets. *ApJ*, 777(2):95.
- Seager, S., Kuchner, M., Hier-Majumder, C. A., and Militzer, B. (2007). Mass-Radius Relationships for Solid Exoplanets. *ApJ*, 669(2):1279–1297.
- Seager, S., Richardson, L. J., Hansen, B. M. S., Menou, K., et al. (2005). On the Dayside Thermal Emission of Hot Jupiters. *ApJ*, 632(2):1122–1131.
- Sedaghati, E., Boffin, H. M. J., Csizmadia, S., Gibson, N., et al. (2015). Regaining the FORS: optical ground-based transmission spectroscopy of the exoplanet WASP-19b with VLT+FOR2. *A&A*, 576:L11.
- Sedaghati, E., Boffin, H. M. J., MacDonald, R. J., Gandhi, S., et al. (2017). Detection of titanium oxide in the atmosphere of a hot Jupiter. *Nature*, 549:238–241.
- Segura, A. (2018). *Star-Planet Interactions and Habitability: Radiative Effects*, page 73. Springer International Publishing AG.
- Segura, A., Krelow, K., Kasting, J. F., Sommerlatt, D., et al. (2003). Ozone Concentrations and Ultraviolet Fluxes on Earth-Like Planets Around Other Stars. *Astrobiology*, 3(4):689–708.
- Selsis, F., Kasting, J. F., Levrard, B., Paillet, J., et al. (2007). Habitable planets around the star Gliese 581? *A&A*, 476(3):1373–1387.
- Sheppard, K. B., Mandell, A. M., Tamburo, P., Gandhi, S., et al. (2017). Evidence for a Dayside Thermal Inversion and High Metallicity for the Hot Jupiter WASP-18b. *ApJL*, 850:L32.
- Showman, A. P., Cooper, C. S., Fortney, J. J., and Marley, M. S. (2008). Atmospheric Circulation of Hot Jupiters: Three-dimensional Circulation Models of HD 209458b and HD 189733b with Simplified Forcing. *ApJ*, 682(1):559–576.

- Showman, A. P., Fortney, J. J., Lian, Y., Marley, M. S., et al. (2009). Atmospheric Circulation of Hot Jupiters: Coupled Radiative-Dynamical General Circulation Model Simulations of HD 189733b and HD 209458b. *ApJ*, 699(1):564–584.
- Showman, A. P. and Guillot, T. (2002). Atmospheric circulation and tides of “51 Pegasus b-like” planets. *A&A*, 385:166–180.
- Showman, A. P., Tan, X., and Parmentier, V. (2020). Atmospheric Dynamics of Hot Giant Planets and Brown Dwarfs. *SSRv*, 216(8):139.
- Shporer, A., Collins, K. A., Astudillo-Defru, N., Irwin, J., et al. (2020). GJ 1252 b: A 1.2 R_{\oplus} Planet Transiting an M3 Dwarf at 20.4 pc. *ApJL*, 890(1):L7.
- Shporer, A. and Hu, R. (2015). Studying Atmosphere-dominated Hot Jupiter Kepler Phase Curves: Evidence that Inhomogeneous Atmospheric Reflection Is Common. *AJ*, 150(4):112.
- Shporer, A., O’Rourke, J. G., Knutson, H. A., Szabó, G. M., et al. (2014). Atmospheric Characterization of the Hot Jupiter Kepler-13Ab. *ApJ*, 788(1):92.
- Shporer, A., Wong, I., Huang, C. X., Line, M. R., et al. (2019). TESS Full Orbital Phase Curve of the WASP-18b System. *AJ*, 157(5):178.
- Sing, D. K., Désert, J. M., Fortney, J. J., Lecavelier Des Etangs, A., et al. (2011). Gran Telescopio Canarias OSIRIS transiting exoplanet atmospheric survey: detection of potassium in XO-2b from narrowband spectrophotometry. *A&A*, 527:A73.
- Sing, D. K., Fortney, J. J., Nikolov, N., Wakeford, H. R., et al. (2016). A continuum from clear to cloudy hot-Jupiter exoplanets without primordial water depletion. *Nature*, 529:59–62.
- Sing, D. K., Huitson, C. M., Lopez-Morales, M., Pont, F., et al. (2012). GTC OSIRIS transiting exoplanet atmospheric survey: detection of sodium in XO-2b from differential long-slit spectroscopy. *MNRAS*, 426(2):1663–1670.
- Sing, D. K., Wakeford, H. R., Showman, A. P., Nikolov, N., et al. (2015). HST hot-Jupiter transmission spectral survey: detection of potassium in WASP-31b along with a cloud deck and Rayleigh scattering. *MNRAS*, 446(3):2428–2443.
- Siverd, R. J., Beatty, T. G., Pepper, J., Eastman, J. D., et al. (2012). KELT-1b: A Strongly Irradiated, Highly Inflated, Short Period, 27 Jupiter-mass Companion Transiting a Mid-F Star. *ApJ*, 761(2):123.
- Skilling, J. (2006). Nested sampling for general bayesian computation. *Bayesian Anal.*, 1(4):833–859.
- Skrutskie, M. F., Cutri, R. M., Stiening, R., Weinberg, M. D., et al. (2006). The Two Micron All Sky Survey (2MASS). *AJ*, 131(2):1163–1183.
- Snellen, I. A. G., de Kok, R. J., de Mooij, E. J. W., and Albrecht, S. (2010). The orbital motion, absolute mass and high-altitude winds of exoplanet HD209458b. *Nature*, 465:1049–1051.

- Snellen, I. A. G., de Mooij, E. J. W., and Albrecht, S. (2009). The changing phases of extrasolar planet CoRoT-1b. *Nature*, 459(7246):543–545.
- Southworth, J. (2010). Homogeneous studies of transiting extrasolar planets - III. Additional planets and stellar models. *MNRAS*, 408(3):1689–1713.
- Southworth, J. (2012). Homogeneous studies of transiting extrasolar planets - V. New results for 38 planets. *MNRAS*, 426(2):1291–1323.
- Southworth, J., Hinse, T. C., Dominik, M., Glittrup, M., et al. (2009). Physical Properties of the 0.94-Day Period Transiting Planetary System WASP-18. *ApJ*, 707(1):167–172.
- Southworth, J., Mancini, L., Madhusudhan, N., Mollière, P., et al. (2017). Detection of the Atmosphere of the 1.6 M_{\oplus} Exoplanet GJ 1132 b. *AJ*, 153(4):191.
- Spake, J. J., Sing, D. K., Evans, T. M., Oklopčić, et al. (2018). Helium in the eroding atmosphere of an exoplanet. *Nature*, 557(7703):68–70.
- Spiegel, D. S., Burrows, A., Ibgui, L., Hubeny, I., and Milsom, J. A. (2010). Models of Neptune-Mass Exoplanets: Emergent Fluxes and Albedos. *ApJ*, 709(1):149–158.
- Spiegel, D. S., Silverio, K., and Burrows, A. (2009). Can TiO Explain Thermal Inversions in the Upper Atmospheres of Irradiated Giant Planets? *ApJ*, 699:1487–1500.
- Stassun, K. G., Collins, K. A., and Gaudi, B. S. (2017). Accurate Empirical Radii and Masses of Planets and Their Host Stars with Gaia Parallaxes. *AJ*, 153(3):136.
- Stassun, K. G., Oelkers, R. J., Paegert, M., Torres, G., et al. (2019). The Revised TESS Input Catalog and Candidate Target List. *AJ*, 158(4):138.
- Stevenson, D. J. (1999). Life-sustaining planets in interstellar space? *Nature*, 400(6739):32.
- Stevenson, K. B. (2016). Quantifying and Predicting the Presence of Clouds in Exoplanet Atmospheres. *ApJL*, 817(2):L16.
- Stevenson, K. B., Bean, J. L., Madhusudhan, N., and Harrington, J. (2014a). Deciphering the Atmospheric Composition of WASP-12b: A Comprehensive Analysis of its Dayside Emission. *ApJ*, 791:36.
- Stevenson, K. B., Désert, J.-M., Line, M. R., Bean, J. L., et al. (2014b). Thermal structure of an exoplanet atmosphere from phase-resolved emission spectroscopy. *Science*, 346(6211):838–841.
- Stevenson, K. B., Line, M. R., Bean, J. L., Désert, J.-M., et al. (2017). Spitzer Phase Curve Constraints for WASP-43b at 3.6 and 4.5 μm . *AJ*, 153(2):68.
- Sugimura, E., Komabayashi, T., Hirose, K., Sata, N., et al. (2010). Simultaneous high-pressure and high-temperature volume measurements of ice vii and its thermal equation of state. *Phys. Rev. B*, 82:134103.
- Sumi, T., Kamiya, K., Bennett, D. P., Bond, I. A., et al. (2011). Unbound or distant planetary mass population detected by gravitational microlensing. *Nature*, 473(7347):349–352.

- Swain, M., Deroo, P., Tinetti, G., Hollis, M., et al. (2013). Probing the extreme planetary atmosphere of WASP-12b. *Icarus*, 225(1):432–445.
- Swain, M. R., Estrela, R., Roudier, G. M., Sotin, C., et al. (2021). Detection of an Atmosphere on a Rocky Exoplanet. *arXiv e-prints*, page arXiv:2103.05657.
- Tan, X. and Komacek, T. D. (2019). The Atmospheric Circulation of Ultra-hot Jupiters. *ApJ*, 886(1):26.
- Taylor, J., Parmentier, V., Irwin, P. G. J., Aigrain, S., et al. (2020). Understanding and mitigating biases when studying inhomogeneous emission spectra with JWST. *MNRAS*, 493(3):4342–4354.
- Tennyson, J., Yurchenko, S. N., Al-Refaie, A. F., Barton, E. J., et al. (2016). The ExoMol database: Molecular line lists for exoplanet and other hot atmospheres. *Journal of Molecular Spectroscopy*, 327:73–94.
- Thomas, S. W. and Madhusudhan, N. (2016). In hot water: effects of temperature-dependent interiors on the radii of water-rich super-Earths. *MNRAS*, 458(2):1330–1344.
- Thompson, M. A., Telus, M., Schaefer, L., Fortney, J. J., et al. (2021). Composition of terrestrial exoplanet atmospheres from meteorite outgassing experiments. *Nature Astronomy*.
- Thorngren, D., Gao, P., and Fortney, J. J. (2019). The Intrinsic Temperature and Radiative-Convective Boundary Depth in the Atmospheres of Hot Jupiters. *ApJL*, 884(1):L6.
- Todorov, K. O., Line, M. R., Pineda, J. E., Meyer, M. R., et al. (2016). The Water Abundance of the Directly Imaged Substellar Companion κ And b Retrieved from a Near Infrared Spectrum. *ApJ*, 823(1):14.
- Toon, O. B., McKay, C. P., Ackerman, T. P., and Santhanam, K. (1989). Rapid calculation of radiative heating rates and photodissociation rates in inhomogeneous multiple scattering atmospheres. *J. Geophys. Res.*, 94:16287–16301.
- Tremblin, P., Amundsen, D. S., Chabrier, G., Baraffe, I., et al. (2016). Cloudless Atmospheres for L/T Dwarfs and Extrasolar Giant Planets. *ApJL*, 817(2):L19.
- Tremblin, P., Amundsen, D. S., Mourier, P., Baraffe, I., et al. (2015). Fingering Convection and Cloudless Models for Cool Brown Dwarf Atmospheres. *ApJL*, 804(1):L17.
- Tremblin, P., Chabrier, G., Baraffe, I., Liu, M. C., et al. (2017). Cloudless Atmospheres for Young Low-gravity Substellar Objects. *ApJ*, 850(1):46.
- Triaud, A. H. M. J. (2014). Colour-magnitude diagrams of transiting Exoplanets - I. Systems with parallaxes. *MNRAS*, 439:L61–L64.
- Triaud, A. H. M. J., Lanotte, A. A., Smalley, B., and Gillon, M. (2014). Colour-magnitude diagrams of transiting Exoplanets - II. A larger sample from photometric distances. *MNRAS*, 444(1):711–728.
- Trotta, R. (2008). Bayes in the sky: Bayesian inference and model selection in cosmology. *Contemporary Physics*, 49(2):71–104.

- Trotta, R. (2017). Bayesian Methods in Cosmology. *arXiv e-prints*, page arXiv:1701.01467.
- Tsiaras, A., Rocchetto, M., Waldmann, I. P., Venot, O., et al. (2016). Detection of an Atmosphere Around the Super-Earth 55 Cancri e. *ApJ*, 820(2):99.
- Tsiaras, A., Waldmann, I. P., Tinetti, G., Tennyson, J., and Yurchenko, S. N. (2019). Water vapour in the atmosphere of the habitable-zone eight-Earth-mass planet K2-18 b. *Nature Astronomy*, page 451.
- Tsuji, T. (2002). Dust in the Photospheric Environment: Unified Cloudy Models of M, L, and T Dwarfs. *ApJ*, 575:264–290.
- Turbet, M., Bolmont, E., Bourrier, V., Demory, B.-O., et al. (2020). A Review of Possible Planetary Atmospheres in the TRAPPIST-1 System. *SSRv*, 216(5):100.
- Valencia, D., Guillot, T., Parmentier, V., and Freedman, R. S. (2013). Bulk Composition of GJ 1214b and Other Sub-Neptune Exoplanets. *ApJ*, 775(1):10.
- Vanderspek, R., Huang, C. X., Vanderburg, A., Ricker, G. R., et al. (2019). TESS Discovery of an Ultra-short-period Planet around the Nearby M Dwarf LHS 3844. *ApJL*, 871(2):L24.
- Venot, O., Hébrard, E., Agúndez, M., Dobrijevic, M., et al. (2012). A chemical model for the atmosphere of hot Jupiters. *A&A*, 546:A43.
- Veras, D., Crepp, J. R., and Ford, E. B. (2009). Formation, Survival, and Detectability of Planets Beyond 100 AU. *ApJ*, 696(2):1600–1611.
- Vidal-Madjar, A., Désert, J.-M., Lecavelier des Etangs, A., Hébrard, G., et al. (2004). Detection of Oxygen and Carbon in the Hydrodynamically Escaping Atmosphere of the Extrasolar Planet HD 209458b. *ApJL*, 604:L69–L72.
- Vidal-Madjar, A., Huitson, C. M., Bourrier, V., Désert, J. M., et al. (2013). Magnesium in the atmosphere of the planet HD 209458 b: observations of the thermosphere-exosphere transition region. *A&A*, 560:A54.
- Vidal-Madjar, A., Lecavelier des Etangs, A., Désert, J. M., Ballester, G. E., et al. (2003). An extended upper atmosphere around the extrasolar planet HD209458b. *Nature*, 422(6928):143–146.
- Visscher, C. and Moses, J. I. (2011). Quenching of Carbon Monoxide and Methane in the Atmospheres of Cool Brown Dwarfs and Hot Jupiters. *ApJ*, 738(1):72.
- von Essen, C., Mallonn, M., Piette, A., Cowan, N. B., et al. (2021). TESS unveils the optical phase curve of KELT-1b. Thermal emission and ellipsoidal variation from the brown dwarf companion along with the stellar activity. *A&A*, 648:A71.
- von Essen, C., Mallonn, M., Welbanks, L., Madhusudhan, N., et al. (2019). An optical transmission spectrum of the ultra-hot Jupiter WASP-33 b. First indication of aluminum oxide in an exoplanet. *A&A*, 622:A71.
- Vrba, F. J., Henden, A. A., Luginbuhl, C. B., Guetter, H. H., et al. (2004). Preliminary Parallaxes of 40 L and T Dwarfs from the US Naval Observatory Infrared Astrometry Program. *AJ*, 127:2948–2968.

- Vuitton, V., Moran, S. E., He, C., Wolters, C., et al. (2021). H_2SO_4 and Organosulfur Compounds in Laboratory Analogue Aerosols of Warm High-metallicity Exoplanet Atmospheres. *The Planetary Science Journal*, 2(1):2.
- Wagner, W. and Pruß, A. (2002). The IAPWS Formulation 1995 for the Thermodynamic Properties of Ordinary Water Substance for General and Scientific Use. *Journal of Physical and Chemical Reference Data*, 31(2):387–535.
- Wakeford, H. R. and Sing, D. K. (2015). Transmission spectral properties of clouds for hot Jupiter exoplanets. *A&A*, 573:A122.
- Wakeford, H. R., Sing, D. K., Deming, D., Lewis, N. K., et al. (2018). The Complete Transmission Spectrum of WASP-39b with a Precise Water Constraint. *AJ*, 155(1):29.
- Wakeford, H. R., Sing, D. K., Kataria, T., Deming, D., et al. (2017). HAT-P-26b: A Neptune-mass exoplanet with a well-constrained heavy element abundance. *Science*, 356(6338):628–631.
- Wakeford, H. R., Sing, D. K., Stevenson, K. B., Lewis, N. K., et al. (2020). Into the UV: A Precise Transmission Spectrum of HAT-P-41b Using Hubble’s WFC3/UVIS G280 Grism. *AJ*, 159(5):204.
- Waldmann, I. P., Rocchetto, M., Tinetti, G., Barton, E. J., et al. (2015). Tau-REx II: Retrieval of Emission Spectra. *ApJ*, 813(1):13.
- Weiss, L. M., Rogers, L. A., Isaacson, H. T., Agol, E., et al. (2016). Revised Masses and Densities of the Planets around Kepler-10. *ApJ*, 819(1):83.
- Welbanks, L. and Madhusudhan, N. (2019). On Degeneracies in Retrievals of Exoplanetary Transmission Spectra. *AJ*, 157(5):206.
- Welbanks, L. and Madhusudhan, N. (2021). Aurora: A Generalized Retrieval Framework for Exoplanetary Transmission Spectra. *ApJ*, 913(2):114.
- Welbanks, L., Madhusudhan, N., Allard, N. F., Hubeny, I., et al. (2019). Mass-Metallicity Trends in Transiting Exoplanets from Atmospheric Abundances of H_2O , Na, and K. *ApJL*, 887(1):L20.
- Western, C. M., Carter-Blatchford, L., Crozet, P., Ross, A. J., et al. (2018). The spectrum of N_2 from 4,500 to 15,700 cm^{-1} revisited with PGOPHER. *JQSRT*, 219:127–141.
- White, W. B., Johnson, S. M., and Dantzig, G. B. (1958). Chemical equilibrium in complex mixtures. *The Journal of Chemical Physics*, 28(5):751–755.
- Whitworth, A., Bate, M. R., Nordlund, Å., Reipurth, B., and Zinnecker, H. (2007). The Formation of Brown Dwarfs: Theory. *Protostars and Planets V*, pages 459–476.
- Wiktorowicz, S. J. and Ingersoll, A. P. (2007). Liquid water oceans in ice giants. *Icarus*, 186(2):436–447.
- Winn, J. N. (2018). *Planet Occurrence: Doppler and Transit Surveys*, page 195. Springer International Publishing AG.

- Winters, J. G., Medina, A. A., Irwin, J. M., Charbonneau, D., et al. (2019). Three Red Suns in the Sky: A Transiting, Terrestrial Planet in a Triple M-dwarf System at 6.9 pc. *AJ*, 158(4):152.
- Woitke, P., Helling, C., Hunter, G. H., Millard, J. D., et al. (2018). Equilibrium chemistry down to 100 K. Impact of silicates and phyllosilicates on the carbon to oxygen ratio. *A&A*, 614:A1.
- Wolf, E. T., Shields, A. L., Kopparapu, R. K., Haqq-Misra, J., and Toon, O. B. (2017). Constraints on Climate and Habitability for Earth-like Exoplanets Determined from a General Circulation Model. *ApJ*, 837(2):107.
- Wong, I., Benneke, B., Shporer, A., Fetherolf, T., et al. (2020a). TESS Phase Curve of the Hot Jupiter WASP-19b. *AJ*, 159(3):104.
- Wong, I., Shporer, A., Daylan, T., Benneke, B., et al. (2020b). Systematic Phase Curve Study of Known Transiting Systems from Year One of the TESS Mission. *AJ*, 160(4):155.
- Wordsworth, R. D. and Pierrehumbert, R. T. (2013). Water Loss from Terrestrial Planets with CO₂-rich Atmospheres. *ApJ*, 778(2):154.
- Wright, E. L., Eisenhardt, P. R. M., Mainzer, A. K., Ressler, M. E., et al. (2010). The Wide-field Infrared Survey Explorer (WISE): Mission Description and Initial On-orbit Performance. *AJ*, 140(6):1868–1881.
- Wright, J. T. (2018). *Radial Velocities as an Exoplanet Discovery Method*, page 4. Springer International Publishing AG.
- Wright, J. T. and Gaudi, B. S. (2013). *Exoplanet Detection Methods*, page 489. Springer Science+Business Media Dordrecht.
- Wunderlich, F., Scheucher, M., Grenfell, J. L., Schreier, F., et al. (2021). Detectability of biosignatures on LHS 1140 b. *A&A*, 647:A48.
- Wytenbach, A., Ehrenreich, D., Lovis, C., Udry, S., and Pepe, F. (2015). Spectrally resolved detection of sodium in the atmosphere of HD 189733b with the HARPS spectrograph. *A&A*, 577:A62.
- Yan, F. and Henning, T. (2018). An extended hydrogen envelope of the extremely hot giant exoplanet KELT-9b. *Nature Astronomy*, 2:714–718.
- Yang, J., Cowan, N. B., and Abbot, D. S. (2013). Stabilizing Cloud Feedback Dramatically Expands the Habitable Zone of Tidally Locked Planets. *ApJL*, 771(2):L45.
- Yu, X., Moses, J. I., Fortney, J. J., and Zhang, X. (2021). How to Identify Exoplanet Surfaces Using Atmospheric Trace Species in Hydrogen-dominated Atmospheres. *ApJ*, 914(1):38.
- Yurchenko, S. N., Al-Refaie, A. F., and Tennyson, J. (2018). ExoCross: A general program for generating spectra from molecular line lists. *A&A*, 614:A131.
- Yurchenko, S. N., Barber, R. J., and Tennyson, J. (2011). A variationally computed line list for hot NH₃. *MNRAS*, 413:1828–1834.

- Yurchenko, S. N., Lodi, L., Tennyson, J., and Stolyarov, A. V. (2016). Duo: A general program for calculating spectra of diatomic molecules. *Comput. Phys. Commun.*, 202:262 – 275.
- Yurchenko, S. N. and Tennyson, J. (2014). ExoMol line lists - IV. The rotation-vibration spectrum of methane up to 1500 K. *MNRAS*, 440:1649–1661.
- Yurchenko, S. N., Tennyson, J., Barber, R. J., and Thiel, W. (2013). Vibrational transition moments of CH₄ from first principles. *Journal of Molecular Spectroscopy*, 291:69–76.
- Zahnle, K., Marley, M. S., Freedman, R. S., Lodders, K., and Fortney, J. J. (2009). Atmospheric Sulfur Photochemistry on Hot Jupiters. *ApJL*, 701:L20–L24.
- Zalesky, J. A., Line, M. R., Schneider, A. C., and Patience, J. (2019). A Uniform Retrieval Analysis of Ultra-cool Dwarfs. III. Properties of Y Dwarfs. *ApJ*, 877(1):24.
- Zeng, L. and Sasselov, D. (2013). A Detailed Model Grid for Solid Planets from 0.1 through 100 Earth Masses. *PASP*, 125(925):227.
- Zhang, M., Knutson, H. A., Kataria, T., Schwartz, J. C., et al. (2018). Phase Curves of WASP-33b and HD 149026b and a New Correlation between Phase Curve Offset and Irradiation Temperature. *AJ*, 155(2):83.
- Zharkov, V. N. (1983). Models of the Internal Structure of Venus. *Moon and Planets*, 29(2):139–175.
- Zhou, Y., Apai, D., Bedin, L. R., Lew, B. W. P., et al. (2020). Cloud Atlas: High-precision HST/WFC3/IR Time-resolved Observations of Directly Imaged Exoplanet HD 106906b. *AJ*, 159(4):140.
- Zurlo, A., Vigan, A., Galicher, R., Maire, A. L., et al. (2016). First light of the VLT planet finder SPHERE. III. New spectrophotometry and astrometry of the HR 8799 exoplanetary system. *A&A*, 587:A57.

A

Retrieval of 2MASS J2339+1352 without Na and K

In Figures A.1 and A.2, we show the results of the retrieval of 2MASS J2339+1352 without Na and K. The results are consistent with the retrieval which includes Na and K, as discussed in Section 2.6. However, when K is not included, the spectral feature at $\sim 1.25 \mu\text{m}$ is not fitted. The retrieved model parameter values are shown in Table A.1

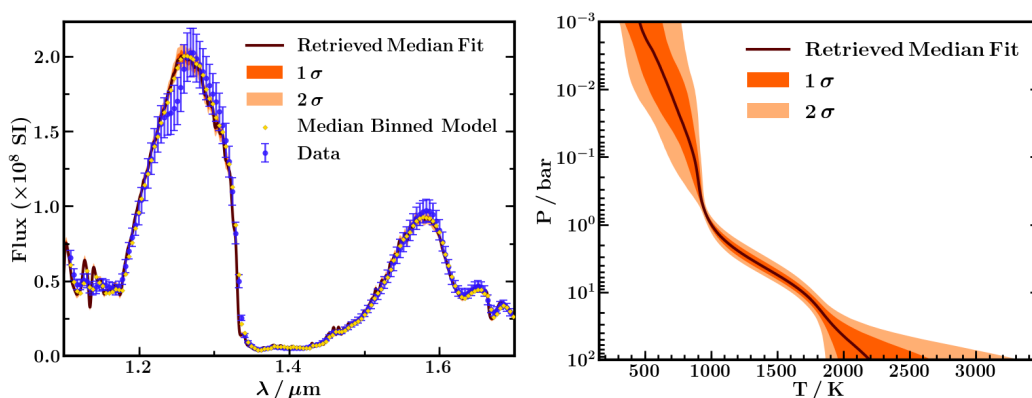


Fig. A.1 Spectrum and P - T profile retrieved for 2MASS J2339+1352 without including Na and K in the retrieval model. Left: The median retrieved spectrum (maroon line) and 1σ and 2σ confidence intervals (dark and light orange shading, respectively). Data points are shown by blue circles, and error bars depict the median retrieved tolerance. Yellow diamonds show the median binned model. Flux axis is shown in SI units ($\text{Wm}^{-2}\text{m}^{-1}$). Right: Median retrieved P - T profile (maroon line) and 1σ and 2σ confidence intervals (dark and light orange shading, respectively).

Table A.1 A summary of the retrieved atmospheric properties of 2MASS J2339+1352 without including Na and K in the retrieval. These values are consistent with the results of the retrieval which includes Na and K (Section 2.6).

Parameter	Retrieved value
$\log(X_{\text{H}_2\text{O}})$	-3.88 ± 0.08
$\log(X_{\text{CH}_4})$	-4.5 ± 0.1
$\log(X_{\text{NH}_3})$	< -5.9
$\log(X_{\text{CO}})$	< -3.7
$T_{3.2\text{b}} / \text{K}$	1230^{+130}_{-110}
R/d	$0.059^{+0.004}_{-0.003}$
$\log(g)$	3.9 ± 0.2
x_{tol}	$8.1^{+0.2}_{-0.08} \%$

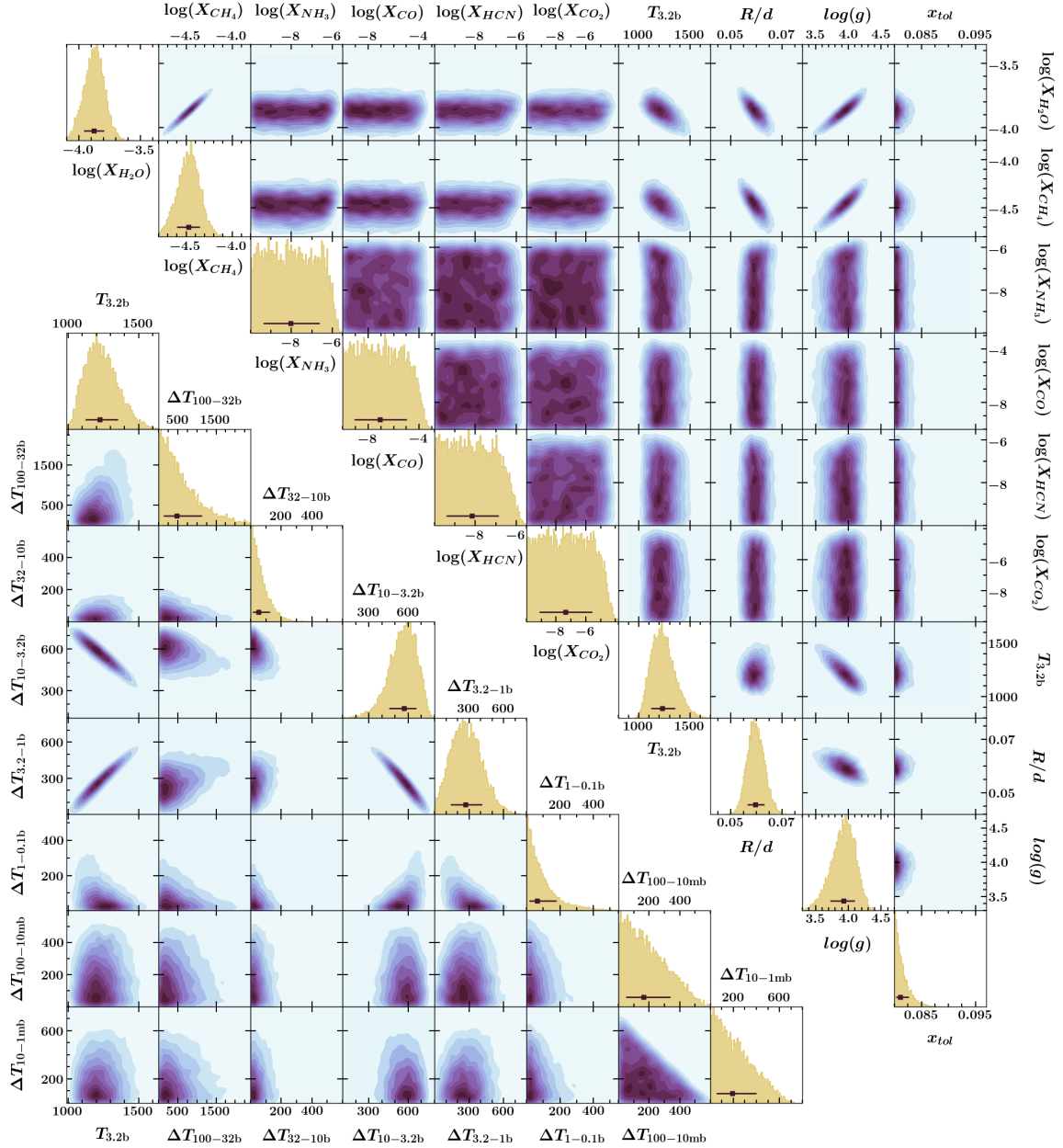


Fig. A.2 Marginalised posterior probability distributions from the retrieval of 2MASS J2339+1352 without Na and K. 1D marginalised posteriors are shown for each parameter along the diagonals, with median values and 68% confidence intervals shown by the dark squares and error bars, respectively.

B

Equilibrium TiO Chemistry & High-Resolution Spectroscopy

B.1 Equilibrium Chemistry Calculations

In the equilibrium chemistry calculations performed using the HSC CHEMISTRY software package, we use the species given in Bond et al. (2010) and Harrison et al. (2018) and include additional relevant species, as listed in Table B.1. Although potassium and vanadium are not present in the equilibrium chemistry calculations, we include them in our atmospheric models by giving them the same vertical profiles as sodium and titanium, respectively, scaled according to the solar K/Na and V/Ti ratios, respectively.

B.2 Effect of Temperature Gradient on High-Resolution Spectra

Beyond line position accuracy, detecting a chemical signature from high-resolution Doppler spectra with cross-correlation methods also requires the planetary spectral features to be sufficiently strong. A significant factor in determining the strength of features in a spectrum is the atmospheric temperature gradient; a steeper temperature slope results in stronger absorption or emission lines (depending on the direction of the gradient).

Here, we consider the effect of the temperature gradient on line strength in high-resolution spectra. Figure B.1 shows high-resolution spectra for two different temperature gradients relative to an isotherm (red and blue lines correspond to the steep and shallow

Table B.1 Species added to the HSC CHEMISTRY equilibrium chemistry calculations, on top of those used in Bond et al. (2010) and Harrison et al. (2018). All species listed here are in the gas phase.

Element	Species added
H	H^- , H^+ , H_2^- , H_2^+ , H_3^+ , H_3 , $(H_3)_2$, $H(H_3)$
O	O^- , O^+ , O^{-2} , O_2^- , O_2^+ , O_2^{-2} , O_3
C	C^- , C^+ , C_2^- , C_2^+ , C_2 , C_3 , C_4 , C_5 , C_6 , C_7 , C_8 , C_{60} , C_{70}
N	N^- , N^+ , N_2^- , N_2^+ , N_3^- , N_3
Ti	Ti^- , Ti^+ , Ti^{3+} , Ti_2
Na	Na , Na^- , Na^+ , Na_2
Other	OH , OH^- , OH^+ , C_2H_2 , C_2H_4 , e^-

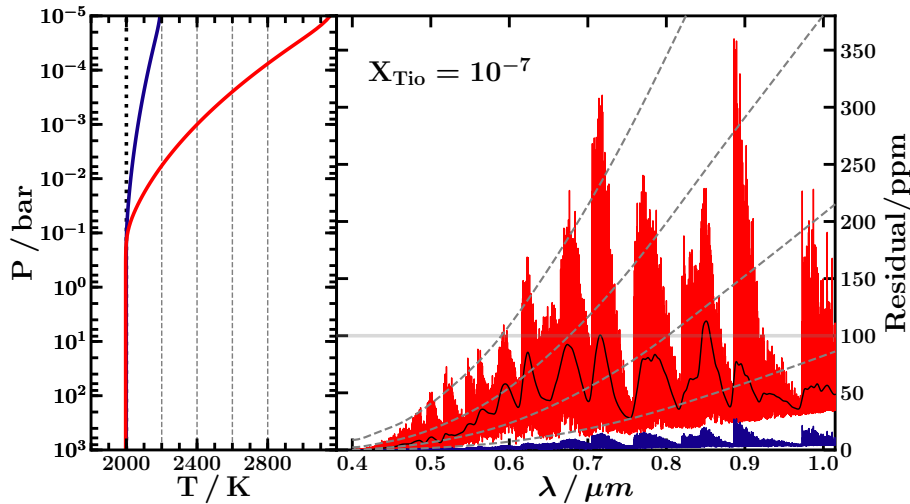


Fig. B.1 Line strengths of high-resolution ($R \sim 10^5$) spectra compared to a blackbody spectrum for different temperature gradients. Residuals are calculated as the planet-star flux ratio of the atmosphere in question minus the planet-star flux ratio of an atmosphere whose P - T profile is a 2000 K isotherm (dashed black line in left panel). Right panel: red and blue residuals correspond to the red and blue P - T profiles in the left panel, respectively. Dashed grey lines correspond to isothermal P - T profiles at 2200 K, 2400 K, 2600 K and 2800 K, respectively (shown by dashed grey lines in left panel). The solid black line is the residual for the same spectra as the red line, but with both spectra smoothed by a Gaussian of width 2.3 nm (similar to the PSF of HST/WFC3) to show representative line strengths for low-resolution spectra. The 100 ppm level is shown by the solid light grey line. These models only include opacity from TiO and CIA to highlight the TiO spectral lines. A constant-with-depth TiO mixing ratio of 10^{-7} is used.

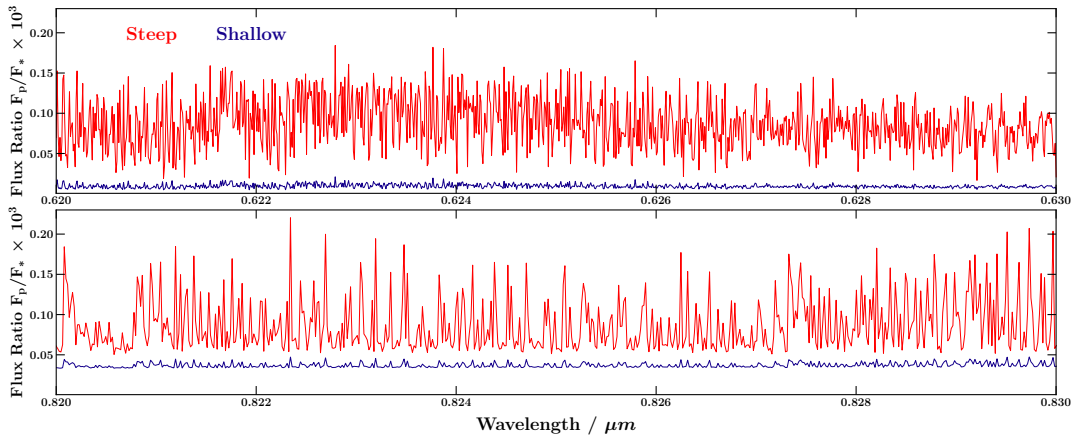


Fig. B.2 High-resolution ($R \sim 10^5$) model spectra corresponding to a steep (red) and shallow (blue) P - T profile (steep and shallow P - T profiles are shown in the left panel of Figure B.1 in red and blue, respectively). The spectra are calculated in the same way as in Figure B.1. Each panel spans $0.01 \mu\text{m}$ in the range 0.62 - $0.83 \mu\text{m}$ to give an overview of the differences in line strength between the two spectra in this range.

temperature gradients, respectively). It is clear that the steeper temperature gradient results in significantly stronger features. This suggests that chemical signatures are acutely sensitive to the temperature gradient, especially at high resolution. For example, a 400 K temperature difference at 1 mbar can cause differences in the spectrum of up to 200 ppm, which may be observable. Conversely, the absence of any detectable chemical signatures in a high-resolution Doppler spectrum could be the result of a P - T profile which is very close to isothermal. Although this is also true of low-resolution spectra, high-resolution spectra are more sensitive to temperature gradient and a lack of spectral features could potentially place a tighter constraint on this gradient compared to low-resolution spectra. This can be seen from Figure B.1; the solid black line in the right panel shows the residual spectrum at lower-resolution (to generate this, the spectra used to calculate the red line are smoothed by a Gaussian of width 2.3 nm before calculating the residual, to represent smoothing by the PSF of HST/WFC3). By comparing the high-resolution (red) and low-resolution (black) residuals, we see that the features are smoothed out and weakened at low-resolution and, as such, high-resolution spectra are more sensitive to shallow temperature gradients given a fixed observation sensitivity. This effect can be seen in greater detail in Figure B.2, which shows a zoomed-in view of the high-resolution spectra corresponding to the blue and red P - T profiles from figure 6.

Figure B.1 also demonstrates that high-resolution spectra are sensitive to very low pressures in the atmosphere. The dashed grey lines in the right panel correspond to

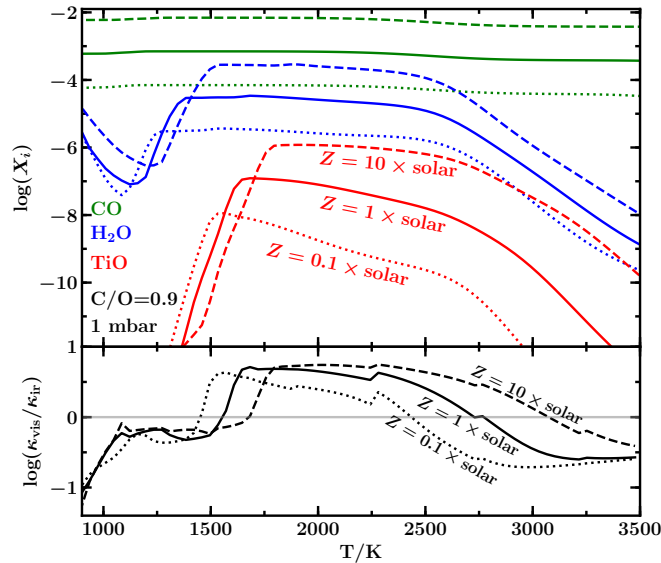


Fig. B.3 Top panel: abundances of TiO (red), H₂O (blue) and CO (green) as a function of temperature for metallicities of 0.1, 1 and 10× solar (dotted, solid and dashed lines, respectively). Abundances are shown for a pressure of 1 mbar and a C/O ratio of 0.9. Lower panel: $\kappa_{\text{vis}}/\kappa_{\text{ir}}$ for metallicities of 0.1, 1 and 10× solar (dotted, solid and dashed lines, respectively), also evaluated at 1 mbar and C/O=0.9.

isotherms at 2200 K, 2400 K, 2600 K and 2800 K, and their crossing points with each residual spectrum indicate the temperatures probed by the spectrum at those wavelengths. For example, the strongest features in the red spectrum cross the spectrum corresponding to 2800 K, showing that this high-resolution spectrum is sensitive down to pressures of $\sim 10^{-4}$ bar or lower (i.e. the pressure at which the temperature of the red P - T profile is 2800 K). Conversely, the low-resolution residual spectrum does not probe temperatures hotter than ~ 2600 K, which corresponds to a pressure of $\sim 3 \times 10^{-4}$ bar for this P - T profile, and does so with a significantly smaller signal.

B.3 Effect of metallicity on equilibrium chemistry

Figure B.3 shows the effect of metallicity on the equilibrium abundances of TiO, H₂O and CO as well as $\kappa_{\text{vis}}/\kappa_{\text{ir}}$. As expected, the abundances increase with metallicity. Furthermore, as metallicity increases, the partial pressure of TiO also increases and the temperatures at which TiO is depleted by condensation or thermal dissociation also increase. As a result, $\kappa_{\text{vis}}/\kappa_{\text{ir}}$ peaks at higher temperature for higher metallicity.



Optimal targets for rocky exoplanet thermal emission

In Table C.1, we list the known rocky exoplanets whose thermal emission in secondary eclipse can be observed to $S/N=3$ in fewer than 10 eclipses at $R \sim 10$. We have explored the potential for atmospheric characterisation of LHS 3844 b and GJ 1132 b in Section 6.4 and found that as few as 4 MIRI LRS eclipses are sufficient to detect species such as CO_2 and H_2O depending on the composition of the atmosphere. This list of promising targets therefore represents a population of rocky exoplanets whose atmospheres may be readily characterised in thermal emission using JWST MIRI.

Table C.1 Properties of known rocky exoplanets whose thermal emission in secondary eclipse can be measured to $S/N=3$ (at $R \sim 10$) in $E_{S/N=3} \leq 10$ eclipses with MIRI LRS (see Section 6.3), listed in order of observability.

Planet	$R_p (R_\oplus)$	$T_{eq} (K)$	$R_s (R_\odot)$	$T_{eff} (K)$	K mag	$E_{S/N=3}$	Refs
55 Cnc e	1.92	2381	0.96	5250	4.01	0.01	1,2,3
LHS 3844 b	1.30	809	0.19	3036	9.14	0.16	1,4
HD 3167 b	1.70	1752	0.86	5261	7.07	0.17	1,5
HD 219134 b	1.60	1020	0.78	4699	3.26	0.17	1,6
K2-141 b	1.54	2046	0.67	4373	8.40	0.19	1,7
GJ 9827 b	1.58	1186	0.60	4340	7.19	0.26	1,8
HD 213885 b	1.75	2138	1.10	5978	6.42	0.28	1,9
GJ 1252 b	1.19	1091	0.39	3458	7.92	0.29	1,10
LTT 3780 b	1.33	891	0.37	3331	8.20	0.48	1,11
HD 219134 c	1.51	786	0.78	4699	3.26	0.55	1,6
HD 80653 b	1.61	2421	1.22	5838	8.02	0.59	1,12,13
Kepler-21 b	1.64	2034	1.90	6305	6.95	0.73	1, 14
L 168-9 b	1.39	985	0.60	3800	7.08	0.97	1,15
HD 15337 b	1.70	993	0.84	5131	7.04	1.23	1,16
GJ 1132 b	1.13	586	0.21	3270	8.32	1.32	1,17
GJ 357 b	1.22	528	0.34	3505	6.47	1.64	1,18
K2-291 b	1.59	1403	0.90	5520	8.35	1.85	1,19
L 98-59 c	1.35	516	0.31	3412	7.10	2.20	1,20
TOI-1235 b	1.74	758	0.63	3872	7.89	2.47	1,21
LTT 1445 A b	1.38	438	0.28	3337	6.50	2.59	1,22
Kepler-10 b	1.47	2190	1.06	5708	9.50	2.74	1,23
WASP-47 e	1.82	2209	1.16	5576	10.19	3.25	1,24
GJ 9827 c	1.24	821	0.60	4340	7.19	3.54	1,8
CoRoT-7 b	1.58	1766	0.82	5259	9.81	3.85	1,25,26
K2-265 b	1.71	1427	0.98	5477	9.26	3.87	1,27
K2-229 b	1.16	1964	0.79	5185	9.05	3.94	1,28
Kepler-93 b	1.48	1140	0.92	5655	8.37	4.13	1,3,29
EPIC 220674823 b	1.52	2291	0.87	5470	10.34	4.14	1,30
K2-216 b	1.75	1104	0.72	4503	9.72	4.43	1,31
K2-111 b	1.90	1233	1.23	5730	9.38	5.69	1,32
K2-36 b	1.43	1351	0.72	4916	9.45	5.79	1,33
LHS 1140 c	1.28	436	0.21	3216	8.82	9.73	1,34
L 98-59 d	1.57	408	0.31	3412	7.10	9.84	1,20

Values obtained from: 1. Skrutskie et al. (2006), 2. Demory et al. (2016b), 3. Stassun et al. (2019), 4. Vanderspek et al. (2019), 5. Christiansen et al. (2017), 6. Gillon et al. (2017a), 7. Barragán et al. (2018), 8. Rice et al. (2019), 9. Espinoza et al. (2020), 10. Shporer et al. (2020), 11. Cloutier et al. (2020a), 12. Frustagli et al. (2020), 13. Gaia Collaboration et al. (2018), 14. López-Morales et al. (2016), 15. Astudillo-Defru et al. (2020), 16. Dumusque et al. (2019), 17. Bonfils et al. (2018), 18. Luque et al. (2019), 19. Kosiarek et al. (2019), 20. Cloutier et al. (2019a), 21. Cloutier et al. (2020b), 22. Winters et al. (2019), 23. Weiss et al. (2016), 24. Almenara et al. (2016), 25. Barros et al. (2014), 26. Dai et al. (2019), 27. Lam et al. (2018), 28. Santerne et al. (2018), 29. Dressing et al. (2015), 30. Guenther et al. (2017), 31. Persson et al. (2018), 32. Fridlund et al. (2017), 33. Damasso et al. (2019), 34. Ment et al. (2019).